

Flow-Induced Vibration of Circular and Square Cylinders with Low Mass and Damping

by

Jisheng Zhao

A Thesis submitted to Monash University
for the degree of
Doctor of Philosophy

July 2012

Department of Mechanical and Aerospace Engineering
Monash University

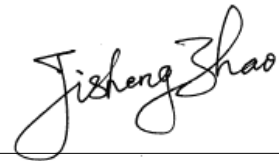
Notices

1. Under the Copyright Act 1968, this thesis must be used only under the normal conditions of scholarly fair dealing. In particular no results or conclusions should be extracted from it, nor should it be copied or closely paraphrased in whole or in part without the written consent of the author. Proper written acknowledgement should be made for any assistance obtained from this thesis.
2. I certify that I have made all reasonable efforts to secure copyright permissions for third-party content included in this thesis and have not knowingly added copyright content to my work without the owner's permission.

*This thesis is dedicated to
My dear wife Qingxia,
and
My parents Lianying and Youcheng.*

Statement of Originality

I, Jisheng Zhao, declare that this thesis is my own work and contains no material that has been accepted for the award of a degree or diploma in this, or any other, university. To the best of my knowledge and belief, information derived from the published and unpublished work of others has been acknowledged in the text of the thesis and a list of references is provided in the bibliography.

A handwritten signature in black ink that reads "Jisheng Zhao". The signature is written in a cursive style with a horizontal line underneath it.

Candidate: Jisheng Zhao

Submitted: 30 Jun 2012

Abstract

This thesis investigates cross-flow flow-induced vibration of elastically mounted rigid circular and square cylinders with low mass and damping ratio over a range of flow and vibration parameters. In particular, two typical body oscillator phenomena of flow-induced vibration, vortex-induced vibration and galloping, are studied experimentally. Thus, the study consists of two main parts. The first part, using simultaneous displacement, force and vorticity measurements, investigates the dynamic response of a circular cylinder undergoing transverse free vortex-induced vibrations and controlled trajectory-following vibrations. The second part characterises the amplitude and frequency responses of a square cylinder with angle of attack variation.

Despite extensive work has been undertaken to understand the fundamental characteristics of free and forced vibrations of a circular cylinder, there are still a number of unresolved questions in the literature concerning the similarities and differences between the free and forced vibration cases. In order to directly compare these two vibration cases, a low-friction air-bearing rig and a real-time feedback control system were therefore designed and implemented in experiments. The major results obtained show that the transverse lift force and the decomposed vortex force experienced by a cylinder forced to follow the trajectory of free VIV are identical to the free vibration case, when both the total phase and the vortex phase relative to the body motion are constantly stable. However, significant differences between the two vibration cases are found at a reduced velocity located in the middle upper branch of VIV where largest-scale body vibration occur with complex switching phenomena in the total phase and the vortex phase.

The results from the second part, flow-induced vibration of a square cylinder with angle of attack variation, show that the cylinder, as expected, experiences galloping at the zero angle of attack orientation ($\alpha = 0^\circ$) and vortex-induced vibration at the diamond orientation ($\alpha = 45^\circ$). As the angle of attack is varied from 45° to 0° , the body can undergo combinations of both vortex-induced vibration and galloping in a mixed response region. In this region, the oscillation amplitude response exhibits a new branch that exceeds the responses resulting from the two body-oscillator phenomena independently. For velocities above this resonant region, the body oscillation frequency splits into two diverging branches. Further, analysis of the amplitude reveals that the transition between galloping and vortex-induced vibrations occurs over a narrow range of angle of incidence. Despite the rich set of states found in the parameter space the vortex shedding modes remain very similar to those found previously in vortex-induced vibration.

Acknowledgements

Having just completed my PhD thesis, I feel like I have accomplished one of the most challenging activities of my life. One of the joys of completion is to look over and remember all the best and worst moments of my doctoral journey that have been shared with many people who have helped and supported me along this long but fulfilling road.

First of all, I would like to acknowledge the guidance and support from my primary supervisor, Prof. John Sheridan. John provided me the opportunity to do this research project. He steadfastly supported my research, and patiently taught me how to think logically and scientifically. He also provided significant financial support which helped cover my living expenses and allowed me to attend scientific conferences. His understanding, encouraging and constructive comments have been of great value for me to proceed through the doctoral study and complete this thesis.

Secondly, I would like to extend my sincere thanks to my co-supervisor Dr. David Lo Jacono. David has been a strong and supportive adviser to me. I have learnt a lot working with David and appreciate the time and energy that he invested in my research project.

I would also like to acknowledge the financial support from Australian Research Council (ARC) Discovery Project (DP0774525) which allowed me to undertake this research. Throughout my candidature, I also received scholarships in the forms of a Faculty of Engineering International Postgraduate Research Scholarship (FEIPRS) and a Monash Departmental Scholarship, and therefore I would like to acknowledge the Engineering Faculty and the Department of Mechanical and Aerospace Engineering for their financial support.

I would like to take this opportunity to extend my thanks to the the Department of Mechanical and Aerospace Engineering's staff, especially Helen Frost, Yvonne Arnold, Alex Bain, and Hugh Venables, for their support. I must also acknowledge the creative workmanship of the mechanical engineering workshop staff, especially Heinrich Nowak, Nat DeRose, Ken Sheridan, and Mark Symonds, who constructed my experimental rigs and modes. I would like to thank Dr. Chao Chen, Dr. Hoam Chung and Mr. Richard Chen for their help in the design of motion control system. Dr. Andreas Fouras is thanked for his assistance in providing some experimental equipments, and in particular his work on the PIV software. I would also like to acknowledge the wind tunnel group, especially Dr. David Burton, Mr. Steve Dunell, Mr. Don McMaster, and Mr. Michael Easton, for their technical support and assistance in providing some experimental equipments.

I wish to thank my colleagues for many constructive discussions over the years. Many have become close friends. I must thank Dr. Justin Leontini for his support and countless critical discussions on the topic of flow-induced vibration. For making my candidature such an enjoyable experience, I am grateful to my friends: Mr. Michael Sherry, Mr. Andras Nemes, Mr. Alexander Radi, Mr James Venning, Mr. Anirudh Rao, Dr. Martin Griffith, Dr. Mehdi Nazarinia and Dr. Elham Tolouei.

I am forever indebted to my family who has always been there encouraging me. I just would not have been capable of completing this thesis without the unwavering support of my family: Youcheng, Lianying, Chunchun, Suhua, Meiping, Jigui and Huixiu. My thanks go to my cousins, Ronghua and Chengchang, for their moral support all the time.

Lastly, but most importantly, I must extend my heartfelt gratitude to my wife, Qingxia. Your love, support and understanding continue to astound me, and inspire me. Thank you.

Nomenclature

English Symbols

Symbol	Description
2D	two dimensional
3D	three dimensional
A	Oscillation amplitude
A^*	Normalised oscillation amplitude
A_{10}^*	Mean of the top 10 percent of the normalised oscillation amplitude
A_{\max}^*	Maximum normalised oscillation amplitude
c	Damping coefficient
c_{crit}	Critical damping coefficient
C	Spring index
C_A	Hydrodynamic mass coefficient
C_D	Drag force coefficient
C_L	Lift force coefficient
C_{vortex}	Vortexforce coefficient
C_y	Transverse lift force coefficient
CCD	charge coupled device
D	Cylinder diameter
DAC	digital-to-analog converter
DNS	Direct Numerical Simulation
e	Error
e_{ss}	Steady-state error
e_y	Position tracking error
E	Youngs modulus of the material
E_{in}	Energy input

Continued on next page...

Continued from previous page...

Symbol	Description
E_d	Dissipated energy
f	Oscillation frequency (Hz)
f_N	Natural frequency of the system in still fluid (Hz)
f_{Nvac}	Natural frequency of the system in vacuum (Hz)
f_{na}	Natural frequency of the system in air (Hz)
f_{nw}	Natural frequency of the system in water (Hz)
f_P	Pump frequency of the water channel facility (Hz)
f_{St}	Vortex shedding frequency of a stationary cylinder (Hz)
f^*	Normalised oscillation frequency, $f^* = f/f_N$
f_{vacuum}^*	Normalised oscillation frequency, $f_{vacuum}^* = f/f_{Nvac}$
f_{water}^*	Normalised oscillation frequency, $f_{water}^* = f/f_{nw}$
F	External force
F_d	Drag force
F_D	Drag force
F_L	Total lift force
F_{vortex}	Vortex force
F_y	Transverse lift force
FIV	Flow-induced vibration
FLAIR	Fluids Laboratory for Aeronautical and Industrial Research
G	Shear modulus of the material
H	Frontal projected length of the cylinder
Hz	Hertz
k	Spring constant
L	Immersed length of the cylinder
L/D	cylinder length/diameter ratio
LDV	laser Doppler velocimetry
m_A	Added mass
m_d	Displaced fluid mass, $\pi\rho D^2l/4$
m_{eff}	Effective mass
m^*	Mass ratio
\mathcal{M}	camera magnification factor (px/mm)

Continued on next page...

Continued from previous page...

Symbol Description

PID	Proportional-Integral-Derivative
PIV	particle image velocimetry
px	pixels
Re	Reynolds number based on free-stream velocity and the frontal projected length of the cylinder
St	Strouhal number
t	Time
\mathcal{T}	Temperature ($^{\circ}\text{C}$)
T	Oscillation period
TTL	transistor-transistor logic
U, V, W	Velocity components in the x, y and z directions respectively
U_{\max}	Peak velocity of an oscillating cylinder
U_{∞}	Free-stream velocity
V	Voltage
V_{EX}	Excitation voltage
V_{out}	Output voltage
VIV	Vortex-induced vibration
V_R	Relative velocity
x, y, z	rectangular Cartesian coordinates in physical space (mm)
X, Y, Z	rectangular Cartesian coordinates in image space (px)

Greek Symbols

Symbol Description

\S	Thesis section
\int	Integration
α	Angle of attack
β	Relative angle
δ	standard deviation
$\Delta x, \Delta y, \Delta z$	change in x, y, z location in physical space (mm)
$\Delta X, \Delta Y$	change in X, Y location in image space (px)
Δt	PIV time interval separating each image pair (ms)
Γ	circulation
η	Free decay rate

Continued on next page...

Continued from previous page...

Symbol	Description
λ	Wavelength
λ^*	Normalised wavelength
μ	Dynamic viscosity ($\text{kg.m}^{-1}.\text{s}^{-1}$), Floquet multiplier
ν	Kinematic viscosity, μ/ρ ($\text{m}^2.\text{s}$)
ω	Angular oscillation frequency
ω_d	Damped angular oscillation frequency
ω_{na}	Angular natural frequency in air
ω_{nw}	Angular natural frequency in water
$\omega_x, \omega_y, \omega_z$	Vorticity components along the x, y and z axis respectively (s^{-1})
ψ	Angle between translational oscillation and free-stream flow
ρ	Density (kg.m^{-3})
σ	Stress
θ	Angular displacement
ε	Strain of the material
ϕ	Phase angle bwteen the force and the cylinder displacement
ϕ_{total}	Phase angle bwteen the transverse lift force and the cylinder displacement
ϕ_{vortex}	Phase angle bwteen the vortex force and the cylinder displacement
ζ	Structural damping ratio
ζ_a	Structural damping ratio in air
ζ_w	Structural damping ration in water

Subscripts

Symbol	Description
<i>cyl</i>	cylinder
<i>i, j, k</i>	spatial coordinate indices
<i>max</i>	maximum addition value
<i>rand</i>	random component
<i>rms</i>	root mean square value
<i>t</i>	translational oscillation component
∞	free-stream value

Superscript

Symbol	Description
/	fluctuating value

Contents

1	Introduction	1
1.1	General overview	1
1.2	Structure of the thesis	3
2	A Review of the Literature	5
2.1	Introduction	5
2.2	Flow past a stationary circular cylinder	6
2.2.1	Flow regimes	6
2.2.2	Fundamentals of vortex shedding	8
2.3	Vortex-induced vibration of a circular cylinder	11
2.3.1	Amplitude and frequency responses	12
2.3.1.1	Lock-in	15
2.3.2	Fluid forces, phases and wake modes	16
2.4	Forced oscillations of a circular cylinder	23
2.4.1	Fluid forces and wake modes	23
2.4.2	Energy transfer and prediction of free vibration response	26
2.5	Galloping response of a square cylinder	33
2.6	Summary of the review and the questions for research	38
3	Experimental Methodology	41
3.1	Introduction	41
3.2	Flow system	41
3.3	Air bearing system	43
3.4	Motion control system	47
3.4.1	PID controller and controller tuning	48
3.5	Cylinder models	54
3.6	Experimental measurement systems	55
3.6.1	Data acquisition (DAQ) system	55
3.6.2	Linear displacement measurement	56
3.6.3	Force measurement	58
3.6.4	Flow visualization – Particle Image Velocimetry (PIV) system	66
3.6.5	Temperature measurement	71
3.7	Experimental procedures	71
3.7.1	Structural damping	71
3.7.2	Free decay test in air	71
3.7.2.1	Free decay test in still water	73
3.8	Chapter summary	77

4	Vortex-Induced Vibration of Circular Cylinders	79
4.1	Introduction	79
4.2	Experimental validation for VIV of a circular cylinder	79
4.2.1	Experimental details	79
4.2.2	Amplitude and frequency responses	80
4.2.3	Fluid forces and phases	82
4.3	Comparison of a free cylinder and a tracking cylinder	85
4.3.1	Experimental details	85
4.3.2	Dynamic response of free vibrations	87
4.3.3	Comparison between free and forced vibrations	87
4.4	Summary of the chapter	103
5	Flow-Induced Vibrations of A Square Cylinder	111
5.1	Introduction	111
5.2	FIV of a square cylinder with angle of attack variation	112
5.2.1	Experimental details	112
5.2.2	VIV response at $\alpha = 45^\circ$	112
5.2.2.1	Amplitude, frequency and phase responses	112
5.2.2.2	Wake modes	116
5.2.3	Galloping response at $\alpha = 0^\circ$	119
5.2.3.1	Amplitude and frequency responses	119
5.2.3.2	Wake modes	120
5.2.4	Dynamic response with varying angle of attack	122
5.2.4.1	Amplitude response	122
5.2.4.2	Frequency response	125
5.2.4.3	Wake modes	128
5.2.5	Intermittency	131
5.3	VIV of a diamond cylinder with different mass ratios	131
5.3.1	Experimental details	131
5.3.2	Amplitude and frequency responses	134
5.3.3	Wake mode transition	134
5.4	Summary of the chapter	139
6	Conclusions and Recommendations for Future Work	143
6.1	Conclusions	143
6.1.1	Vortex-induced vibration of a circular cylinder	143
6.1.2	Flow-induced vibration of a square cylinder	144
6.2	Recommendations for future work	145
6.2.1	Vortex induced vibration of a circular cylinder	145
6.2.2	Flow-induced vibration of a square cylinder	145
A	Wheatstone Bridge	147
	Bibliography	149

List of Tables

3.1	Effects of increasing independent PID controller parameters	51
3.2	PID gain tuning using Ziegler-Nichols frequency response method.	51
3.3	Geometric parameters of the rigid smooth cylinder models.	54
3.4	Specifications of the PCO cameras used in the present study.	67
5.1	Experimental parameters of a diamond cylinder with different mass ratios.	133

List of Figures

2.1	Flow regimes of a smooth circular cylinder at low Reynolds numbers. . .	6
2.2	Formation of vortex shedding from a circular cylinder.	9
2.3	Strouhal number - Reynolds number relationship for circular cylinders. .	9
2.4	Visualisation of oblique shedding and parallel shedding.	10
2.5	Comparison of the forces between oblique and parallel shedding modes of a stationary circular cylinder.	11
2.6	Definition sketch for cross-flow VIV of a circular cylinder.	12
2.7	Amplitude and frequency responses of VIV of a circular cylinder.	13
2.8	Two distinct types of amplitude response of VIV of a circular cylinder. .	14
2.9	Frequency response of lock-in region of a circular cylinder undergoing VIV in air and in water.	15
2.10	State-selection diagram for laminar wakes of a circular cylinder under- going forced sinusoidal oscillations.	16
2.11	A diagram of force decomposition.	18
2.12	Maps of wake mode regimes a circular cylinder undergoing sinusoidally- driven oscillations.	19
2.13	Wake modes near the synchronisation region of an oscillating cylinder. .	19
2.14	VIV response of a circular cylinder with $m^* = 8.63$ and $\zeta = 1.51 \times 10^{-3}$.	20
2.15	Wake modes of a freely vibrating circular cylinder with a low mass- damping ratio.	21
2.16	Characterisation diagram for VIV response of a circular cylinder with low mass and damping.	22
2.17	Total and vortex phases for free vibration at low mass and damping. . .	24
2.18	Comparison of vorticity fields between a freely-vibrating circular cylinder and a sinusoidally-driven cylinder.	24
2.19	Contours of the magnitude of the total force and the vortex force. . . .	26
2.20	Contours of the total phase and the vortex phase.	27
2.21	Maps of wake mode regimes for sinusoidally-driven circular cylinders. . .	28
2.22	Vorticity fields of a sinusoidally-driven circular cylinder.	29
2.23	Contours of forced-oscillation transverse lift in phase with velocity. . . .	31
2.24	Contours of the transverse lift force in phase with velocity.	32
2.25	Amplitude response prediction for a freely vibrating circular cylinder. . .	32
2.26	Cross-flow galloping of an ice-coated cable.	33
2.27	Cross-flow galloping model of a square cylinder.	34
2.28	The mean of the transverse lift coefficient versus the angle of attack of a square cylinder at $Re = 22\,300$	37
2.29	Amplitude response of a square cylinder experiencing galloping.	37
3.1	Schematic views and a photograph of the water channel facility.	42

List of Figures

3.2	LDV measurement of the free-stream velocity.	43
3.3	Experimental arrangement for free FIV of a cylindrical body	44
3.4	The air bearing system transversely placed on top of the water channel	45
3.5	Schematic of orifice and porous media air bearings	46
3.6	Reduction of one-pair-spring-one-mass system.	46
3.7	Diagram of Quanser Q4 H.I.L motion control system elements	48
3.8	The motion control rig used for forced oscillation experiments.	48
3.9	A block diagram of a closed-loop motion control system	49
3.10	Block diagram of a PID servo position control system	50
3.11	Step response of a control system	50
3.12	Step response of PID experimental tuning.	52
3.13	Time trace of real-time motion tracking.	53
3.14	A schematic showing dimensions of the cylinder models	55
3.15	Schematic showing the square cylinder with variable angle of attack. . .	56
3.16	A diagram showing LVDT circuit.	56
3.17	Examples of LVDT measurement.	57
3.18	Photographs showing the force balance and the signal amplifier.	59
3.19	A diagram showing Wheatstone bridge.	59
3.20	A photograph showing the experimental set-up for static force calibration.	61
3.21	A typical force balance static calibration.	62
3.22	Lift force measurement of a circular cylinder at different Reynolds numbers.	63
3.23	Schematic for force measurement correction of a cross-flow FIV system.	64
3.24	Time traces of the displacement and the lift force of a circular cylinder.	65
3.25	Analysis algorithm of cross-correlation digital PIV recordings	66
3.26	Photographs showing the PIV system set-up.	69
3.27	An example of real-time phase-locked sampling of PIV measurements. .	70
3.28	PIV phase-band averaging method.	70
3.29	Response of an underdamped ($0 \leq \zeta < 1$) single-DOF system.	72
3.30	An example of free decay tests of a circular cylinder of $m^* = 2.4$	76
4.1	Comparison of experimental results of a circular cylinder with $m^* = 2.4$.	81
4.2	Time traces of the dynamic response of a circular cylinder.	83
4.3	Force and phase angle variation with the reduced velocity of a circular cylinder.	84
4.4	Time traces of the total phase and the vortex phase at different reduced velocities of a circular cylinder.	86
4.5	The amplitude and frequency responses of freely vibrating circular cylin- ders.	88
4.6	Force and phase angle variation with the reduced velocity of circular cylinders.	89
4.7	The amplitude response of a circular cylinder with $m^* = 2.66$	90
4.8	Power spectra of the cylinder displacement response at $m^* = 2.66$	90
4.9	Time traces of the fluid forces and phases of free and tracking vibrations of a cylinder.	91
4.10	Phase-averaged PIV results of a circular cylinder with $m^* = 2.66$	92
4.11	Time traces of the forces of free and tracking cylinders at $U^* = 4.93$. . .	93
4.12	The presence of $2S$ wake mode for both free and forced cylinders.	94
4.13	Time traces of the forces of a sinusoidally-driven cylinder at $\lambda^* = 4.90$. .	96
4.14	Co-existence of $2S$ and $2P_o$ modes of a sinusoidally-driven cylinder. . . .	97
4.15	Time traces of the forces of free and forced cylinders at $U^* = 5.91$	99

4.16 Co-existence of $2S$ and $2P_o$ wake modes in the upper branch of free vibration.	100
4.17 Time traces of the phases of tracking vibration of a cylinder at $\lambda^* = 5.45$	101
4.18 Co-existence of $2S$ and $2P$ wake modes in tracking forced vibration.	101
4.19 Wake modes of a cylinder undergoing free and tracking vibrations at $\lambda^* = 5.45$	102
4.20 Time traces of the forces of a sinusoidally-driven cylinder at $\lambda^* = 5.45$	104
4.21 Wake modes of a cylinder undergoing free and sinusoidally-driven vibrations at $\lambda^* = 5.45$	105
4.22 Time traces of the forces of a cylinder undergoing free and tracking vibrations at $U^* = 8.05$	106
4.23 Presence of the $2P$ mode in both free and tracking vibrations of a cylinder at $\lambda^* = 6.31$	107
4.24 Time traces of the forces of a cylinder undergoing sinusoidally-driven vibration at $\lambda^* = 6.31$	108
4.25 Presence of $2P$ wake mode of a cylinder undergoing a free and sinusoidally-driven vibrations at $\lambda^* = 6.31$	109
5.1 Comparison of the dynamic responses of a circular cylinder and a diamond cylinder.	113
5.2 Displacement time histories of a circular cylinder and a diamond cylinder.	115
5.3 $2P$ modes of the lower branch of a circular cylinder and a diamond cylinder.	117
5.4 Galloping response of a square cylinder at $\alpha = 0^\circ$	121
5.5 Wake modes of a circular cylinder and a square cylinder at $U^* = 8$	122
5.6 Amplitude response of a square cylinder with angle of attack variation.	123
5.7 Frequency response of a square cylinder with angle of attack variation.	126
5.8 Wake mode of a square cylinder at $\alpha = 20^\circ$ and $U^* = 8$	129
5.9 Map of flow-induced vibration response of a square cylinder.	132
5.10 Intermittency response of a square cylinder at $\alpha = 7.5$	133
5.11 The amplitude and frequency responses of a diamond cylinder with different mass ratios.	135
5.12 Dynamic response of a diamond cylinder with $m^* = 15$	137
5.13 Time traces of the dynamic response of a diamond cylinder with $m^* = 15$	138
5.14 $2S \leftrightarrow 2P$ wake mode transition of a diamond cylinder.	140
A.1 A diagram of full Wheatstone bridge circuit.	147

Chapter 1

Introduction

1.1 General overview

The phenomenon of flow-induced vibration (FIV) of bluff (non-streamlined) bodies is around us. Most people have watched a flag pole or a power cable oscillating in high wind. These are examples of structural vibration due to the wind flow resulting in fluctuating forces on the bodies. Other examples of FIV of structures are more widely seen in engineering applications, such as risers (flexible pipes) and structures in the offshore oil fields, cylinder bundles in the cooling system of nuclear power plants, civil bridges, tall chimneys and buildings. The problem of FIV is critical in engineering applications due to its undesired impact on the fatigue life of structures, which can potentially lead to structural damage or catastrophic failure. One classic example of structural failure due to FIV is the original Tacoma Narrows Bridge which experienced large-scale oscillations caused by natural winds ultimately leading to its destruction in 1940. Thus, the potential risks can add substantial cost to the design of structures. (Lim & Howells 2000) note that due to the uncertainties in predictions of vortex-induced vibration designers have adopted a safety factor of 50 to 100 in the design of risers, which can lead to unnecessary use of suppression devices that cost considerably at \$400/foot. This is especially concerning when they further note that in shallow water, such as the Gulf of Mexico, the cost for 10 risers of over 500 feet in length would be \$2 Million.

In the last 50 years, extensive research has been motivated and undertaken to understand the fundamental characteristics of FIV of bluff bodies. The current state of research in the field has been dictated well in the books by (Blevins 1990), (Naudascher & Rockwell 2005), and (Païdoussis *et al.* 2010). Fundamentally, flow-induced vibration can occur in so many forms in terms of body oscillators, fluid oscillators and sources of excitation (Naudascher & Rockwell 2005). Of particular interest in this thesis, two typical body-oscillator phenomena of VIV are presented: vortex-induced vibration (VIV) and galloping. Vortex-induced vibration occurs when the vortices shed alternatively from a bluff body result in fluctuating forces that cause the flexible or elastically-mounted body to vibrate. For this reason, VIV is categorized as a type of *instability-induced excitation* (IIE) that is caused by an intrinsic flow instability, the phenomenon of vortex shedding (Naudascher & Rockwell 2005). VIV can occur for any cylindrical bluff bodies whose cross-section has an appreciable afterbody, downstream of the flow separation points (Bearman *et al.* 1987). One of the profound phenomena in VIV known as synchronization or “lock-in” occurs when the body oscillation frequency and the vortex shedding frequency are close to the natural frequency of the

system, which results in large-scale body motion or resonance. However, VIV occurs only in a discrete range of flow speeds, and it is self-limited in a sense that the body oscillation amplitudes are limited to the order of magnitude of one characteristic length (*i.e.* the diameter of a circular cylinder). Galloping, on the other hand, is a type of *movement-induced excitation* (MIE) that is caused by the aerodynamic instability of the structures under certain conditions of the fluid-structure system. Like VIV, an appreciable afterbody is also required for galloping to occur. Both VIV and galloping can co-exist under certain conditions. However, two major differences between VIV and galloping are, firstly, that galloping occurs typically for all flow speeds above a critical speed value that depends on the properties of the system, and secondly, that galloping oscillations are not self-limited where much larger amplitudes can be built up.

The current state of research in the field of VIV has focused on the fluid-structure interaction of a rigid circular cylinder constrained to oscillate transverse to a uniform free-stream. This is primarily because the geometry of a circular cylinder can be defined simply by its diameter and length without any other parametric considerations relating to the flow orientation. In addition, the axial symmetry of a circular cross-section also allows VIV to be studied in isolation from other FIV phenomena, such as galloping that arises from the aerodynamically unstable cross-sections (Blevins 1990). From an applied standpoint, VIV of circular cross-sections have received considerable attention as an important phenomenon particularly in ocean engineering where ocean currents can induce vibrations in oil risers, cable and offshore platforms.

Since a pioneering study by Feng (1968), a great deal of work has been done VIV, with experimental and numerical studies that have covered a large number of parameters involved. In order to understand, model and predict the complex coupling of the fluid-structure interaction, researchers have characterised the response of circular cylinders undergoing free and forced vibrations. Forced vibrations, as a complementary approach allowing to decouple the fluid-structure interaction, is of significant interest to provide a good insight into the fundamental characteristics of free vibrations. Comparisons between the free and forced vibration cases in the literature have shown that although both cases exhibit many characteristic similarities in the wake modes and fluid forcing, there still exist major differences in energy transfer between the fluid and the structure.

The second body-oscillator phenomenon of FIV, galloping, has also been extensively studied since Den Hartog (1932) first proposed his stability criterion (well known as the Den Hartog criterion) to estimate the susceptibility of a section to cross-flow galloping in a wind flow. Though any bluff body with non-circular cross section is susceptible to galloping, flow over a cylinder with square cross section at a zero angle of attack has been studied most frequently. Parkinson & Brooks (1961) and Parkinson & Smith (1964) have developed the foundations for the current state of the art with a model to predict galloping response of a square cylinder at zero angle of attack using a quasi-steady theory based on the lift forces acting on the stationary body with angle of attack variation. The quasi-steady theory can accurately predict the amplitude response of a square cylinder, including the critical velocity required for the onset of galloping and a velocity dependent hysteresis in the amplitude response. However, in contrast to VIV of a circular cylinder and galloping of a square cylinder at zero angle of attack, much less research has been undertaken on FIV of a square cylinder with a physical angle of attack variation.

The investigation of this thesis is composed of two components:

1. Comparison between free and forced vibrations of a circular cylinder. Investi-

gation in this part focuses on comparison of the wake modes and fluid forcing between a freely-vibrating cylinder and a motion-tracking cylinder.

2. FIV of a square cylinder with variation of angle of attack. Investigation in this part focuses on the influence of the angle of attack on the amplitude and frequency responses of FIV of a square cylinder.

1.2 Structure of the thesis

Apart from the Introduction, there are five chapters in this thesis. Each chapter begins with a brief introduction of the content, and ends with a brief summary highlighting the key discussion and findings. The thesis is structured as follows:

Chapter 2: A brief review of the relevant literature is presented in order to assess the current state of knowledge, and to highlight some key areas where unanswered questions and gaps are present.

Chapter 3: The experimental methodology used is described, including details of the water channel facilities, experimental rigs and measurement techniques.

Chapter 4: Results of vortex-induced vibration of circular cylinders with low mass and damping ratios are presented. In particular, this chapter also deals with direct comparisons between free and controlled vibrations.

Chapter 5: Flow-induced vibration of a square cylinder with angle of attack variation is investigated. This study focuses primarily on vibrational response influenced by the angle of attack variation.

Chapter 6: The overall conclusions of the thesis, summarising the most important findings from the previous chapters. In addition, potential future work for research in this area is also discussed.

Appendix A: A brief description of Wheatstone bridge circuit is given in order to provide supporting knowledge for the design of force balance used in the experiments.

Bibliography: A bibliography is provided to list all the references cited in this thesis.

Chapter 2

A Review of the Literature

2.1 Introduction

Research on flow-induced vibration of bluff bodies has been extensively undertaken in the past half century, due to its wide concern with a variety of engineering applications. A rich literature arising from the research progress has been comprehensively reviewed by Blevins (1990), Naudascher & Rockwell (2005), and Païdoussis *et al.* (2010). In this chapter, a brief literature review of research on flow-induced vibration of a bluff body is presented, aiming to describe the fundamentals and the state of art on topics that relate to the present PhD research. In particular, two typical body-oscillator phenomena of flow-induced vibration, VIV and galloping, which provide the motivation for this research, will be examined and discussed in detail.

This chapter begins with a discussion of flow past a stationary cylinder in §2.2, providing a basic insight into the flow regimes behind a circular cylinder and the mechanism of vortex shedding. Next, §2.3 presents the previous work on vortex-induced vibration of circular cylinders. This section mainly deals with the vibrational responses (*i.e.* the amplitude, frequency and phase responses) and wake modes of a freely vibrating circular cylinders. To predict and potentially suppress VIV, researchers have employed sinusoidally-driven cylinders as a complementary model. It allows them to decouple the fluid-structure interaction, to better understand fundamental aspects such as the phase difference between the fluid forces and body displacement, and the energy transfer between the fluid and the structure. Thus, a discussion on circular cylinders undergoing forced oscillations will be then given in §2.4.

The second typical body-oscillator phenomenon of flow-induced vibration, galloping, has also received extensive research attention since Den Hartog (1932) first proposed his criterion for galloping of ice-coated cables. In particular, transverse galloping of a square cylinder has been well studied by researchers (such as Parkinson & Brooks (1961); Parkinson & Smith (1964); Bearman *et al.* (1987); Blevins (1990), and many more). Parkinson & Smith (1964) proposed a quasi-steady theory that laid the foundations for the current state of the art to predict the amplitude response of galloping of a square cylinder. The state of knowledge in the field of galloping of a square cylinder is discussed lastly, in §2.5.

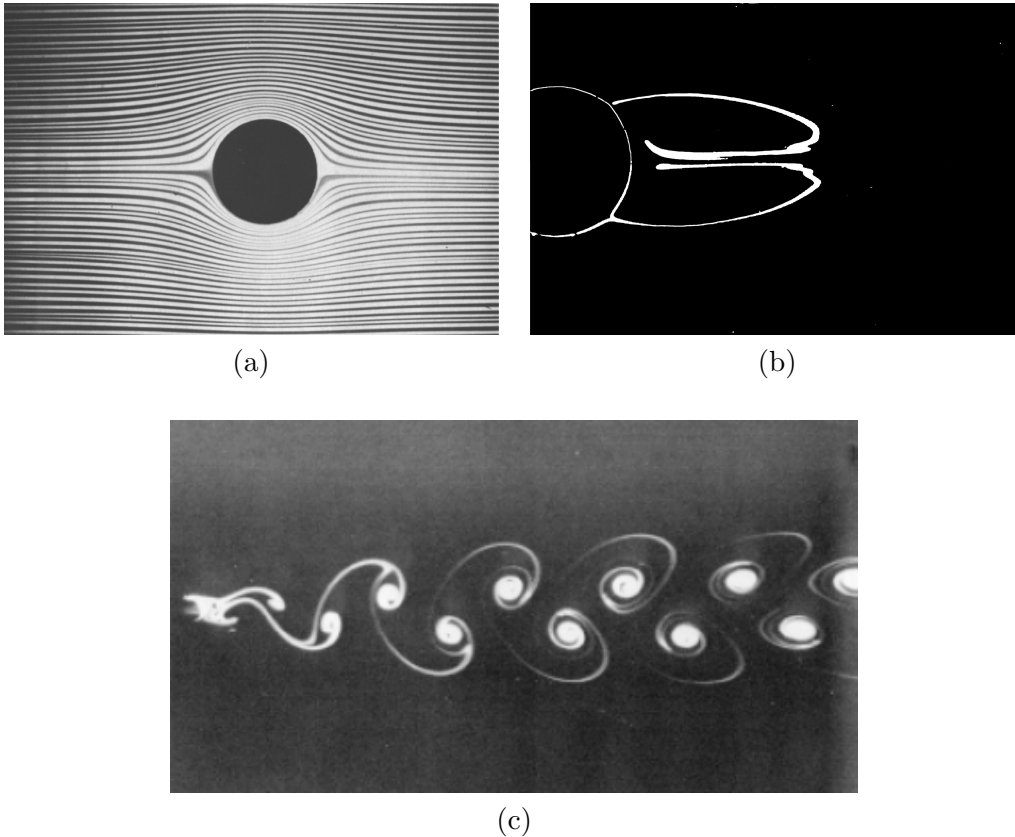


FIGURE 2.1: Flow regimes of a smooth circular cylinder at low Reynolds numbers. (a) Creeping flow, $Re < 5$. (b) A fixed pair of symmetric vortices, $5 \leq Re < 47$. (c) Kármán vortex street behind a circular cylinder at $Re = 105$. Images taken from Van Dyke (1982).

2.2 Flow past a stationary circular cylinder

2.2.1 Flow regimes

A circular cylinder is often described as the canonical model for bluff bodies in steady flow. Its geometrical simplicity can be easily defined by its diameter and length. For well over a century, extensive work has been conducted to characterise the flow past a stationary cylinder.

For a rigid circular cylinder in a steady flow of Newtonian fluid, the flow characteristics can be quantitatively described by an important dimensionless parameter, the Reynolds number. This parameter represents a measure of the ratio of inertial to viscous forces, and it is defined by

$$Re = \frac{U_\infty \ell}{\nu}, \quad (2.1)$$

where U_∞ is the free-stream velocity, ℓ is the characteristic length of the body (here it is referred to the cylinder diameter D), and ν is the kinematic viscosity of the fluid. As the Reynolds number is increased from zero, the flow undergoes a series of distinct transitions of topology and dynamics. The flow regimes experienced by the cylinder with increasing Reynolds number have been summarised by Lienhard (1966); Williamson (1996); Sumer & Fredsøe (1997); Zdravkovich (1997); Leontini (2007); Nazarinia (2010).

At very low Reynolds number values ($5 < Re$), the flow dynamics around the cylinder is dominated by viscous effects of the fluid. As a result, flow streamlines in the

vicinity of the cylinder adapt to the cylinder contour, and recover to steady flow in the downstream, as shown in Figure 2.1 (a). This is referred to as creeping flow, in which no separation occurs and the flow pattern does not vary with time. The onset of flow separation occurs at $Re \simeq 5$ when a pair of symmetric vortices are formed in the near wake of the cylinder, resulting in a recirculation region (Taneda 1956; Sumer & Fredsøe 1997), as shown in Figure 2.1 (b). The flow separation is caused by excessive momentum loss near the wall in a boundary layer trying to move downstream against the adverse pressure gradient ($dp/dx > 0$) where the pressure is increasing in the flow direction (White 2003), in this case because of the body's shape. The vortex formation length increases linearly with the Reynolds number (Taneda 1956). This trend continues to reach a length of three times of the cylinder diameter (Nishioka & Sato 1978). As the Reynolds number is further increased, the cylinder wake becomes unstable and then vortices are shed alternately from either side of the cylinder at a certain frequency. This frequency can be defined as a non-dimensional quantity known as the Strouhal number $St = f_{St}D/U_\infty$, where f_{St} is the vortex shedding frequency, D is the cylinder diameter, and U_∞ is the free-stream velocity (see §2.2.2 for more details). Above this Reynolds number of $Re \simeq 46$ (Taneda 1956; Roshko 1993; Williamson 1996; Thompson & Le Gal 2004), the flow undergoes its second major transition to the phenomenon of vortex shedding. The time-periodic vortices stagger in a two-row configuration in the wake to form a laminar vortex street, which is well known as Kármán vortex street named after Theodore von Kármán in honour of his observation and analysis based on the earlier observation of this vortex street by Bénard (1908). Figure 2.1 (c) shows a classic flow visualisation example of the Kármán vortex street. Investigations by von Kármán (1911) and Robinson & Saffman (1982) showed that the ratio of the longitudinal spacing between the two rows to the lateral spacing of two consecutive vortices in the same row was 0.281 when the vortex street was stable. As a result, the vortex shedding in turn exerts fluctuating forces on the cylinder, which would excite the cylinder to vibrate if it is elastic or elastically mounted. Therefore, vortex shedding is highly significant with respect to vortex-induced vibration. More detailed discussion on the vortex shedding mechanism will be given later in §2.2.2.

For $46 < Re < 190$, the flow remains laminar and two-dimensional, where the vortex shedding does not vary in the axial direction of the cylinder. The shedding frequency is a unique function of Reynolds number if the boundary conditions are carefully manipulated to produce vortex shedding parallel to the axis of the cylinder (Williamson 1989). As Reynolds number is increased within the laminar shedding regime, there exists a critical Reynolds number at which the wake undergoes transition from laminar and two-dimensional vortex shedding to three-dimensional turbulence. This transition was identified by a distinct discontinuous drop in the Strouhal number – Reynolds number ($St - Re$) function curve in the experimental study of Williamson (1988), who identified two distinct stages associated with discontinuity in $St - Re$ curve, each leading to a distinct transition of the wake mode. These wake modes have become known as mode A and B, after the manner in which Williamson (1988) originally referred to them. The onset of mode A associated with the first discontinuity occurs at $Re \approx 190$, which is also characterised by the formation of vortex loops along with a spanwise wavelength of $\lambda \approx 4D$ (Williamson 1996; Thompson *et al.* 1996; Henderson & Barkley 1996; Henderson 1997; Barkley *et al.* 2000), indicating the wake undergoes a transition from laminar vortex shedding to three-dimensionality. The second discontinuity is associated with the three-dimensional wake transition to mode B. This mode is observed for $230 < Re < 260$, where finer scale vortex structures are formed with a spanwise

wavelength of $\lambda \approx 0.8D$ (Williamson 1996; Henderson & Barkley 1996; Henderson 1997; Barkley *et al.* 2000).

As Reynolds number is further increased it enters a regime $260 < Re < 3 \times 10^5$ in which the wake becomes fully turbulent; however, the boundary layer over the cylinder surface remains laminar (Sumer & Fredsøe 1997).

2.2.2 Fundamentals of vortex shedding

It has been noted previously in § 2.2.1 that a pair of symmetric vortices of opposite sign becomes unstable and susceptible to disturbances for $Re > 46$. This instability will cause vortices to be shed periodically from the cylinder into its downstream wake. Development of vortex formation in the near wake of a circular cylinder has been described by Gerrard (1966), and a detailed description of the mechanism of vortex shedding has also been given by Sumer & Fredsøe (1997). Due to the disturbances from the flow for $Re > 46$, one vortex will grow larger in length and stronger in strength than the other, As illustrated in Figure 2.2 a, vortex A in clockwise direction is larger than the opposite vortex B in anti-clockwise direction. When the growing vortex A becomes strong enough, its action will draw the opposite shear layer containing anti-clockwise vortex B to roll up across the wake axis, as shown in Figure 2.2 b. As vortex B being drawn towards the shear layer connected with vortex A, the anti-clockwise vorticity carried in vortex B will then cut off the supply of clockwise vorticity to vortex A from its shear layer, and then vortex A breaks away as a free vortex convected downstream by the flow, as shown in Figure 2.2 c. A new vortex (vortex C in Figure 2.2 c) is formed by the shear layer on the upper side of the cylinder. Vortex B will repeat the same role as vortex A, and when grown sufficiently to draw the upper shear layer across the wake, it eventually be shed due to vorticity annihilation. This process repeats itself leading to a vortex street forming in the wake. Gerrard (1966) implied that the continuous interaction of the two shear layers causes vortices to be periodically shed alternatively from either side of the cylinder. If this interaction is inhibited, the vortex shedding would be suppressed or prevented (Sumer & Fredsøe 1997).

Furthermore, vortex shedding is a self-excited *global* instability in the sense that the whole wake is affected (Huerre & Monkewitz 1990; Williamson 1996; Paidoussis *et al.* 2010), and also it is a robust process that the self-sustained vortices are shed with a well defined dominant frequency observed over a wide range of Reynolds number. This dominant frequency is referred to as vortex shedding frequency. For non-dimensional analysis, the vortex shedding frequency is normalised by the characteristic length of the body (the cylinder diameter here) and the free-stream velocity, as express by

$$St = \frac{f_{St}D}{U_\infty}, \quad (2.2)$$

where f_{St} is the dominant vortex shedding frequency of a stationary cylinder (also known as Strouhal frequency), D is the cylinder diameter, and U_∞ is the free-stream velocity. This dimensionless number St is called *Strouhal number*, which is named after Vincenc Strouhal, a Czech physicist who reported that the dimensionless vortex shedding frequency remained constant in his experiments (Strouhal 1878). For a smooth circular cylinder, the Strouhal number is a function of Reynolds number, and it remains nearly constant at $St \approx 0.2$ over a wide range of Reynolds number of $300 < Re < 2 \times 10^5$ (see Fey *et al.* 1998; Williamson & Brown 1998; Norberg 2001), as shown in Figure 2.3.

It has been discussed previously that a discontinuity associated with the onset of mode A occurs at $Re \approx 190$ in the $St - Re$ curve. However, this discontinuity was not

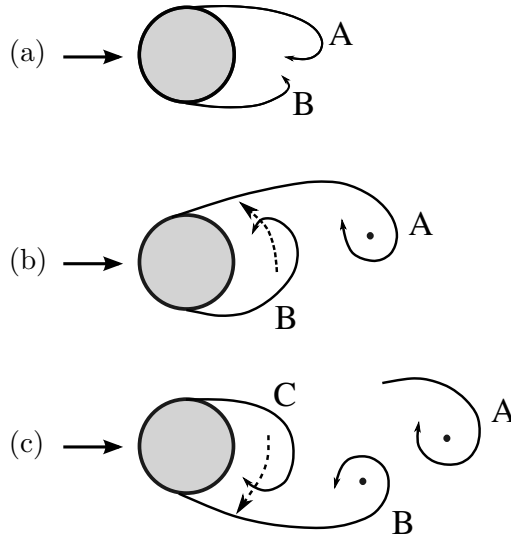


FIGURE 2.2: Formation of vortex shedding from a circular cylinder. (a): Vortex A in clockwise direction grows larger and stronger than the opposing vortex B in anti-clockwise direction; (b): Prior to shedding of vortex A, vortex B is being drawn across the wake axis; (c): Free vortex A is convected downstream by the flow, and prior to shedding of vortex B, vortex C is being drawn across the wake. Images modified from Sumer & Fredsøe (1997).

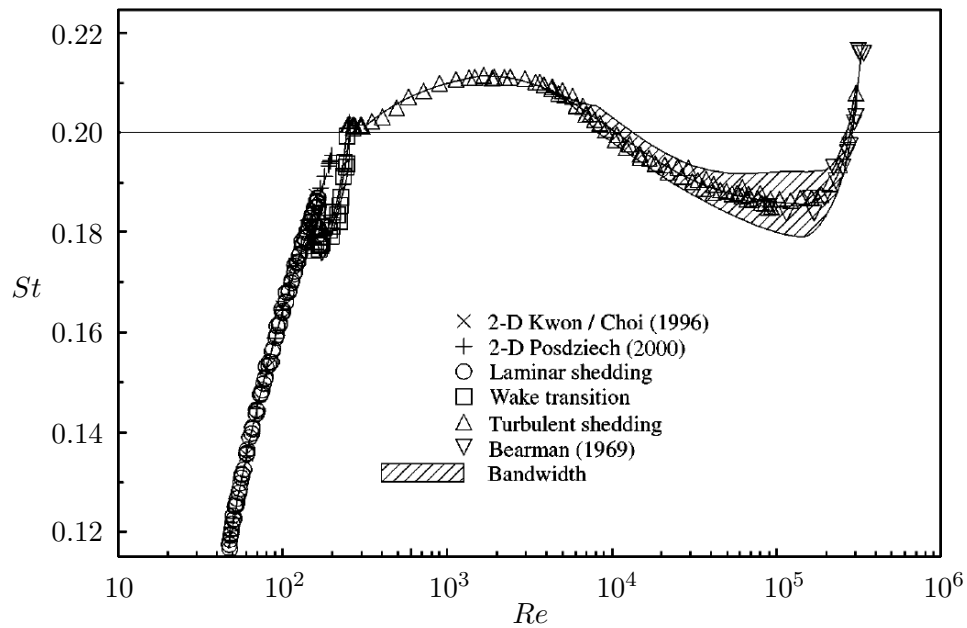


FIGURE 2.3: Strouhal number - Reynolds number relationship for circular cylinders. Figure and references from Norberg (2001).

observed by all researchers, and a number of explanations were proposed in the past [see Tritton (1959); Gaster (1969, 1971)]. These discrepancies were effectively resolved by Williamson (1989) who revealed that this discontinuity was attributed to the transition of one mode of oblique vortex shedding to another due to end effects of the cylinder. In oblique shedding mode, as shown in Figure 2.4 (a), the vortices shed are parallel to

each other but inclined at an angle with respect to the axis of the cylinder. In contrast, in the parallel shedding mode, as shown in Figure 2.4 (b), the vortices are shed parallel to the axis of the cylinder over most of the span. Williamson (1989) also found that the Strouhal numbers of oblique shedding St_θ collapse on the $St - Re$ curve for parallel shedding by simply applying the equation $St_\theta = St \cos \theta$, where θ is the angle of oblique shedding. Alternatively, parallel shedding *over the whole span* can also be induced by manipulating the end boundary conditions, which then results in a single continuous $St - Re$ curve (Williamson 1989; Hammache & Gharib 1991).

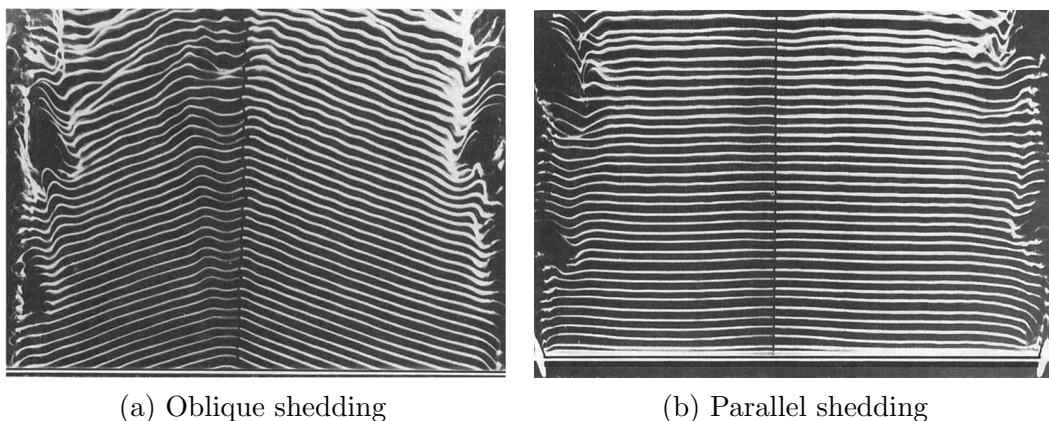


FIGURE 2.4: Visualisation of oblique shedding (a) at $Re = 85$ and parallel shedding (b) at $Re = 110$ Williamson (1989). Note that flow is upwards.

In contrast to parallel shedding, the presence of oblique shedding can have a significant effect on the properties of the wake and the oscillating fluid forces acting on the cylinder. Khalak & Williamson (1996) experimentally investigated the effects of oblique shedding on the drag and lift, and vortex shedding frequency of a stationary cylinder ($2000 < Re < 13000$), as shown in Figure 2.5. Compared to the oblique shedding induced by free end conditions, parallel shedding induced using an end-conditioning platform technique showed an increase of 15 – 20% in the time-averaged drag throughout the investigated Reynolds number range. The lift produced by parallel shedding had higher r.m.s. (root-mean-square) values and was more periodic than that of oblique shedding. The spectrum analysis in Figure 2.5 (c) also showed that the lift of parallel shedding is dominated by a single frequency, while oblique shedding resulted in a more complicated time trace of the lift force that was dominated by two weaker dominant frequency peaks. Consequently, proper end conditions, such as end plates and platforms, are used in experiments for cylinders to promote parallel shedding.

Additionally, the wake properties are also found to depend on the aspect ratio (L/D) of the cylinder. Szepessy & Bearman (1992) found that the aspect ratio of $L/D = 0.12 - 12$ had a striking effect on the fluctuating lift and vortex shedding frequency for $8 \times 10^3 < Re < 1.4 \times 10^5$. Norberg (1994) showed that the critical Reynolds number for the onset of vortex shedding was significantly delayed at low aspect ratios of $L/D < 40$, and he also suggested that aspect ratios as large as $L/D = 60 - 70$ were needed to approximate an infinite cylinder for $Re \approx 4 \times 10^3 - \times 10^4$. However, Szepessy & Bearman showed that the lift and vortex shedding frequency measured at $L/D = 6.7$ with end plates had very little variation with Reynolds number. Therefore, in general, a cylinder must have an aspect ratio of at least $L/D > 6.7$ for end effects to minimise their influence on the flow properties.

2.3. Vortex-induced vibration of a circular cylinder

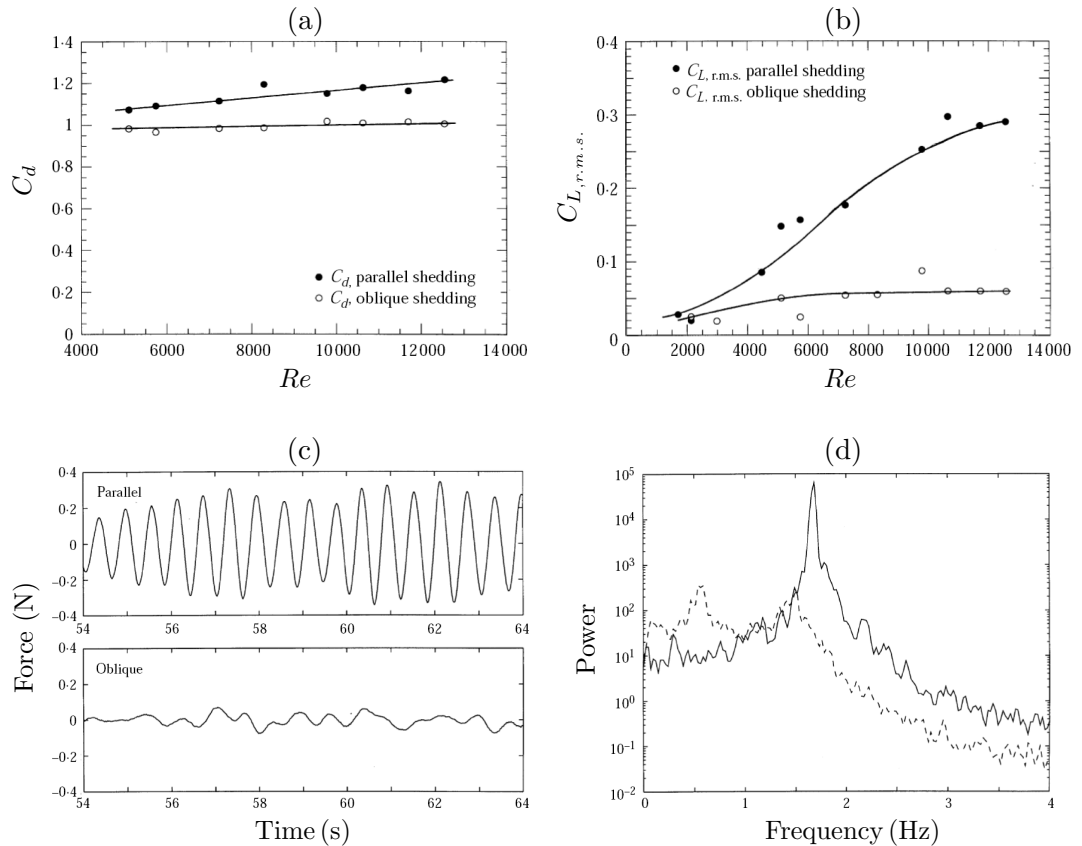


FIGURE 2.5: Comparison of (a) time-averaged drag, (b) root-mean-square (r.m.s.) lift coefficients, (c) lift force time trace and (d) vortex shedding frequency of a stationary circular cylinder between oblique and parallel shedding modes. Oblique shedding is induced by free end condition, while parallel shedding is promoted using a platform end condition technique. Images taken from (Khalak & Williamson 1996).

2.3 Vortex-induced vibration of a circular cylinder

As discussed previously in § 2.2, the fluctuating pressures generated by vortex shedding exerts fluctuating force components on the cylinder. The lift force fluctuates at the vortex-shedding frequency, while the drag force fluctuates at twice the vortex-shedding frequency (Bishop & Hassan 1964; Sumer & Fredsøe 1997). If the cylinder is flexible or elastically-mounted, these fluctuating forces can cause the body to vibrate. The lift force can induce the cylinder to vibrate in the cross-flow direction, while the drag force can induce the cylinder to vibrate in the direction in-line to the flow (see Sumer & Fredsøe 1997). These phenomena are generally known as vortex-induced vibrations (VIV). Experimentally, these complex VIV motions are often simplified to cross-flow VIV of a rigid circular cylinder, as a means of understanding the fundamental characteristics of the flow-structure interaction. This arises simply from: (1) structures with circular cross-sectional shapes are widely used in engineering applications; (2) the geometrical simplicity of a circular cylinder can be easily defined by its diameter and length, without any other parametric considerations relating to the flow orientation; (3) a circular cylinder is immune to the galloping instability in a steady flow; (4) cross-flow VIV produces vibration amplitudes much larger than in-line VIV.

A schematic description of cross-flow VIV of a rigid circular cylinder is given in

Figure 2.6: a circular cylinder is subjected to a uniform free-stream (U_∞), and is given one degree-of-freedom (DOF) to oscillate freely transverse to the free-stream, due to the fluctuating forces ($F_y(t)$) exerted by the vortex shedding. The governing equation of motion for cross-flow VIV of a cylinder can be expressed by

$$m\ddot{y} + c\dot{y} + ky = F_y, \quad (2.3)$$

or in terms of the natural frequency of the damping of the system by

$$\ddot{y} + 2\zeta\omega_n\dot{y} + \omega_n^2 y = \frac{F_y}{m}, \quad (2.4)$$

where m is the system's mass, c is the structural damping, k is the spring constant, $\omega_n = \sqrt{k/m}$ is the angular natural frequency of the system, $\zeta = c/(2m\omega_n)$ is the damping ratio, and F_y is the lift force in the direction transverse to the free-stream.

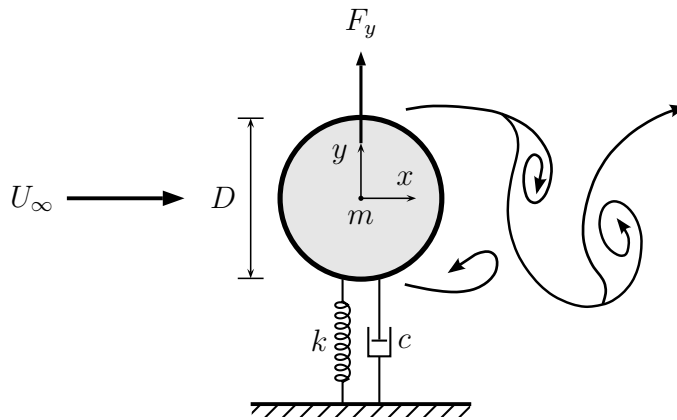


FIGURE 2.6: Definition sketch for cross-flow VIV of a circular cylinder. The cylinder undergoes free vibrations constrained in the transverse y direction to the free-stream U_∞ in x direction. Note that m is the system's mass, c is the structural damping, k is the spring constant, and F_y is the transverse lift force.

Comprehensive reviews on cross-flow VIV of a circular cylinder have been documented in articles (Bearman 1984; Sarpkaya 2004; Williamson & Govardhan 2004; Gabbai & Benaroya 2005), and in books (Blevins 1990; Sumer & Fredsøe 1997; Naudascher & Rockwell 2005; Paidoussis *et al.* 2010). The following sections will focus on some key findings relating to this topic.

2.3.1 Amplitude and frequency responses

As in the analysis for other vibration phenomena, the vibration amplitude and frequency are the two fundamental variables of interest in VIV study. However, the amplitude and frequency responses of VIV are usually presented in VIV with reference to a parameter known as the reduced velocity, defined as $U^* = U/f_N D$, where U is the free-stream velocity, f_N is the natural frequency of system measured in the still fluid. A pioneering experimental study in a wind tunnel by Feng (1968) characterised the vibration amplitude and frequency responses of a circular cylinder at high mass ratios of $m^* = m/m_d = \mathcal{O}(100)$, where m is the system mass and m_d is the displaced fluid mass by the cylinder, over a range of reduced velocities. Feng found that the cylinder experienced its largest oscillation amplitudes in a synchronisation (also known as “lock-in” or “lock-on”) region over a range of $5 \leq U^* \leq 8$ where the cylinder's oscillation

2.3. Vortex-induced vibration of a circular cylinder

frequency, denoted by f , matched the vortex shedding frequency for the fixed body (f_{St}), and both frequencies were approximately equal to the natural frequency of the system (f_N): $f \cong f_{St} \cong f_N$.

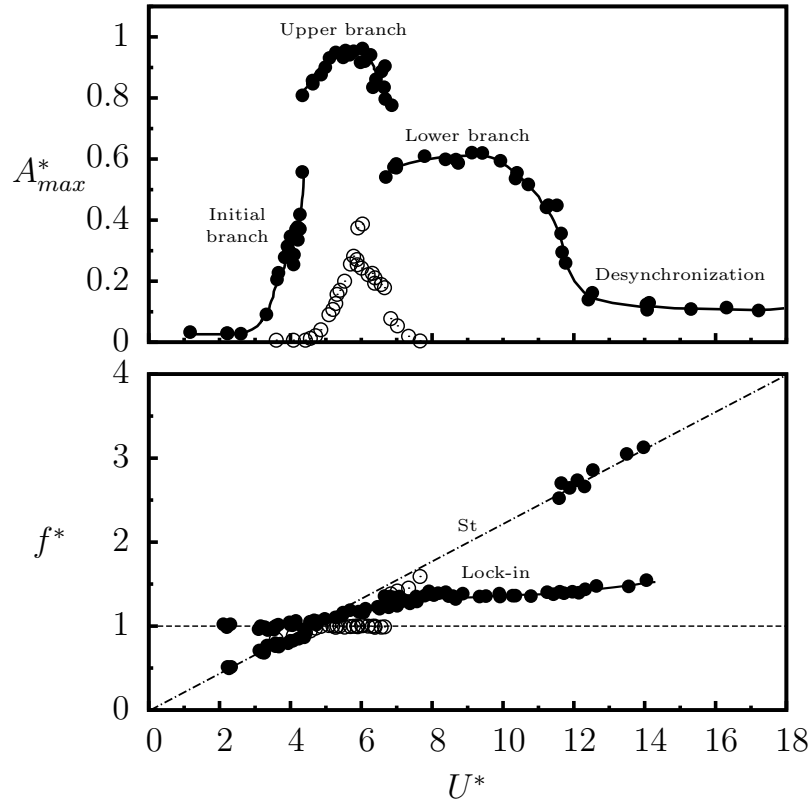


FIGURE 2.7: Amplitude and frequency responses of VIV of a circular cylinder. Open circles represent results at $m^* = 248$ and $\zeta = 0.00145$ by Feng (1968). Solid circles represent results at $m^* = 2.4$ and $m^*\zeta = 0.013$ by Khalak & Williamson (1997a).

However, a significant addition to the classification of VIV response was made more recently by Khalak & Williamson (1996, 1997a,b, 1999) who observed three distinct branches in the amplitude response of a cylinder system at low mass ratios ($m^* = \mathcal{O}(1)$) in water-channel experiments. They termed these branches as the “initial”, “upper” and “lower” branches, as shown in Figure 2.7 Only two of the branches (the initial and the lower) were seen in the high mass ratio case of Feng. Compared to Feng’s results, they also found that the body oscillations occurred at much lower reduced velocities and the “lock-in” region was much wider, extending from $U^* = 5$ up to $U^* = 12$. Within “lock-in” the normalised oscillation frequency $f^* = f/f_N$ departed away from unity and increased monotonically with the reduced velocity. Additionally, much larger oscillation amplitudes were observed with the peak value of $A_{max}^* \approx 1D$ approximately twice that of Feng.

Further, the number of amplitude-response branches is found to depend on a non-dimensionalised parameter contributed by the mass and damping ratio of the system, $m^*\zeta$, as schematically illustrated in Figure 2.8 (see Khalak & Williamson 1999). For a high- $m^*\zeta$ system of Feng’s type, there are only the initial and the lower branches, and the transition between these branches is hysteretic. In contrast, for a system at a relatively low value of $m^*\zeta$, the amplitude response exhibits three branches: initial, upper and lower branches. This form of three-branch amplitude response and the phe-

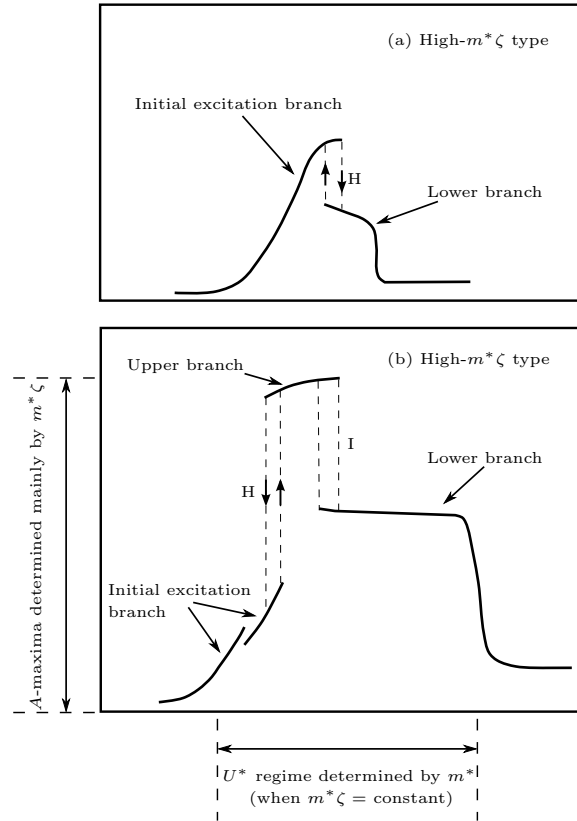


FIGURE 2.8: A schematic illustration for the two distinct types of amplitude response of VIV of a circular cylinder: (a) the Feng-type of high- $m^*\zeta$ response exhibits only two branches (initial and lower), while (b) the low- $m^*\zeta$ response exhibits three branches (initial, upper and lower). The transitions are either hysteretic (H) or intermittent (I). Reproduced from Khalak & Williamson (1999)

nomenon of frequency response departure from the natural frequency of the system response have subsequently been confirmed experimentally and numerically by a number of other researchers, notably Govardhan & Williamson (2000, 2002); Branković (2004); Leontini *et al.* (2006c); Klamo (2007). The initial branch occurs at very low reduced velocities ($U^* \approx 1$ in experiments), and is characterised by moderate oscillation amplitudes with the dominant frequencies following the Strouhal frequency trend for the fixed body. However, the oscillations in the initial branch are not highly periodic but quasi-periodic, due to the influence from the vortex shedding frequency and the natural frequency of the system (see Khalak & Williamson 1999; Leontini 2007). As U^* is increased, the system undergoes a hysteretic transition from the initial branch to the upper branch at $U^* \approx 1/St \approx 4.8$ as the cylinder oscillation frequency begins to lock on to the natural frequency of the system. The upper branch is characterised by the largest-scale oscillations with unstable amplitudes due to the resonant oscillations of the near wake, which inputs substantial energy to the structure (Blevins 1990). Although the maximum amplitude reported could reach up to $A_{\max}^* = 1.2D$ for very low m^* (see Govardhan & Williamson 2000), the oscillation amplitudes of VIV are self-limited to the order of one cylinder diameter. Further experiments by Govardhan & Williamson (2006), and Klamo (2007) found that the magnitude of the maximum amplitudes in the upper branch are influenced not only by the parameters of mass ratio and damping ratio but also by Reynolds number. As U^* is further increased the ampli-

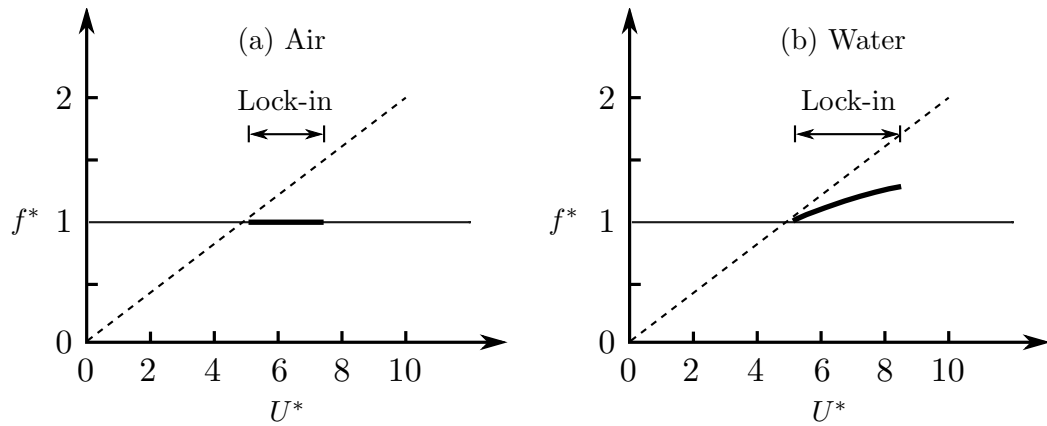


FIGURE 2.9: Schematic illustrations of frequency response of lock-in region of a circular cylinder undergoing VIV in air and in water. (a) shows that the frequency response f^* locks on to the natural frequency, namely $f^* \cong f_N$, through the lock-in region of VIV in air. (b) shows that the frequency response f^* departs from unity and increases monotonously with U^* through the lock-in region of VIV in water. Images reproduced from (Sumer & Fredsøe 1997).

tude response undergoes a transition to the lower branch, with intermittent switching between these two modes. This intermittent switching phenomenon has been clearly seen in the instantaneous phase between the lift and displacement measured by Khalak & Williamson (1999). There is good agreement in the literature that the oscillations in the lower branch are highly periodic with very stable amplitudes of $A^* \approx 0.6D$. The lower branch has a relatively wider response region, followed by a gradually declining drop in amplitude indicating the end of the synchronisation regime. At even higher U^* there is the desynchronisation region where the body oscillations with chaotic amplitudes are influenced significantly by both the vortex shedding frequency and the natural frequency of the system.

More detailed discussion on the phenomenon of “lock-in”, fluid forces, phases and wake modes relating to VIV of a circular cylinder is presented in a later section.

2.3.1.1 Lock-in

Lock-in, or synchronisation is one of most significant phenomena in VIV. In the lock-in region, the vortex shedding frequency no longer follows the Strouhal frequency for the stationary body, but matches the oscillation frequency of the body. Traditionally, for a high- $m^*\zeta$ system, such as in air shown in Figure 2.9 (a), the lock-in phenomenon is identified by the proximity of the body oscillation frequency to the natural frequency of the system. However, for a low- $m^*\zeta$ system, typically in water, the body oscillation frequency departs from the natural frequency through the lock-in region, with f^* departing from unity as shown in Figure 2.9 (b). This departure is due to the effect of the added mass arising from the acceleration of the body’s motion (see Sumer & Fredsøe 1997; Govardhan & Williamson 2000). Therefore, discrepancies still exist over the definition of lock-in, as some researchers define lock-in as the matching of the periodic wake vortex mode with the cylinder oscillation frequency (see Gabbai & Benaroya 2005). A useful definition of lock-in given by Sarpkaya (1995) is that the lift frequency must match the body’s oscillation frequency. This definition is also constantly adopted by Williamson’s group, and also in this thesis.

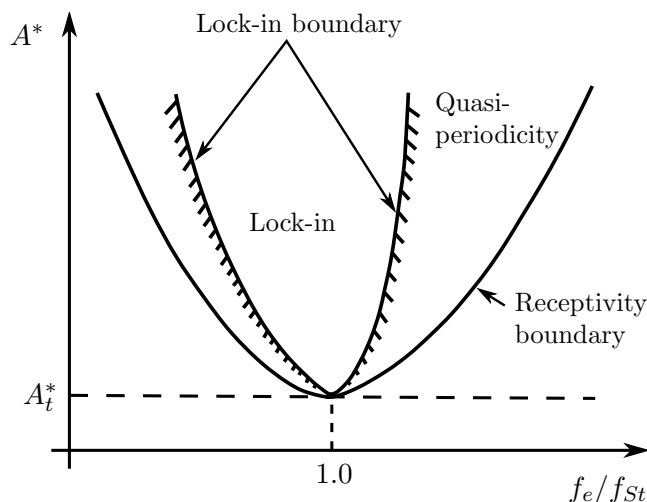


FIGURE 2.10: State-selection (amplitude versus frequency) diagram for laminar wakes of a circular cylinder undergoing forced sinusoidal oscillations. The plot should only be interpreted in a qualitative sense. Note that A_t^* is the threshold of the normalised amplitude required for the onset of lock-in, and f_e is the oscillation frequency of excitation. Reproduced from Karniadakis & Triantafyllou (1989).

The effect of mass ratio plays a significant role in the “lock-in” regime. Govardhan & Williamson (2000, 2002) were the first to observe experimentally an interesting phenomenon of a critical mass ratio, $m_{crit}^* = 0.54 \pm 0.02$, below which the lock-in region of large-amplitude motion extends to an infinite range of reduced velocity. The existence of critical mass has also been reported experimentally and numerically by other researchers. The experimental results of Branković (2004), following the analysis of Govardhan & Williamson (2000), gave a critical mass ratio of $m_{crit}^* = 0.4$. The numerical study by Ryan *et al.* (2005) showed that the critical mass ratio varied in a range of $0.075 \leq m_{crit}^* < 0.51$ as a function of Reynolds number in a range of $30 \leq Re \leq 200$. Despite the discrepancy in the obtained values of m_{crit}^* , the studies consistently indicate the existence of this parameter.

Lock-in phenomenon has also been observed in forced oscillations when the cylinder oscillation frequency is close to the Strouhal frequency. This was first noticed in the early experiments of sinusoidally-driven cylinders by Bishop & Hassan (1964). Later, the studies of Koopmann (1967) and Stansby (1976) showed that as the oscillation amplitude increased, the range of oscillation frequency over which lock-in was observed also increased. Figure 2.10 shows a schematic diagram by Karniadakis & Triantafyllou (1989) illustrating the lock-in region for a forced-oscillating cylinder as a function of the oscillation amplitude and frequency. The general shape of the lock-in region shown in Figure 2.10 is consistent with the experimental observations by Koopmann (1967), Stansby (1976) and Williamson & Roshko (1988), and the numerical simulations by Blackburn & Karniadakis (1993), Meneghini & Bearman (1995) and Leontini *et al.* (2006b). A review on the lock-in of forced-oscillating cylinders has been documented by Griffin & Hall (1991).

2.3.2 Fluid forces, phases and wake modes

Recent research attention has been given to characterising the fluid forces, the phases and wake modes of a freely-vibrating cylinder, which would potentially help to predict

2.3. Vortex-induced vibration of a circular cylinder

and suppress VIV.

The first direct force measurements on freely-vibrating cylinders were conducted experimentally by Khalak & Williamson (1997a), although extensive force measurements had been carried out for cylinders undergoing forced oscillations (see Bishop & Hassan 1964; Staubli 1983; Gopalkrishnan 1993) in the past. Khalak & Williamson (1997a) applied the Hilbert transform (HT) to calculate the instantaneous total phase, denoted by ϕ_{total} , between the lift and displacement, and found intermittent switching between $\phi_{total} \approx 0^\circ$ for the upper branch and $\phi_{total} \approx 180^\circ$ for the lower branch corresponded with intermittent switching between the upper and lower branches in transition.

Further, Govardhan & Williamson (2000), following the fluid force decomposition method proposed by Lighthill (1986), decomposed the total transverse lift force (F_y) of Eq. (2.3) into a *potential force* component, denoted by $F_{potential}$, contributed by the potential added-mass force and a *vortex force* component, denoted by F_{vortex} , arising from the dynamics of vorticity, as follows:

$$F_y = F_{potential} + F_{vortex}. \quad (2.5)$$

The above Eq. (2.5) can be divided by $\frac{1}{2}\rho U_\infty D L$ to become

$$C_y(t) = C_{potential}(t) + C_{vortex}(t). \quad (2.6)$$

The instantaneous potential force acting on the cylinder is given by

$$F_{potential}(t) = -m_A \ddot{y}(t) = -C_A \frac{\rho \pi D^2 L}{4} \ddot{y}(t), \quad (2.7)$$

where m_A is the added mass and C_A is the potential flow added-mass coefficient ($C_A = 1$ for a circular cylinder). When the oscillation frequency of the cylinder is synchronised with that of the periodic vortex shedding, the excitation transverse lift force, $F_y(t)$, and the response displacement, $y(t)$, are well approximated by sinusoidal functions (Khalak & Williamson 1999; Govardhan & Williamson 2000), given by:

$$F_y(t) = F_Y \sin(\omega t + \phi_{total}) \quad (2.8)$$

$$y(t) = A_o \sin(\omega t), \quad (2.9)$$

where F_Y and A_o are the magnitude of the lift and displacement, respectively. Then, the potential force can be simplified as

$$C_{potential}(t) = 2\pi^3 \frac{y(t)/D}{(U^*/f^*)^2}, \quad (2.10)$$

where $\omega = 2\pi f$ is the angular oscillation frequency, and ϕ_{total} is the phase angle between the transverse lift force and the cylinder's displacement. As it can be seen in Eq. (2.10), the potential force $C_{potential}(t)$ is always in phase with the displacement $y(t)$.

Thus, when a VIV system is considered to be subjected to harmonic excitation, its governing equation of motion can be expressed by

$$m\ddot{y} + c\dot{y} + ky = F_o \sin(\omega t + \phi_{total}). \quad (2.11)$$

Combining Eq. (2.5) and Eq. (2.7), the above equation of motion Eq. (2.11) is then rewritten, retaining only the vortex force on the right-hand side, by

$$(m + m_A)\ddot{y} + c\dot{y} + ky = F_{vortex} \sin(\omega t + \phi_{vortex}), \quad (2.12)$$

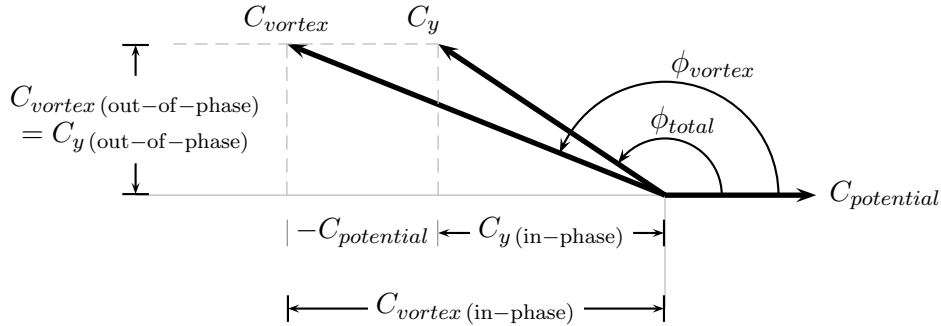


FIGURE 2.11: A diagram of force decomposition showing the relationships between the force components and phases.

where ϕ_{vortex} is the phase angle between the vortex force and displacement. Consequently, the relationships between the force components and phases are shown in Figure 2.11.

Before proceeding to a discussion on the phase responses and wake modes for a freely-vibrating cylinder, it is helpful to first review the characterisation of wake modes for a cylinder undergoing forced sinusoidal oscillations, since the vortex shedding is significant in that it influences the fluid forces, the phases and consequently the energy transfer between the fluid and the structure. A systematic map for the wake mode regions of a sinusoidally-driven cylinder was explored by Williamson & Roshko (1988). In this map, as shown in Figure 2.12, the wake modes identified using flow visualisation were categorised into different regions in an amplitude – wavelength ($A^* - \lambda^*$) plane. The amplitude is normalised by $A^* = A/D$, and the wavelength is normalised by $\lambda^* = U/(f_e D)$, where A is the excitation amplitude, and f_e is the excitation frequency. Using this scaling, the normalised wavelength is equivalent to the reduced velocity, but also has the advantage that it conveys the sine wave trajectory along which the cylinder travels relative to the flow. The cylinder was forced to oscillate with the amplitude up to $A^* = 5$ (not shown in Figure 2.12) over a wavelength range of $0 < \lambda^* < 10$. The Reynolds number for the experiments was in the range $300 \leq Re \leq 1000$, but was not held constant. Consequently, the wake modes were classified in terms of the vortex wake pattern comprising single vortices (S) and vortex pairs (P) shed per oscillation cycle. Three main wake modes found near the synchronisation region were $2S$, $P + S$, and $2P$ modes: the $2S$ mode comprises two single vortices shed per oscillation cycle (*i.e.* the class Kármán vortex street); the $P + S$ mode is an asymmetric mode, representing one single and one vortex pair being shed per oscillation cycle; the $2P$ mode consists of two pairs of vortices shed per oscillation cycle. Examples of these wake modes are shown in Figure 2.13. Williamson & Roshko also suggested the sudden transition of the wake modes (*i.e.* $2S \rightarrow 2P$) through the lock-in regime would help to explain the sharp change in fluid forces observed by Bishop & Hassan (1964), and also the jump in the total phase between the lift and displacement.

The vortex wake modes also play an important role in vortex-induced vibration. The flow visualisation results of free vibration by Brika & Laneville (1993) and Khalak & Williamson (1999) show that the wake mode changes from $2S$ to $2P$ corresponding to the amplitude response jumping from the initial branch to the lower branch. Govardhan & Williamson (2000) were the first to employ digital particle image velocimetry (DPIV) to investigate the wake modes of cylinders undergoing VIV, after this technique had been used in forced oscillation experiments for the first time by Rockwell’s group at

2.3. Vortex-induced vibration of a circular cylinder

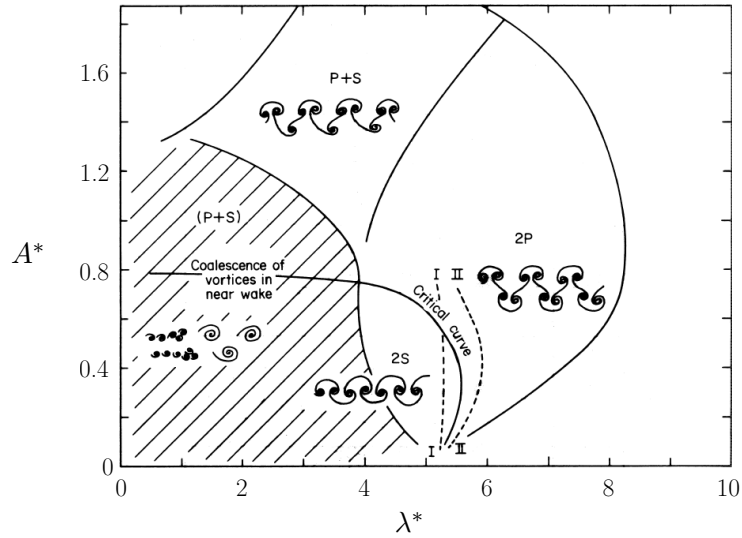


FIGURE 2.12: Maps of wake mode regimes over a $A^* - \lambda^*$ plane for a circular cylinder undergoing sinusoidally-driven oscillations. $A^* = A/D$ and $\lambda^* = U_\infty/(f_e D)$, where A is the oscillation amplitude and f_e is the oscillation frequency of excitation. The “critical curve” represents the boundary between the wake modes. Curves I and II represent locations where the forces on the body show a sharp change. The Reynolds number is within a range of $300 \leq Re \leq 1000$, but it is not held constant. Williamson & Roshko (1988).

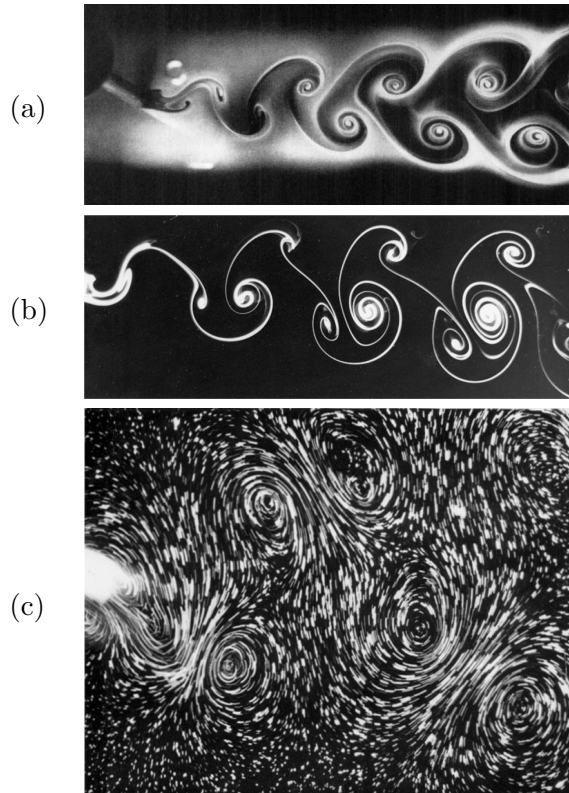


FIGURE 2.13: Three main wake modes near the synchronisation region of an oscillating cylinder. (a): the $2S$ mode of a cylinder undergoing free VIV (Koopmann 1967). (b): the $P + S$ mode of a cylinder undergoing sinusoidally-driven oscillations (Williamson & Govardhan 2004). (c) the $2P$ mode of a cylinder undergoing sinusoidally-driven oscillations (Williamson & Govardhan 2004).

Lehigh University to measure the wake vorticity behind a cylinder (see Gu *et al.* 1994). Govardhan & Williamson showed that there existed two distinct types of response in free vibrations, depending on whether the system had a high or low value of $m^*\zeta$. For a high- $m^*\zeta$ system, only one wake mode transition was found corresponding to the amplitude-response jump from the initial branch to the lower branch, whereas for a low- $m^*\zeta$ system two wake mode transitions were observed.

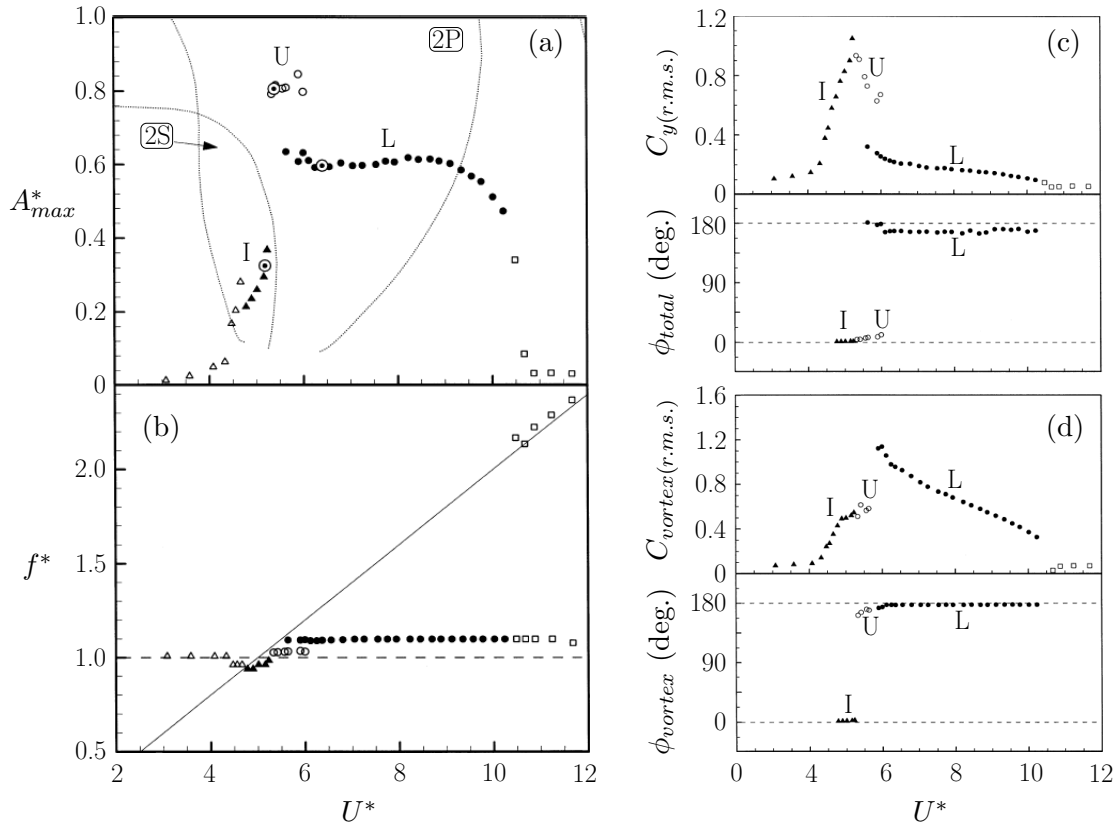


FIGURE 2.14: Plots of VIV response of a circular cylinder with $m^* = 8.63$ and $\zeta = 1.51 \times 10^{-3}$: (a) amplitude response, (b) frequency response, (c) the root-mean-square total transverse lift coefficient ($C_{y(r.m.s.)}$) and the total phase (ϕ_{total}), and (d) the root-mean-square vortex force coefficient ($C_{vortex(r.m.s.)}$) and the vortex force phase (ϕ_{vortex}). \blacktriangle , Initial (I) branch; \circ , upper branch (U); \bullet , lower branch (L); \square , Desynchronisation region; \odot , PIV measurement locations. \cdots , boundaries between the wake modes of Williamson & Roshko (1988)'s map. Images taken from Govardhan & Williamson (2000).

Figure 2.14 show the results of VIV responses of a low $m^*\zeta$ ($m^* = 8.64$ and $\zeta = 1.51 \times 10^{-3}$) system studied by Govardhan & Williamson to understand the relationships between the amplitude response, frequency response, fluid forces, phases and the wake modes. The amplitude and frequency responses are shown in Figure 2.14 (a) and (b), respectively, where PIV measurements were taken at the locations indicated by the bull's-eye symbols. As expected from Williamson & Roshko's map of wake modes for forced oscillations, Govardhan & Williamson observed the presence of $2S$ mode in the initial branch, and $2P$ mode in the upper and lower branches in free vibrations. The results of PIV measurements for these wake modes are shown in Figure 2.15. The $2S$ mode sequence in Figure 2.15 (a) shows two single vortex structures of opposite sign were alternately shed per oscillation cycle to form a narrow single-row pattern concentrated along the wake centre-line. This $2S$ mode then underwent a transition

2.3. Vortex-induced vibration of a circular cylinder

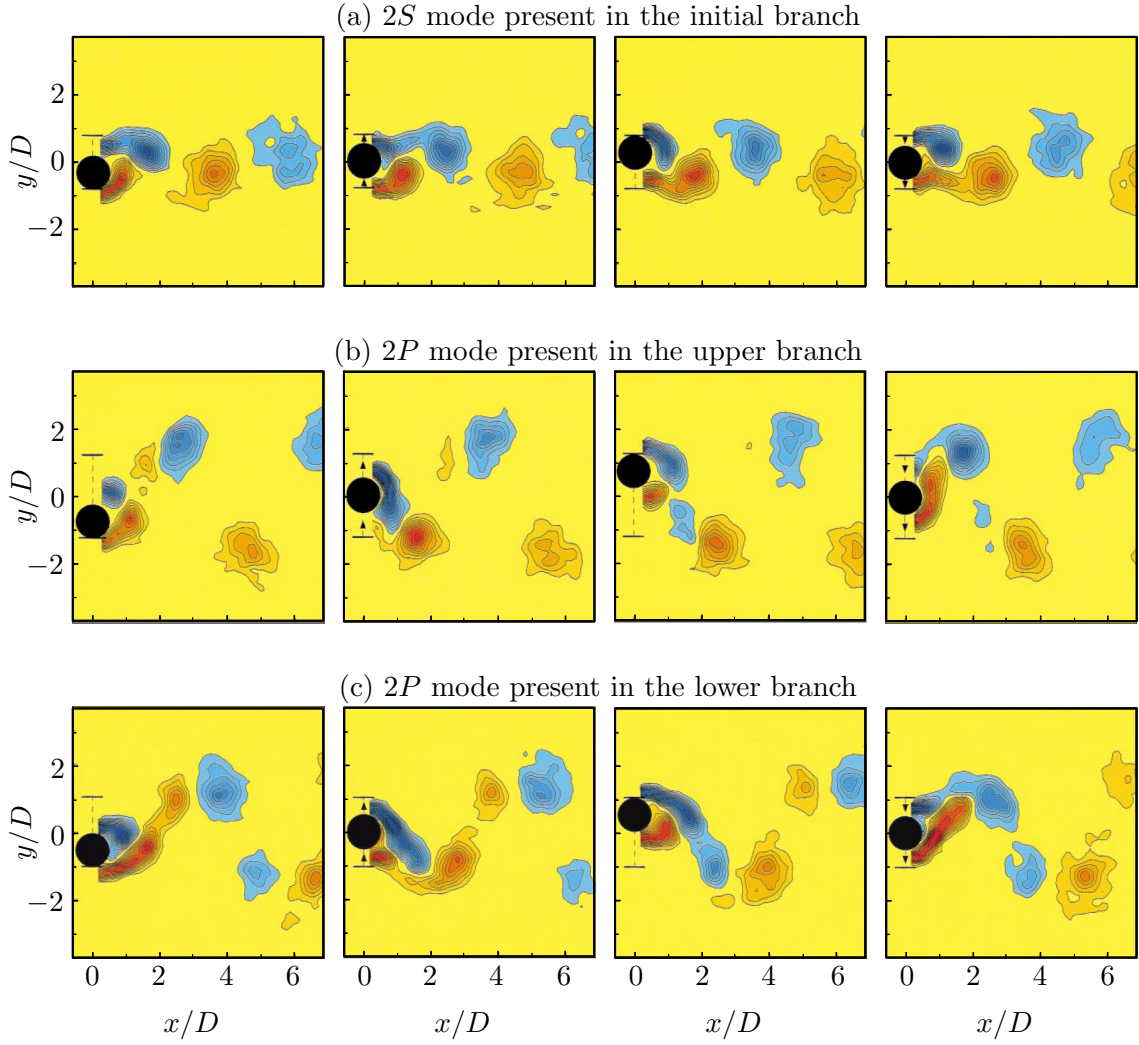


FIGURE 2.15: Plots of wake modes of a freely vibrating circular cylinder with a low mass-damping ratio ($m^* = 8.63$ and $\zeta = 1.51 \times 10^{-3}$). The Initial branch is associated with the $2S$ mode ($A^* = 0.33$ at $U^* = 5.18$); the upper branch is associated with the $2P$ mode ($A^* = 0.81$ at $U^* = 5.39$); the lower branch is also associated with the $2P$ mode ($A^* = 0.6$ at $U^* = 6.40$). Anti-clockwise vortices in red and clockwise vortices in blue. Images taken from Govardhan & Williamson (2000).

to a $2P$ mode, which was associated with the amplitude response transition from the initial to the upper branch as the body oscillation frequency passed through the natural frequency of the system in water. As shown in Figure 2.15 (b), a weekly $2P$ mode consisting of a strong first and a weak second (20% in strength of the first one) vortex were shed per half oscillation cycle. The weaker vortex was dissipated rapidly downstream, at around $x/D = 4$, due to the interaction with the relatively stronger first vortex. Correspondingly, Govardhan & Williamson found that this $2S \rightarrow 2P$ wake mode transition was associated with a jump in the vortex phase. As shown in Figure 2.14 (d), the vortex phase experienced a large jump from around $\phi_{vortex} = 0^\circ$ in the initial branch to $\phi_{vortex} \approx 160^\circ$ in the upper branch, whereas the total jump, shown in Figure 2.14 (c), remained constantly around $\phi_{total} = 0^\circ$ in the initial branch and increased slightly with U^* during the upper branch. A second jump phenomenon was observed when the total phase jumped from $\phi_{total} = 0^\circ$ to 180° , which was associated with the amplitude

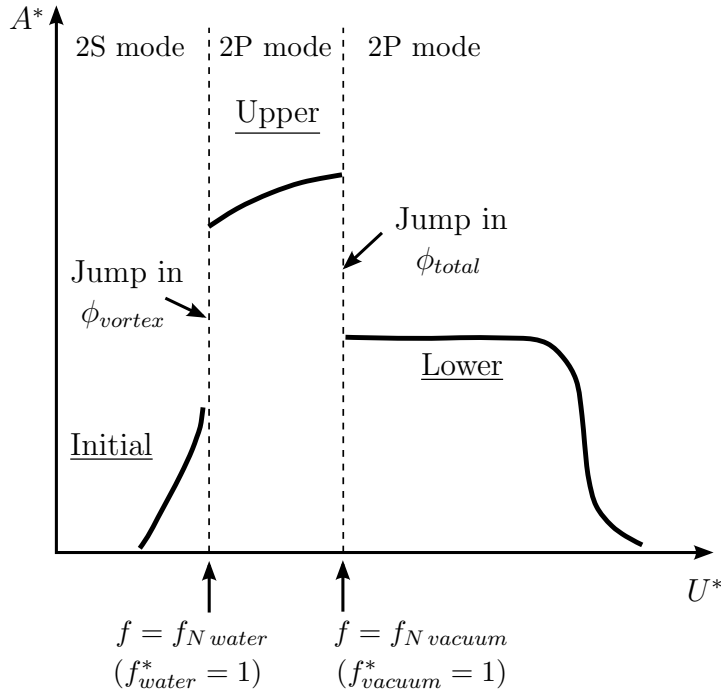


FIGURE 2.16: A characterisation diagram for VIV response of a circular cylinder with low $m^*\zeta$ showing the three-branch amplitude response, the wake modes and correspondingly the two jump phenomena. Reproduced from (Govardhan & Williamson 2000).

response transition from the upper to the lower branch. However, the vortex phase continued to remain around $\phi_{vortex} = 180^\circ$ throughout the lower branch, where the $2P$ mode, shown in Figure 2.15 (c), became clearer and stronger than that found in the upper branch. In addition, the vortex force increased sharply in this transition to reach a peak value of $C_{vortex(r.m.s.)} \approx 1.2$ at the beginning of the lower branch, before it gradually declined at higher reduced velocities. Consistently, the locations of the wake modes in free vibration found by Govardhan & Williamson agreed well with the wake mode regions of Williamson & Roshko's map. The $2S$ and $2P$ modes have been observed experimentally and numerically in free VIV (see Leontini *et al.* 2006b), and $P+S$ has only been seen in numerical studies of VIV at low Reynolds number (see Leontini *et al.* 2006b). However, the $P+S$ mode has not yet been observed experimentally in free vibrations.

Figure 2.16 shows a general characterisation diagram originally provided by Govardhan & Williamson for the VIV response of a low- $m^*\zeta$ cylinder system. This diagram illustrates that the initial \leftrightarrow upper transition occurs as the body oscillation frequency passes through the natural frequency of the system in the fluid (*i.e.* $f \approx f_{N\ water}$). At this point, the wake mode undergoes a transition from $2S$ to $2P$ which involves a jump in the vortex phase. The second amplitude transition, the upper \leftrightarrow lower branch, occurs at $f \approx f_{N\ vacuum}$, which involves a jump in the total phase. However, there is no jump in the vortex phase within the upper and lower branches, meaning the $2P$ wake mode remains present in the lower branch. This diagram is consistent with the experimental results of Govardhan & Williamson (2000) for the cases of m^* substantially greater than the given critical mass ratio of $m^*_{crit} = 0.54$, *i.e.* $m^* = 8.64$. However, as m^* approaches m^*_{crit} , the upper \leftrightarrow lower branch transition tends to occur at a frequency well above the predicted $f_{N\ vacuum}$ (see Govardhan & Williamson (2000)).

2.4 Forced oscillations of a circular cylinder

In order to better understand and then to predict the response of free vibrations, researchers have employed cylinders undergoing forced oscillations as a complementary model, by decoupling the fluid-structure interaction, to simplify the problems of VIV. This has led to a large number of experimental and numerical studies on the subject, including Bishop & Hassan (1964); Koopmann (1967); Sarpkaya (1978); Staubli (1983); Williamson & Roshko (1988); Gopalkrishnan (1993); Hover (1997); Hover *et al.* (1998); Carberry *et al.* (2001); Carberry (2002); Carberry *et al.* (2004a, 2005); Leontini *et al.* (2006a, 2007); Morse & Williamson (2006, 2009a,b), and many more.

2.4.1 Fluid forces and wake modes

Most of the forced oscillation studies involves investigation on the fluid forces and wake modes of cylinders undergoing forced or controlled sinusoidal oscillations (see Bishop & Hassan 1964; Carberry *et al.* 2001, 2005; Leontini 2007; Morse & Williamson 2009a,b), simply because the results of free vibrations have shown that the cylinder motion and the lift force in the lock-in region are well represented by sinusoidal functions (Feng 1968; Griffin & Koopmann 1977; Khalak & Williamson 1996, 1997a, 1999; Govardhan & Williamson 2000). Thus, the body motion and the fluid forcing are represented by the following equations:

$$y(t) = A \sin(2\pi f_e t), \quad (2.13)$$

$$F_y(t) = F_Y \sin(2\pi f_e t + \phi_{total}), \quad (2.14)$$

where A is the oscillation amplitude, f_e is the oscillation frequency respectively, F_Y is the magnitude of the transverse lift force, and ϕ_{total} is the phase between the lift force and displacement.

In a pioneering study, Bishop & Hassan (1964) found that a sharp increase in the magnitude of the lift force accompanied simultaneously with a jump of approximately 180° in the total phase occurred as the oscillation frequency increased through the Strouhal frequency for a stationary body, given a constant oscillation amplitude. Similar changes in the lift force and the total phase have also been observed in number of subsequent experiments of forced-oscillating cylinders, including Sarpkaya (1977); Gopalkrishnan (1993); Carberry *et al.* (2001). Following the findings in free vibrations by Govardhan & Williamson (2000) that a wake mode transition from $2S$ to $2P$ is associated with a jump of approximately 180° in the vortex phase, Carberry *et al.* (2001) suggested the changes in the lift and the total phase in forced oscillations also corresponded to an alternation in both the timing of vortex shedding and vortex pattern in the near wake.

Furthermore, Carberry (2002); Carberry *et al.* (2004a, 2005) directly compared the fluid forces and wake modes of forced-oscillating cylinders with the corresponding properties of freely-vibrating cylinders studied by Govardhan & Williamson (2000), and found a number of remarkable similarities in the vorticity field and variation in the total and vortex phases. Figure 2.17 shows a direct comparison of the total and vortex phases between a freely-vibrating cylinder and a sinusoidally-driven cylinder studied by Carberry *et al.* (2004a). The oscillation amplitude of the driven system was kept constant, while the oscillation frequency f_e was varied over a range of $0.77 < f_e/f_{St} < 0.91$, where f_{St} is the Strouhal frequency for a stationary cylinder. In both the freely and forced oscillating cases, similar distinct jumps in the total and vortex phases were observed. For the forced oscillating cylinder, as the oscillation frequency was increased from low

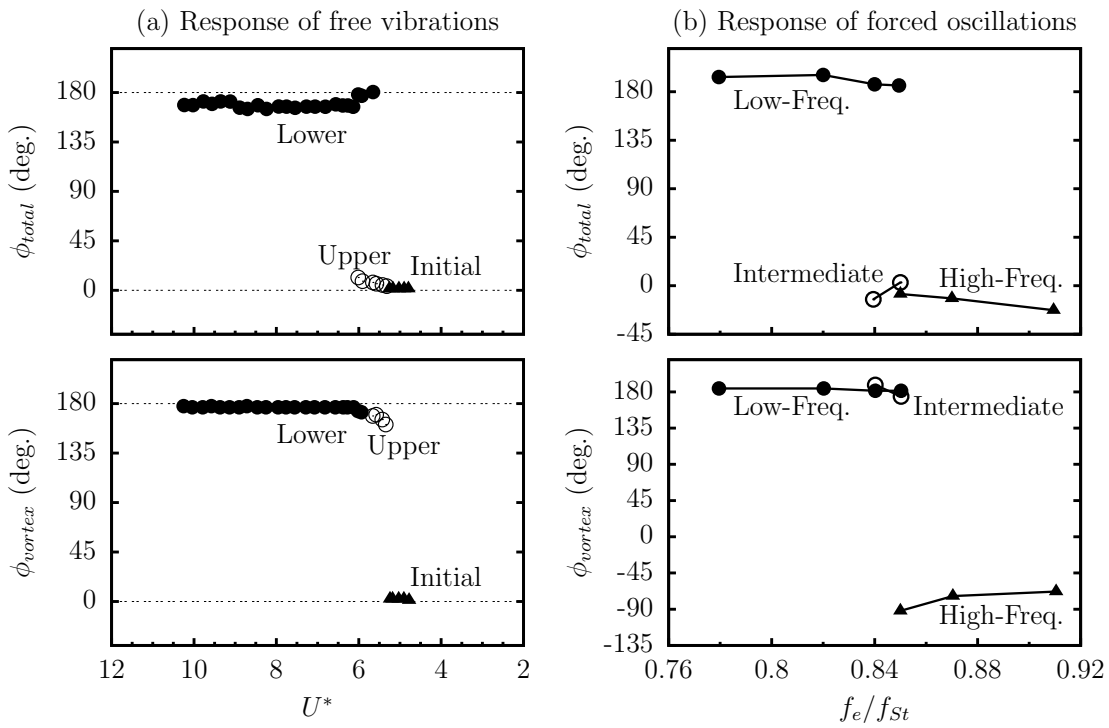


FIGURE 2.17: Total and vortex phases for (a) the three amplitude-response branches of free vibration at low $m^*\zeta$ values and (b) the corresponding forced wake states at $A/D = 0.6$. Reproduced from Carberry *et al.* (2004a).

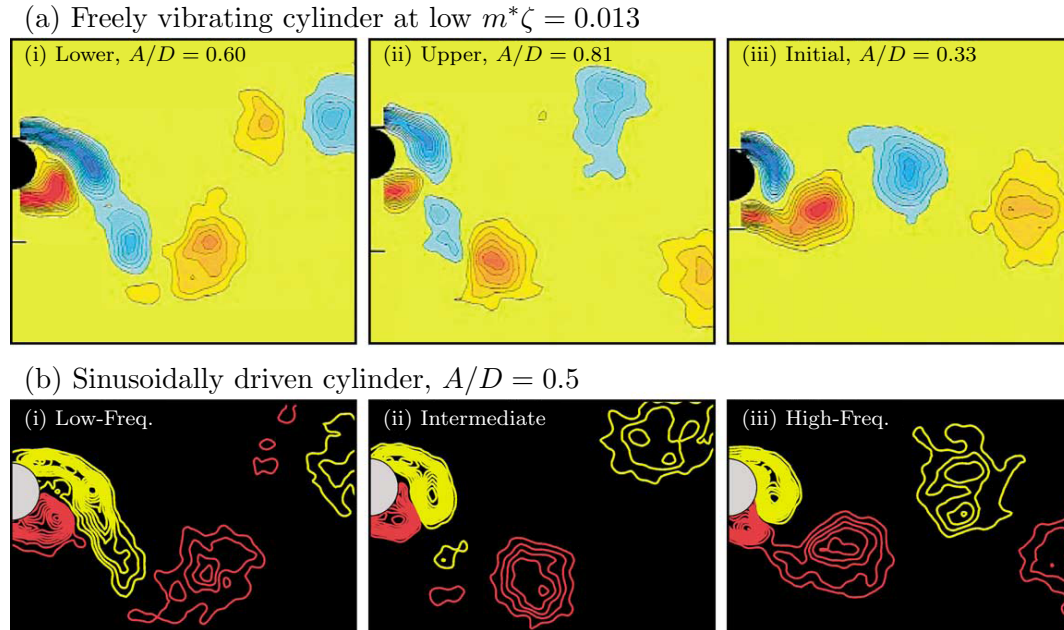


FIGURE 2.18: Comparison of vorticity fields between (a) a freely vibrating circular cylinder and (b) the corresponding sinusoidally-driven cylinder. (i) The lower branch and low-frequency state occurred at low f_e/f_{St} values, (ii) the upper branch and intermediate state were observed as f_e/f_{St} approached unity while (iii) the initial branch and high-frequency state occurred at higher values of f_e/f_{St} . Reproduced from (Carberry *et al.* 2004a).

2.4. Forced oscillations of a circular cylinder

to intermediate values, a jump of approximately 180° in the total phase occurred at $f_e/f_{St} \approx 0.84$, which was similar to the jump in total phase during the lower \leftrightarrow upper branch transition of the freely-vibrating case. On the other hand, a sharp jump in vortex phase was also observed as the driven oscillation frequency was increased from intermediate to high values, which was similar to the jump in vortex phase during the initial \leftrightarrow upper branch transition of the freely-vibrating case. Corresponding to the jump in vortex phase, the forced oscillating system also experienced a wake mode transition of $2S \leftrightarrow 2P$ which was consistent with the results of free vibration of Govardhan & Williamson (2000), as shown in Figure 2.18. Interestingly, the “low-frequency wake state” is similar to the lower branch response, the “intermediate wake state” is similar to the upper branch response, and the “high-frequency wake state is similar to the initial branch response. Despite strong similarities found in the phases and wake modes, however, one key difference between the freely and forced oscillating cylinders is found in the sign of energy transfer between the fluid and the structure. The energy transfer must be positive from the fluid to the oscillating system in free vibration, while negative energy transfer is observed in the forced oscillating system. More discussion on the topic of energy transfer will be presented in the future section §2.4.2.

More recently, Morse & Williamson (2006) directly compared the fluid forces of freely and forced oscillating cylinders, and suggested that *if the experimental conditions are carefully matched*, the fluid forces acting on the forced-oscillating cylinder are in very close agreement with the results of free vibration over an entire response plot. Later, Morse & Williamson (2009a,b) performed a large amount of experiments on a sinusoidally-driven cylinder over a high-resolution amplitude – wavelength plane. The normalised amplitude (A^*) was varied from 0.02 up to 16 with a resolution of 0.02, and the normalised wavelength (λ^*) was varied from 2 up to 16 with a resolution of 0.2, amounting a total of 5680 experimental runs. The Reynolds number was kept constant at two Reynolds number $Re = 4000$ and $10\,000$. In these studies, Morse & Williamson conducted extensive force measurements to create high-resolution contour plots of the magnitude of fluid forcing and its phase, and then to precisely identify the locations of jumps in these parameters.

The contours of the magnitude of lift force and vortex force from Morse & Williamson (2009a) are shown in Figure 2.19, and the corresponding phases are shown in Figure 2.20. Of particular interest as found by Morse & Williamson, dramatic changes in these contour plots show clear boundaries that are highly similar to the boundaries separating different wake modes in the map of Williamson & Roshko (1988), indicating similar wake mode regimes could be identified based solely on force measurements. Consequently, Morse & Williamson identified the regimes of $2S$ and $2P$ modes based on contours of the magnitude of the total force and the vortex phase, and the regime of $P + S$ wake mode based on the asymmetry in the time trace of the lift due to the asymmetric pattern of the wake. These regimes of wake modes were further confirmed by their PIV vorticity measurements. Figure 2.21 shows the map of wake mode regimes of Williamson & Roshko in (a) and the new map of Morse & Williamson in (b). As compared, both maps shows a remarkable similarity in the boundaries between the wake modes. In addition to the known regimes of $2S$, $2P$ and $P + S$ modes identified by Williamson & Roshko, Morse & Williamson revealed the existence of two regions where two modes overlapped. These overlap regions were found in the desynchronisation region where $2P$ intermittently appeared, and in a region labelled as “ $2P_o$ ” where $2S$, $2P$ and $2P_o$ modes overlapped. Figure 2.22 shows the results of PIV measurements of these wake modes. As defined by Morse & Williamson, $2P_o$ mode, as shown

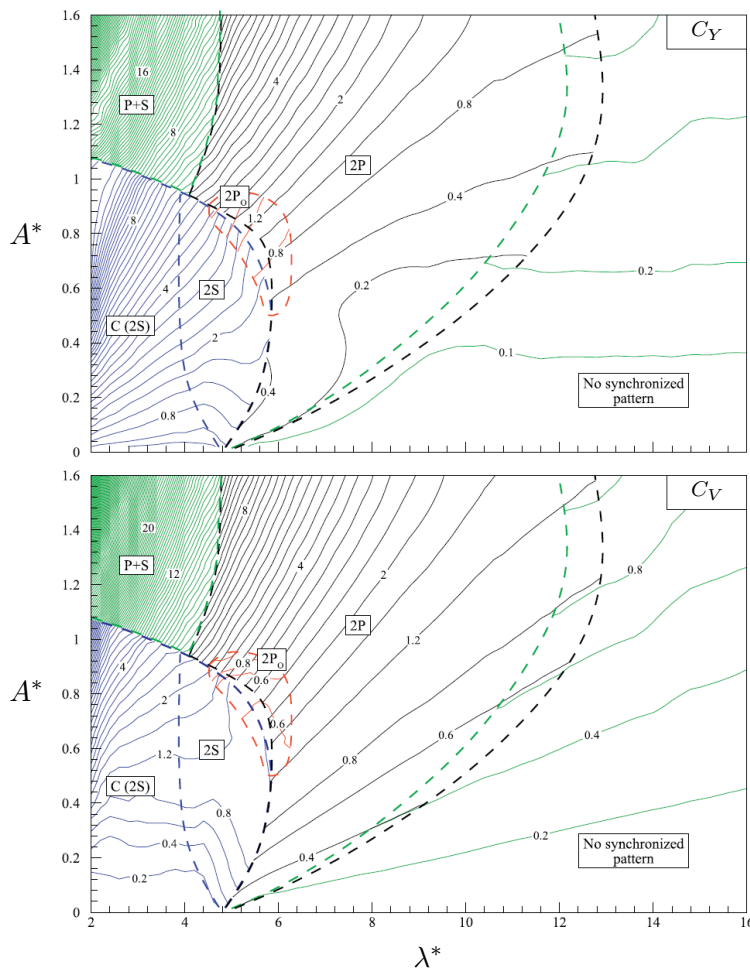


FIGURE 2.19: Contours of the magnitude of the total force, C_Y , and the vortex force, C_V . Boundaries between the wake modes are indicated by the dashed lines. for $Re = 4000$. Morse & Williamson (2009a).

in Figure 2.22 (b), is a variation of $2P$ mode where two pairs of vortices are shed per oscillation cycle but the secondary vortex is much weaker and decays rapidly as the vortex pair moves downstream. This $2P_o$ mode, similar to the weakly pattern of $2P$ mode in the upper branch of free vibration captured by Govardhan & Williamson (2000), is equivalent to the “intermediate wake state” observed by (Carberry *et al.* 2004a).

2.4.2 Energy transfer and prediction of free vibration response

Researchers have attempted to predict VIV response of cylinders using the fluid force measurement data obtained from forced oscillations. One of such studies is that by Staubli (1983) who used his experimental measurements of the lift and total phase contours of a sinusoidally-driven cylinder to calculate the response of an elastically-mounted cylinder that was then compared with that of Feng (1968). The comparison showed that the calculated amplitude response matched well with Feng’s results at very low reduced velocities, but major discrepancies were observed at relatively high reduced velocities. However, more recent studies for VIV prediction by using forced-oscillating cylinders have focused on the energy transfer between the fluid and the structure.

It is helpful to first introduce some fundamental equations relating to the energy

2.4. Forced oscillations of a circular cylinder

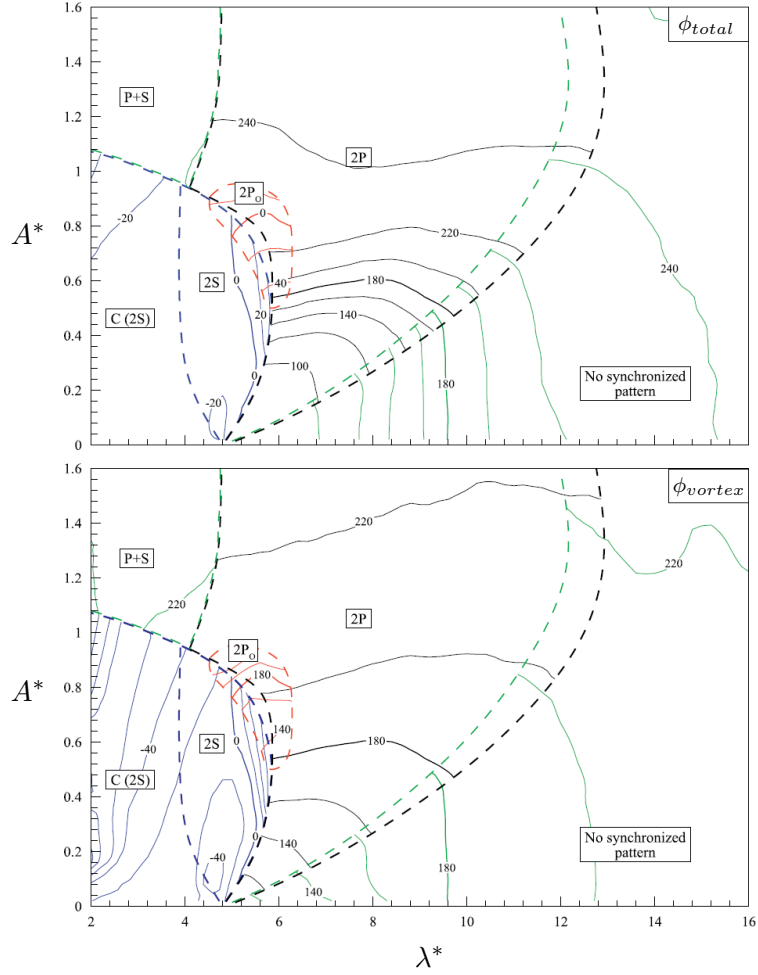


FIGURE 2.20: Contours of the total phase, ϕ_{total} , and the vortex phase, ϕ_{vortex} . Boundaries between the wake modes are indicated by the dashed lines. $Re = 4000$. Morse & Williamson (2009a).

transfer before proceeding reviewing the literature on this topic. As described previously in Eq. (2.8) and Eq. (2.8), when the cylinder motion is synchronised with the vortex shedding, the body motion $y(t)$ and the fluid force $F_y(t)$ are well represented by sinusoidal functions:

$$y(t) = A \sin(2\pi ft), \quad (2.15)$$

$$F_y(t) = F_Y \sin(2\pi ft + \phi), \quad (2.16)$$

where A is the oscillation amplitude, f is the oscillation frequency, F_Y is the magnitude of the transverse lift force, and ϕ is the phase between the lift force and the body motion (for convenience here). Therefore, the energy transfer from the fluid to the oscillating structure per oscillation cycle can be determined by

$$\begin{aligned} E_{in} &= \oint F_y(t) dy = \int_0^T F_y(t) \dot{y}(t) dt \\ &= \pi A F_Y f \sin \phi \left[\frac{2\pi ft}{2} + \frac{\sin(2 \cdot 2\pi ft)}{4} \right]_{t=0}^{t=T} \\ &= \pi A F_Y \sin \phi, \end{aligned} \quad (2.17)$$

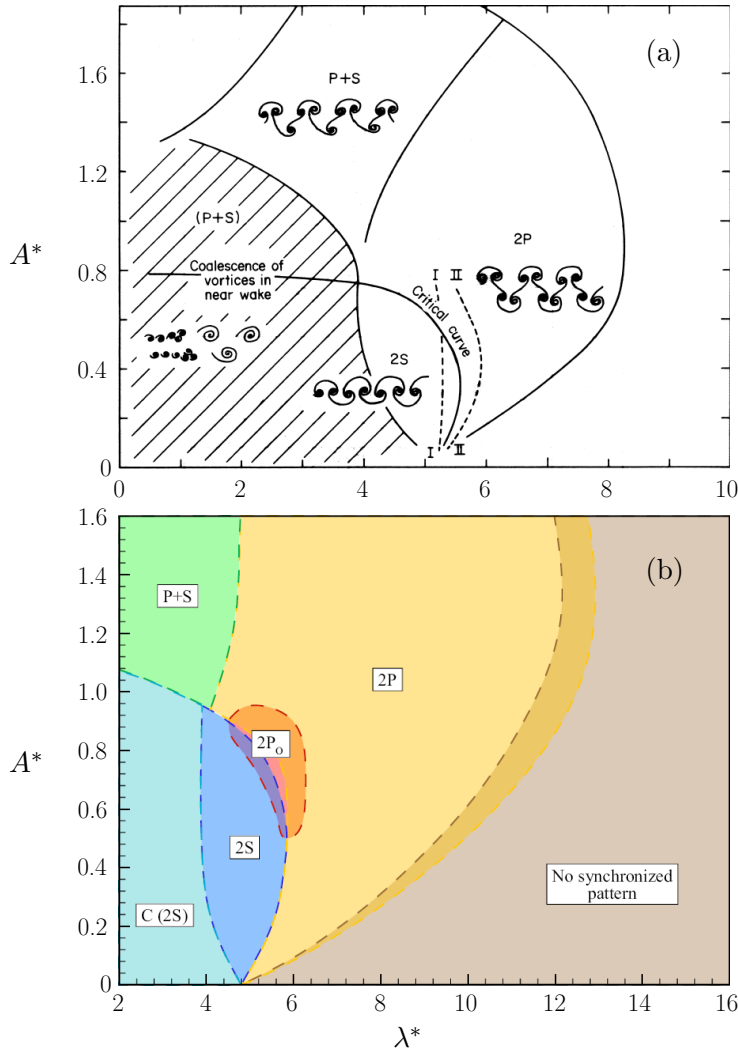


FIGURE 2.21: Maps of wake mode regimes for sinusoidally-driven circular cylinders: (a) the map of Williamson & Roshko (1988), and (b) the map of Morse & Williamson (2009a), revealing new regions (in overlapping colours) where two vortex shedding modes coexist.

where $T = 1/f$ is the vibration period. Then, the energy transfer coefficient is given by

$$C_E = \frac{E_{in}}{\frac{1}{2}\rho U^2 DL} = \pi A^* C_Y \sin \phi, \quad (2.18)$$

where $C_Y = F_Y/(\frac{1}{2}\rho U^2 DL)$ is the magnitude of the lift coefficient. Fundamentally, the phase must be $0^\circ < \phi < 180^\circ$ for positive energy transfer from the fluid to the oscillating structure. Ideally, if the cylinder motion and lift force in free vibration are pure sinusoidal functions, the phase is always between 0° and 180° as the energy transfer is always positive. However, the phase might be observed out of the range of $0^\circ < \phi < 180^\circ$ in experiments, because the cylinder motion and the fluid forcing are not purely sinusoidal functions in reality. For a freely-vibrating cylinder, on the other

2.4. Forced oscillations of a circular cylinder

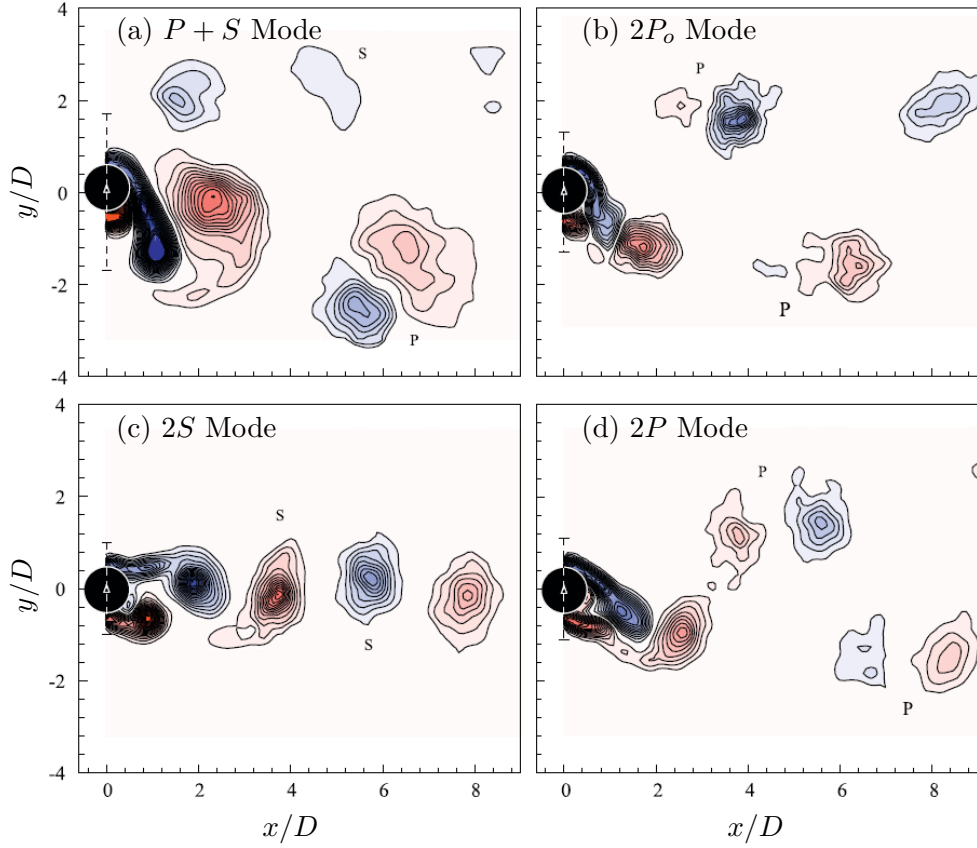


FIGURE 2.22: Vorticity fields for the wake modes of a circular cylinder undergoing sinusoidally-driven oscillations (Morse & Williamson 2009a).

hand, the energy lost per cycle due to the structural damping is computed by

$$E_{out} = \oint c \dot{y}(t) dy = \int_0^T c \dot{y}(t)^2 dt \quad (2.19)$$

$$= (2\pi f)^2 c A^2 \int_0^T \cos^2(2\pi ft) dt = 2\pi^2 c A^2 f. \quad (2.20)$$

Following the approach of Khalak & Williamson (1999), the response amplitude and frequency may be derived as follows:

$$A^* = \frac{1}{4\pi^3} \frac{C_Y \sin \phi}{(m^* + C_A)\zeta} \left(\frac{U^*}{f^*}\right)^2 f^*, \quad (2.21)$$

$$f^* = \sqrt{\frac{m^* + C_A}{m^* + C_{EA}}}, \quad (2.22)$$

where C_A is the potential added-mass coefficient, and C_{EA} is an “effective” added mass coefficient due to the transverse lift force in-phase with the body acceleration ($C_Y \cos \phi$):

$$C_{EA} = \frac{1}{2\pi^3} \frac{C_Y \cos \phi}{A^*} \left(\frac{U^*}{f^*}\right)^2. \quad (2.23)$$

As proposed recently by Morse & Williamson (2009b), if the system is freely oscillating with a constant amplitude and frequency, the energy into the system must be equal to

the energy out of the system, which gives

$$\underbrace{C_Y \sin \phi}_{E_{in}^*} = \frac{4\pi^3 A^* (m^* + C_A) \zeta}{\underbrace{\left(\frac{U^*}{f^*}\right)^2 f^*}_{E_{out}^*}}, \quad (2.24)$$

where $C_Y \sin \phi$ is the transverse lift in phase with the cylinder velocity (Sarpkaya 1977), representing the normalised energy into the system, E_{in}^* , per cycle (also defined by Morse & Williamson as the “fluid excitation”).

As noted that the parameter of $C_Y \sin \phi$ plays an important role to decide the direction of energy transfer between the fluid and structure, contour plots of $C_Y \sin \phi$ have been presented in experimental and numerical studies. Gopalkrishnan (1993) and Hover *et al.* (1998) reported the contours of transverse lift in phase with velocity ($C_Y \sin \phi$) and in phase with acceleration ($C_Y \cos \phi$) over a wide range of amplitude – wavelength plane from a series of experiments at MIT Testing Tank Facility. Hover *et al.* (1998) also developed a closed-loop feedback control servo system to simulate VIV response of free cylinders with “user-defined” mass and damping ratios. Figure 2.23 shows the contours of $C_Y \sin \phi$ of forced oscillations of Hover *et al.* with an overlay of the amplitude response of “virtual” free vibration at extremely low damping ratio over the same parametric space. It can be seen that the largest A^* response values of the free vibration closely matched the contour of $C_Y \sin \phi = 0$; however, the majority of the lower branch and the desynchronisation region of the free vibration were observed in regions of negative fluid excitation ($C_Y \sin \phi < 0$). This phenomenon of negative energy transfer was also reported in later experimental studies by Carberry *et al.* (2001); Carberry (2002); Carberry *et al.* (2005). Later, Leontini *et al.* (2006a,b); Leontini (2007) conducted a series of comprehensive numerical studies on the topics of energy transfer and prediction of VIV response from driven oscillation results at different low Reynolds numbers ($50 \leq Re \leq 300$) and mass ratios ($1 \leq m^* \leq 10$). Their results indicated that the VIV response in the periodic regime (the lower branch) was successfully predicted from sinusoidal driven oscillations, as the amplitude response of free vibration fell in the positive energy transfer regions of $0 < C_E$ of the driven oscillations. However, the response results of free vibration in the quasi-periodic (the initial branch) and chaotic (the upper branch) regimes were situated outside of the positive C_E regions of the driven oscillations.

However, significant progress in predicting VIV response has been made by Morse & Williamson (2009b). Beside providing extensive force measurement results, Morse & Williamson also gave an in-depth discussion on the energy transfer of forced-oscillating cylinders and then demonstrated accurate predictions of the VIV response by using their contours of the fluid force. In addition, a new concept of *energy portraits* has been introduced by Morse & Williamson. An energy portrait is defined as a plot of the energy of excitation (E_{in}^*) and the energy lost (E_{out}^*) due to the structural damping as a function of the oscillation amplitude (A^*) with the reduced velocity kept constant. This concept provides stability and instability solutions for the equilibrium points of energy transfer as follows:

$$\text{stable, } dE^*/dA < 0, \quad (2.25)$$

$$\text{unstable, } dE^*/dA > 0, \quad (2.26)$$

where $E^* = E_{in}^* - E_{out}^*$ is the net energy transfer from the fluid to the structure. According to Morse & Williamson (2009b), free vibrations would occur at the stable-equilibrium points. Figure 2.24 shows the contours of the transverse lift in phase with

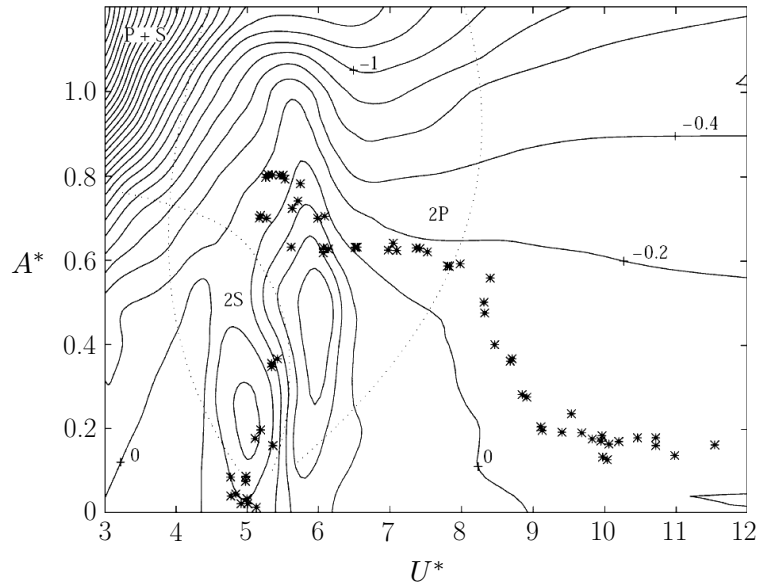


FIGURE 2.23: Contours of forced-oscillation transverse lift in phase with velocity ($C_Y \sin \phi$) (—), with an overlay of the amplitude response of virtual free-vibration (*) and wake mode regimes of Williamson & Roshko (1988) (···). $Re = 3800$. Hover *et al.* (1998).

velocity. The regime of possible free vibration falls inside the regions of $C_Y \sin \phi = 0$ and $dE^*/dA < 0$. Figure 2.25 shows comparisons of measured and predicted amplitude response for a freely-vibrating cylinder at low and high $m^*\zeta$ values. The predicted responses are in remarkable agreement with the measured free-vibration responses. These results demonstrate much better predictions of VIV response than the previous studies, probably because of high-resolution force measurements and the careful matching of the experimental conditions between the free vibration and forced oscillation cases (Morse & Williamson 2009b).

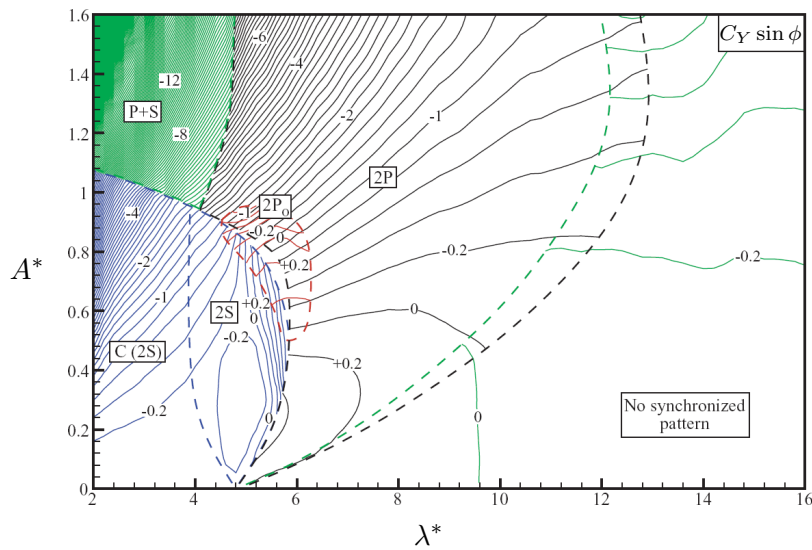


FIGURE 2.24: Contours of the transverse lift force in phase with velocity (normalised “fluid excitation”, $C_Y \sin \phi$), with an overlay of the map of wake modes for $Re = 4000$. Boundaries between the wake modes are indicated by the dashed lines. Morse & Williamson (2009a).

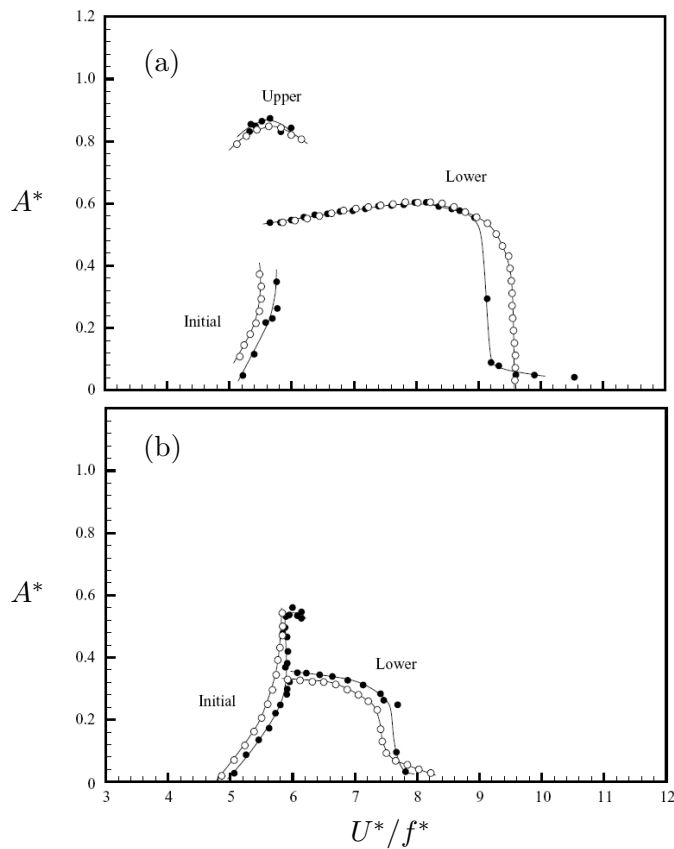


FIGURE 2.25: Amplitude response prediction for a freely vibrating circular cylinder at (a) low mass damping, $(m^* + C_A)\zeta = 0$, and (b) high mass damping $(m^* + C_A)\zeta = 0.340$: \circ , predicted response from sinusoidally-driven oscillations; \bullet , free vibration response measured by Govardhan & Williamson (2006). In both cases, $m^* = 10.49$. $Re = 4000$ for the forced oscillation case; $Re = 4000$ at the peak amplitude for the free-vibration case. Plot from Morse & Williamson (2009b).

2.5 Galloping response of a square cylinder

All non-circular cross-sectional structures with fixed flow separation locations may experience the phenomenon of galloping, due to the aerodynamic forces that are induced by the transverse movement of the structure. This is referred to as *aerodynamic instability* (Blevins 1990). Thus, galloping is categorised as a type of movement-induced excitation (MIE) (Naudascher & Rockwell 2005). A typical example that has potential to experience galloping instability is an iced-coated electric transmission cable in winter winds (Den Hartog 1932, 1956). As illustrated in Figure 2.26 (a), a plain circular cylinder, moving downwards with velocity \dot{y} , is subjected to a free stream U_∞ , and the effective flow velocity, with an angle of φ relative to the free stream, is $U_{rel} = \sqrt{U_\infty^2 + \dot{y}^2}$. Consequently, the resultant force F_R is always in the same direction of the effective relative flow U_{rel} . Therefore, the upward component of this force will be opposite to the cylinder's motion, which damps the cylinder's motion and denies the possibility of movement-induced vibration. In contrast, an ice-coated cable shown in Figure 2.26 (b) modifies its cross-sectional geometry, which may result in an instantaneous force component F_y in the same direction of the cable velocity. In this scenario, vibration of the cable will be strengthened, leading to galloping phenomenon with large oscillation amplitudes. Unlike vortex-induced vibrations with their oscillation amplitudes limited to the order of magnitude of one cylinder diameter over a relatively small discrete range of flow velocity (Corless & Parkinson 1988), galloping is not self-limited. Comparatively, much larger amplitudes can be built up in galloping oscillations, having been observed to be as much as 100 times the diameter of the structure for some ice-coated transmission cables, but their frequencies are normally found to be much lower than the vortex shedding frequency (*i.e.* $f^* \ll 1/(2\pi)$) (Corless & Parkinson 1988).

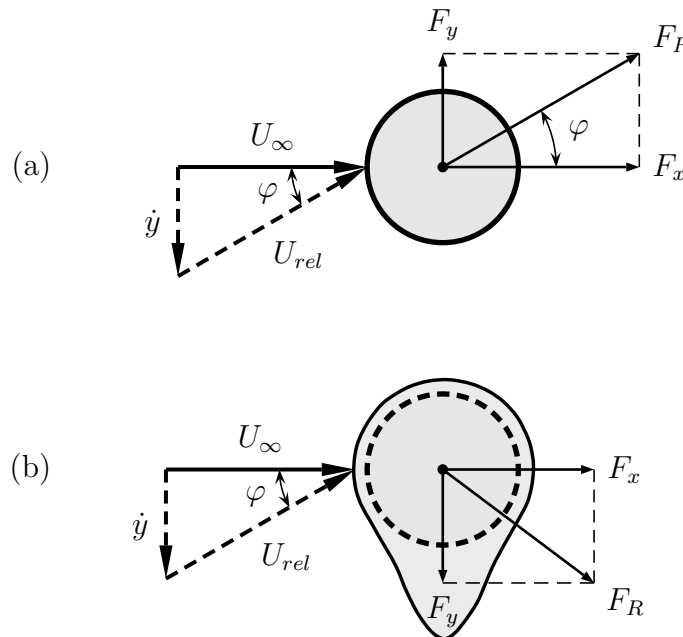


FIGURE 2.26: Cross-flow galloping of an ice-coated cable. (a) Force components on a plain circular cylinder. (b) An ice-coated circular cylinder. Note that the bodies (cables) are moving downwards with a velocity of \dot{y} .

Extensively work has been undertaken on galloping of non-circular cross-sectional structures, particularly on the cross-flow galloping of a rigid square cylinder, since Den

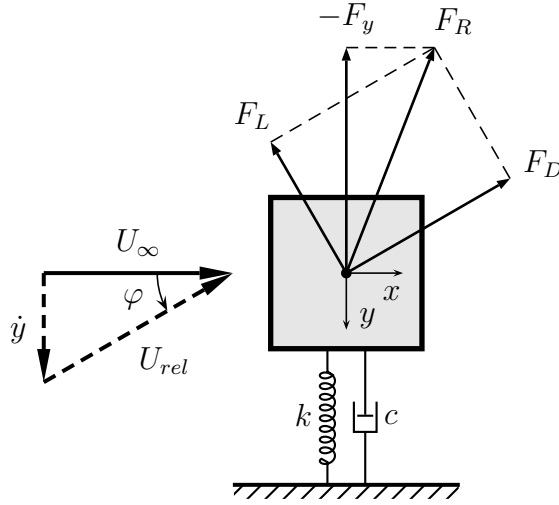


FIGURE 2.27: Cross-flow galloping model of a square cylinder. At the instant, the square cylinder is moving downwards with velocity \dot{y} .

Hartog (1932) first proposed his stability criterion (well known as the Den Hartog criterion) to estimate the susceptibility of a section to cross-flow galloping in a wind flow. Figure 2.27 shows a spring-mounted square cylinder model adopted from Blevins (1990) for the Den Hartog criterion analysis. At a time instant, the effective flow relative to the square cylinder moving downwards has an angle of incidence given by

$$\varphi = \arctan \left(\dot{y}/U_\infty \right), \quad (2.27)$$

where $\dot{y} = dy/dt$ is the cylinder moving velocity transverse to the free stream. The steady fluid dynamic forces on the square cylinder are the drag force component (F_D) in the same direction as the effective flow, defined by

$$F_D = \frac{1}{2} \rho U_{rel}^2 D L C_D, \quad (2.28)$$

and the lift force component (F_L) in the direction normal to the effective flow, defined by

$$F_L = \frac{1}{2} \rho U_{rel}^2 D L C_L, \quad (2.29)$$

where C_D and C_L are the drag and lift coefficients with respect to the effective flow, respectively. Therefore, the resultant cross-flow lift force F_y can be determined by

$$F_y = -F_L \cos \varphi - F_D \sin \varphi = \frac{1}{2} \rho U_\infty^2 D L C_y, \quad (2.30)$$

where C_y is the transverse lift force coefficient, given by

$$C_y = -\frac{U_{rel}^2}{U_\infty^2} \left(C_L \cos \varphi + C_D \sin \varphi \right). \quad (2.31)$$

As shown in Figure 2.27, the stability of the system can be assessed by analysing the variation of lift F_y with respect to φ . If $dF_y/d\varphi > 0$, the upward fluid force F_y will increase for negative φ and decrease for positive φ , which means ΔF_y and $\Delta \dot{y}$ will be in the same direction, potentially resulting in galloping. Otherwise, if $dF_y/d\varphi < 0$,

2.5. Galloping response of a square cylinder

Δy will be in the opposite direction, and hence the vibrations will be damped by F_y . Thus, the criterion for dynamic stability given by Den Hartog (1956) is as follows:

$$\frac{dF_y}{d\varphi} \simeq -\left(\frac{dF_L}{d\varphi} + F_D\right) < 0, \quad \text{stable.} \quad (2.32)$$

$$\frac{dF_y}{d\varphi} \simeq -\left(\frac{dF_L}{d\varphi} + F_D\right) > 0, \quad \text{unstable} \quad (2.33)$$

For small values of φ , the relative flow speed can be approximated to the free stream velocity as $U_{rel} \simeq U_\infty$, and Eq.(2.31) can be expanded using Taylor's series expansion:

$$C_y(\varphi) \simeq C_y|_{\varphi=0} + \left.\frac{\partial C_y}{\partial \varphi}\right|_{\varphi=0} \cdot \varphi. \quad (2.34)$$

Differentiating the above Eq. (2.34) yields

$$\left.\frac{\partial C_y}{\partial \varphi}\right|_{\varphi=0} = -\left(\left.\frac{\partial C_L}{\partial \varphi} + C_D\right)_{\varphi=0}, \quad (2.35)$$

which implies that the square cylinder model will be unstable if

$$\left.\frac{\partial C_y}{\partial \varphi}\right|_{\varphi=0} > 0, \quad (2.36)$$

or equivalently

$$\left.\frac{\partial C_L}{\partial \varphi} + C_D\right|_{\varphi=0} < 0. \quad (2.37)$$

In other words, *a section is dynamically unstable if the negative slope of the lift curve is greater than the ordinate of the drag curve*, as Den Hartog (1932) states. On the other hand, the square cylinder will be stable if $\partial C_y/\partial \varphi < 0$.

Assuming a one-DOF linear mass-spring-damper system, the governing equation of motion is

$$m\ddot{y} + 2m\zeta\omega_n\dot{y} + ky = F_y = \frac{1}{2}\rho U_\infty^2 DLC_y, \quad (2.38)$$

where ζ is the structural damping ratio, and ω_n is the angular natural frequency of the system. Substituting Eq. (2.34) into Eq. (2.38) gives

$$m\ddot{y} + 2m\omega_n\left(\zeta - \frac{\rho U_\infty DL}{4m\omega_n} \left.\frac{\partial C_y}{\partial \varphi}\right|_{\varphi=0}\right)\dot{y} + ky = F_y = \frac{1}{2}\rho U_\infty^2 DLC_L|_{\varphi=0}. \quad (2.39)$$

Thus, the equivalent structural damping ratio is the sum of the structural and aerodynamic components, given by

$$\zeta_E = \zeta - \frac{\rho U_\infty DL}{4m\omega_n} \left.\frac{\partial C_y}{\partial \varphi}\right|_{\varphi=0}. \quad (2.40)$$

When $\zeta_E > 0$, the equivalent structural damping is positive, and the system is stable. Otherwise, when $\zeta_E < 0$, the equivalent structural damping is negative leading to amplitude growth, and thus the system becomes unstable. The critical reduced velocity U_{crit}^* for the onset of galloping instability can also be determined by setting $\zeta_E = 0$:

$$U_{crit}^* = \frac{U_{crit}}{f_N D} = \frac{4m(2\pi\zeta)}{\rho D^2 L} \left/ \frac{\partial C_y}{\partial \varphi} \right., \quad (2.41)$$

where U_{crit} is the critical free stream velocity, and $f_N = \omega_n/(2\pi)$ is the natural frequency of the system. If the flow velocity exceeds the critical velocity threshold, the energy transferred from the flow to the structure at the rate of $F_y \dot{y}$ overcomes the energy dissipated by the structural damping, which will lead to unstable galloping oscillations.

To predict the critical velocity threshold and the response of galloping of a square cylinder, quasi-steady theory has been developed and implemented in wind tunnel experiments by Parkinson & Brooks (1961); Parkinson & Smith (1964), after its idea was firstly introduced by Den Hartog (1932). In this quasi-steady theory approach, the instantaneous transverse aerodynamic force F_y acting on the square cylinder moving downwards with velocity \dot{y} during its oscillation cycle in the presence of flow velocity U_∞ is approximated to that measured on a stationary cylinder placed at the corresponding physical angle of attack of $\alpha = \arctan(\dot{y}/U_\infty)$ with a flow velocity of U_{rel} . Therefore, the aerodynamic force coefficient, C_y , of the stationary cylinder is a function of α , and can be approximated by a polynomial in \dot{y}/U_∞ as

$$C_y = \sum_{i=1}^p a_i \left(\frac{\dot{y}}{U_\infty}\right)^i = a_1 \frac{\dot{y}}{U_\infty} + a_2 \left(\frac{\dot{y}}{U_\infty}\right)^2 + a_3 \left(\frac{\dot{y}}{U_\infty}\right)^3 + \cdots + a_m \left(\frac{\dot{y}}{U_\infty}\right)^p. \quad (2.42)$$

As suggested by Parkinson & Smith, this polynomial approximation requires at least a seventh degree solution for a close result, because of five significant changes of curvature in the particular range of $16^\circ < \alpha < 16^\circ$. Therefore, Eq. (2.42) is rewritten as

$$C_y = a_1 \frac{\dot{y}}{U_\infty} - a_3 \left(\frac{\dot{y}}{U_\infty}\right)^3 + a_5 \left(\frac{\dot{y}}{U_\infty}\right)^5 - a_7 \left(\frac{\dot{y}}{U_\infty}\right)^7, \quad (2.43)$$

where a_1 , a_3 , a_5 and a_7 are positive constants. According to Eq. (2.41), the critical reduced velocity required for the onset of galloping can be determined by

$$U_{crit}^* = \frac{4\pi\zeta}{na_1}, \quad (2.44)$$

where $n = \rho D^2 L / (2m) = 1/(2m^*)$ is the mass parameter.

Figure 2.28 shows the transverse lift force measurements of Parkinson & Smith (1964) on a stationary square cylinder at different angles of attack, along with a seventh-degree polynomial approximation. Similar measurements at different Reynolds numbers have also been reported by Bearman *et al.* (1987), Luo & Bearman (1990), and Norberg (1993). With the obtained polynomial parameters (a_1 , a_3 , a_5 and a_7), Parkinson & Smith, following the method of Krylov & Bogoliubov (Minorsky 1962), resolved the differential governing equation of motion, Eq. (2.38), and then successfully predicted the galloping response for square cylinders freely vibrating in wind tunnel, including the amplitude response, the critical reduced velocity for the onset of galloping, and a hysteresis phenomenon shown in Figure 2.29.

Subsequently, the quasi-steady was further developed by researchers. Novak (1969, 1972) extended Parkinson & Smith's quasi-steady model to other prismatic structures. Novak & Tanaka (1974) and Bearman *et al.* (1987) investigated the effect of turbulence, finding that the shape of the C_y versus α curve is influenced significantly by the turbulence level. Corless & Parkinson (1988) proposed a model to describe the combined effects of vortex-induced vibration and galloping. Luo *et al.* (2003) studied numerically the hysteresis phenomenon in the galloping oscillation of a square cylinder, and revealed that the hysteresis phenomenon is related to the inflection in the curve of C_y versus α of the stationary body.

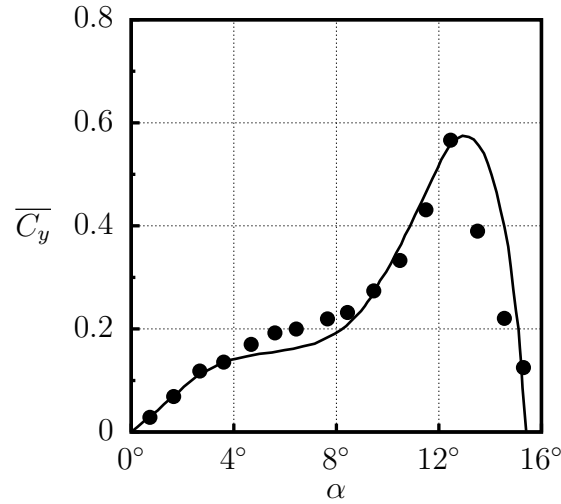


FIGURE 2.28: The mean of the transverse lift coefficient, \bar{C}_y , plotted against the angle of attack α for a square cylinder at $Re = 22300$. Solid circles are experimental data, and the solid line is the polynomial approximation with $a_1 = 2.69$, $a_3 = 168$, $a_5 = 6270$ and $a_7 = 59900$. (Parkinson & Smith 1964).

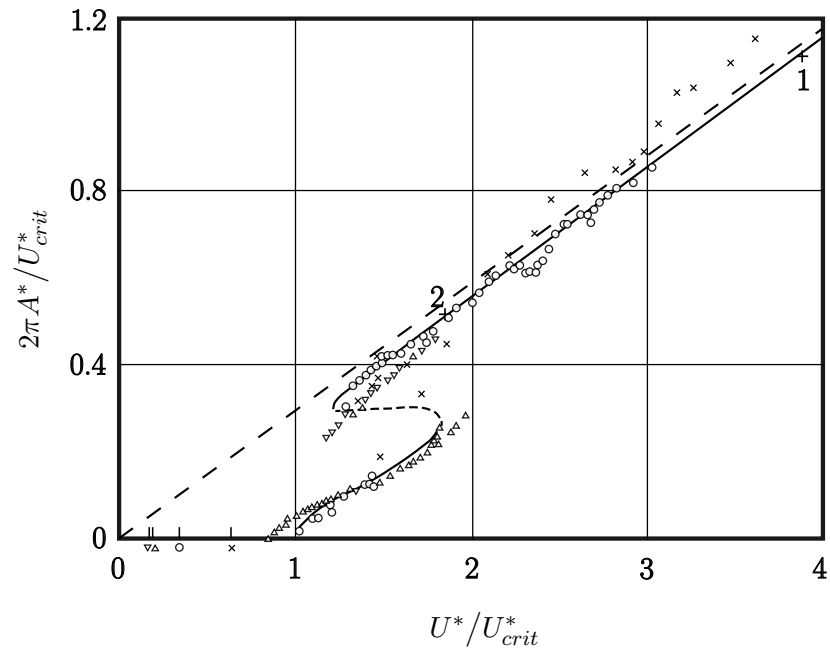


FIGURE 2.29: Amplitude response of a square cylinder experiencing galloping. —, Theoretical stable limit cycle; - -, theoretical unstable limit cycle; \times , $\zeta = 0.00107$; \circ , $\zeta = 0.00196$; \triangle , $\zeta = 0.00364$; ∇ , $\zeta = 0.00372$; +1, $\zeta = 0.0012$; +2, $\zeta = 0.0032$; Reynolds number range of $Re = 4000 - 20000$; the mass parameter $n = 1/(2m^*) = 4.3 \times 10^{-3}$. Plot reproduced from Parkinson & Smith (1964).

Furthermore, the limitations of quasi-steady theory have also received extensive attention. A basic requirement given by Parkinson & Smith for the quasi-steady theory to be appropriate is that the Strouhal frequency should be appreciably higher than the natural frequency of the system. This arises from the fact that a square cylinder can experience both phenomena of galloping and vortex-induced vibration if the vortex shedding frequency is close to the natural frequency of the system. In fact, significant interaction effects of galloping and vortex-induced vibration, having been reported by Sullivan (1977); Wawzonek (1979); Bearman *et al.* (1987); Corless & Parkinson (1988), makes the quasi-steady theory developed for galloping as inapplicable. Therefore, conditions are required to separate the two phenomena for individual consideration. A number of studies, including Blevins (1977, 1990); Bearman *et al.* (1987); Parkinson (1989); Païdoussis *et al.* (2010), have indicated that the quasi-steady is applicable if a elastically-mounted square cylinder is placed in a flow with sufficiently high reduced velocity. Blevins (1977) proposed a criterion for the applicability of the quasi-steady theory that the vortex shedding frequency must be at least twice as large as the natural frequency. Assuming the Strouhal number $St = 0.2$, this criterion was translated to be $2(U_\infty/(f_{St}D)) \leq U_\infty/(f_N D)$, giving a requirement of $U^* = U_\infty/(f_N D) > 10$. However, this requirement was then revised by Blevins (1990) to $U^* = U_\infty/(f_N D) > 20$, without further detailed explanation. Bearman *et al.* (1987), based on their investigation on the interaction of vortex shedding and galloping, concluded that galloping response of square cylinders can be predicted by the quasi-steady theory for $U_\infty/(2\pi f_N D) \geq 4(2\pi St)^{-1} \simeq 5$, which is translated to be $U^* = U_\infty/(f_N D) > 10\pi$. According to these criteria, the threshold reduced velocity for the applicability of the quasi-steady theory trends to be $U^* > 30$.

2.6 Summary of the review and the questions for research

The preceding review of the literature has concentrated largely on the fundamental characteristics of flow-induced vibration of circular and square cylinders. It is apparent that a large body of research has been undertaken to investigate transverse vortex-induced vibration of a circular cylinder, and transverse galloping of a square cylinder. However, several questions remain as highlighted by the following list:

1. As the results of circular cylinders forced to oscillate sinusoidally have shown some remarkable similarities to the freely-vibrating cylinder cases, one might expect that as if the body motions were identical, and therefore the forces on the body, the phases, and thus the energy transfer and the wake modes would also be identical (Carberry 2002). Therefore, the first question for investigation is arisen below:

What are the similarities and differences between free and forced vibrations of a circular cylinder in a three-dimensional flow?

2. The literature has shown that a square cylinder at zero angle of attack is susceptible to both galloping and vortex-induced vibration, as the body has fixed flow separation points and an appreciable afterbody. Extensive research has been undertaken to characterise the galloping response of a square cylinder at zero angle of attack. However, much less research attention has been given to the other symmetric orientation at 45° , the diamond orientation. Compared with a circular cylinder, a diamond cylinder has similar afterbody and locations of flow separation points, and then it would be expected to experience vortex-induced

2.6. Summary of the review and the questions for research

vibration over a similar reduced velocity range as the circular cylinder. Therefore, the second question for research is arisen below:

What body-oscillator phenomenon does a diamond cylinder experience over a reduced velocity range of $0 < U^ < 18$ where circular cylinders have been seen undergoing vortex-induced vibration?*

3. If a diamond cylinder would experience VIV over $0 < U^* < 18$, one might expect the body to undergo transitions of the body-oscillator phenomenon between galloping of VIV, as the angle of attack is varied from 0° to 45° . Of particular interest in this study, the third question for research is therefore arisen below:

How does the angle of attack vibration influence the vibration response of a square cylinder?

To answer these questions, experimental investigations are therefore required to expand understanding of FIV of circular and square cylinders. The experimental investigations will be divided into two major components: VIV of circular cylinders, and FIV of square cylinders. Firstly, VIV of a circular cylinder with low mass and damping ratio will be characterised and then directly compared with the cases of the body forced to follow the trajectories of the free vibration and sinusoidal functions. Secondly, FIV of a square cylinder with angle of attack variation will be investigated over a range of reduced velocity.

Chapter 3

Experimental Methodology

3.1 Introduction

This chapter outlines the experimental facilities and apparatus, techniques and procedures used to acquire the data to be presented in the future chapters. The chapter begins with a description of the water channel facilities in §3.2. Details of the air bearing rig used for free FIV experiments are presented in §3.3, followed by details of the motion control system used for forced oscillations in §3.4, where fundamentals of PID control algorithm and components of the control system used are given. The circular and square cylinder models used are described in §3.5. Furthermore, §3.6 presents the primary devices and techniques employed to record the quantitative experimental measurements for analysis, which include linear displacement measurement using a linear variable differential transformer (LVDT), rotary measurement using an optical encoder, force measurements using strain gauges, temperature measurement using a resistance temperature detector (RTD), and flow visualisation using particle image velocimetry (PIV) technique. A brief description is followed in §3.7 to explain the experimental procedures to measure a free FIV system's parameters such as the natural frequencies, and the structural damping ratio. Lastly, the chapter concludes with a summary of the experimental methodologies.

3.2 Flow system

The experiments were conducted in the recirculating free-surface water channel of FLAIR in the Department of Mechanical and Aerospace Engineering at Monash University, Australia. Schematic views and a photograph of the water channel facilities are shown in Figure 3.1. The closed-loop water flow is driven by a centrifugal pump system. The flow is conditioned by upstream combined sections of vane, mesh, settling chamber, honeycomb and fine mesh, before it proceeds through a three-dimensional contraction section (ratio of 3:1). The test section locates in between an upstream contraction section and a downstream diffuser, and its interior dimensions measure 4 m in length, 0.6 m in width, and 0.8 m in depth. The transparent glass walls of the test section are supported on steel frames, which allows flow visualisation imaging. The free-stream velocity in the test section can be varied continuously in a range of $U_\infty = 0.048 - 0.456$ m/s corresponding to the pump frequency range of $f_P = 5.00 - 50.00$ Hz. The pump frequency was programmed and controlled via software LabVIEW™. Due to the upstream combined conditioning and contraction sections, the free-stream turbulence level in the test section was reduced to less than 1%. More characterization details of the

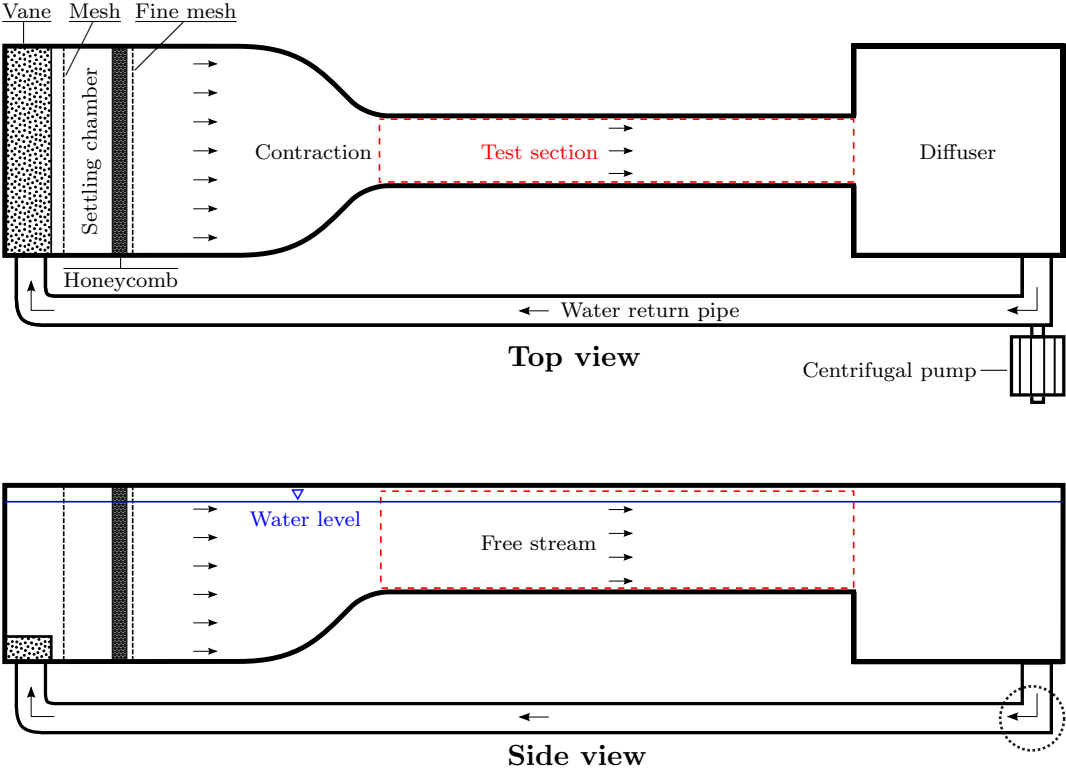


FIGURE 3.1: Schematic views and a photograph of the water channel facility.

water channel have been reported by Leweke (2002). The free-stream velocity was evaluated using two non-intrusive techniques: particle image velocimetry (PIV) and laser Doppler velocimetry (LDV). The PIV evaluation method was normally used along with the wake structure measurements, while the LDV evaluation method was used for a series of free-stream velocities at different pump frequencies. Figure 3.2 shows a LDV measurement of the free-stream velocity varying with the pump frequency at a water level height of 780 mm. The results showed that the free-stream velocity U_∞ varied linearly with the pump frequency f_P , and thus U_∞ in the automated-pump experiments was evaluated based on the linear fitting equation.

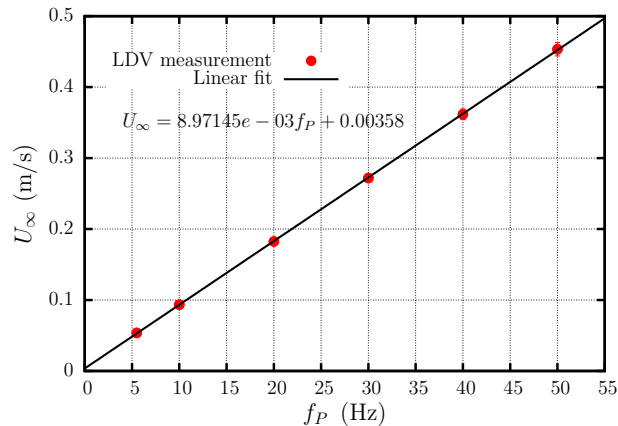


FIGURE 3.2: LDV measurement of the free-stream velocity (U_∞) varied with the pump frequency (f_P) of the water channel (with a water level height of 780 mm).

3.3 Air bearing system

To investigate fundamental behaviors of VIV of a circular cylinder with low damping ratio, researchers have experimentally modeled the fluid-structure system on air bearings to achieve extremely low-friction and precise linear motion (see Feng 1968; Khalak & Williamson 1996; Govardhan & Williamson 2000; Branković 2004; Klamo 2007). In the present study, such an air bearing system was built in conjunction with the water channel facilities to characterize free FIVs of a circular/square cylinder. Figure 3.3 schematically shows the experimental arrangement of the air bearing rig, and the laser and camera of the PIV (particle image velocimetry) system.

Figure 3.4 shows a photograph of the air bearing system used in the present study. This air bearing system utilized four commercial porous carbon media air bushings (Model: S302502) from NEWWAY[®] Air Bearings, USA. The air bushings were individually mounted in four aluminium pillow blocks which were supported on top of a fine machined aluminium base frame. The base frame measured 208 mm in width, 800 mm in length and 16 mm in thickness, and it had four screw-threaded pads at the corners allowing the vertical height adjustment. A digital inclinometer and a digital angle measurement device (both had a resolution of 0.05°) were used to ensure that the system was horizontally placed and transverse to the free-stream direction. To reduce the system's mass, two light carbon fiber tubes (measured 700 mm and 600 mm in length respectively, and both had a wall thickness of 1.5 mm), clamped by an aluminium cross carriage in the middle, were used as moving guide shafts passing through the air bearings. The shafts yielded a total stroke length of 160 mm, which provided

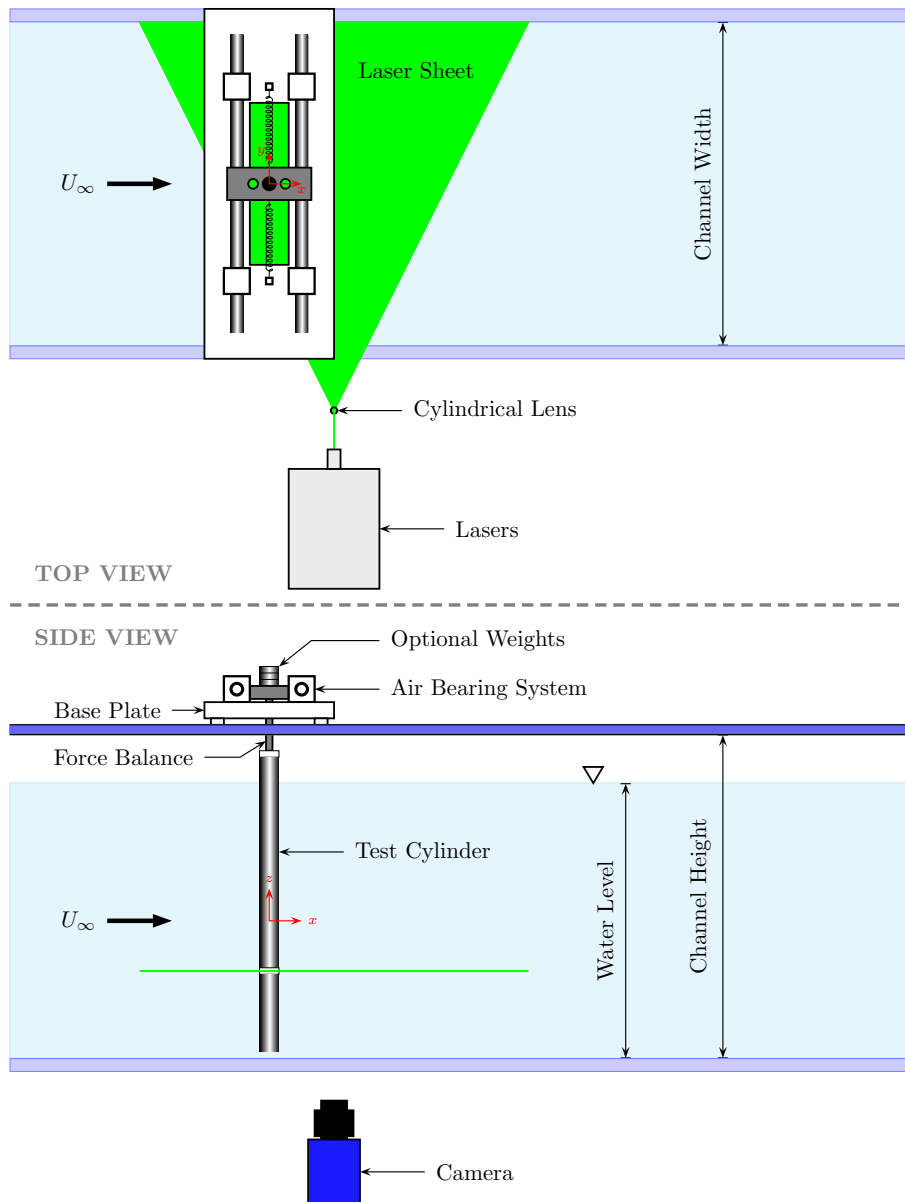


FIGURE 3.3: Experimental arrangement for free FIV of a cylindrical body

enough space for the movement of FIV. Given a recommended diameter tolerance of $\varnothing 25.0000_{0.0076}^{0.0000}$ mm for the guide shafts, the original thicker carbon fiber tubes were fine polished down by machine to obtain a tolerance of $10 \mu\text{m}$. In application, the alignment of the parts was found crucial to achieve extremely low friction for the system, as the shafts' straightness played an important role. Pains were taken to made the straight and precise guide shafts with the required lengths. The performance of porous media air bearings also required proper quality air flow without dirt, oil, water, and other foreign materials, thus the compressed air supply was conditioned by a general-purpose filter, an air dryer, and then a pressure regulator with gauge. The outlet pressure read on the regulator gauge was approximately 90 PSI for the present set-up.

Fundamentally, an air bearing is a non-contact system where a pressurized air flow is supplied through to form a thin film that acts as lubricant between the solid surfaces in relative motion. In terms of the technology to control the air flow to form the fluid

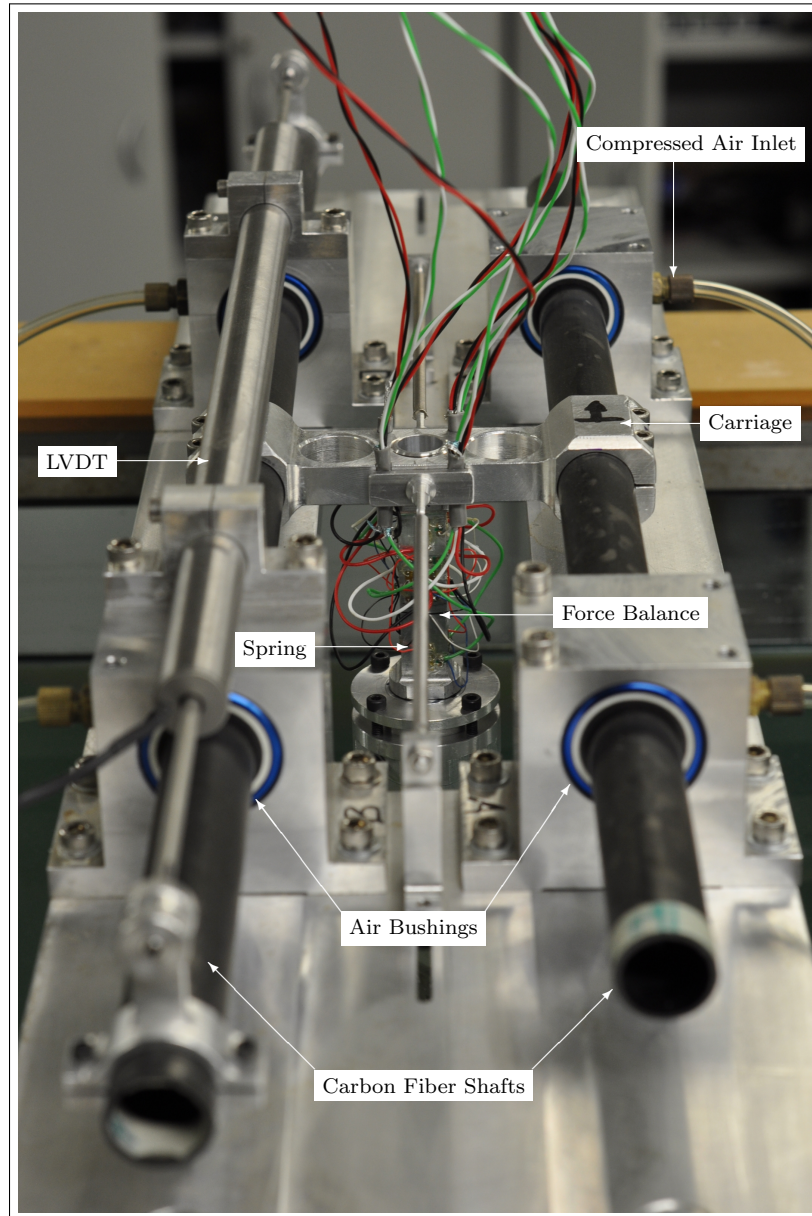


FIGURE 3.4: The air bearing system transversely placed on top of the water channel

film, there are two typical types of air bearings: orifice type and porous media type, as schematically shown in Figure 3.5. The orifice air bearings have been implemented in engineering since 1820s, while the porous media air bearings were developed later in 1960s to overcome some disadvantages of the orifice air bearings. For example, as pressurized air flow goes through the orifice it expands and so its pressure drops as it flows across the face of bearing resulting in variances of pressure in the air gap, which might cause the system to be unstable or vibrate; while, as for porous media air bearings, the pressurized air flow evenly bleeds through the porous layer and distributes even pressure on the entire bearing face resulting in a more uniform pressure in the air gap. With this significant advantage, porous media type air bearings were selected for the present experimental rig.

The stiffness of the oscillating parts on the air bearings was given by a number of extension springs as shown in Figure 3.4. The springs were horizontally attached

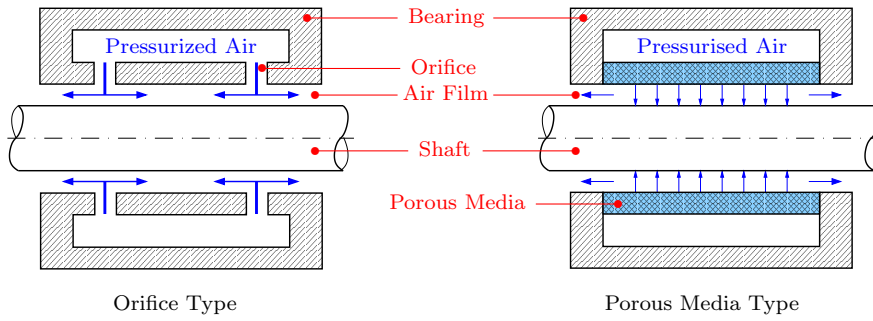


FIGURE 3.5: Schematic of orifice and porous media air bearings

from the center of the cross carriage's sides to a pair of posts fixed on the base plate's longitude center line, which constrained the springs to extend in the same direction as the shafts' movement. These springs (Model: LE014B13S, Lee Spring, UK) were made of stainless steel, and each had an outside diameter of $D = 4.775$ mm, a wire diameter of $d = 0.355$ mm, a number of counting coils of $N = 151.9$, and a free length of $L_s = 63.50$ mm. The individual spring constant was estimated to be $k \approx 0.01$ N/mm, according to the following equation:

$$k = \frac{Gd}{8C^3N}, \quad (3.1)$$

where G is the shear modulus of the material, and $C = D/d$ is the spring index (Budynas & Nisbett 2008).

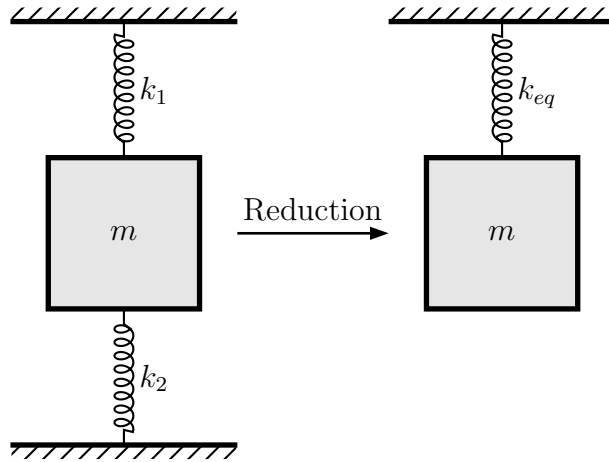


FIGURE 3.6: Reduction of one-pair-spring-one-mass system to an equivalent single-spring-mass system.

Since the system is a one-pair-spring-one-mass arrangement, this pair of springs act in parallel, thus the system can be reduced to an equivalent single-spring-mass system, as illustrated in Figure 3.6. Hence the equivalent spring constant of the system is given by Eq. (3.2) (Inman 2008):

$$k_{eq} = k_1 + k_2. \quad (3.2)$$

It should be noted that the system's stiffness could be adjusted by adding the number of spring pairs when excessive extra weights were applied to achieve high mass ratio

values, and the system's stiffness was then to be adjusted to keep the natural frequency in a certain range to ensure the investigated free-stream velocities were within the water channel's capacity.

Furthermore, the test cylinder was vertically adapted to a force balance sting that was coupled with the carriage of the air bearing system. Additionally, a friction-free linear displacement sensor (LVDT) was placed on top of one pair of pillow blocks. More details of the force balance and the displacement sensor will be presented later in § 3.6

The basic moving parts of the air bearing system, excluding the cylinder model, comprised the carbon fiber guide shafts, the force balance sting, the carriage, the LVDT core and its supporting structures. The mass of these components was measured of 575.6 g in total. This air bearing system had a capacity of extra weights up to 6000 g, which could be added on top of the carriage to give the system a mass ratio range of $0.95 \leq m^* \leq 15$ depending on the properties of the test cylinder model. The structural damping ratio and natural frequency of the system were experimentally measured by free decay tests, and examples will be reported later in § 3.7.1.

3.4 Motion control system

In order to replicate the motion time traces obtained from free FIV, a digital closed-loop motion control system was designed by the author. An overall diagram of this control system is illustrated in Figure 3.7. In this system, the intelligent tasks, such as time-dependent position “profiling”, numeric calculating, and digital triggering to other devices and systems, were performed by a hardware-in-the-loop (H.I.L) control board (Model: Q4, Quanser Inc., Canada) embedded in a PC desktop (Intel® Core™ Quad CPU Q6600 2.4 GHz, 4 G RAM, Microsoft Windows™ XP Professional) which was running on a combined software platform of MATLAB R2010a, Simulink and Real-Time Windows Target™ (MathWorks®), and QUARC® 2.1 (Quanser Inc., Canada). The motion plant consisted of a digital servo drive (Model: DPRANIE-015A400, Advanced Motion Controls, USA), a brushless DC rotary motor (Model: SM231AL-NMSN, Parker Hannifin, USA) with high resolution incremental encoder feedback device (5000 pulses per revolution or 20,000 counts per revolution post quadrature) attached to a linear ball-screw actuator (12.7 mm in lead and 150 mm in stroke, Model: ERS50-B02LA20-FSR150-A, Parker Hannifin, USA). Figure 3.8 shows the experimental set-up of the motion control rig.

Fundamentally, as shown in the block diagram of Figure 3.9, the motion controller generates a time-dependent function as the desired motion profile reference $R(t)$, decodes the plant's actual output position $Y(t)$ fed back from the encoder attached to the motor shaft every sampling period T_s , and then calculates the difference between the desired position and the actual position as error, $e(t) = R(t) - Y(t)$, assuming the feedback has a unit gain. As it is the objective of the control system to keep the position error to a minimum at all times, which guarantees that the actual position tracks the desired trajectory accurately, the position error $e(t)$ is to be amplified and compensated by a PID controller, whose output, $u(t)$, is then converted periodically by a digital-to-analog converter (DAC) into ± 10 V DC analog command signals to the servo drive. The servo drive works as an amplifier converting the low-power ± 10 V DC command signals into a high-power source, and it provides current, $I(t)$, to drive the brushless DC servo motor.

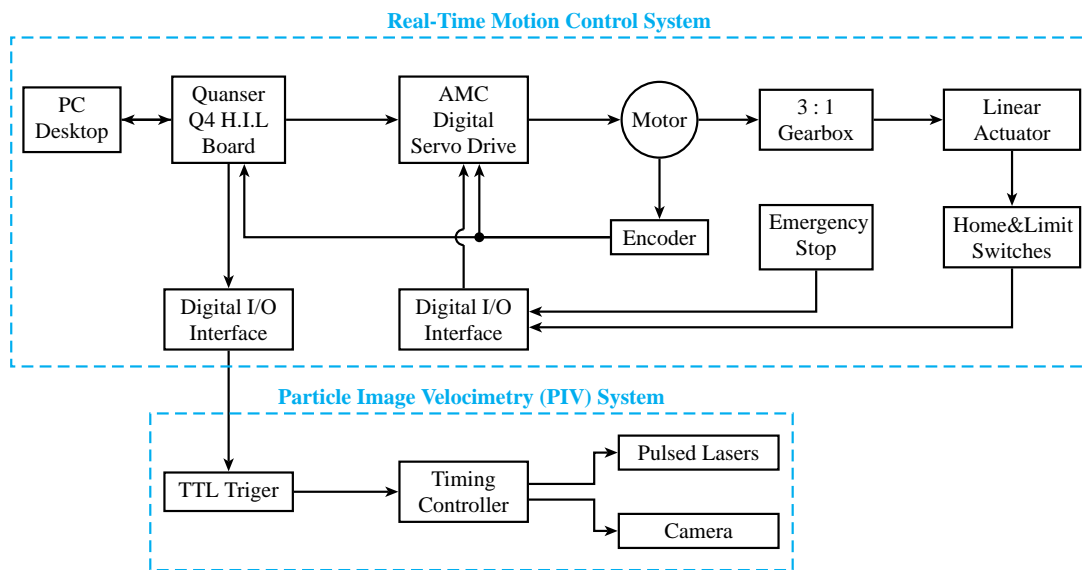


FIGURE 3.7: Diagram of Quanser Q4 H.I.L motion control system elements

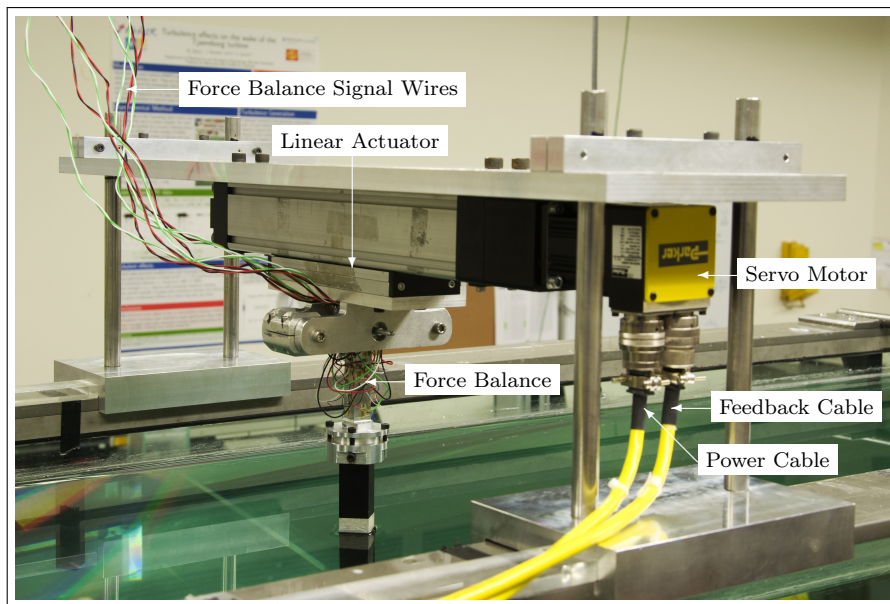


FIGURE 3.8: A photograph showing the motion control rig used for forced oscillation experiments.

3.4.1 PID controller and controller tuning

Proportional-Integral-Derivative (PID) feedback control algorithm was first described by Callender *et al.* (1936). Due to its simplicity, effectiveness and robustness, PID controller has been widely implemented in various industrial processes, such as servomechanic control, flight control, temperature control, and other control systems. It involves tuning the proportional, integral and derivative terms (also referred to as gains) to compensate the feedback error to produce a control signal to optimize the system's stability, response speed, and accuracy. The differential equation for the PID controller

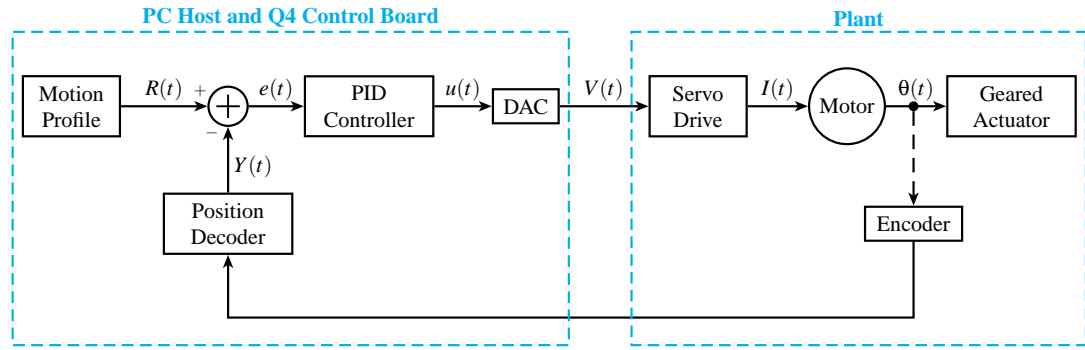


FIGURE 3.9: A block diagram of a closed-loop motion control system

output in time domain is given by

$$u(t) = K_P e(t) + K_I \int e(t) dt + K_D \frac{de(t)}{dt}. \quad (3.3)$$

The proportional gain (K_P) is analogous to the spring constant in a damped oscillatory system, whose action controls the natural frequency of the system. The integral gain (K_I) processes the accumulation of past errors over time, and it is to reduce the steady state error to minimum. Lastly, the derivative gain (K_D) is analogous to the damping factor of the oscillatory system, and its action contributes to the prediction of future errors, and improves the system's stability.

The difficulty of modelling a system represented by a differential equation as a block diagram can be algebraically simplified by using the Laplace transformation (Nilsson, J.W. and Riedel 1996). The Laplace transformation for a function of time, $f(t)$, is defined by

$$F(s) = \int_{0^-}^{\infty} f(t) e^{-st} dt = \mathcal{L}[f(t)]. \quad (3.4)$$

The inverse Laplace transform, which allows us to find $f(t)$, is given by

$$f(t) = \mathcal{L}^{-1}[F(s)] = \frac{1}{2\pi j} \int_{\sigma-j\infty}^{\sigma+j\infty} F(s) e^{+st} ds. \quad (3.5)$$

Thus, the transfer function of a PID controller can be written as

$$G_c(s) = K_P + \frac{K_I}{s} + K_D s = \frac{K_D s^2 + K_P s + K_I}{s}. \quad (3.6)$$

Typically, the transfer function of a DC servo motor system under position control is written in terms of the time constants of the servo motor system as

$$G_p(s) = \frac{\frac{1}{K_e}}{s(\tau_m s + 1)(\tau_e s + 1)}, \quad (3.7)$$

where K_e is the electrical constant of the motor, τ_m is the total mechanical time of the servo system, and τ_e is the total electrical time of the servo system. These specification parameters of the motor used can be easily found in the data sheet provided by the manufacturer.

The performance of a control system is typically characterized by its response to a time-dominant step input, as illustrated in Figure 3.11. The response speed is measured

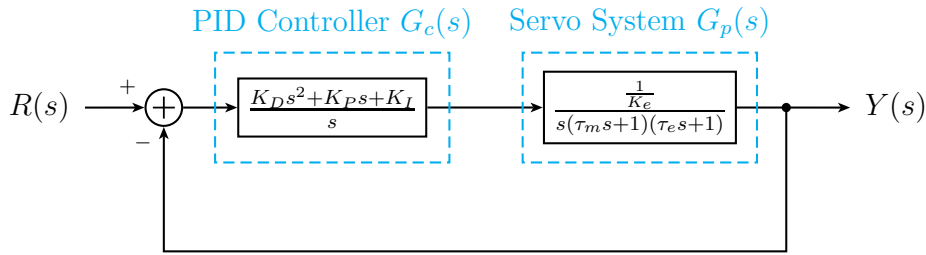


FIGURE 3.10: Block diagram of a PID servo position control system

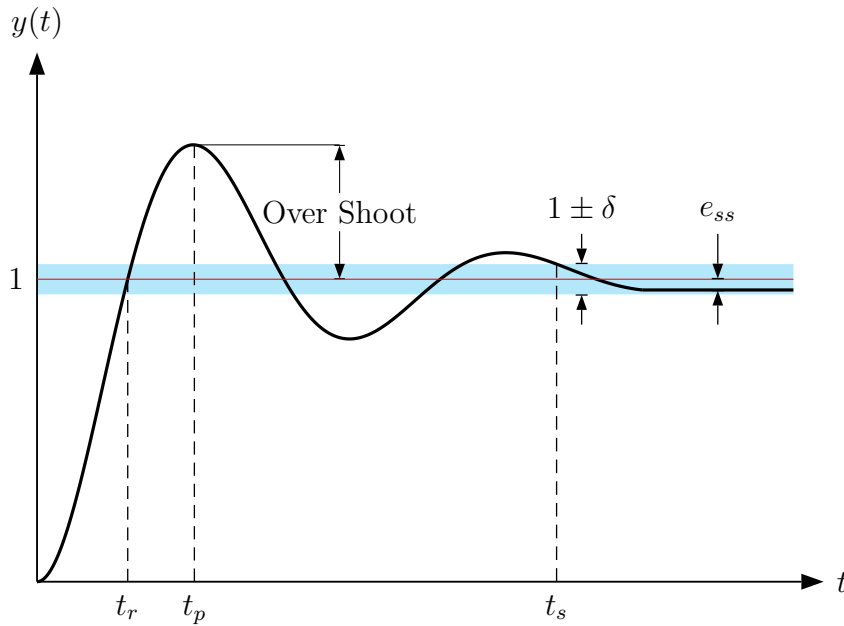


FIGURE 3.11: Step response of a control system

by the rise time t_r and the peak time t_p . The *rise time* is the time at which the actual response first reaches the desired response level. The *peak time* is the time at which the actual response reaches its maximum peak value. The *settling time*, t_s , is defined as the time required for the system to settle within a certain percentage δ of the input amplitude (Bishop & Dorf 2011). The accuracy of the actual response following the desired response is characterized by the parameters of the percent overshoot $P.O.$, the settling time t_s and the steady-state error e_{ss} . The *percent overshoot* is defined as

$$P.O. = \frac{M_p - fv}{fv} \times 100\% \quad (3.8)$$

for a unit step input, where M_p is the maximum peak value of the actual response, and fv is the final value of the response (Bishop & Dorf 2011). The steady-state error is defined by

$$e_{ss} = \lim_{t \rightarrow \infty} e(t), \quad (3.9)$$

or in a form of Laplace transform as

$$e_{ss} = \lim_{s \rightarrow \infty} sE(s). \quad (3.10)$$

Closed-Loop Response	Rise Time	Overshoot	Settling Time	Steady-State Error	Stability
Increasing K_P	Decrease	Increase	Small Increase	Decrease	Degrade
Increasing K_I	Small Decrease	Increase	Increase	Large Decrease	Degrade
Increasing K_D	Small Decrease	Decrease	Decrease	Minor Change	Improve

TABLE 3.1: Effects of increasing independent PID controller parameters on the step response (Bishop & Dorf 2011; Ang *et al.* 2005).

Controller Type	K_P	K_I	K_D
P	$0.5K_U$	-	-
PI	$0.45K_U$	$0.54K_U/T_U$	-
PID	$0.6K_U$	$1.2K_U/T_U$	$0.6K_U T_U/8$

TABLE 3.2: PID controller gain tuning using Ziegler-Nichols frequency response method (Bishop & Dorf 2011).

The PID gains individually have different effects on the system's performance. Table 3.1 describes the effects of increasing an individual gain on the transient response of the system. Thus, designing a PID system design requires trade-off between tracking accuracy and stability. There are many methods available to determine the PID gains to achieve acceptable performance of the system (see Åström & Hägglund 2006). The process of determining the PID gains is also referred to as *PID tuning*. Two classic methods for PID tuning, developed by (Ziegler & Nichols 1942), are known as the step response method and the frequency response method. In the present study, the servo system was first tuned using the Ziegler-Nichols frequency response method to achieve the basis of the PID gains for further fine tuning. The Ziegler-Nichols frequency response approach is to first set $K_I = 0$ and $K_D = 0$. The proportional gain K_P is then gradually increased from zero value until it reaches the *ultimate gain*, denoted by K_U , at which the point of marginal *instability* is reached where the output of the closed-loop system presents periodic oscillations with a constant amplitude. The oscillation period is referred to as *ultimate period*, denoted by T_U , is then measured to determine the PID gains according to the equations given in Table 3.2. For $K_p < K_U$, the oscillation amplitudes decay with time, and the system is *stable*. On the other hand, for $K_U < K_p$, oscillation amplitudes increase with time, and the system is *unstable*, which is undesired in applications. After obtaining the basis of the PID gains, manual fine tuning was followed to achieve acceptable PID gains for the system, according to the effects of the gains described in Table 3.1.

Figure 3.12 shows the results of PID tuning of the system response to a pulse signal. Given an input pulse train signal with the amplitude of 1 mm (approximately 1575 counts) and frequency of 1 Hz, with the PID parameters set at $K_P = 1.2$, $K_I = 0.0001$ and $K_D = 0.0033$, respectively, the raise time of the response was found to be 20 ms, the over shoot was less than 0.3%, and the steady-state errors were within $4 \mu\text{m}$. These PID gain values were implemented in the future forced oscillation experiments.

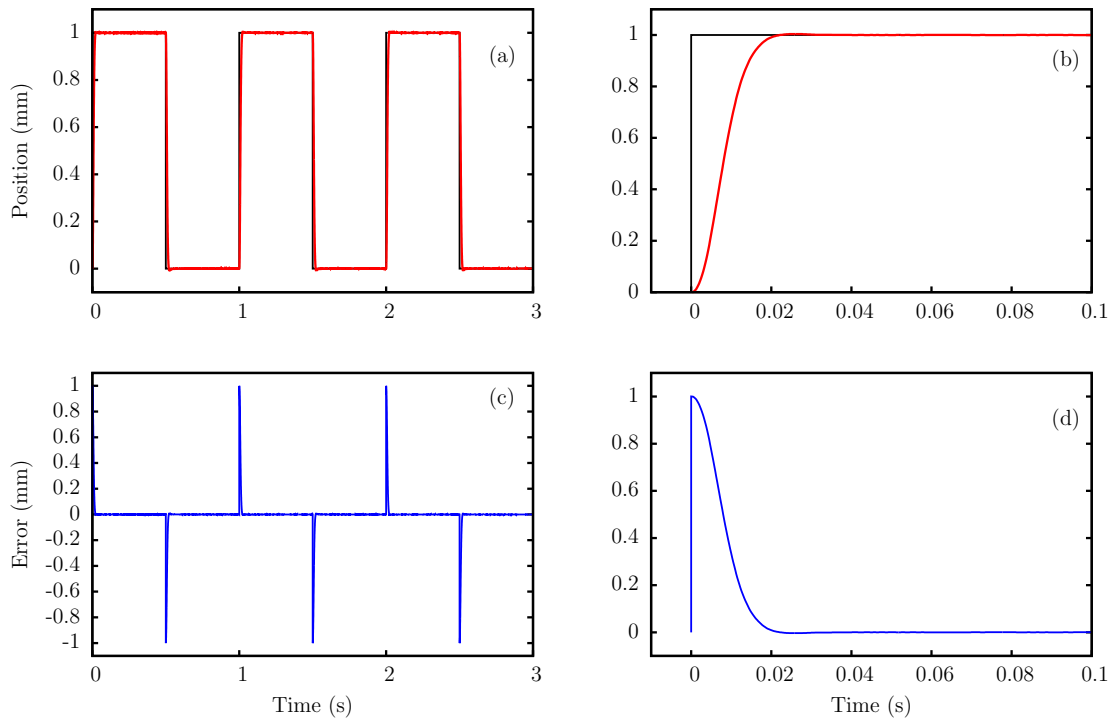


FIGURE 3.12: Step response of PID experimental tuning. (a) shows the time traces of both the input pulses with the amplitude of 1 mm and frequency of 1 Hz (as step signals) and response. (b) shows the first 0.1 s (or 100 ms) of the time traces. (c) shows the error time trace, and (d) shows the first 0.1 s of the error time trace.

Figure 3.13 shows the test results of the system tracking a sinusoidal input signal (with the amplitude of 25 mm and frequency of 1 Hz) and a motion trajectory replicated from a real VIV experiment of a circular cylinder with a diameter of 25 mm. The results indicate that the system was able to track the given input signals smoothly and accurately. The errors were found to be within $10\ \mu\text{m}$, which was approximately $0.0004D$ of the circular cylinder.

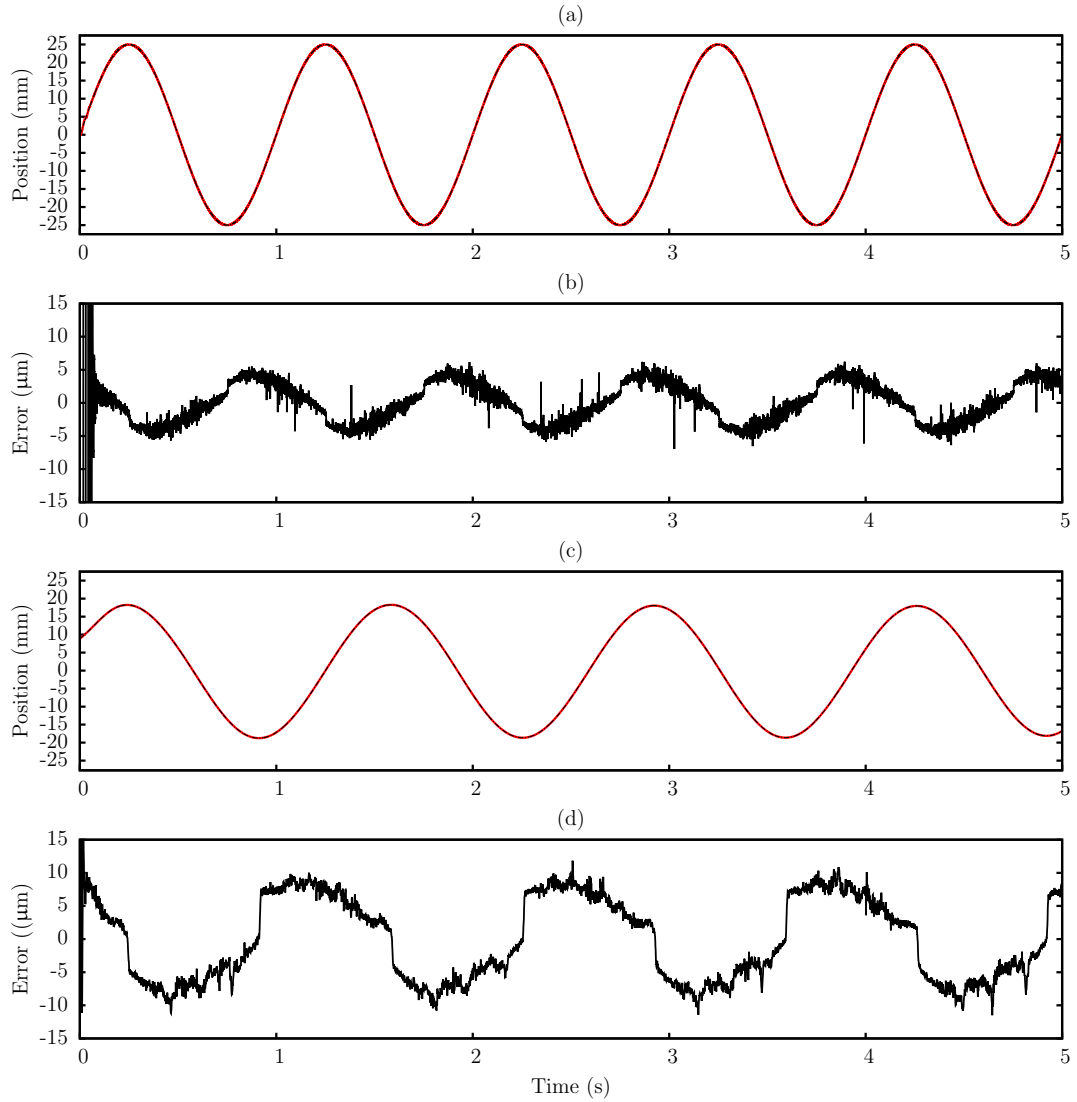


FIGURE 3.13: Time trace of real-time motion tracking. Black dot-dashed lines represent the motion trajectory reference, and the solid lines represent the actual motion tracking response. (a) shows the time trace of tracking a built-in sinusoidal oscillation function with the amplitude of 25 mm and the frequency of 1 Hz, and the motion tracking errors are shown in (b); (c) shows the time trace of tracking an amplitude response of VIV of a circular cylinder of $D = 25$ mm at $U^* = 5.0$ and $m^* = 2.64$, and the tracking errors are shown in (d).

3.5 Cylinder models

During the candidate’s PhD study, a number of rigid smooth circular and square cross-sectional cylinders were used as the experimental models. Specifications of the cylinder models are provided in Table 3.3.

Body	Cross-Sectional Shape	Material	Diameter (D) or Side Width (W)	Total Length (L_{total})	Immersed Length (L)	L/D or L/W
I	Circular	Carbon Fiber	$D = 25$ mm	865 mm	778 mm	31.1
II	Circular	Carbon Fiber	$D = 25$ mm	700 mm	620 mm	24.8
III	Circular	Carbon Fiber	$D = 40$ mm	700 mm	620 mm	15.5
IV	Circular	Carbon Fiber	$D = 40$ mm	865 mm	778 mm	19.5
V	Square	Aluminium	$W = 25$ mm	865 mm	778 mm	31.1
VI	Square	Aluminium	$W = 25$ mm	700 mm	620 mm	24.8

TABLE 3.3: Geometric parameters of the rigid smooth cylinder models used in the present study.

The circular cylinders were made of carbon fiber tubes having an outside diameter of $D = 25$ or 40 mm and a wall thickness of $t_w = 1.5$ mm. The square cylinders were made of aluminium tubes having an outside width of $W = 25$ mm and a wall thickness of $t_w = 1.6$ mm. Both the circular and square cylinders had two length configurations, depending on the end condition whether was free end or platform control, as shown in Figure 3.14. The aspect ratios ranged from $AR \approx 15.5$ to $AR \approx 24.5$, and the blockage ratios ranged from 4.2% to 6.7%, depending on the geometric dimensions of the body.

The platform, having a top plate of 500 mm \times 500 mm \times 5 mm, was designed as an end condition control for the shorter cylinders (with $L_{total} = 700$ mm described in Table 3.3) to promote parallel vortex shedding, and to reduce the effect of boundary layer associated with the water channel floor. This platform end conditioning technique was used in series of experiments on VIV of a circular cylinder conducted by C.H.K Williamson’s group [see Khalak & Williamson (1996); Govardhan & Williamson (2000); Morse *et al.* (2008) for more details] at Cornell University. As described in Khalak & Williamson (1996), a platform placed close ($0.04D$) to the free end of the cylinder works effectively as the technique using an end plate attached to the cylinder to promote parallel vortex shedding. Beneficially, it does not introduce unwanted extra weight and fluid forces on the body. A second method used to promote parallel vortex shedding is to give the cylinder a relatively small gap of approximately 2 mm between the cylinder free end and the water channel floor. This method was used in Branković (2004). More discussion on effect of the end condition on VIV of a circular cylinder has been reported by Morse *et al.* (2008). However, the effect of end condition on FIV of a bluff body was not a particular focus in the present study.

Furthermore, each cylinder model had a transparent window section made of acrylic material allowing laser sheet to illuminate through for the near wake measurements using PIV. The top of the cylinders was fitted with an aluminium adapter to the force balance sting. For the square cylinders, in particular, the adapter allowed adjustment

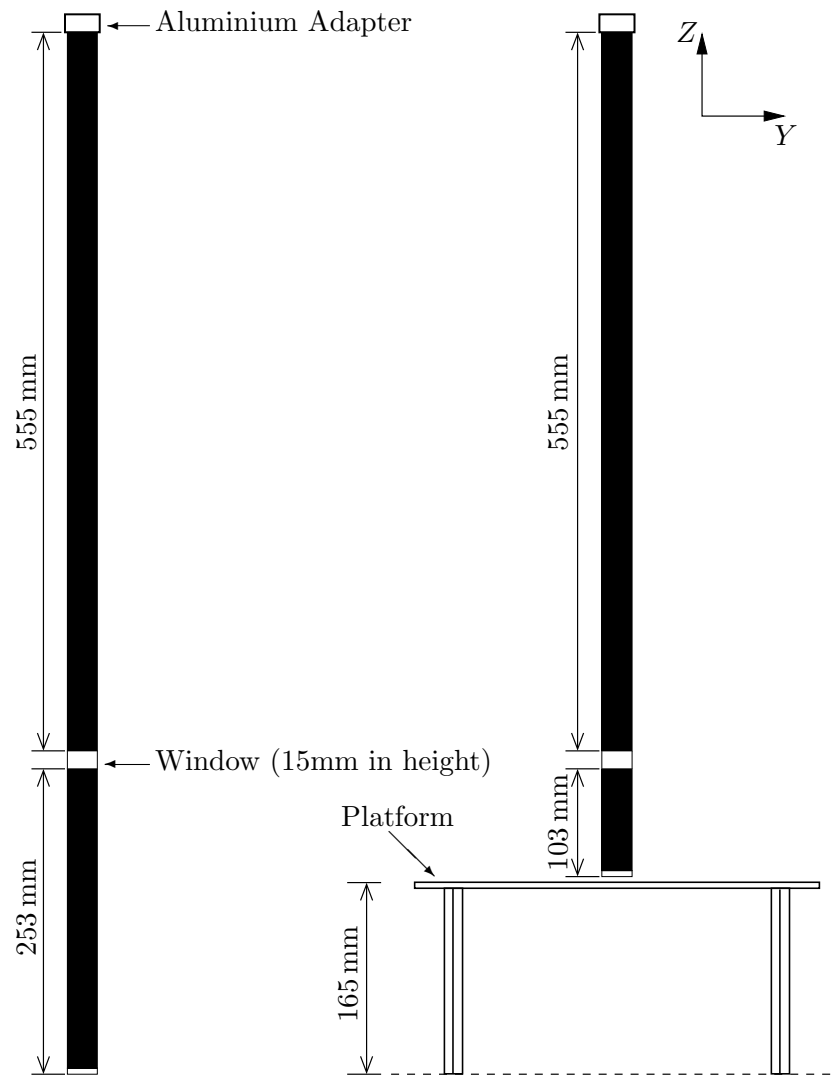


FIGURE 3.14: A schematic showing dimensions of the cylinder models

the cylinder's angle of attack with respect to the free stream flow, as schematically shown in Figure 3.15. The angle of attack values were set up using a digital angle measurement device with a resolution of 0.05° .

3.6 Experimental measurement systems

3.6.1 Data acquisition (DAQ) system

The quantitative variable measurements in the experiments included the free-stream velocity (U_∞) and the water's temperature (T_w) for the reduced velocity and Reynolds number calculation, the cylinder's linear displacement (y), the resulting hydrodynamic lift (F_y) and drag (F_x) forces, and the TTL triggering signals to the PIV system. These measurements were conducted simultaneously using a data acquisition (DAQ) system consisting of a National InstrumentsTM BNC-2110 connector block interfaced with a PCI-6221 (37pin) DAQ board which was embedded in the same PC desktop as used in the motion control system (refer to the early § 3.4 for more details). This

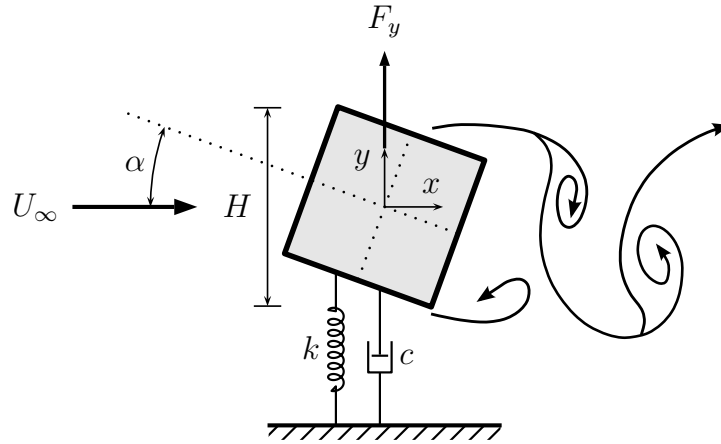


FIGURE 3.15: Schematic showing the square cylinder with variable angle of attack, α , allowed to freely oscillating in the transverse direction, y , to the oncoming flow, U_∞ in the stream-wise direction x . The body is mounted on air bearings and elastically constrained with springs to provide k , the system spring constant, and c , the structural damping. Note that the characteristic length, H , adopted in this study is the projected length of the cross-section normal to the oncoming flow.

DAQ system provided eight channels of ± 10 V DC analog input and two channels of ± 10 V DC analog output with a 16-bit resolution, and two 32-bit digital counters. The maximum sampling frequency of this DAQ system could go as fast as 250 kHz; however, most experimental measurements were sampled at 100 Hz whose Nyquist frequency was more than 20 times higher than that of FIV system. The data sampling and recording of the measurements were controlled via customised LabVIEW™ 8.5 VI programs, while the data post processing and analysis were performed using MATLAB® codes.

3.6.2 Linear displacement measurement

The linear displacement of the cylinder in the air bearing system was measured using a non-contact magnetostrictive linear variable differential transformer (LVDT).

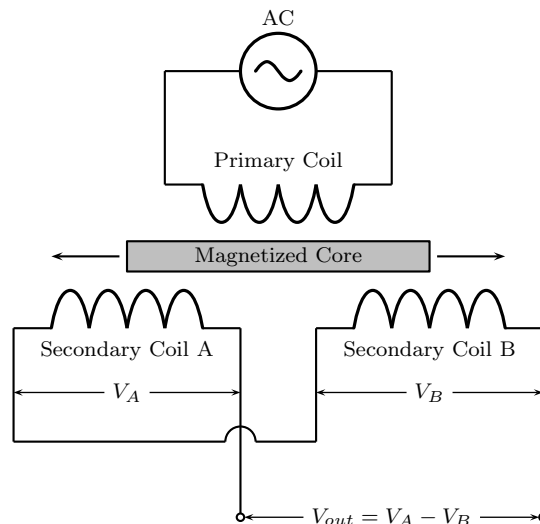


FIGURE 3.16: A diagram showing LVDT circuit.

Typically, a LVDT consists of a coil assembly secured in a cylindrical stainless steel housing, and a solid cylindrical core unit. The coil assembly comprises a primary winding and two secondaries symmetrically wound to the centred primary. The electric input and output (I/O) and signal conditioning modules are also built inside the cylindrical housing, so the coil assembly is usually the stationary element of the sensor. On the other hand, the core is an armature of magnetic material and it can move axially and freely through the coil assembly's hollow housing. Therefore, the core is mechanically coupled to the object whose position measurement is desired. For example of the application in the air bearing system, the coil assembly of LVDT was mounted on a pair of pillow blocks, and the invisible core was extended using straight stainless steel tubes and mechanically coupled on a carbon fibre guide shaft, as shown in Figure 3.4. Operating on the principle of a transformer, the primary winding is excited by a voltage source, and it generates magnetic flux coupled to the two secondary windings which individually induces a voltage, as illustrated in Figure 3.16. The differential output voltage between the secondary windings is linearly controlled by the magnetic core's position. In theory, an infinitesimally small change in the core's position can be detected by a LVDT that relies on the coupling of magnetic flux, and this infinite resolution is only limited by the signal conditioning unit and the resolution of DAQ system. Additionally, a LVDT has other advantages in practice such as high repeatability and unlimited mechanical life.

The LVDT (Model: SE 750-10000, Macro Sensors, USA) used in the present study was excited by a constant 24 V DC, and its DC voltage output range was 0 - 10 V, corresponding to a 0 - 250 mm linear measurement range. The LVDT was statically calibrated after installed in the air bearing system. Figure 3.17 (a) shows example results of a static calibration. Linear calibration results were repeatable in tests. To validate its dynamic measurement, this LVDT was installed on the linear actuator of the motion control system to measure sinusoidally-driven oscillations, and the results were compared with a 1250-line differential encoder (Model: HB5M-1250-250-I-D-D, US Digital, USA), as shown in Figure 3.17 (b). The comparison shows that the LVDT dynamic measurement agreed well with that of the encoder, and both were able to accurately measure a position change of 5 μm after signal conditioning. In the FIV experiments, the LVDT signals were smoothed using a fourth-order low-pass Butterworth filter with a cutoff frequency of 3 Hz. The cylinder oscillation frequency was analysed using Fast Fourier Transforms (FFT) and Continuous Wavelet Transforms (CWT) (see Grinsted *et al.* 2004).

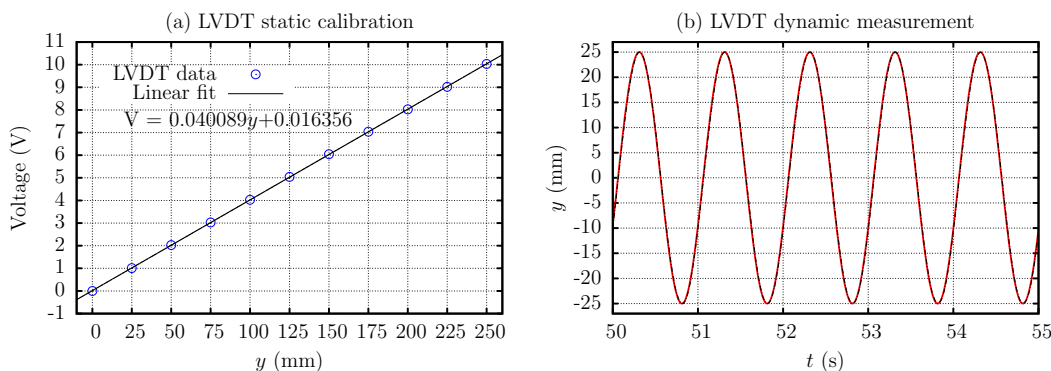


FIGURE 3.17: Examples of LVDT measurement: a static LVDT calibration curve (left) and a sinusoidal motion measurement comparison (right) between LVDT (black dash line) and an encoder (red solid line).

3.6.3 Force measurement

A four-component force balance based on sensitive semiconductor strain gauges was designed and built by the author to measure the lift and drag forces acting on the cylinder. Figure 3.18 (a) shows a photograph of the force balance.

Each force component consisted of four active strain gauges bonded onto the surfaces of the force balance sting. The strain gauge model used was SB1-1000-P2, manufactured by BCM Sensor Technologies, Belgium. Each gauge had a resistance of $R = 1000 \Omega$ and a gauge factor of $GF = (\Delta R/R)/\varepsilon = 150$, where ε is the strain. The strain gauges were configured to form a Wheatstone bridge (see Appendix A for the relevant equations), as illustrated in Figure 3.19 (a). This full Wheatstone bridge fashion with four active strain gauges helps improve temperature compensation of the circuit. Depending on the bonding layout of the stain gauges, a Wheatstone bridge can result either in an adding circuit fashion or in a subtracting circuit fashion.

$$\frac{dV_{out}}{V_{EX}} = \frac{1}{4} \left[\left(\frac{dR_2}{R_2} - \frac{dR_1}{R_1} \right) - \left(\frac{dR_3}{R_3} - \frac{dR_4}{R_4} \right) \right] \quad (3.11)$$

$$= \frac{GF}{4} \left[(\varepsilon_2 - \varepsilon_1) - (\varepsilon_3 - \varepsilon_4) \right] \quad (3.12)$$

or

$$\frac{dV_{out}}{V_{EX}} = \frac{1}{4} \left[\left(\frac{dR_2}{R_2} - \frac{dR_1}{R_1} \right) + \left(\frac{dR_4}{R_4} - \frac{dR_3}{R_3} \right) \right] \quad (3.13)$$

$$= \frac{GF}{4} \left[(\varepsilon_2 - \varepsilon_1) + (\varepsilon_3 - \varepsilon_4) \right] \quad (3.14)$$

According to Hooke's law, the strain is given by the following Eq. (3.15):

$$\varepsilon = \frac{\sigma}{E} = \frac{Mh}{2EI_x}, \quad (3.15)$$

where E is Young's modulus of the beam material, σ is the stress on the beam, M is the applied bending moment, h is the cross-sectional height of the beam, I_x is the cross-sectional area moment of inertia (Hibbeler 2008). The force balance sting (beam) used was made of aluminium ($E \approx 73 \text{ GPa}$), having a square cross section (side width $h = 16 \text{ mm}$) with a circular bore through (diameter $d = 15 \text{ mm}$), and the cross-sectional moment of inertia was calculated to be $I_x = h^4/12 - \pi d^4/64 = 2676.3 \times 10^{-12} \text{ m}^4$.

In the subtracting circuit as shown in Figure 3.19 (b), the gauge pair consisting of R_1 and R_2 are bonded at the same axial location on opposite surfaces. On the other hand, the other gauge pair of R_3 and R_3 are placed at a axial distance of L_g away from R_1 and R_2 . Given an applied force, R_2 and R_3 will be under tension, while R_1 and R_4 will be under compression, thus strain relationship measured by the gauges are $\varepsilon_1 = -\varepsilon_2$, and $\varepsilon_4 = -\varepsilon_3$. Thus, Eq. (3.12) can be rewritten as

$$\frac{dV_{out}}{V_{EX}} = \frac{GF}{4} (2\varepsilon_2 - 2\varepsilon_3) \quad (3.16)$$

$$= \frac{GF}{4} \frac{h}{EI_x} (M_{12} - M_{34}) \quad (3.17)$$

$$= \frac{GF}{4} \frac{hFL_g}{EI_x}, \quad (3.18)$$

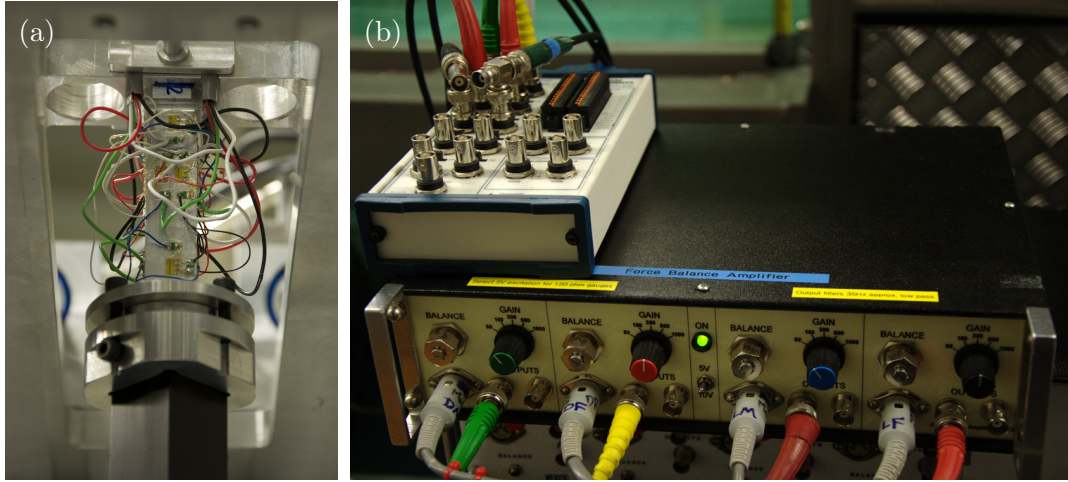


FIGURE 3.18: Photographs showing the strain-gauge force balance and the signal amplifier. (a) shows that the force balance is mounted on the carriage of the air bearing rig, supporting a square cylinder model vertically; (b) shows that the signal amplifier and a National Instruments™ BNC-2110 connector block (white on top).

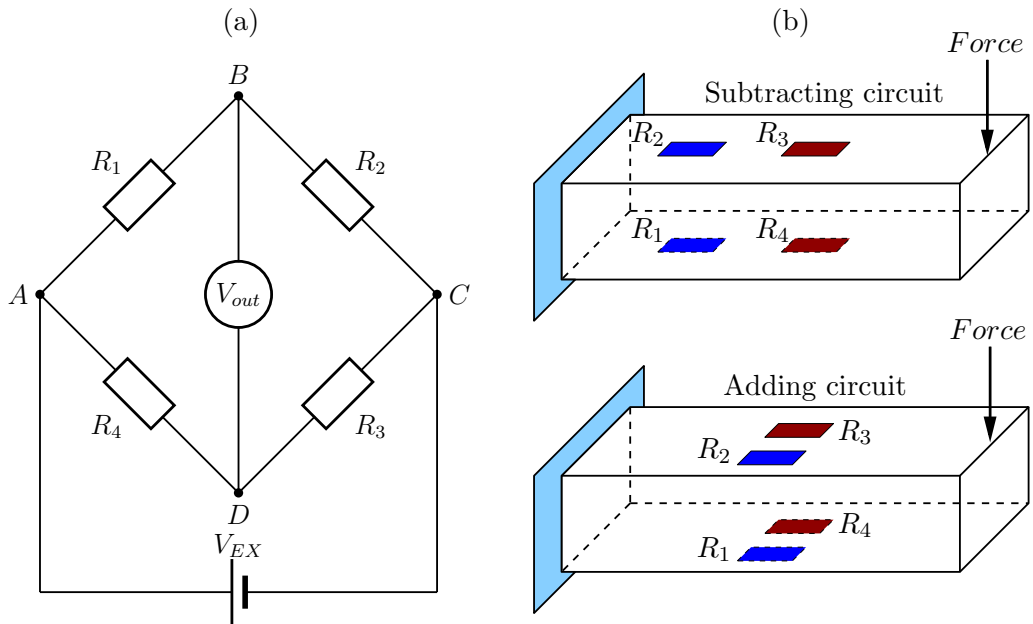


FIGURE 3.19: A diagram showing Wheatstone bridge in (a), and layouts of strain gauges on a force balance sting in (b). Note that each resistance R represents an active strain gauge, V_{EX} is the excitation voltage to the Wheatstone bridge and V_{out} is the output voltage to be conditioned by the amplifier.

Chapter 3. Experimental Methodology

where F is the applied force, M_{12} is the resulting bending moment at the location of the gauge pair of R_1 and R_2 , M_{34} is the resulting bending moment at the location of the gauge pair of R_3 and R_3 , and $FL_g = M_{12} - M_{34}$. Based on Eq. (3.16), a theoretical linear relationship between an applied force and the voltage output ratio is directly given. However, the measurement sensitivity of the subtracting circuit is limited by the axial spacing L_g of the gauge pairs.

In the adding circuit, two gauge pairs are bonded side-by-side at the same axial location, as shown in the bottom of Figure 3.19 (b). The measurement equation is given by Eq.3.14, and it can be rewritten by

$$\frac{dV_{out}}{V_{EX}} = \frac{GF}{4} (2\varepsilon_2 + 2\varepsilon_3) \quad (3.19)$$

$$= \frac{GF}{4} \frac{h}{EI_x} (M_{12} + M_{34}) \quad (3.20)$$

$$= \frac{GF}{4} \frac{2hFL_R}{EI_x}, \quad (3.21)$$

where L_R is the axial distance of the applied force to the center of the gauges, and these two gauge pairs measure the same bending moment as $M_{12} = M_{34}$. This adding circuit ensures large voltage output levels. This wiring method gives an indirect measurement of the fluid forces acting on a cylinder in FIV. Assumed that the fluid forces are evenly distributed on the axial span of the cylinder, the relationship between the bending moments M_{12} and M_{34} and the resultant fluid force F is given by

$$M_{12} = M_{34} = \int_{L_1}^{L_2} F' z dz = \frac{(L_2 + L_1)(L_2 - L_1)F'}{2} = FL_R, \quad (3.22)$$

where $F' = F/L$ is the applied force per unit length, $L = L_2 - L_1$ is the immersed length of the cylinder, and $L_R = (L_2 + L_1)/2$ is the distance of the resultant force to the strain gauges.

Signal conditioning for the output voltage V_{out} from the strain-gauge Wheatstone bridges was processed using a four-channel amplifier with built-in 35 Hz cutoff low-pass filter (LPF). This signal amplifier was customised and built by the electronic workshop of the department, as shown in Figure 3.18 (b). The constant DC excitation voltage V_{EX} to the strain-gauge Wheatstone bridges could be optionally set to +5 V or +10 V. Each channel contained a nulling unit to balance the Wheatstone bridge, and a gain value setting unit (the gain can be set to 50, 100, 300, 500, or 1000). In the experiments, the excitation voltage V_{EX} was set to +5 V, and the gain values of 100 and 300 were used for the moment-channels and the force-channels, respectively. The measurement range was designed to be ± 2.5 N with accuracy of 0.01 N, which was sufficient to measure the forces (within a range of ± 1.5 N) in this FIV study.

To calibrate the force balance, a cylinder model was vertically mounted on the force balance sting coupled with the air bearing system that was horizontally placed on an optical table, as shown in Figure 3.20. A thin fishing line was tied to the middle of calculated immersed length of the cylindrical body, and it was horizontally supported on a fixed smooth pulley, while the other end of the fishing line was attached to a cup for loads. Each force component (the lift and the drag components) was calibrated in both positive and negative directions individually with small progressive weight increments/decrements of approximate 15 g up to approximate 150 g in total. The force balance was found to be able to effectively detect a small load change of ± 0.1 g. Figure 3.21 presents one example of such static calibrations of the force balance. The

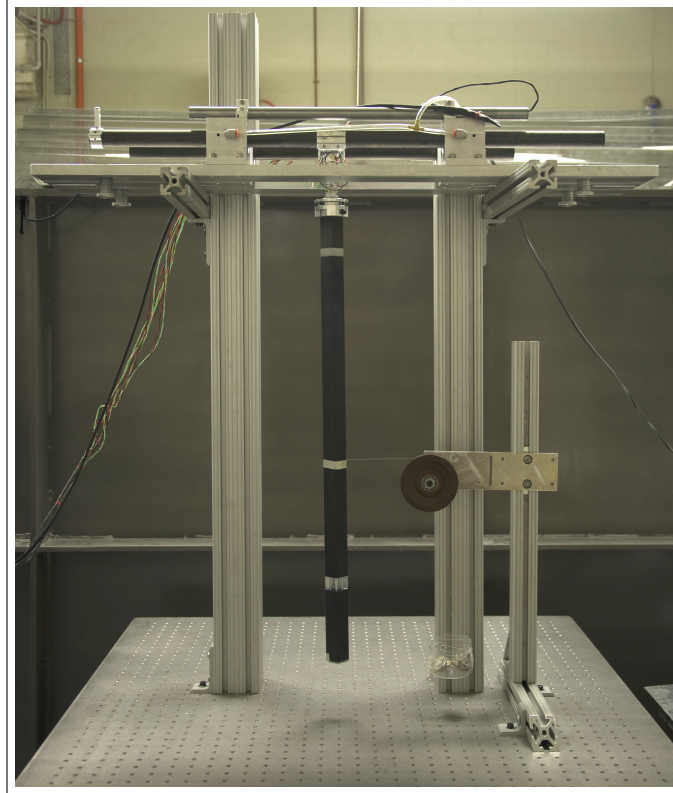


FIGURE 3.20: A photograph showing the experimental set-up for static force calibration.

results showed linear relationships between the applied loads and the output voltages. The repeatability of the results were validated by repeated calibration tests. Furthermore, the calibration coefficients were applied to calculate the lift force acting on a stationary circular cylinder over a Reynolds number range of $4550 \leq Re \leq 12920$ to confirm that the lift force values extracted from the moment channel and the force channel were matched, as shown in Figure 3.22. This confirmation validated the assumption that the lift force is evenly distributed on the cylinder spanwise. In principle, the moment-channels have higher ratios between output signals and input forces, and also higher signal-to-noise (S/N) ratio than those of the force-channels, as a fact that given the same loading force the signals output from a adding circuit are stronger than those from a subtracting circuit. Thus, the moment-channels were primarily used to extract the lift and the drag forces in the experimental measurements. Like the LVDT signals, the force signals were also smoothed using a fourth-order low-pass Butterworth filter with a cutoff frequency of 3 Hz, and frequencies for the lift time histories were also extracted using FFT and CWT as mentioned previously in § 3.6.2.

For a stationary cylinder, the fluid forces acting on the cylinder were measured directly using the force balance. While for an oscillating cylinder, it will experience an inertia force due to the system's acceleration. Like a stationary cylinder, the drag force component can still be directly measured since the system does not move in the x direction. On the other hand, correction calculations are necessary to be applied on the measured force component directly from the force balance, denoted by F_s , to extract the actual transverse lift force acting on a moving cylinder. As illustrated in Figure 3.23, assuming the system is moving instantaneously in the y direction through the air bearings, the strain gauge force balance experiences a relative force F_s due to

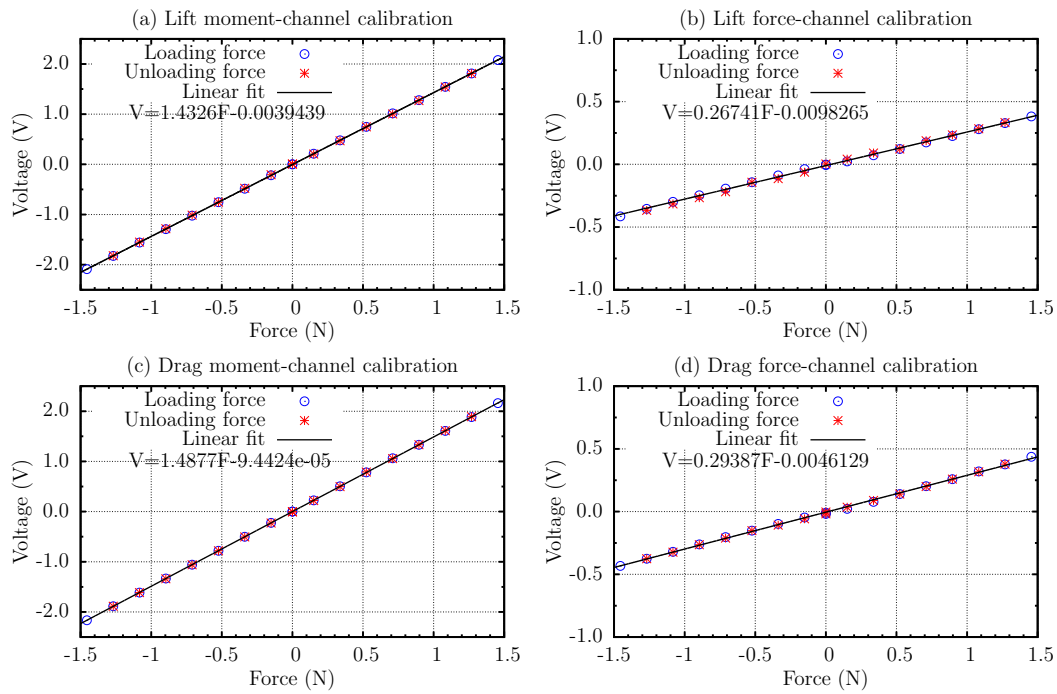


FIGURE 3.21: A typical force balance static calibration.

the bending moment loaded by the fluid force F_y . The moving system can now be divided by the middle line of the force balance (the dash line in Figure 3.23) into two parts for consideration separately.

For the bottom part under the middle line, the equation of motion can be written by

$$F_y - F_s = m_b \ddot{y}, \quad (3.23)$$

where m_b is the mass of the bottom part including half of force balance and the entire cylinder model. While for the upper part above the middle line, the equation of motion is then

$$F_s - c\dot{y} - ky = m_t \ddot{y}, \quad (3.24)$$

where m_t is the mass of the upper part including half of the force balance, the carriage, the moving shafts, the core and its accessories of LVDT, and the extra weights applied if necessary. The transverse fluid force is then determined using Eq. (3.23) as follows:

$$F_y = F_s + m_b \ddot{y}, \quad (3.25)$$

and $F_y \equiv F_s$ when $\ddot{y} = 0$ in the stationary cylinder case. Therefore, combining Eq. (3.23) and Eq. (3.24) yields the governing equation of the dynamic system:

$$m\ddot{y} + c\dot{y} + ky = F_s + m_b \ddot{y}, \quad (3.26)$$

where $m = m_b + m_t$ is the total mass of the system.

To validate the force balance's performance to obtain the transverse lift force acting on a cylinder in motion, Figure 3.24 shows the transverse lift force measurements of a circular cylinder undergoing VIV at different reduced velocities in the initial, the upper and the lower branches. The cylinder had a diameter of 25 mm and an immersed length of 620 mm. The system's mass was measured of $m = 808.4$ g, and the displaced water

3.6. Experimental measurement systems

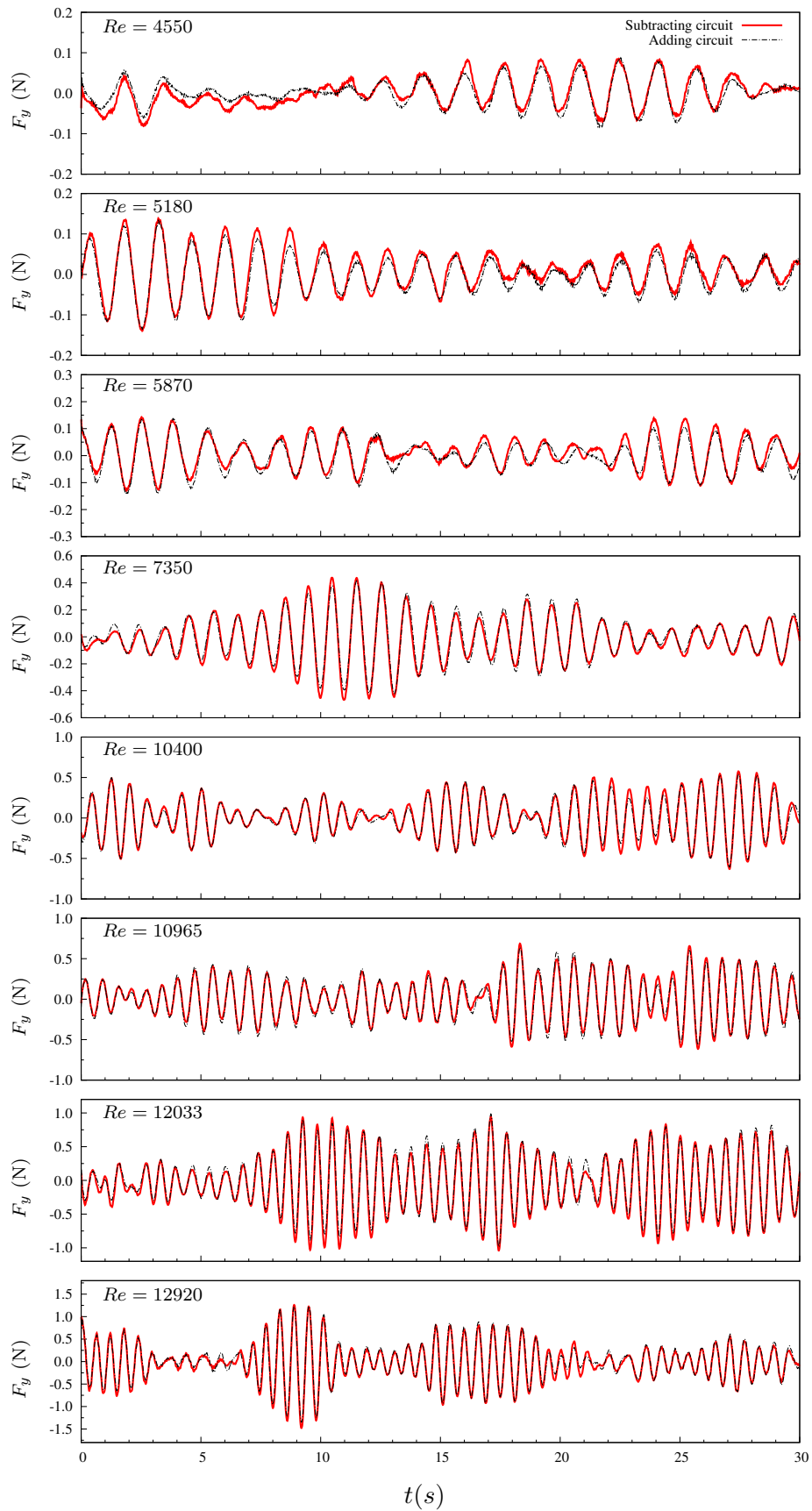


FIGURE 3.22: Lift force measurement of a circular cylinder at different Reynolds numbers.

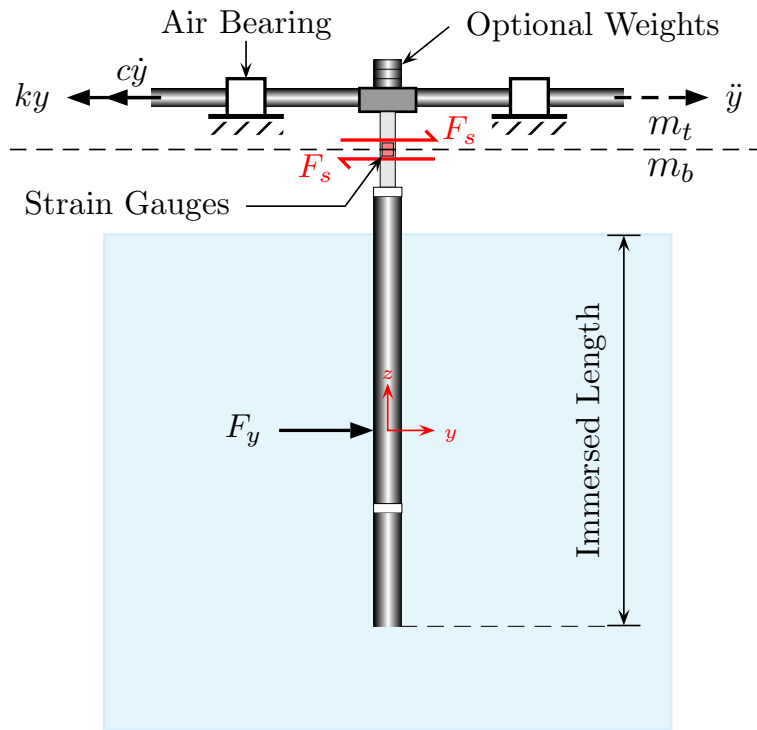


FIGURE 3.23: Schematic for force measurement correction of a cross-flow FIV system, where c is the system's damping and k is the spring constant. The resultant fluid force F_y is applied at the middle of the immersed length of the cylinder. Note that the extension springs of the air bearing system are invisible in this figure.

mass was calculated to be $m_d = 306.2$ g, giving a mass ratio of $m^* = 2.64$. The mass of system's upper and bottom parts were $m_t = 610.2$ g and $m_b = 198.2$ g, respectively. The spring constant was estimated to be $k = 23.14$ N/m, and the damping coefficient was determined to be $c = 0.0275$ Ns/m from free decay tests in air. As compared in Figure 3.24 (b), (d) and (f), the transverse lift forces calculated ($F_{y(calculated)}$) using the parameters in the left-side part of Eq. (3.26) closely match the experimental values ($F_{y(experimental)}$) based on the force balance and inertia forces in the right-side part of Eq. (3.26). The results confirmed the force balance was able to accurately measure the fluid force F_y of a circular cylinder undergoing VIV.

3.6. Experimental measurement systems

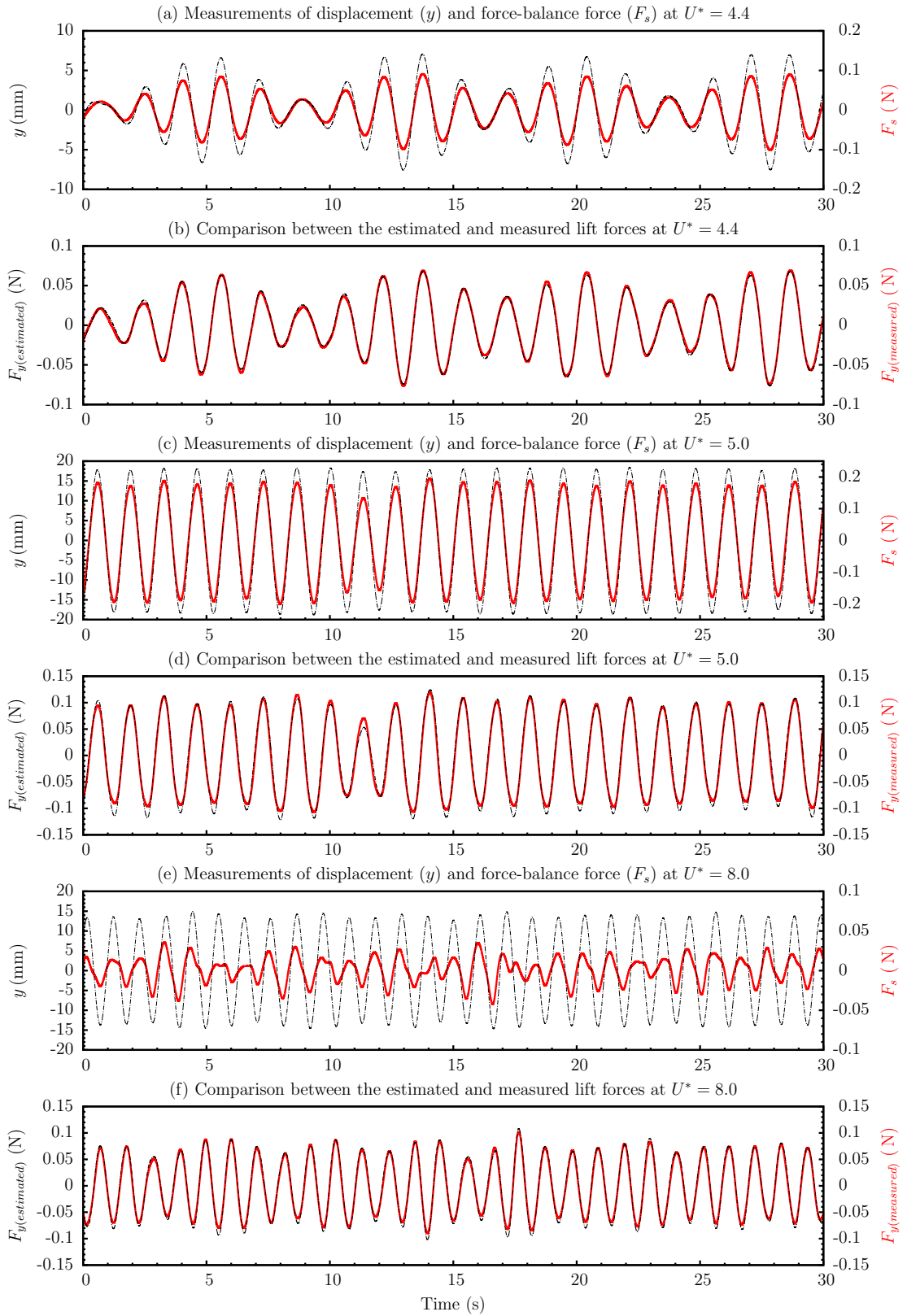


FIGURE 3.24: Time traces of the displacement and the transverse lift force of a circular cylinder at different reduced velocities. In (a),(c) and (e): the cylinder's displacement (y) is represented by the black dot-dashed lines, and the force-balance force (F_s) is represented by the solid red lines. In (b), (d) and (f), the calculated and experimental lift forces are represented by the black dot-dashed lines and the red solid lines, respectively.

3.6.4 Flow visualization – Particle Image Velocimetry (PIV) system

The vortex structures in the near wake of the cylinder in this research were measured using particle image velocimetry (PIV) technique [see Adrian (1991)]. The PIV technique for flow visualisation has been well known and widely used in many fundamental and applied fluid mechanics investigations. PIV has many advantages over the traditional techniques, such as hydrogen bubbles, dye and smoke. It provides non-intrusive measurements of a instantaneous velocity field of a fluid flow in a region of interest, and subsequently other quantities (such as the pressure and the vorticity distributions) in the region can be derived, and it also gives quantitative measurements with high spatial resolution allowing the detection of spatial structures in a fluid field. PIV technique has been well described in the book by Raffel *et al.* (2007). This section will present a brief description of PIV, and some details of the PIV system used in the current experiments.

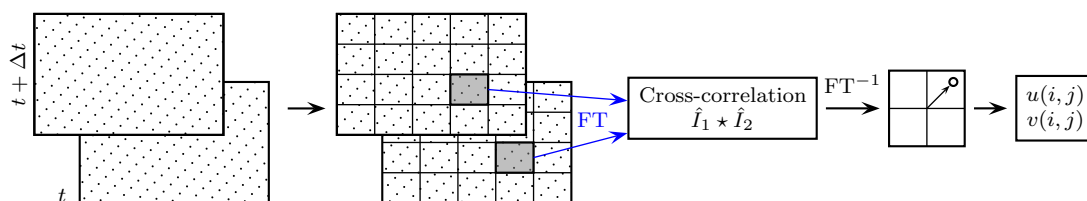


FIGURE 3.25: Analysis algorithm of cross-correlation digital PIV recordings

PIV has various recording methods and data evaluation approaches [see Raffel *et al.* (2007)]. The current PIV system employed the double frames/single exposure recording technique in conjunction with the normalised spatial cross-correlation analysis to evaluate the PIV recordings (Fouras *et al.* 2008), as shown in Figure 3.25. The flow is seeded with sufficiently small tracer particles, thus particles in the plane region of interest can be illuminated by a laser sheet. A camera capable of double frames/single exposure recording feature and pulsed lasers are synchronised by a synchronise, and both are triggered at a sampling frequency using an external TTL signal generator to photographically record the illuminated flow region on to a sequence of a number of image pairs. The images within each image pair have an equal small fine time separation of Δt . Images of pair are divided into interrogation windows, and then Fourier Transform (FT) or Fast Fourier Transform (FFT) is introduced into the calculation of discrete cross-correlation function between two interrogation windows sampled from the image pair. The average displacement ($\Delta x, \Delta y$) of all particles within the interrogation window is statistically calculated by locating the peak value in the cross-correlation calculation. This location is found to sub-pixel accuracy using a least-square fit of Gaussian function (Fouras & Soria 1998). Inverse Fourier transform FT^{-1} is used to evaluate the velocity vectors. To convert the distance unit in pixel of the images to a desired unit (*i.e.* millimetre), the magnification factor \mathcal{M} of the images is measured by taking a photograph of a ruler placed in the plane of interest illuminated by the laser sheet. This procedure is referred to as “*ruler test*”. Thus, with the known time separation value Δt and the image magnification factor, the two-dimensional local velocity vectors within the interrogation windows are accurately determined using the following equations:

$$u = \frac{\Delta x}{\Delta t} \quad (3.27)$$

3.6. Experimental measurement systems

Model	Chip Type	Resolution	Pixel Size	Max Frame Rate
PCO 2000	CCD	4 008 × 2 672 pixel ²	9.0 μm	5.0 frames/s
PCO 4000	CCD	2 048 × 2 048 pixel ²	7.4 μm	14.7 frames/s

TABLE 3.4: Specifications of the PCO cameras used in the present study.

and

$$v = \frac{\Delta y}{\Delta t}, \quad (3.28)$$

where u and v are the velocity components of the particles in x -direction and y -direction respectively. The whole velocity field is calculated by sweeping the window through the entire image frame.

Vorticity field is an important quantity derived from planar velocity vector field to investigate the structures of a flow. The three-dimensional vorticity field, $\boldsymbol{\omega}$, is defined by

$$\boldsymbol{\omega} = \nabla \times \mathbf{u}, \quad (3.29)$$

where \mathbf{u} is the three-dimensional velocity vector field in a x - y - z Cartesian coordinate system. This research is primarily concerned with the out-of-plane z -component vorticity vector denoted by ω_z for the near wake structures behind the cylinder, whose direction abides by the right-hand rule normal to the x - y plane. Its definition is given by

$$\omega_z = \frac{\partial v}{\partial x} - \frac{\partial u}{\partial y}. \quad (3.30)$$

The PIV data evaluation is a process based on statistics, in which the error sources are from bias errors and random errors [see Fouras & Soria (1998); Hart (2000); Raffel *et al.* (2007)]. Fouras & Soria (1998) also reported that the accuracy of the ω_z measurement depends primarily on the the spatial sampling distance between the velocity points and on the accuracy of the velocity vector field measurements. Pertaining to error reduction and accuracy improvement of the out-of-plane vorticity calculation from in-plane velocity measurement, Fouras & Soria (1998) presented their study using a second order polynomial χ^2 fit to the local velocity components with analytic differentiation, where accuracy improvement was found when it was compared to other methods using finite difference calculation. More details of PIV accuracy enhancement discussion have been reported by Dusting (2006) and Nazarinia (2010). Here the present research employed a χ^2_{21} method developed by Fouras & Soria (1998) which uses surrounding 21 velocity sampling points to calculate the vorticity fields. The presented vorticity fields were nondimensionlised by

$$\omega_z^* = \frac{\omega_z H}{U_\infty}, \quad (3.31)$$

where H is the frontal projected length of the cylinder's cross section, and U_∞ is the free-stream velocity. And the nondimensionlized circulation is given by

$$\Gamma^* = \frac{\Gamma}{\pi H U_\infty}. \quad (3.32)$$

The present experimental arrangement for PIV measurements is shown in Figure 3.3 and Figure 3.26. The flow was seeded with hollow microspheres (Spherical 110P8,

Potters Industries Inc.) with a nominal diameter of $13\ \mu\text{m}$ and a specific weight of $1.1\ \text{gcm}^{-3}$. Two miniature Nd:YAG (Neodymium-doped Yttrium Aluminium Garnet) pulsed lasers (Model: MiniliteTM II Q-Switched lasers having a wavelength of 532 nm and a maximum energy output of 25 mJ/pulse, Continuum[®], CA) produced an approximate 2 mm thick horizontal planar sheet, illuminating the particles in the plane of interest. Sequential image pairs were captured by a charge coupled device (CCD) camera of $2048 \times 2048\ \text{pixel}^2$ (PCO 2000, PCO AG), equipped with a 50 mm lens (Nikkor, Nikon Corporation). Table 3.4 shows specifications of the PCO cameras used during the PhD candidature. The PIV image data was analysed with in-house PIV software (Fouras *et al.* 2008), using $32 \times 32\ \text{pixel}^2$ interrogation windows in a grid layout with 50% window overlap. The PIV system's trigger signals along with the displacement and force measurements of the cylinder, and the temperature measurement of the flow were simultaneously sampled by the data acquisition system. The recorded signals provided the timing of captured image pairs along with time histories of the recorded position and lift signals, allowing us to phase average the computed velocity and vorticity fields based on the cylinder position and lift forces.

Two phase-averaging methods were used to average the PIV measurement images in the present study: phase-locked averaging and phase-band averaging. The phase-locked method was used in the previous work by Carberry *et al.* (2001, 2005) and Nazarinia *et al.* (2009), where PIV measurements were triggered at a specific phase of pre-programmed sinusoidal oscillations of a circular cylinder. This method is easily implemented as the cylinder undergoes known sinusoidal oscillations, and the PIV snapshot triggers can be easily programmed at desired phases. However, the vibration of a free cylinder is not as periodic as pure sinusoidal motion, which makes it difficult for the PIV imaging to be triggered at the given phase locations. The phase-locked method has been improved to be able to trigger PIV measurements on-the-fly. This improvement employed the real-time Quanser Q4 control system (as described in §3.4) which monitored the cylinder's real-time position, and output triggers at the desired phases, as shown in Figure 3.27. On the other hand, the phase-band averaging method required the information of the cylinder's position and velocity. As demonstrated in Figure 3.28, the trigger pulses are recorded along with the time trace of the cylinder's displacement in Figure 3.28 (a). According to the trigger timing, the instantaneous PIV images are sorted in different phase bands based on the cylinder's position and velocity in Figure 3.28 (b) and (c). Then the instantaneous PIV images in each phase are joined together to be averaged. The averaged results give clear wake modes behind the cylinder. The phase-band method is not as time efficient as the phase-locked method, because it is initialised manually and costs more time for post-processing. However, both methods are limited in the situations where the oscillation amplitude and frequency of the cylinder were stable. When the cylinder's motion and the vortex shedding are chaotic, there are no means for phase averaging. Correspondingly, PIV measurements were only taken when the spectrum and wavelet analysis showed that the cylinder's displacement and lift force signals were strongly periodic.

3.6. Experimental measurement systems

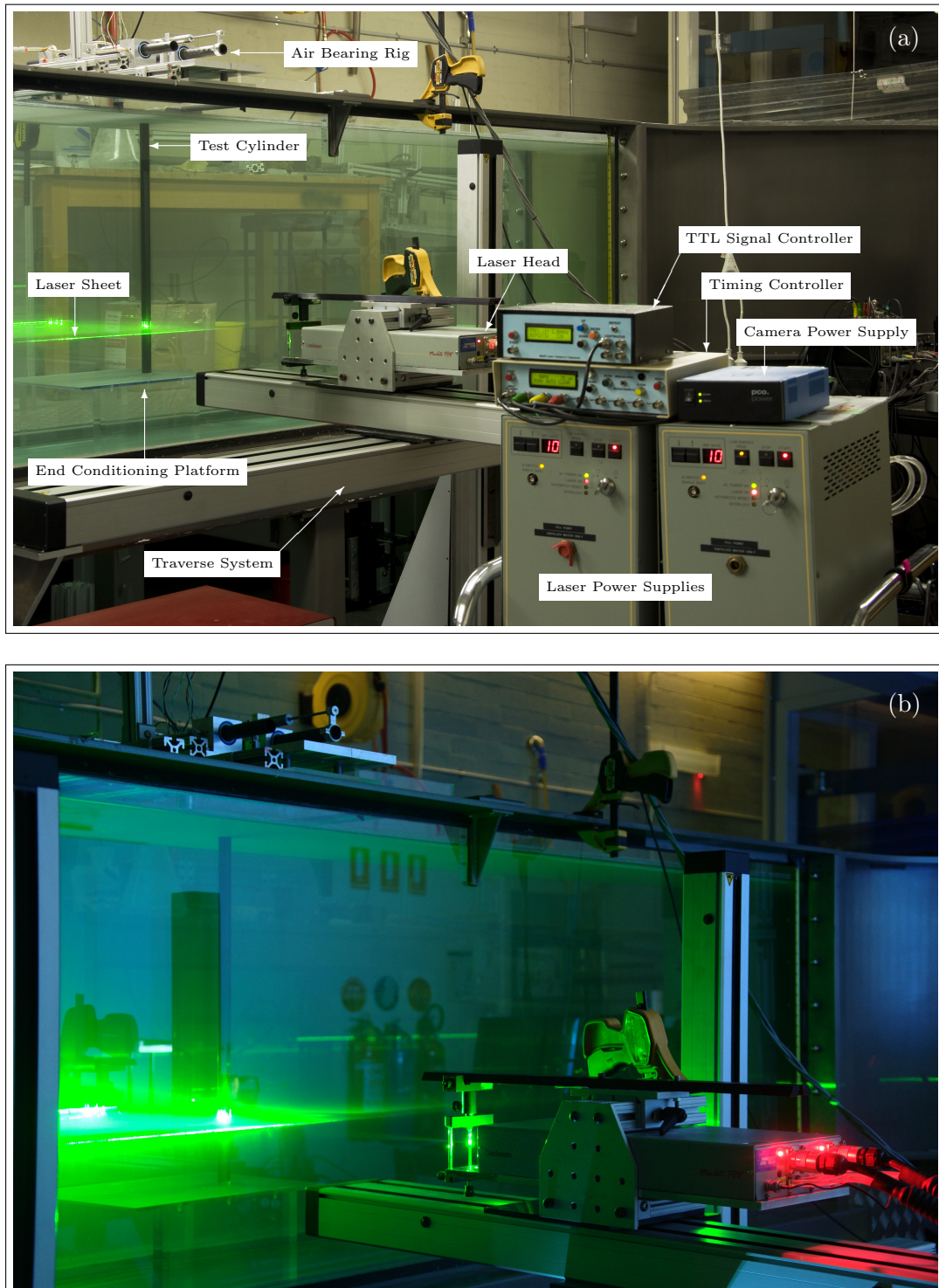


FIGURE 3.26: Photographs showing the PIV system set-up. (a) shows the experimental arrangement for PIV measurement, and (b) shows the lasers operated in high energy mode. Note that the PCO camera placed underneath the water channel is invisible in this figure.

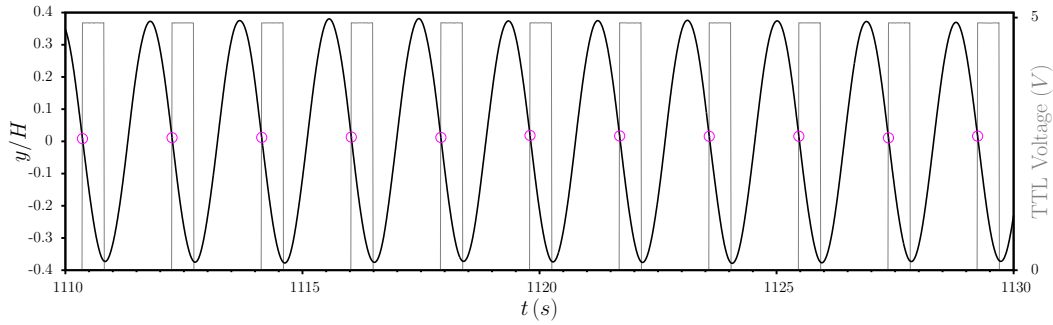


FIGURE 3.27: An example of real-time phase-locked sampling of PIV measurements. The black line represents the cylinder's displacement time trace. The grey line represents the triggering TTL pulses, and the open circles are the cylinder's position (at a phase angle of $\phi = \pi$ of the oscillations) measured at the raising edge of the TTL pulses .

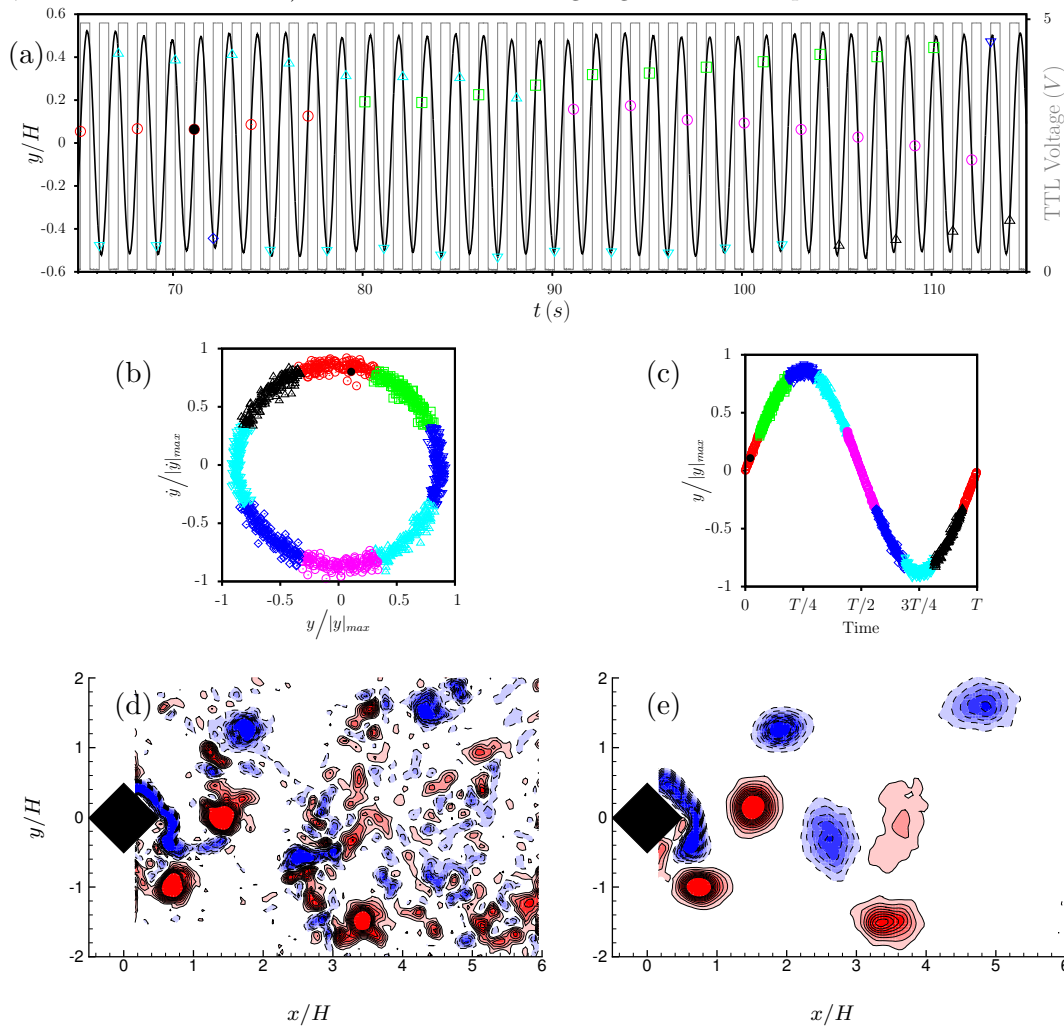


FIGURE 3.28: PIV phase-band averaging method. (a) shows the time history of a cylinder's normalised displacement (black line) and 5V TTL trigger pulses (grey line) of PIV measurements. The symbolic points are cylinder's position in the oscillation waveform when PIV is triggered at TTL signal's raising edges; (c) and (d) show the phase-band binning method based on the cylinder's position and velocity in cycle. The PIV images are binned into 8 phases, and each phase has more than 100 instantaneous images for averaging. (d) shows an instantaneous PIV image captured at the solid black circle as indicated in (a), (b) and (c); (e) shows the averaged result from the phase band No.1 (the red circles).

3.6.5 Temperature measurement

For calculation of Reynolds number, the water temperature was measured using a 100 Ω Platinum (Pt-100) ultra precise resistance temperature detector (RTD) sensor (Model: P-M-1/10-1/8-6-1/8-P-3, Omega Engineering Limited, USA). This sensor was 1/10 DIN class having a measurement range of -29°C to 100°C and an interchangeability of 0.03°C . Signal conditioning of the sensor was processed using a Temperature & Process Controller CNI853 which had a real-time temperature display and also $\pm 10\text{ V DC}$ analog outputs to the DAQ system.

3.7 Experimental procedures

3.7.1 Structural damping

Damping is the result of energy dissipation present in all vibrating systems in practice, which limits the vibrations. FIV systems encounters three different kinds of damping sources: (1) structural damping due to friction, impact, and relative motion between parts of the system (i.e. the shafts moving through air bearings); (2) fluid damping due to hydrodynamic force by the surrounding fluid; (3) material damping due to internal energy dissipation of materials, such as rubber. Since rigid cylinder models are used in the current study, we only consider the two dominant structural damping and fluid damping. In analysis of FIV, the structural damping is an important parameter in the governing equation of motion. It is experimentally measured using free decay method.

3.7.2 Free decay test in air

Free decay test is a convenient way to determine the structural damping and the natural frequency of vibration systems. For a single-DOF damped free vibration system in vacuum situation where no external force is applied $F(t) = 0$, the governing differential equation of motion can be expressed by

$$m\ddot{y} + c\dot{y} + ky = 0, \quad (3.33)$$

or

$$\ddot{y} + 2\zeta\omega_n\dot{y} + \omega_n^2y = 0, \quad (3.34)$$

where m is the mass of system, k is the spring constant, c is the structural damping, the structural damping ratio is defined by $\zeta = c/(2\sqrt{km})$ as the ratio of the structural damping and the critical damping, and $\omega_n = \sqrt{k/m}$ is the natural angular frequency of system.

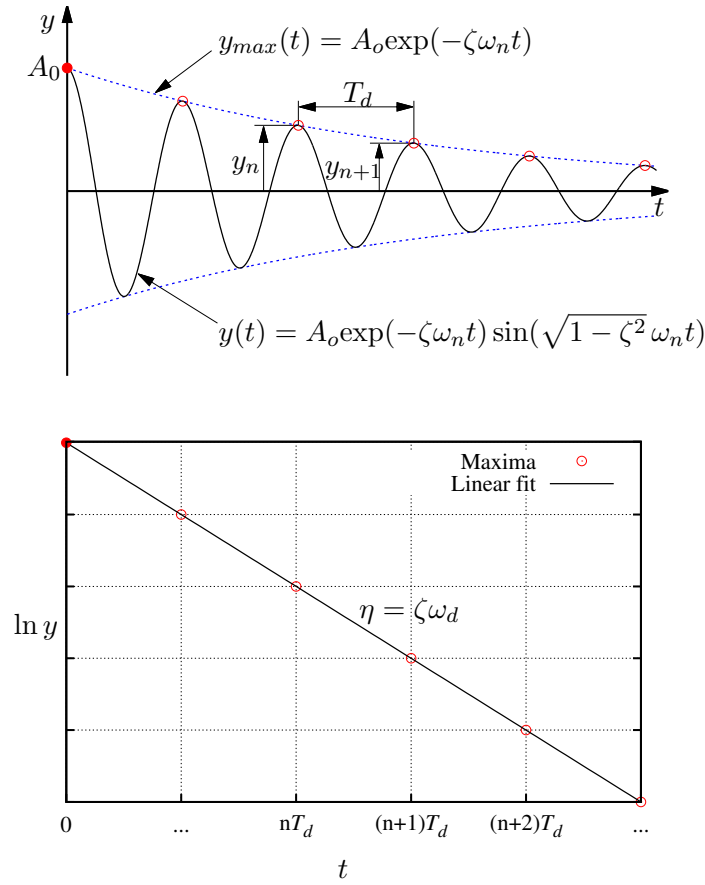
For underdamped free decay ($0 \leq \zeta < 1$) case, the solution to Eq. (3.34) is given by

$$y(t) = A_0 e^{-\zeta\omega_n t} \sin(\sqrt{1 - \zeta^2} \omega_n t), \quad (3.35)$$

which is illustrated in Figure 3.29, where the structure is initially displaced to a certain amount of displacement of A_{max} and then released, and the resulting damped motion of the structure is recorded. The envelope of the maxima from Eq. (3.35) is found by

$$y_{max}(t) = A_0 e^{-\zeta\omega_n t}. \quad (3.36)$$

Hence, the rate of decay, defined as $\eta = -\zeta\omega_n$, can be found by calculating the slope in a plot of $\ln y_{max}$ against t from Eq. (3.36), so that the damping ratio ζ can


 FIGURE 3.29: Response of an underdamped ($0 \leq \zeta < 1$) single-DOF system.

finally be determined as follows

$$\zeta = \frac{-\eta}{\sqrt{k/m}}. \quad (3.37)$$

When ζ is significantly small compared with unity ($\zeta \ll 1$), the damped natural angular frequency, ω_d , can be approximated to the undamped natural angular frequency, ω_n , as described by

$$\omega_d = \frac{2\pi}{T_d} = \omega_n \sqrt{1-\zeta^2} \cong \omega_n. \quad (3.38)$$

In the underdamped case, the ratio of any two consecutive amplitudes is termed by the *logarithmic decrement*, as defined by

$$\delta \triangleq \ln \frac{y_n}{y_{n+1}} = \zeta \omega_n T_d = \frac{2\pi\zeta}{\sqrt{1-\zeta^2}} \cong 2\pi\zeta, \quad (3.39)$$

where $T_d = 2\pi/\omega_d$ is the damped period of the oscillations. The rate of decay, η , is defined by

$$\eta = -\zeta \omega_d = -2\pi\zeta f_d, \quad (3.40)$$

in which f_d is the damped natural frequency given by

$$f_d = \frac{\omega_d}{2\pi} \cong \frac{\omega_n}{2\pi} = \frac{1}{2\pi} \sqrt{\frac{k}{m}} \quad (3.41)$$

In order to minimise the air resistance effects on the moving structure in free decay tests in air, the cylinder model was replaced with an equal concentrated mass placed on top of the carriage of the air bearing rig. Since the air bearing rig is a lightly damped system, it is assumed that the natural frequency in air (f_{na}) is equal to the natural frequency in vacuum (f_n), and that the structural damping ratio obtained from free decay test in air (ζ_{sa}) is also equal to the structural damping ratio in vacuum (ζ_s):

$$f_{na} = \frac{1}{2\pi} \sqrt{\frac{k}{m}} \quad (3.42)$$

and

$$\zeta_{sa} = \frac{c}{2\sqrt{km}}. \quad (3.43)$$

3.7.2.1 Free decay test in still water

In the present study of FIV, the primary purpose of free decay test in still water is to measure the natural frequency of system in water. Details of free decay test in still fluid (water) have described mathematically in the books by Blevins (1990) and Sumer & Fredsøe (1997).

When the structure undergoes free decay test in still water, its vibrations is damped not only by the structural damping but also the fluid damping by the surrounding viscous fluid. The fluid damping is the result of viscous shearing of the fluid at the surface of the structure and flow separation (Blevins 1990). The oscillating system will be subjected to a hydrodynamic force F_y which is referred to Morison force (Sumer & Fredsøe 1997). The Morison force is given by

$$F_y = -\frac{1}{2}\rho C_D D L |\dot{y}| \dot{y} + m_A (-\ddot{y}), \quad (3.44)$$

where m_A is the added mass. The added mass is defined by $m_A = C_A m_d$, in which m_d is the mass of water displaced by the cylinder, and C_A is the potential added mass coefficient ($C_A = 1$ for a circular cylinder).

The governing equation of motion of free decay test in still water can be written by

$$m\ddot{y} + c\dot{y} + ky = F_y = -\frac{1}{2}\rho C_D D L |\dot{y}| \dot{y} + m_A (-\ddot{y}), \quad (3.45)$$

or

$$(m + m_A)\ddot{y} + c\dot{y} + \frac{1}{2}\rho C_D D L |\dot{y}| \dot{y} + ky = 0. \quad (3.46)$$

The solution to Eq. (3.46) then is

$$y(t) = A_o \exp(-\zeta_w \omega_d t) \cos(\omega_d t), \quad (3.47)$$

where ζ_w is the total damping in still water. The total damping ζ_w comprises the structural damping with added mass in still water (ζ_{sw}) and the fluid damping in still water (ζ_{fw}), as expressed by

$$\zeta_w = \zeta_{sw} + \zeta_{fw}. \quad (3.48)$$

Similar to the free decay test in air, the damped natural angular frequency in still water ω_{dw} is given by

$$\omega_{dw} = \omega_{nw} \sqrt{1 - \zeta_w^2}, \quad (3.49)$$

Chapter 3. Experimental Methodology

where ω_{nw} is the undamped natural angular frequency with the added mass consideration in still water, as defined by

$$\omega_{nw} = \sqrt{\frac{k}{m + m_A}}. \quad (3.50)$$

Since the total damping ζ_w is normally found in experiments to be significantly small compared with unity, the damped natural angular frequency measured in the free decay test can be approximated to the undamped natural angular frequency: $\omega_{dw} \cong \omega_{nw}$. Then, the natural frequency in water is determined by

$$f_{nw} = \frac{\omega_{nw}}{2\pi} = \frac{1}{2\pi} \sqrt{\frac{k}{m + m_A}}. \quad (3.51)$$

The total damping is the result of energy dissipation caused by the total damping force F_d , and it is proportional to the ratio of the energy dissipated in one cycle of vibration E_d and the total stored energy E_T , as expressed by

$$\zeta_w = \frac{1}{4\pi} \frac{E_d}{E_T}, \quad (3.52)$$

where the total stored energy is equal to the maximum kinetic energy during vibration:

$$E_T = \frac{1}{2}(m + m_A)\dot{y}_{max}^2. \quad (3.53)$$

The dissipated energy E_d is the work done by the total damping force F_d in one cycle of vibration, and it can be determined by integrating the product of the total damping force with the displacement over one cycle:

$$E_d = \oint F_d dy = \int_t^{t+T_{dw}} F_d \dot{y} dt, \quad (3.54)$$

in which $T_{dw} = 2\pi/\omega_{dw}$ is the damped vibration period of system in still water. The total damping force adversely against the motion of the system. As illustrated in Eq. (3.46), it comprises the structural damping force and the fluid damping force:

$$F_d = \underbrace{c\dot{y}}_{\text{structural damping force}} + \underbrace{\frac{1}{2}\rho DLC_D|\dot{y}|\dot{y}}_{\text{fluid damping force}}. \quad (3.55)$$

Therefore, Eq. (3.54) can be rewritten by

$$E_d = \int_t^{t+T_{dw}} c\dot{y}^2 dt + \int_t^{t+T_{dw}} \frac{1}{2}\rho DLC_D|\dot{y}|\dot{y}^2 dt. \quad (3.56)$$

Then, as illustrated by (Sumer & Fredsøe 1997), Eq. (3.56) substituted into Eq. (3.52) gives

$$\zeta_w = \underbrace{\frac{c}{2(m + m_A)\omega_{dw}}}_{\text{structural damping}} + \underbrace{\frac{\rho D^2 L}{4\pi(m + m_A)} \frac{8}{3} C_D \frac{A}{D}}_{\text{fluid damping}}, \quad (3.57)$$

in which the structural damping ratio with the effect of added mass is

$$\zeta_{sw} = \frac{c}{2(m + m_A)\omega_{dw}} = \frac{c}{2\sqrt{k(m + m_A)}}, \quad (3.58)$$

and the fluid damping ratio is

$$\zeta_{fw} = \frac{\rho D^2 L}{4\pi(m + m_A)} \frac{8}{3} C_D \frac{A}{D}. \quad (3.59)$$

As the definition of the structural damping ratio has apparently led to some confusion to readers, it is important to note that the structural damping ratio, ζ , to be reported in the future experimental results is referred to the structural damping ratio with the effect of added mass, ζ_{sw} given by Eq. (3.58), which has been constantly used in papers by Prof. C.H.K Williamson's group at Cornell University. Thus, combining Eq. (3.51), Eq. (3.58), Eq.3.42 and Eq. (3.43) gives the experimental measurement value of the structural damping ratio:

$$\zeta = \zeta_{sw} = \frac{f_{nw}}{f_{na}} \zeta_{na}, \quad (3.60)$$

and also the measurement value of the potential added mass coefficient:

$$C_{Am} = \left[\left(\frac{f_{na}}{f_{nw}} \right)^2 - 1 \right] m^*. \quad (3.61)$$

Figure 3.30 shows an example of free decay tests of circular cylinder ($D = 40$ mm) in air and in still water. The total mass of the system was $m = 1872.2$ g. The immersed length of the cylinder was 622 mm, and the resulting mass ratio of $m^* = 2.4$ was selected to match that of a case study by Khalak & Williamson (1997a). In the present results, the logarithmic maxima of free decay response closely followed the best linear fitting line in both air and still water tests. The structural damping ratio of the system was found to be $\zeta_{sw} = 2.43 \times 10^{-3}$. According to Eq. (3.61), the potential added mass coefficient was calculated to be $C_{Am} = 1.01$, which agreed well with the assumption of $C_A = 1$ for a circular cylinder reported in the literature.

From the free decay tests in the present study of FIV, results showed that a linear single-DOF mass-spring rig was set up for experiments, and that the performance of the air bearing system was reliable and repeatable to achieve low damping ratios. The structural damping ratio was found to be dependent on the system's parameters, such as the mass of system m and the spring constant k .

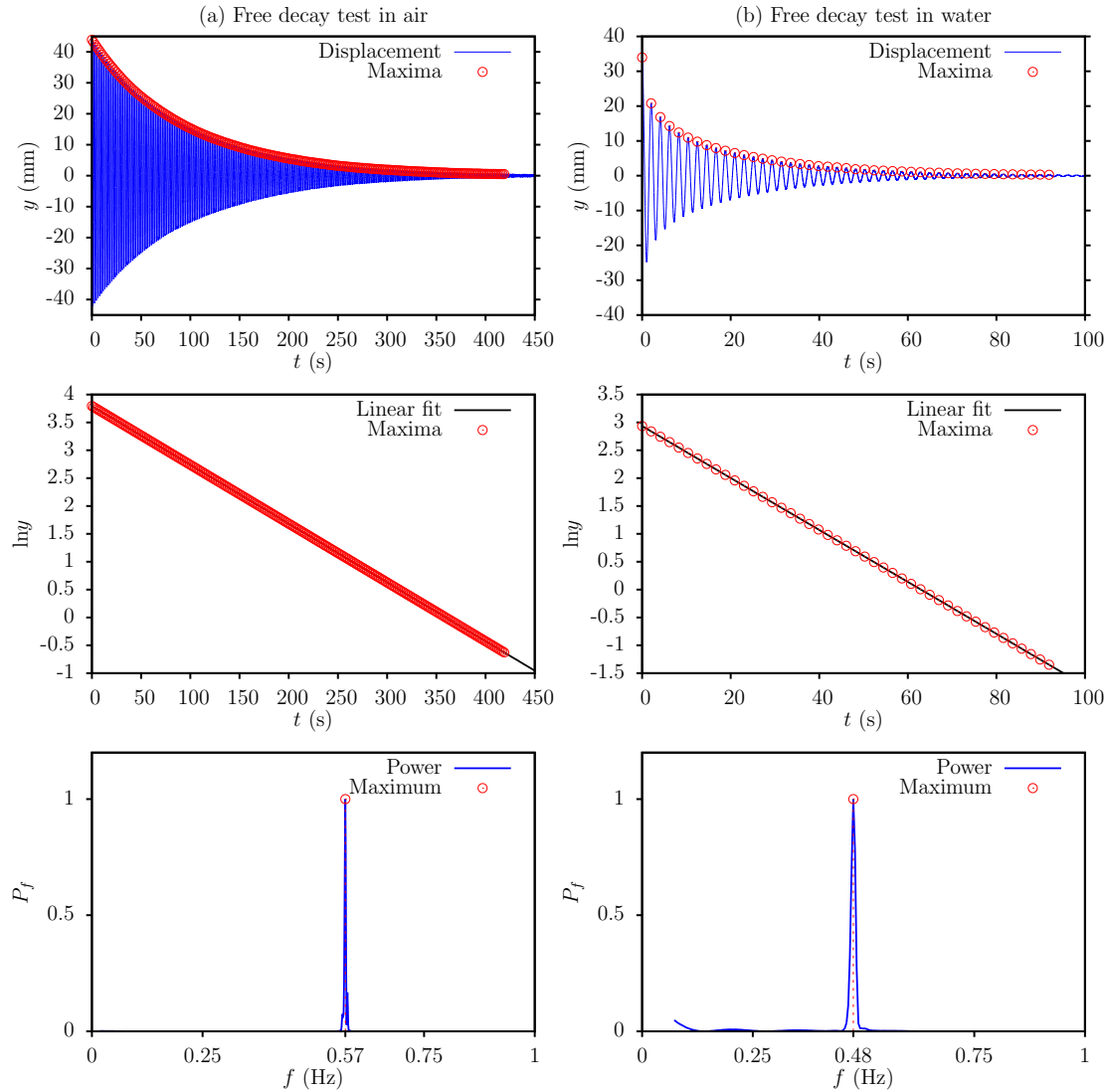


FIGURE 3.30: An example of free decay tests of a circular cylinder of $m^* = 2.4$: column (a) shows free decay test in air and column (b) shows free decay test in still water. The top rows show displacement histories, where maxima above an amplitude of less than 0.5 mm were selected to calculate the free decay rates. The middle rows show the decay rate results based on logarithmic decrement algorithm: the decay rates were calculated to be $\eta_a = 10.33 \times 10^{-3}$ in air and $\eta_w = 51.43 \times 10^{-3}$ in still water, respectively. The bottom rows show FFT calculation results of the power spectral density normalised by the maximum power spectral density of the given signal. The natural frequencies were calculated to be $f_{na} = 0.572$ Hz in air and $f_{nw} = 0.477$ Hz in still water, respectively. Hence, the damping ratio of the system in air was determined to be $\zeta_{sa} = 2.89 \times 10^{-3}$ and the total damping ratio measured in still water was $\zeta_w = 17.34 \times 10^{-3}$. The structural damping ratio was determined to be $\zeta = \zeta_{sw} = 2.43 \times 10^{-3}$, giving a mass-damping ratio $m^*\zeta = 5.83 \times 10^{-3}$.

3.8 Chapter summary

This chapter has shown details of the experimental facilities, air bearing rig for free FIV experiments, and PID position control system for forced oscillation experiments. Free decay tests in both air and water have demonstrated the air bearing rig had very low structural damping ratio for experiments on free FIV. On the other hand, testing results have also shown that the PID position control system was able to accurately and smoothly track simple sinusoidal and complicated motion trajectories.

Furthermore, the measurement techniques, including LVDT for linear displacement, force balance for the fluid forces, and PIV for the near wake modes, have also been described in detail. Validation results of these techniques have also been presented.

In summary, the experimental methodology has been shown and validated for data acquisition in experiments on both free FIV and forced oscillation of a bluff body.

Chapter 4

Vortex-Induced Vibration of Circular Cylinders

4.1 Introduction

With the progress of modern digital particle image velocimetry technique and numerical simulation in the past decade, intensive studies have been undertaken towards understanding the fundamental characteristics of the flow past an oscillating cylinder. Govardhan & Williamson (2000) employed PIV technique for the first time in free vibration to investigate the wake mode transitions. Of particular interest, recent studies of sinusoidal forced vibrations by Carberry *et al.* (2005); Leontini (2007); Morse & Williamson (2006, 2009a,b) have provided better insight into the relationships between the fluid forces and the wake modes. Although many remarkable similarities have been observed in both free and sinusoidal forced vibrations, significant differences also exist. Therefore, the question still remains unaddressed whether precisely-close forced vibration can reproduce the same fluid forces and wake modes of the free vibration case.

As part of the present PhD study, this chapter deals with a close comparison between free and forced vibrations. It begins with an experimental validation in §4.2, where the dynamic responses of a freely-vibrating circular cylinder with $m^* = 2.4$ are compared directly to a typical case with the same mass ratio studied by Khalak & Williamson (1997a). Then, §4.3 presents the results of direct comparison between free vibration of a cylinder with $m^* = 2.66$ and forced vibrations of precise tracking motion and sinusoidal oscillations, including the total transverse lift, vortex forces, phases, and wake modes of the cases of free and forced vibrations. A summary of this chapter is given lastly in §4.4.

4.2 Experimental validation for VIV of a circular cylinder

4.2.1 Experimental details

The methodologies used in the present experiments need to be validated to ensure that the reader has confidence in the new results obtained. For this reason, the circular cylinder model used in this section was the Body III described in Table 3.3, which had comparable geometric parameters to the case study presented by Khalak & Williamson (1997a). This cylinder had a diameter of $D = 40$ mm and an immersed length of $L = 620$ mm, giving an aspect ratio of $AR = L/D = 15.5$ and a displaced water mass

of $m_d = \rho\pi D^2 L/4 = 780.1$ g. The total mass of the oscillating system was $m = 1872.2$ g, resulting in a mass ratio of $m^* = 2.40$. Free decay tests were conducted individually in air and water, as shown in Figure 3.30 in § 3.7.2.1, to determine the natural frequency in air, $f_{na} = 0.572$ Hz, and in water, $f_{nw} = 0.477$ Hz. The structural damping ratio was $\zeta = c/(2\sqrt{k(m+m_A)}) = 2.43 \times 10^{-3}$, resulting in a mass-damping ratio of $m^*\zeta = 5.83 \times 10^{-3}$, which is comparable to the case study with $m^*\zeta = 11.3 \times 10^{-3}$ ($m^* = 2.4$ and $\zeta = 4.5 \times 10^{-3}$) by Khalak & Williamson (1997a). The end condition was controlled using a platform (described in § 3.5) with a gap of approximately 2 mm between the cylinder's free end and the platform.

The dynamic response of VIV was investigated over a reduced velocity of $2.75 < U^* < 17$, corresponding to a flow velocity range of 0.0495 m/s $< U_\infty < 0.3240$ m/s and a Reynolds number range of $2000 < Re < 13000$. The body displacement and fluid forces were measured simultaneously at a sampling frequency of 100 Hz for 20 min (over 500 oscillation cycles) at each reduced velocity investigated.

4.2.2 Amplitude and frequency responses

The response amplitude and frequency of the present work are directly compared directly to the results of Khalak & Williamson (1997a) at the same the mass ratio in Figure 4.1. The comparison shows that the overall agreement is remarkable in terms of the three-branch amplitude response pattern, the amplitude peak value, the lock-in region, and the frequency response. In the initial branch, both cylinders experience extremely low-amplitude oscillations for $U^* < 3$, and then the maximum oscillation amplitude, A_{\max}^* , grows up sharply to above $0.4D$ as the reduced velocity is increased up to $U^* = 4.80$. Figure 4.2 (a) and (b) show examples of the time trace of the cylinder displacement at $U^* = 4.52$. In the initial branch, the oscillation amplitudes are unstable and appear to experience beating, which has also been observed by other researchers (see Leontini 2007; Gopalkrishnan 1993). The oscillations of the body have signatures of two strong frequencies: one matching the natural frequency in water and the other matching the vortex shedding frequency of the body at rest. As U^* is further increased, the amplitude response undergoes a transition from the initial to the upper branch, with A_{\max}^* jumping from 0.46 to 0.84 at $U^* = 1/St = 4.80$ ($St = 0.208$ for a stationary cylinder in the present case). Govardhan & Williamson (2000) has explained and demonstrated that this transition occurs when the frequency response of a cylinder with low $m^*\zeta$ passes the natural frequency in water, namely $f^* = f/f_{nw} = 1$. As the amplitude response jumps up to the upper branch, on the other hand, the onset of lock-in occurs with a well-defined dominant oscillation frequency matching the vortex shedding frequency. Figure 4.2 (c) and (d) show examples of time traces of the cylinder displacement at $U^* = 5.23$. In the upper branch, the cylinder also experiences unstable oscillations with the largest-scale amplitudes. The maximum amplitude value observed is $A_{\max}^* = 1D$ at $U^* = 6$, comparable to that of $A_{\max}^* = 0.96D$ at the same reduced velocity of $U^* = 6$ by Khalak & Williamson (1997a). Also, the frequency increases monotonically with the reduced velocity, which agrees well with the results of Khalak & Williamson (1997a). The cylinder experiences an intermittent switching transition from the upper to the lower branch at $U^* = 7.8$, which has also been seen by Khalak & Williamson (1997a). The lower branch is featured with very stable oscillation amplitudes of $A_{\max}^* \approx 0.6D$, as shown in Figure 4.2 (e) and (f). In this branch, the frequency response remains remarkably constant with a value of $f^* \approx 1.342$ over a reduced velocity range of $7.6 < U^* < 10.5$. For higher reduced velocities, the oscillation amplitudes gradually decreases, and the frequency response exhibits a second weaker component

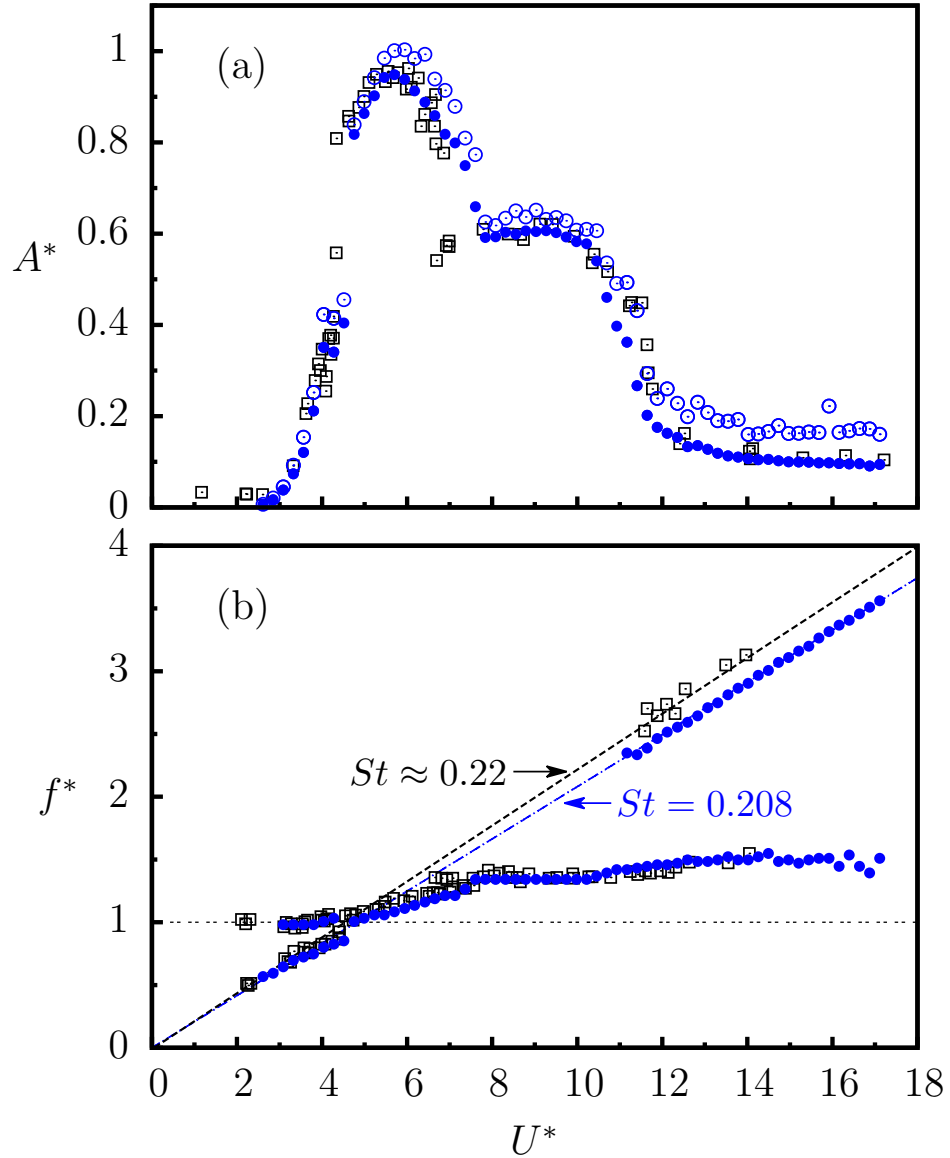


FIGURE 4.1: Comparison of experimental results of a circular cylinder with $m^* = 2.4$. The top plot shows the comparison of amplitude responses, in which the blue open circles represent the normalised amplitude peaks, A_{max}^* , of the present results ($\zeta = 2.43 \times 10^{-3}$), the solid circles represent the mean of top 10% of the oscillation amplitudes, A_{10}^* , of the present results, and open squares represent the results of Khalak & Williamson (1997a) ($\zeta = 4.5 \times 10^{-3}$). The bottom plot shows the comparison of normalised frequency responses.

following the Strouhal number functional trend, indicating end of the lock-in region. Compared to $St \approx 0.22$ of Khalak & Williamson (1997a), the Strouhal number of the cylinder at rest of the present case is $St = 0.208$ which is consistent with $St \approx 0.21$ for $1000 < Re < 10\,000$, as is widely reported in the literature (see Norberg 2001).

To date A_{\max}^* has been used primarily because it provides a basis to validate the results against those of other studies. The A_{\max}^* gives an extreme measure that is the value of a single sample, and can denote an outlier that is not necessarily representative of the average of a larger sample and hence the behaviour of the amplitude response. An alternative, as used by Hover *et al.* (1998); Klamó (2007); Morse *et al.* (2008), is the mean of the top 10 percent of the peak amplitudes, A_{10}^* . This scalar provides a more appropriate measure for comparing amplitude response, being statistically robust when comparing results of different, independent studies, and across different geometries, especially in the absence of transitory behaviours such as intermittent branch switching. These two scalars, A_{\max}^* and A_{10}^* , are both valuable for engineering applications, where A_{\max}^* is a useful measure to demonstrate the maximum observable amplitudes in free FIV, and is primarily of importance to determine design conditions for the deflection of structures and supports, while A_{10}^* can provide a more meaningful value for assessing the typical amplitudes to consider in determining cyclic loading fatigue. Hence, the scalar A_{10}^* is primarily used to analyse the amplitude response of FIV of a bluff body in this thesis.

Figure 4.1 (a) shows A_{10}^* , represented by the blue solid circles, of the oscillation amplitudes. Compared to the A_{\max}^* response, the A_{10}^* values show a smoother response retaining the same trend, despite the expected reduction of the oscillation amplitudes particularly in the regions where the oscillation amplitudes are unstable.

4.2.3 Fluid forces and phases

Since VIV of a bluff body is driven by the fluctuating fluid forces caused by the vortex shedding, it is of significant interest to analyse the transverse lift force, the vortex force, and the corresponding phases with respect to the cylinder displacement. Khalak & Williamson (1997a) firstly provided direct force measurements on a freely oscillating cylinder, and Govardhan & Williamson (2000) further decomposed the total lift force (F_y) into a potential force component ($F_{potential}$) and a vortex force component (F_{vortex}). This decomposition method revealed two jumps in the total phase (ϕ_{total}) and the vortex phase (ϕ_{vortex}) were associated with the wake mode transitions of a freely vibrating cylinder with low mass-damping ratio. In this section, results of the lift and vortex forces, and the corresponding phases relative to the cylinder motion are discussed.

Figure 4.3 (a) compares root-mean-square lift coefficient ($C_{y(r.m.s.)}$) variation with the reduced velocity of the present cylinder and the results from previous studies by Khalak & Williamson (1997a) and Govardhan & Williamson (2000). The blue solid circles represent the present directly measured values, and the red open circles are the estimated values; the black solid and open squares represent the directly measured and estimated values, respectively, of a cylinder with $m^* = 3.3$ and $\zeta = 2.60 \times 10^{-3}$ by Khalak & Williamson (1997a); the black open triangle represent the measured values of a cylinder with $m^* = 8.63$ and $\zeta = 1.51 \times 10^{-3}$ by Govardhan & Williamson (2000). The present measured $C_{y(r.m.s.)}$ values agree well with the estimated values, particularly in the lower branch and desynchronisation (at high reduced velocities of $7.8 < U^*$). The measured $C_{y(r.m.s.)}$ values of Khalak & Williamson (1997a) also generally matched their estimated values, with a peak of $C_{y(r.m.s.)} \approx 2.5$ observed at $U^* \approx 4.4$ which is over 50% higher than that of $C_{y(r.m.s.)} = 1.6$ at $U^* = 4.8$ of the present case. However, the

4.2. Experimental validation for VIV of a circular cylinder

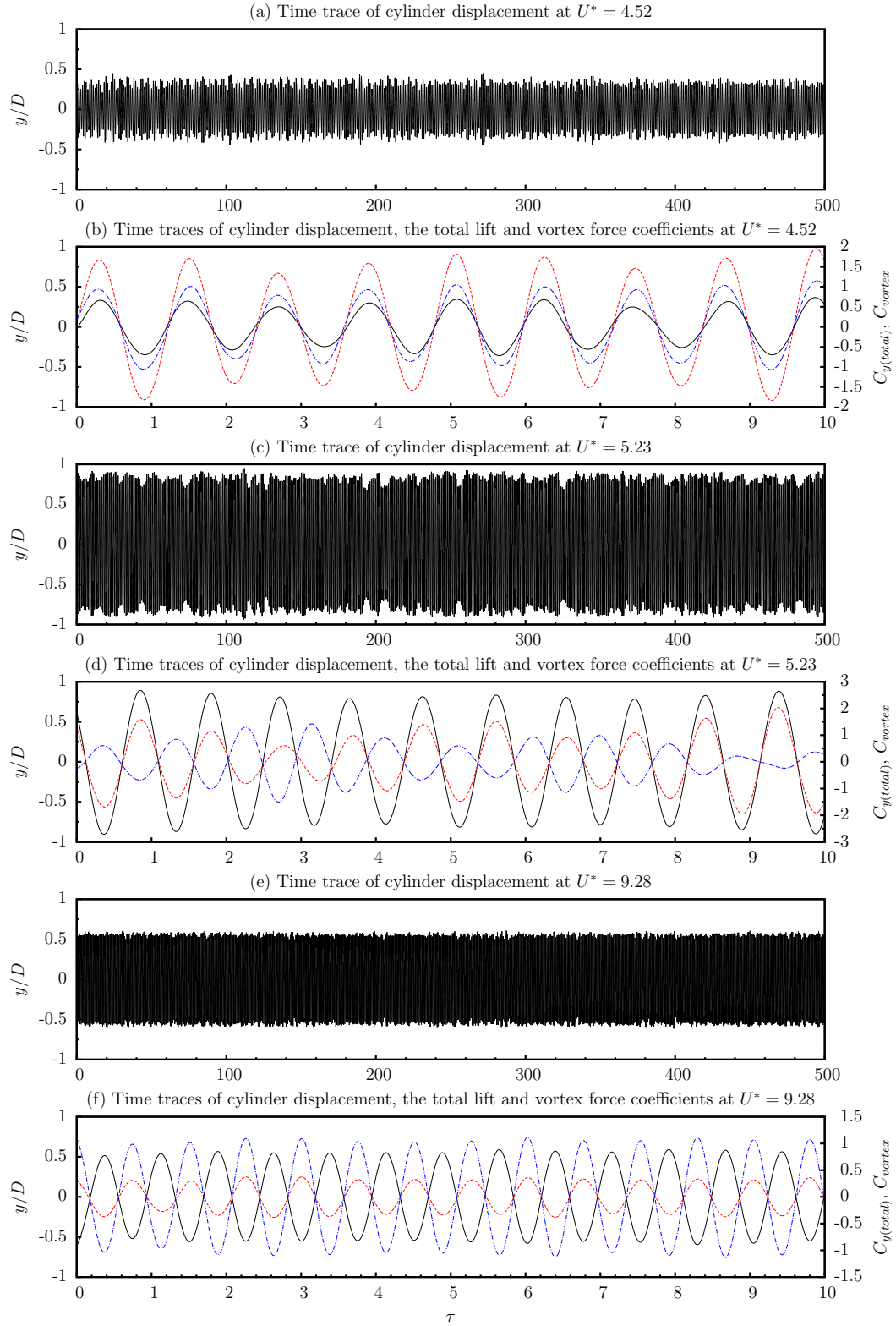


FIGURE 4.2: Time traces ($\tau = t/T_{nw} = f_{nw} t$) of cylinder displacement (black solid lines), the total lift (red dashed lines) and vortex coefficients (blue dot-dashed lines). (a)–(b): the displacement, the total lift and vortex forces are in phase at $U^* = 4.52$ in the initial branch. (c)–(d): the lift force is in phase with the displacement, while the vortex force is leading (approximately 180°) the displacement at $U^* = 5.23$ in the upper branch. (e)–(f): both the lift and the vortex forces are leading (approximately 180°) the displacement at $U^* = 9.28$ in the lower branch.

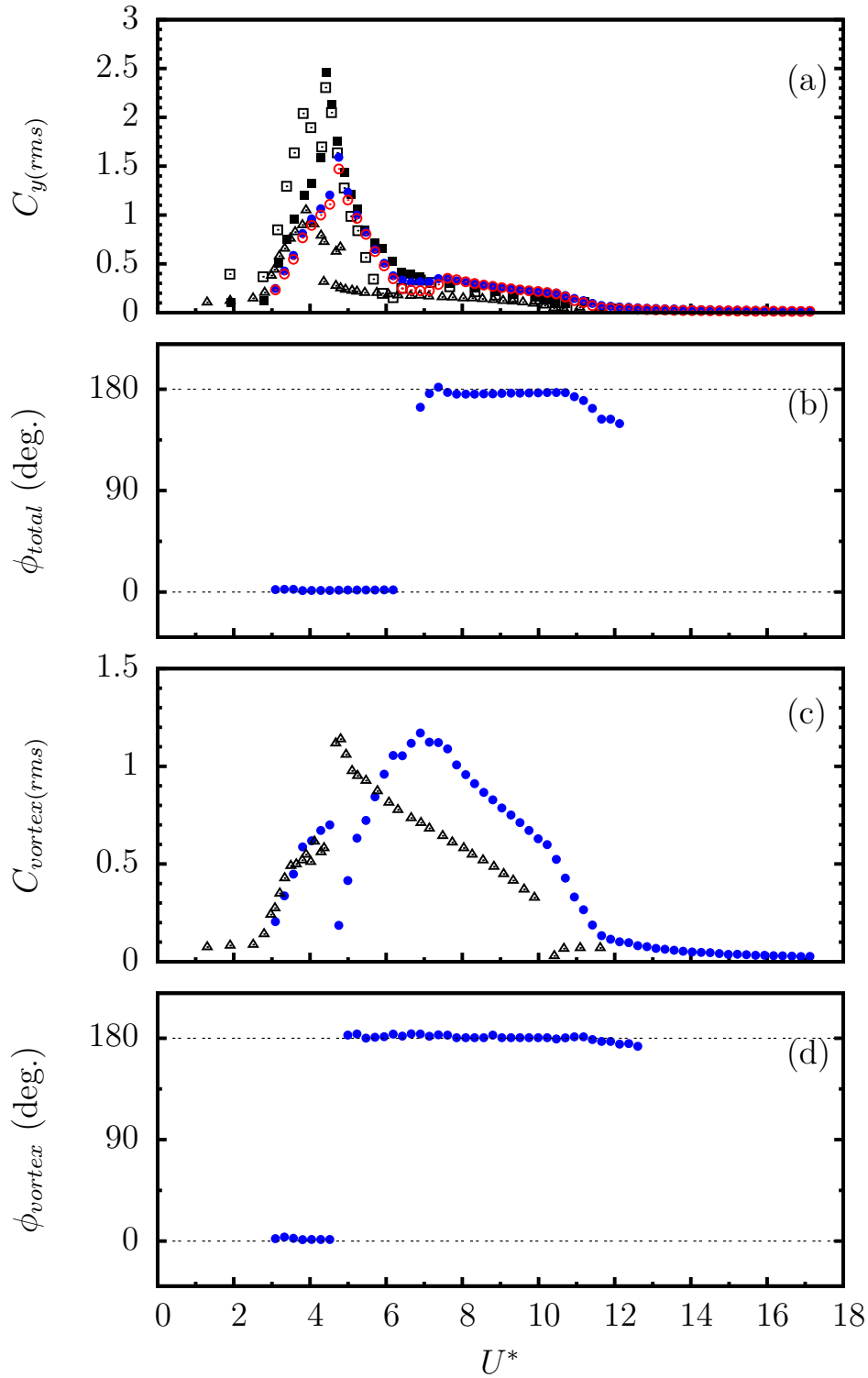


FIGURE 4.3: Force and phase angle variation with the reduced velocity. (a) the total transverse lift coefficient (root-mean-square). The blue solid circles represent the present directly measured values, and the red open circles are the estimated values; The black solid and open squares represent the measured and estimated values, respectively, of a cylinder with $m^* = 3.3$ and $\zeta = 2.60 \times 10^{-3}$ by Khalak & Williamson (1997a); the black open triangles represent the measured values of a cylinder with $m^* = 8.63$ and $\zeta = 1.51 \times 10^{-3}$ by Govardhan & Williamson (2000). (b) shows the present total phase jump associated with the transition of the upper to lower branch. (c) shows the present vortex force coefficient (root-mean-square), and (d) shows the present vortex phase jump associated with the transition of the initial to upper branch.

4.3. Comparison of a free cylinder and a tracking cylinder

measured results by Govardhan & Williamson (2000) show a peak of $C_{y(r.m.s.)} \approx 1.1$ at $U^* \approx 4$ for a cylinder of $D = 38.1$ mm with a higher mass ratio of $m^* = 8.3$. The difference of $C_{y(r.m.s.)}$ between the above three cases could arise from the fact that the differences in experimental conditions, such as the Reynolds number and mass ratio, make the comparison more complicated.

Following the fluid force decomposition method used by Govardhan & Williamson (2000), the total transverse lift force is decomposed to yield a vortex force component, C_{vortex} , using Eq. 2.6 combined with Eq. 2.10, assuming the cylinder displacement approximates to a sinusoidal function as $y(t) = \sin(2\pi ft)$. Figure 4.3 (b) shows the root-mean-square vortex force coefficient ($C_{vortex(r.m.s.)}$) variation with the reduced velocity of the present case compared with the case of Govardhan & Williamson (2000). Both cases show a similar trend and comparable magnitude of the peaks. At the beginning, the $C_{vortex(r.m.s.)}$ increases with U^* in the initial branch. However, as the cylinder undergoes the transition from the initial to the upper branch, the present $C_{vortex(r.m.s.)}$ also experiences a sudden jump from 0.7 down to 0.19, while this sudden jump was not reported by Govardhan & Williamson (2000). One possible reason for this is that the cylinder with high mass ratio ($m^* = 8.63$) of Govardhan & Williamson (2000) resulted in a very narrow upper branch as shown in Figure 2.14. After the sudden jump, the present $C_{vortex(r.m.s.)}$ gradually increases in the upper branch, reaching the peak of $C_{vortex(r.m.s.)} = 1.17$ at $U^* = 6.9$ before the cylinder undergoes the second transition from the upper to the lower branch. In the lower branch, the $C_{vortex(r.m.s.)}$ declines smoothly as U^* is increased, and eventually flattens out at in the desynchronisation region with high U^* values. Another salient difference between these two cases is that the $C_{vortex(r.m.s.)}$ values of Govardhan & Williamson (2000) experiences a sudden jump from around 0.6 to 1.15 as the cylinder undergoes the initial \rightarrow upper branch transition. This could also be due to the higher mass ratio resulting in a much narrower upper branch.

Figure 4.3 (b) and (d) show the total phase (ϕ_{total}) and the vortex phase (ϕ_{vortex}) varying with the reduced velocity, respectively. Figure 4.4 shows examples of time traces of the phases calculated using Hilbert transform (HT) (see Khalak & Williamson 1997a, 1999; Govardhan & Williamson 2000). The results agree with Govardhan & Williamson (2000) that a jump in ϕ_{total} from around 0° to around 180° is associated with the upper-to-lower branch transition, while another jump in ϕ_{vortex} from around 0° to around 180° is associated with the initial-to-upper branch transition.

In summary, the experimental methodologies have been validated based on comparisons of the present results compared with the literature. Performance of the air bearing rig is confirmed from the free decay tests described in § 3.7.1 and the present experiments. The force measurements also agree well with the estimated results and those found in the literature.

4.3 Comparison of a free cylinder and a tracking cylinder

4.3.1 Experimental details

The circular cylinder model used in this section was the cylinder Body II described in Table 3.3. This cylinder had an outside diameter of $D = 25$ mm, which was smaller than that of the Body III ($D = 40$ mm) used for the experimental validation in §4.2 previously. This choice was made because the PIV system which could not provide a large enough field of view for the wake measurement of cylinders with larger diameters. The immersed length of the body was $L = 620$ mm, giving an aspect ratio of $AR =$

Chapter 4. Vortex-Induced Vibration of Circular Cylinders

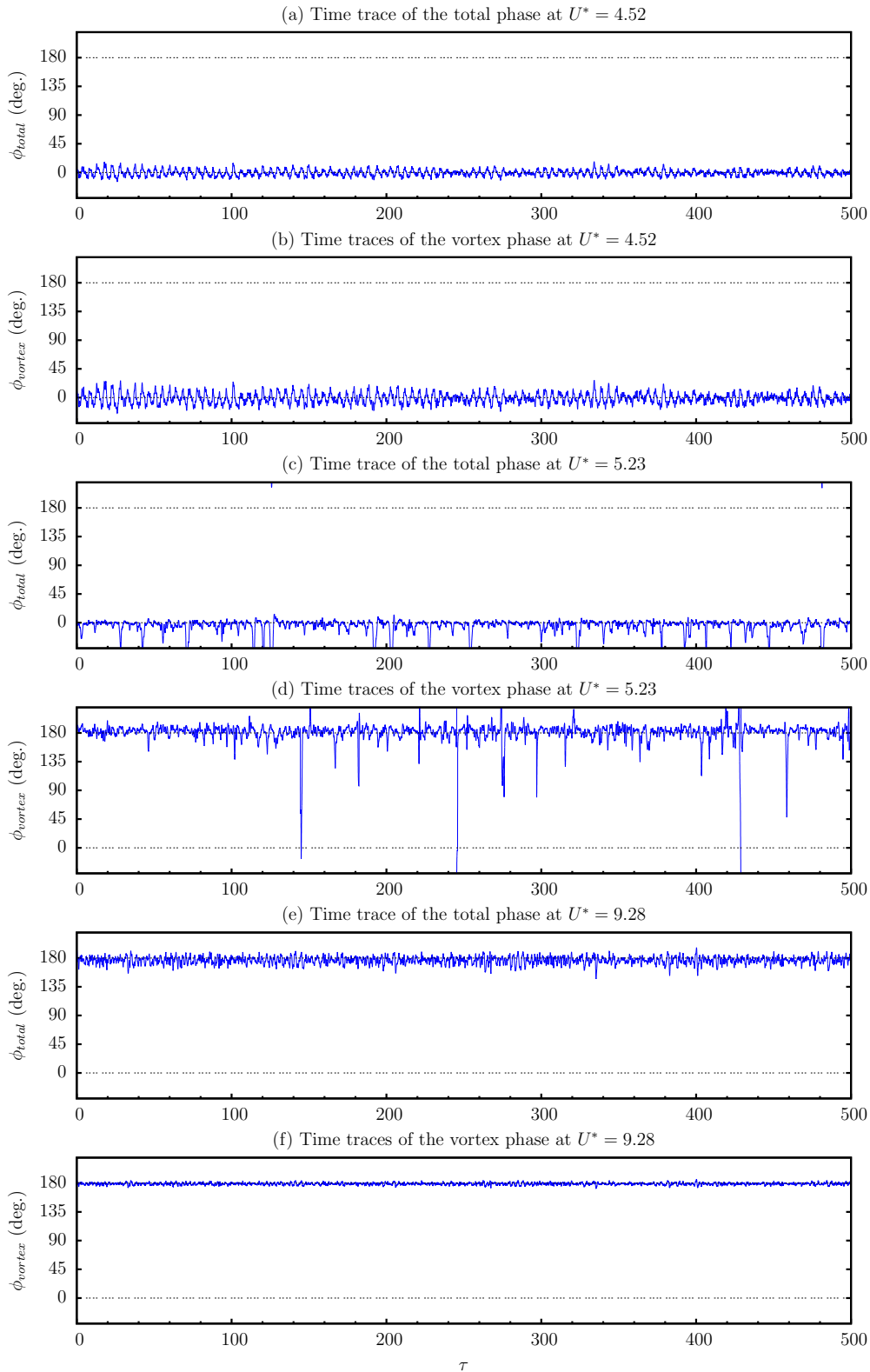


FIGURE 4.4: Time traces of the total phase and the vortex phase at different reduced velocities. (a)–(b): both ϕ_{total} and ϕ_{vortex} are in phase with the cylinder displacement at $U^* = 4.52$ in the initial branch. (c)–(d): the lift force is still in phase with the displacement, while the vortex force is leading (approximately 180°) the displacement at $U^* = 5.23$ in the upper branch. (e)–(f): both the lift and the vortex forces are leading (approximately 180°) the displacement at $U^* = 9.28$ in the lower branch.

4.3. Comparison of a free cylinder and a tracking cylinder

$L/D = 24.8$ and a displaced water mass of $m_d = 306.2$ g. The total mass of the oscillating system was $m = 813.2$ g, resulting in a mass ratio of $m^* = 2.66$. The natural frequency of the system was determined to be $f_{na} = 0.874$ Hz in air and $f_{nw} = 0.740$ Hz in water. The structural damping ratio was $\zeta = 2.74 \times 10^{-3}$, resulting in a mass-damping ratio of $m^*\zeta = 7.28 \times 10^{-3}$.

The dynamic response of free vibration was investigated over a reduced velocity range of $2.5 < U^* < 115$, corresponding to a flow velocity range of 0.056 m/s $< U_\infty < 0.287$ m/s and a Reynolds number range of $1450 < Re < 7500$.

4.3.2 Dynamic response of free vibrations

For close comparison with a cylinder undergoing forced oscillations, the dynamic response of the cylinder undergoing free VIV is firstly obtained. The amplitude and frequency responses of the cylinder with $m^* = 2.66$ and $\zeta = 2.74 \times 10^{-3}$ are shown in Figure 4.5, compared with the previous case of $m^* = 2.4$ and $\zeta = 2.43 \times 10^{-3}$. As expected the response results of case $m^* = 2.66$ closely match the case of $m^* = 2.4$ in terms of the initial and lower branches of A_{\max}^* and A_{10}^* responses, the frequency response and the lock-in region. The major difference between these two cases is the amplitude magnitude of the upper branch, due to the difference in Reynolds number. The effect of Reynolds number on VIV of a circular cylinder has been well discussed by Klamo *et al.* (2006); however, it is not a major focus of the investigation in this thesis. The A_{\max}^* peak of the present case $m^* = 2.66$ observed is $A_{\max}^* = 0.88$, 12% less than that ($A_{\max}^* = 1.0$) of the case $m^* = 2.4$, and the A_{10}^* peak of case $m^* = 2.66$ is $A_{10}^* = 0.84$, 11% less than that ($A_{10}^* = 0.94$) of the case $m^* = 2.4$. Additionally, it can also be seen in Figure 4.6 that the measured forces and phases of the case at $m^* = 2.66$ closely match those of the case at $m^* = 2.4$, including general profiles of the lift and vortex forces, and two jumps in the total and vortex force phases.

4.3.3 Comparison between free and forced vibrations

To compare the free and forced vibrations, the amplitude response of the free vibration is plotted firstly in an amplitude-wavelength plane with an overlay on the Morse & Williamson map of the wake regimes of a cylinder undergoing sinusoidal forced oscillations, as shown in Figure 4.7. For the convenience of comparison, the wavelength of free vibration is given by $\lambda^* = U^*/f^*$, where f^* is the normalised dominant oscillation frequency (*i.e.* in the lock-in region as shown in Figure 4.8 (b) – (d)) or the component close to unity if there are multiple frequencies (*i.e.* at low reduced velocities as shown in Figure 4.8 (a)). The red bull’s-eye symbols in Figure 4.7 represent the four different locations (one in the initial branch, two in the upper branch, and one in the lower branch) where comparisons between free and forced vibrations were investigated. These locations were chosen to examine across the typical wake mode regimes of free vibration.

The first comparison location was conducted at $\lambda^* = 4.33$, corresponding to $U^* = 4.19$ and $f^* = 0.968$ in the initial branch of free vibration. Figure 4.9 shows the time traces of the free vibration and tracking motion of the cylinder, the total lift force, the vortex force, and the corresponding phases. As shown in Figure 4.9 (a), the free cylinder undergoes quasi-periodic oscillations with unstable amplitudes dominated by the vortex shedding frequency ($f^* = 0.809$) and a relatively weaker component ($f^* = 0.968$) close to the natural frequency of the system shown in Figure 4.8 (a). This quasi-periodic motion response is consistent with the literature and the previous

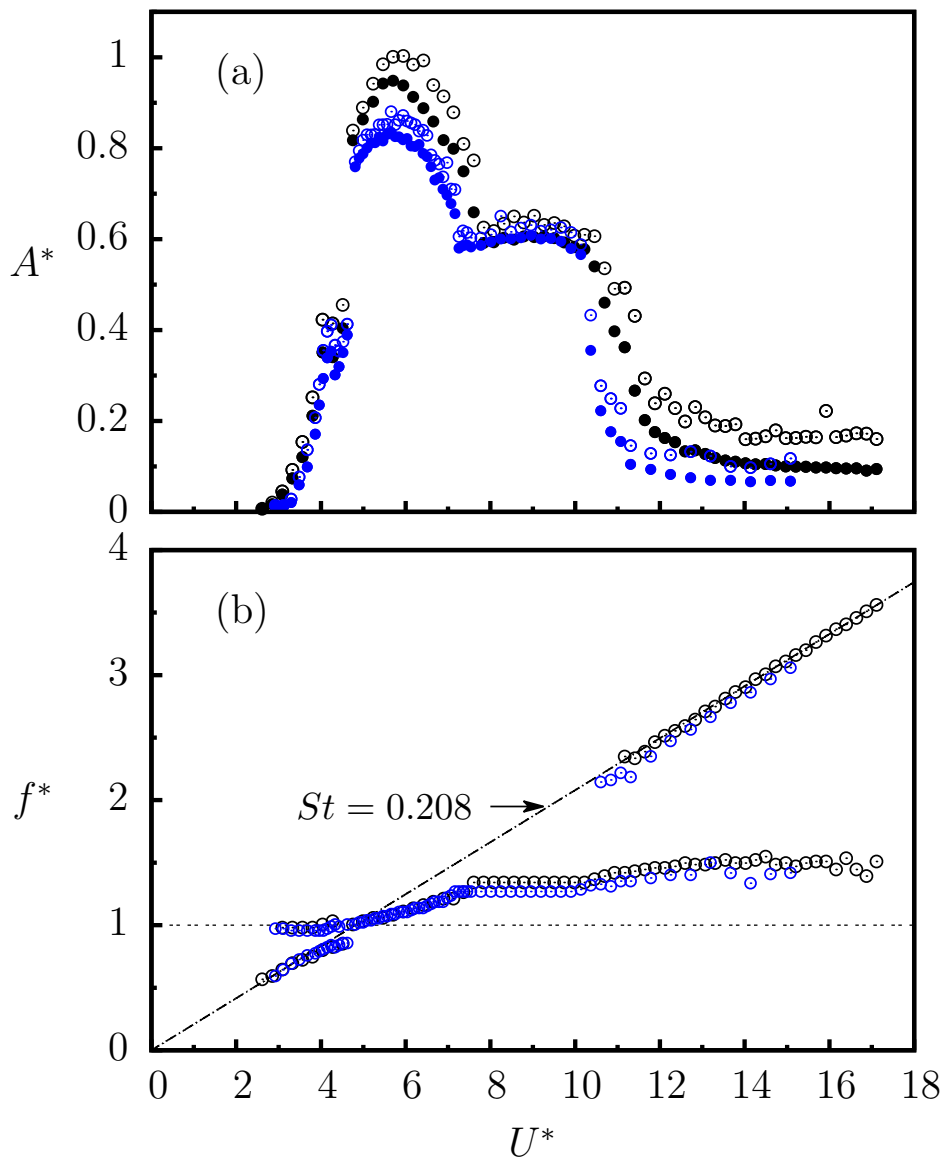


FIGURE 4.5: Plots of the amplitude and frequency responses of freely vibrating circular cylinders. The black open and solid circles represent the A_{\max}^* and A_{10}^* values, respectively, of a cylinder with $D = 40$ mm ($m^* = 2.40$ and $\zeta = 2.43 \times 10^{-3}$), while the blue open and solid circles represent the A_{\max}^* and A_{10}^* values, respectively, of a cylinder with $D = 25$ mm ($m^* = 2.66$ and $\zeta = 2.74 \times 10^{-3}$).

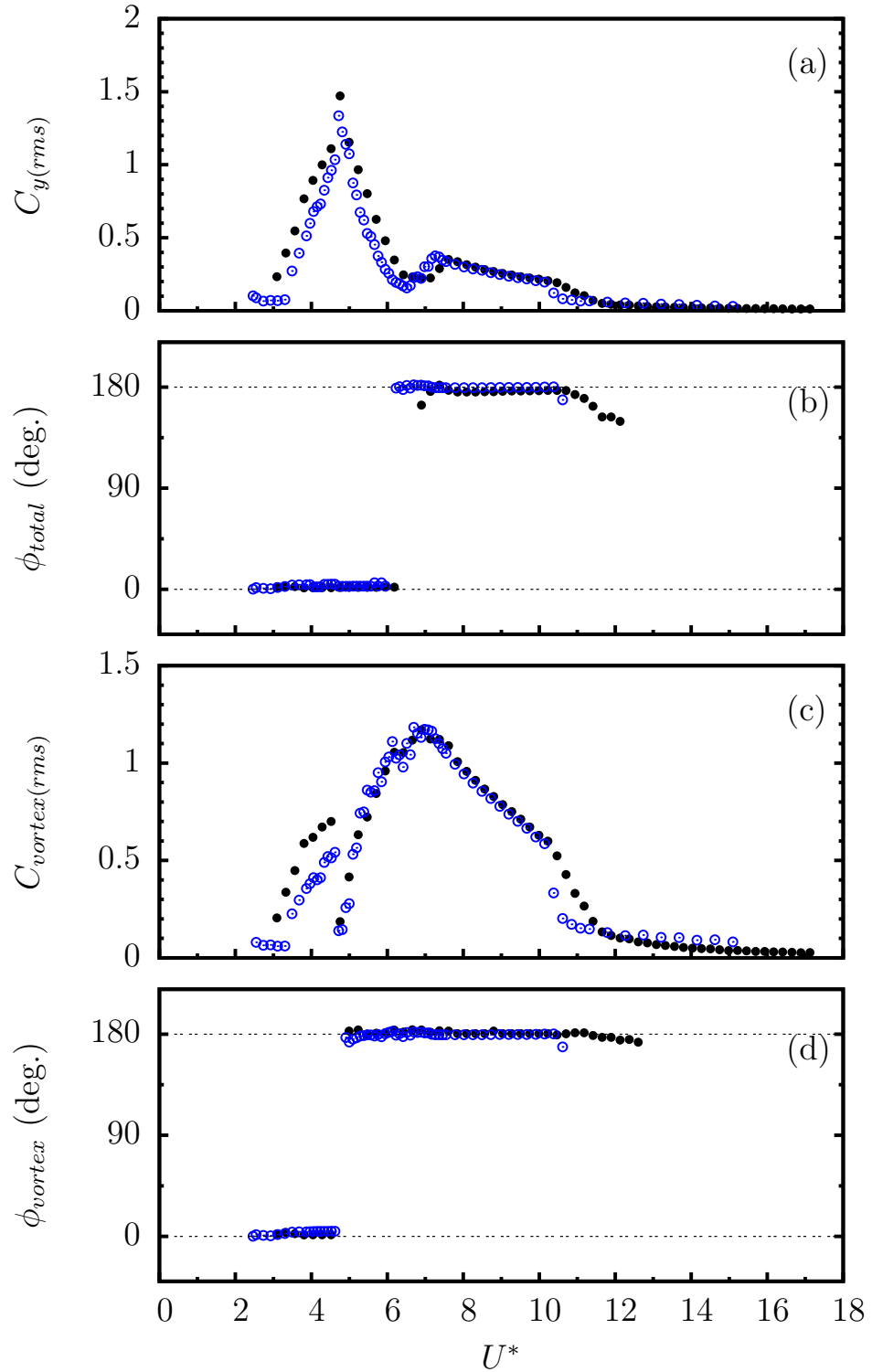


FIGURE 4.6: Force and phase angle variation with the reduced velocity: (a) the total transverse lift coefficient (root-mean-square), (b) the total phase, (c) the vortex force coefficient (root-mean-square), and (d) the vortex phase. The black solid circles represent the results of a cylinder with $m^* = 2.40$ and $\zeta = 2.43 \times 10^{-3}$ ($D = 40$ mm), blue open circular represent the results of a cylinder with $m^* = 2.66$ and $\zeta = 2.74 \times 10^{-3}$ ($D = 25$ mm).

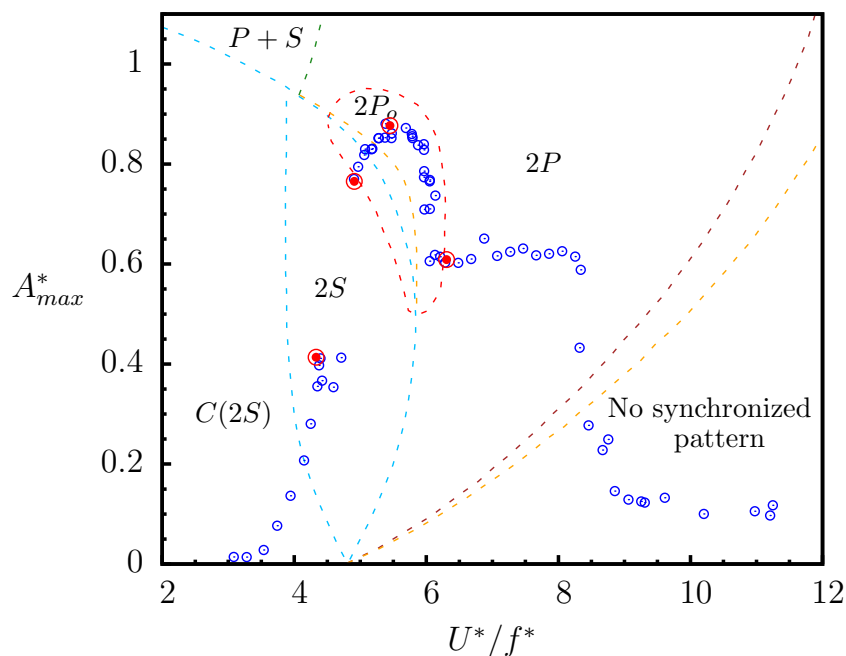


FIGURE 4.7: Plot of the amplitude response of a freely-vibrating circular cylinder with $m^* = 2.66$, with an overlay of the map of the wake regimes by Morse & Williamson (2009a). The open circles represent the maximum amplitude at each normalised wavelength value of $\lambda^* = U^*/f^*$, where f^* is the normalised frequency close to the natural frequency of the system. The red bull's-eye symbols represent the locations where forced-vibration experiments are conducted for comparison. The boundaries between the wake modes of Morse & Williamson are dictated by the dashed lines.

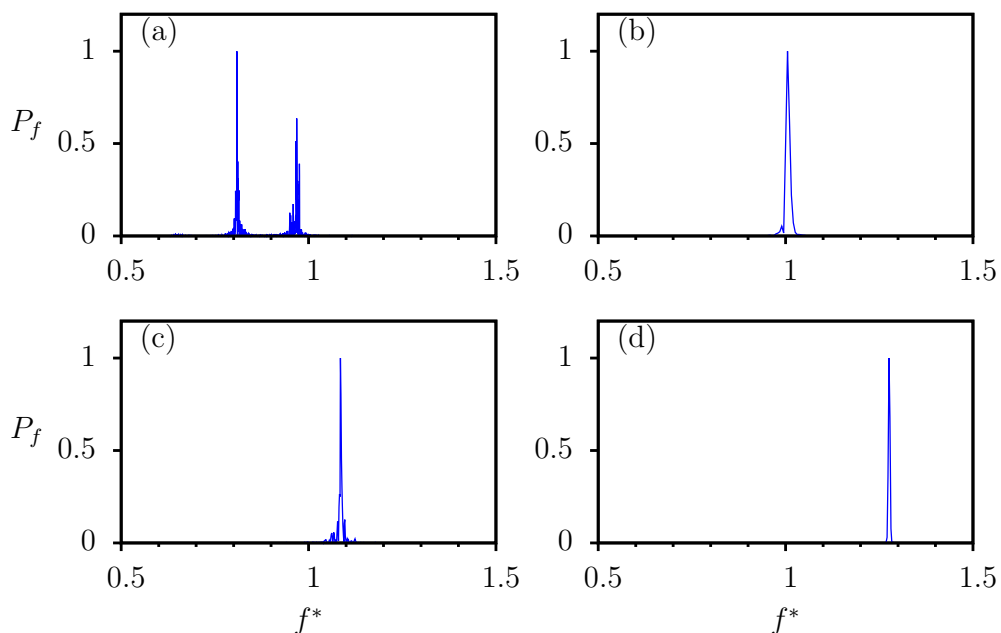


FIGURE 4.8: Normalised power spectra of the cylinder displacement response at $m^* = 2.66$ for the four comparison locations: (a) $U^* = 4.19$ in the initial branch, (b) $U^* = 4.93$ in the upper branch, (c) $U^* = 5.91$ in the upper branch and (d) $U^* = 8.05$ in the lower branch.

4.3. Comparison of a free cylinder and a tracking cylinder

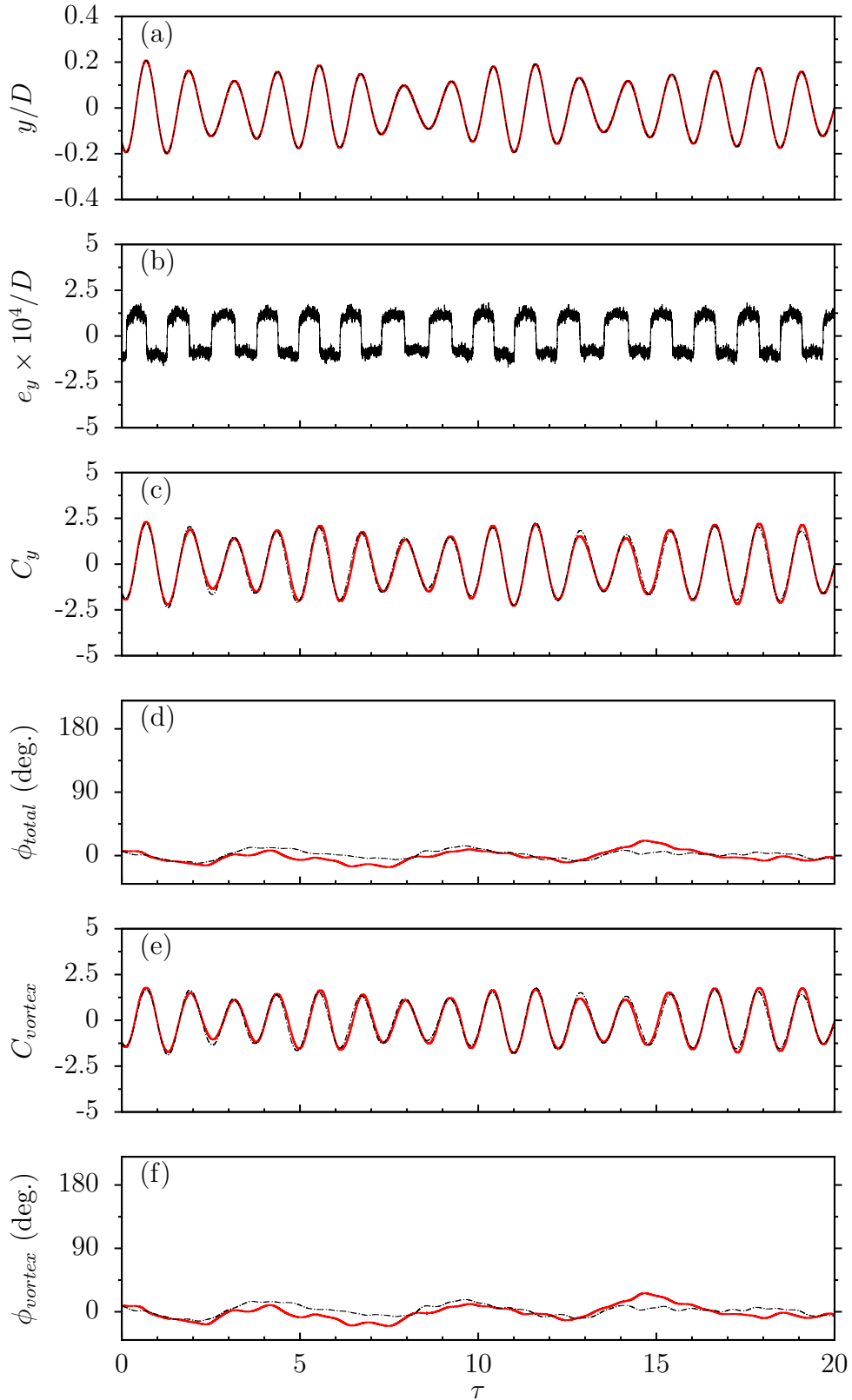


FIGURE 4.9: Time traces of the fluid forces and phases of free and tracking vibrations of a cylinder at $U^* = 4.09$ and $Re = 2030$: (a) the body motion, (b) the position tracking errors, e_y , (c) the transverse lift coefficient, (d) the total phase, (e) the vortex force coefficient, and (f) the vortex phase. The black dot-dashed lines represent the response of freely-vibrating cylinder and the solid red lines represent the response of the tracking cylinder.

results of the cylinder case at $m^* = 2.4$. Figure 4.9 (b) shows the position tracking errors of the cylinder driven by the motion control system. The errors are extremely low within $2 \times 10^{-4}D$ (corresponding to $5 \mu\text{m}$). As the experimental conditions, such as the flow speed and Reynolds number, are carefully matched, it is expected that the cylinder body in both free and tracking cases should experience the same fluid forces. Figure 4.9 (c) and (d) show that the total lift of the tracking cylinder are consistent with the free vibration case, while the total phases of the two cases are also in good agreement, remaining $\phi_{total} \approx 0^\circ$ despite slight fluctuations. Further the vortex forces in Figure 4.9 (e) also show remarkable match between the two cases. As implied by the vortex phases of $\phi_{vortex} \approx 0^\circ$ in Figure 4.9 (e), $2S$ wake modes are present in both free and tracking cases. Figure 4.10 shows the phase-band averaged results of PIV measurements which are triggered by the Q4 Controller Board at the same timing locations. Although the quasi-periodic oscillations with unstable amplitudes make it fairly difficult to capture sufficient PIV images for each phase, the phase-averaged results of the two cases in Figure 4.10 still clearly show the same $2S$ mode configured in a single-row pattern with the vortices of opposite signs being shed alternatively along the centerline of the downstream. In particular, the distribution of the vortices of the two case are remarkably matched. This $2S$ mode response is consistent with the $2S$ regime in the Morse & Williamson map.

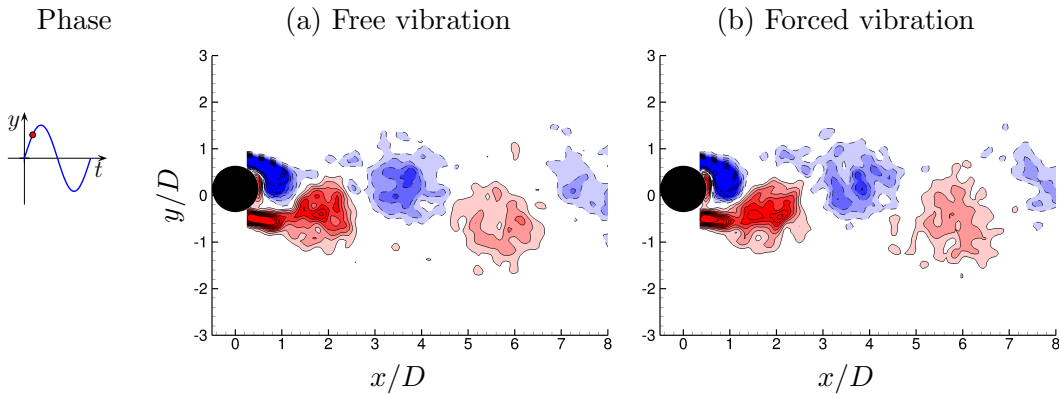


FIGURE 4.10: Phase-averaged PIV results showing the presence of $2S$ wake mode for both a freely vibrating cylinder at $U^* = 4.19$, and a tracking cylinder at $\lambda^* = 4.33$. The Reynolds number of both cases is $Re = 2030$. The dashed iso-lines (filled blue) represent clockwise (negative) vorticity, and the solid iso-lines (filled red) represent counter-clockwise (positive) vorticity.

The second comparison location is conducted at $\lambda = 4.91$, corresponding to $U^* = 4.93$ and $f^* = 1$ at the beginning of the upper branch of free vibration. At this reduced velocity the frequency spectrum in Figure 4.8 (b) shows the body oscillation frequency matches the natural frequency of the system ($f^* = 1$), indicating the onset of lock-in. Figure 4.11 shows the time traces of the forces and phases of both free and tracking cases. The oscillation amplitudes, shown in Figure 4.11 (a), become much larger and more stable than in the initial branch. The time traces in Figure 4.11 (a)-(e) show that the total lift, the vortex and the corresponding phases of both the free and tracking cases are well matched. The results of $\phi_{total} \approx 0^\circ$ and $\phi_{vortex} \approx 0^\circ$ suggest the presence of $2S$ mode at this flow speed for the two cases. The phase-averaged results of the vorticity fields in Figure 4.12 shows both the free and tracking cases experiences the same $2S$ mode organised in a double-row configuration. In particular, the flow structures in

4.3. Comparison of a free cylinder and a tracking cylinder

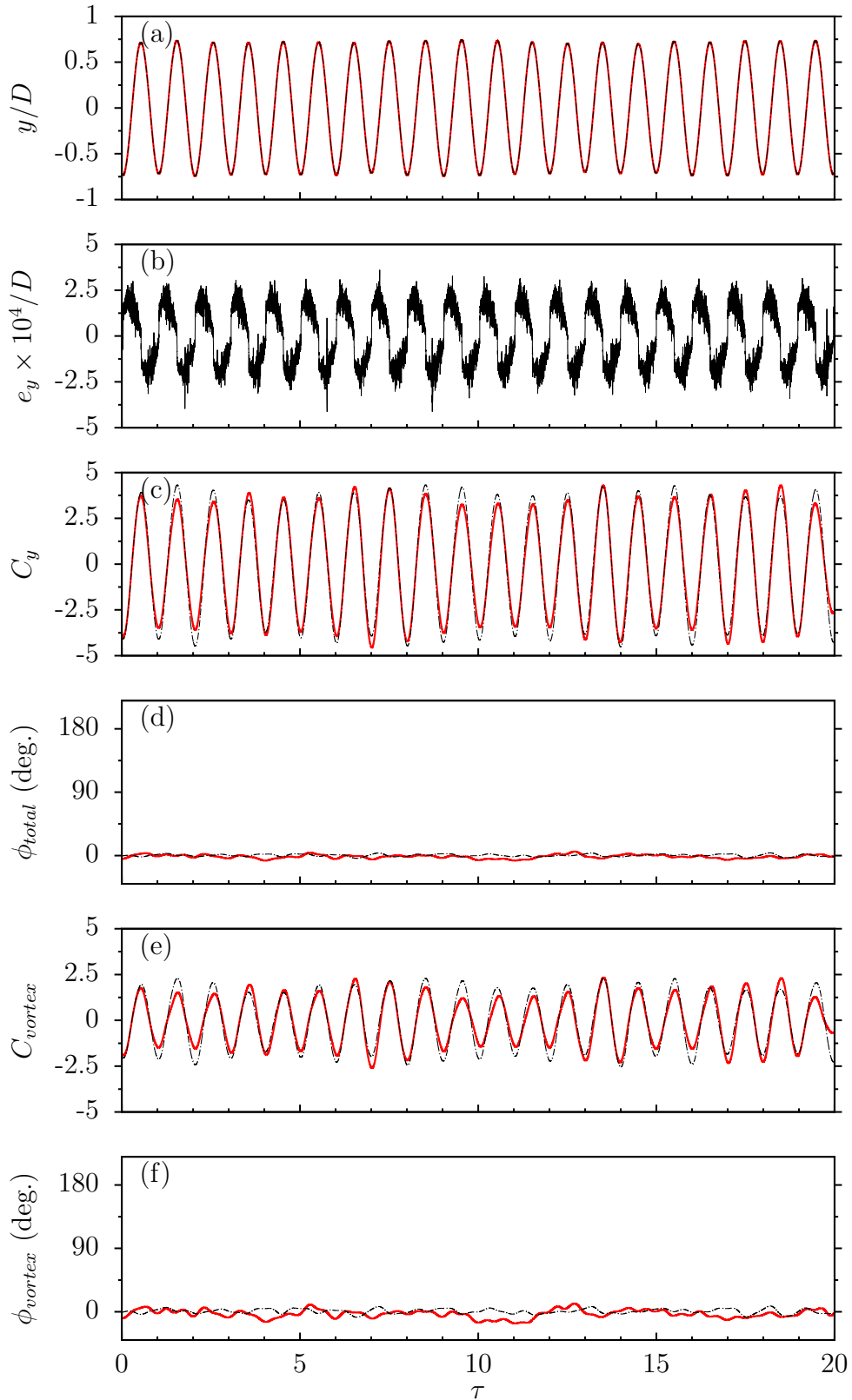


FIGURE 4.11: Time traces of the fluid forces and phases of free and tracking cylinders at $U^* = 4.93$ and $Re = 2330$: (a) the body motion, (b) the position tracking errors, e_y , (c) the transverse lift coefficient, (d) the total phase, (e) the vortex force coefficient, and (f) the vortex phase. The black dot-dashed lines represent the response of freely-vibrating cylinder and the solid red lines represent the response of the tracking cylinder.

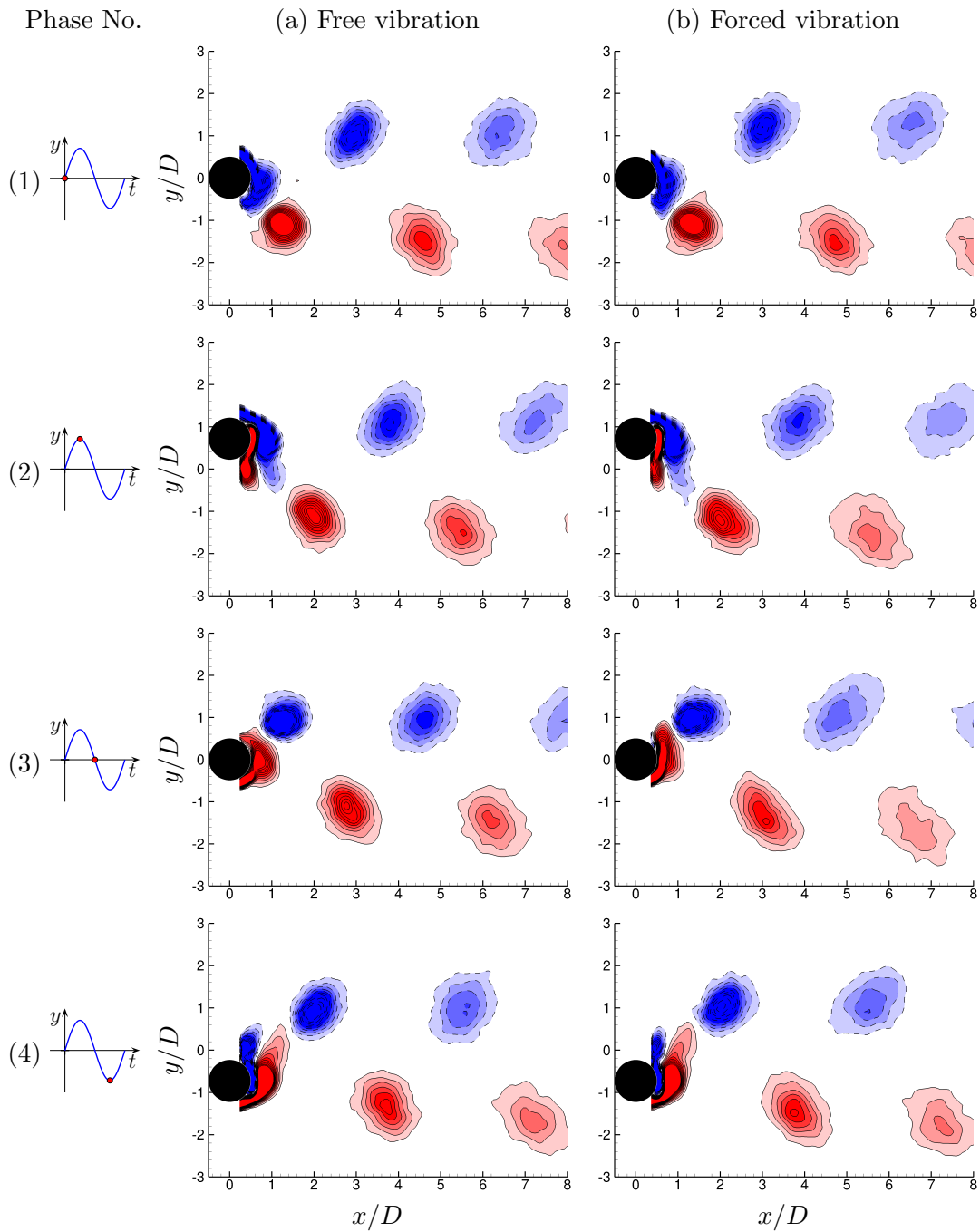


FIGURE 4.12: Phase-averaged PIV results showing the presence of $2S$ wake mode for both a freely vibrating cylinder at $U^* = 4.93$, and a sinusoidally forced-oscillating cylinder at $\lambda^* = 4.91$. The Reynolds number of both cases is $Re = 2390$. Four phases are shown over one oscillation cycle. The dashed iso-lines (filled blue) represent clockwise (negative) vorticity, and the solid iso-lines (filled red) represent counter-clockwise (positive) vorticity.

4.3. Comparison of a free cylinder and a tracking cylinder

the very near wake of the two cases are remarkably matched in all the four phases presented here. It is interesting how well this observation of the $2S$ mode in the upper branch agrees well with the Morse & Williamson's map of a forced-oscillating cylinder. The previous study of Govardhan & Williamson (2000) proposed that a freely-vibrating cylinder with low- $m^*\zeta$ value experienced a wake mode transition from $2S$ to $2P$ which was associated with the amplitude response jump from the initial to the upper branch, as the oscillation frequency passed through the natural frequency of the system in water. However, the present results suggest that the jump in the amplitude response from the initial to the upper branch in free vibration does not necessarily correspond to a wake mode transition from $2S$ to $2P$ mode. More evidence supporting this finding will be presented later.

As the cylinder displacement and the transverse lift force in the lock-in region are often approximated by sinusoidal functions (see Khalak & Williamson 1999; Govardhan & Williamson 2000; Morse & Williamson 2006, 2009b), it is of significant interest to investigate the cylinder undergoing sinusoidal forced oscillations under the same flow conditions. For this purpose, the forced oscillation amplitude is set to $A_o^* = A_{10}^* = 0.745$, while the oscillation frequency is set to $f_e = f \cong f_{nw} = 0.74 \text{ Hz}$ (or $f_e/f_{St} = 1.02$), where A_{10}^* is the top 10 percent of the amplitude response and f is the dominant frequency of the free vibration case. Figure 4.13 shows the time traces of the cylinder displacement, the total lift, the vortex force and the corresponding phases. The magnitude of the total lift measured is $C_Y = \max(C_y) = 4.0$ which agrees well with the C_Y contour levels of Morse & Williamson (2009a) shown in Figure 2.19 (a). The total phase, as shown in Figure 4.13 (c), remains at $\phi_{total} \approx 0^\circ$. Figure 4.13 (e) and (f) show the vortex force and the vortex phase, respectively. Compared to the previous tracking case, the vortex force loses its periodicity, as evidenced by the vortex phase intermittently switching between around $\phi_{vortex} = 0^\circ$ and 180° in Figure 4.13 (f). Morse & Williamson (2009a) found that this intermittent switching behaviour corresponds to the wake mode switching between $2S$ and $2P_o$, which is also confirmed by the present vorticity field measurements shown in Figure 4.14. The instantaneous PIV snapshots of $2S$ and $2P_o$ modes are sorted based on the instantaneous vortex phase values. The vortices of the $2S$ mode in Figure 4.14 (a) are organised in a parallel double-row pattern with a cross-flow spacing of approximately $2D$ between the positive and negative vortices. On the other hand, the vortices of the $2P$ mode in Figure 4.14 (b) spread slightly wider in the cross-flow direction than the $2S$ mode, and move with a slight oblique angle with respect to the centre line into the downstream. Additionally, the relatively weaker vortices of the vortex pairs dissipate quickly around $3D$ of the downstream. Compared to the free and tracking cases, the results of sinusoidal forced oscillations have shown that slight modulation in the cylinder motion can result in significant differences in fluid forces, phases and the wake modes.

The third comparison location is conducted at $\lambda^* = 5.45$, corresponding to $U^* = 5.91$ and $f^* = 1.085$ in the middle of the upper branch of free vibration where the free cylinder experiences largest-scale oscillations ($A_{\max}^* = 0.88$). Figure 4.15 shows time traces of the cylinder displacement, fluid forces and the phases of both the free and tracking cases. As expected, the total lift is in phase with the body displacement in free vibration, with $\phi_{total} \approx 0^\circ$ in Figure 4.15 (d). However, an important result is found in the vortex phase of the free case experiences intermittent switching between $\phi_{vortex} \approx 0^\circ$ and $\phi_{vortex} \approx 180^\circ$, as shown in Figure 4.15 (f). Although this behaviour has been observed in forced vibrations, it has not been reported in the previous studies of free vibration. Further, the phase-averaged vorticity fields in Figure 4.16 show that

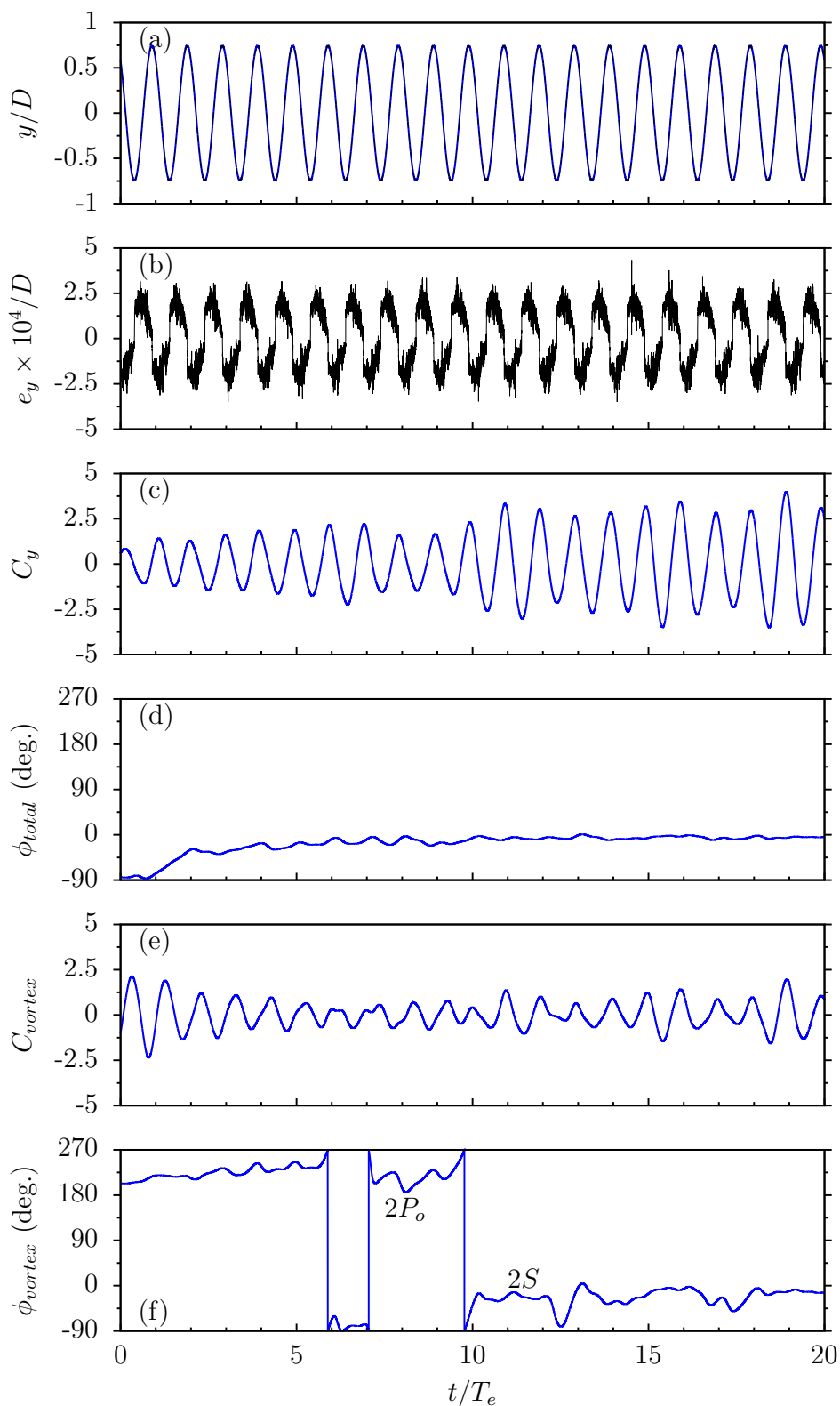


FIGURE 4.13: Time traces of the fluid forces and phases of a cylinder undergoing sinusoidal forced oscillations with $A_o^* = 0.745$ and $f_e/f_{St} = 1.02$ at $\lambda^* = U_\infty/(f_e D) = 4.90$ and $Re = 2390$: (a) the body motion, (b) the position tracking errors, e_y , (c) the transverse lift coefficient, (d) the total phase, (e) the vortex force coefficient, and (f) the vortex phase, suggesting the presence of both $2S$ and $2P_o$ modes. The black dot-dashed lines represent the position reference and the solid blue lines represent the response of the tracking cylinder. Note that $T_e = 1/f_e$ is the cylinder oscillation period.

4.3. Comparison of a free cylinder and a tracking cylinder

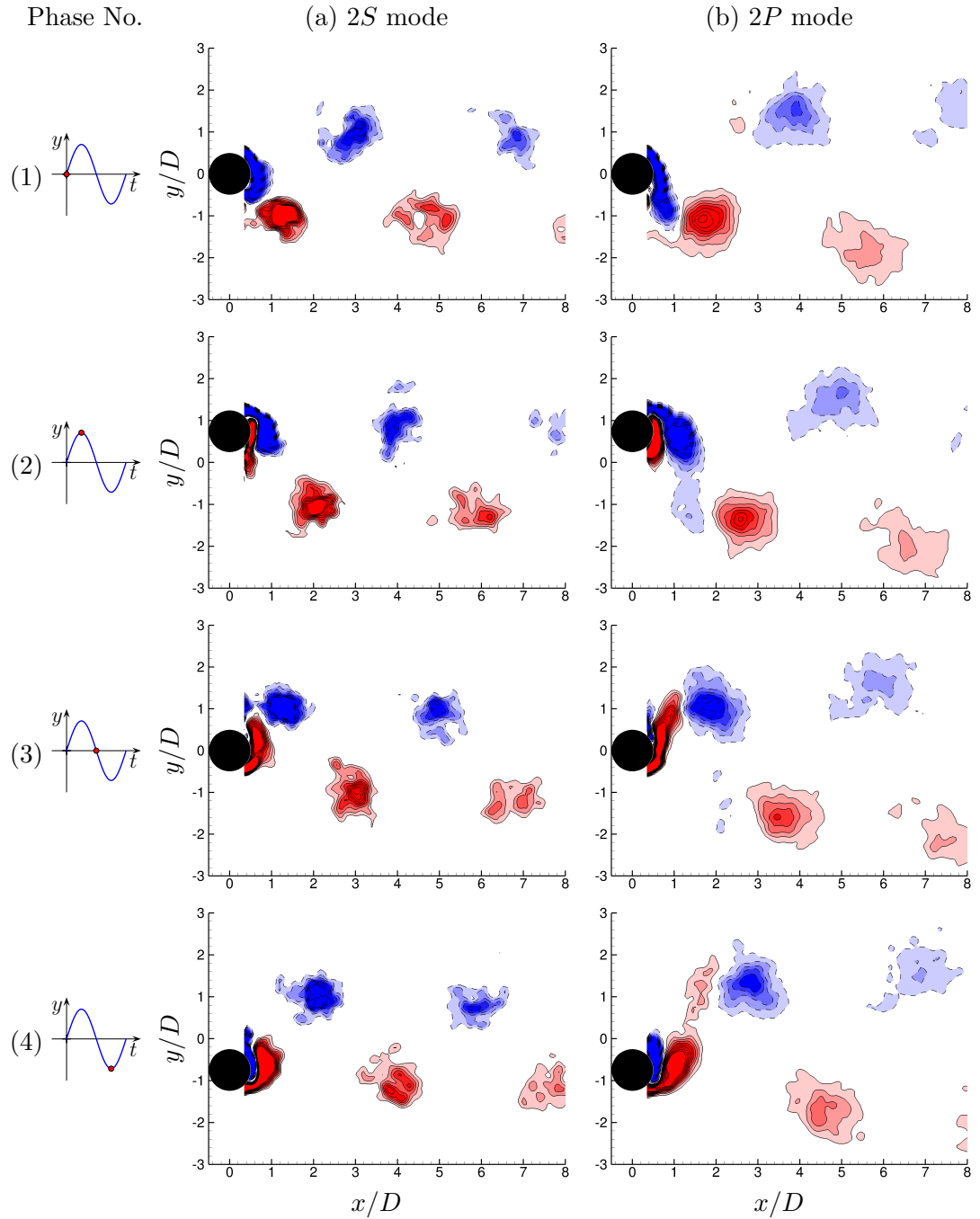


FIGURE 4.14: Phase-averaged PIV results showing that $2S$ and $2P_o$ modes co-exist in sinusoidal forced oscillation of a cylinder with $A_o^* = 0.745$ and $f_e/f_{St} = 1.02$ at $\lambda^* = 4.90$. The Reynolds number is $Re = 2390$. Four phases are shown over one oscillation cycle. The dashed iso-lines (filled blue) represent clockwise (negative) vorticity, and the solid iso-lines (filled red) represent counter-clockwise (positive) vorticity.

both $2S$ and $2P_o$ wake modes, corresponding to the two modes of ϕ_{vortex} , co-exist in the middle of the upper branch of free vibration. This result is consistent with the $2S - 2P_o - 2P$ overlapping region of the Morse & Williamson map, and it also confirms that the $2S \leftrightarrow 2P$ wake mode transition in free vibration corresponds to a sharp jump of $0^\circ \leftrightarrow 180^\circ$ in the vortex force but does not necessarily correspond to the initial \leftrightarrow upper branch transition.

Of particular interest in this scenario is that the total lift response of the tracking case no longer matches that of the free case, which results in significant differences in the total phase, the decomposed vortex force and vortex phase, as shown in Figure 4.15 (c)–(f). The total lift of the tracking case in Figure 4.15 (c) is out of phase with that of the free vibration case. The magnitude and root-mean-square values of the lift measured in the tracking vibration are $C_Y = 2.66$ and $C_{y(r.m.s.)} = 1.33$, respectively, which are comparable to $C_Y = 2.56$ and $C_{y(r.m.s.)} = 1.23$ measured in the free vibration. However, as shown in Figure 4.15 (c), the vortex force in the tracking vibration is larger than the total force in magnitude, $C_V = 4.48$, due to a change in the timing of vortex shedding. Compared to the free vibration case, the vortex force is also more periodic, giving $C_V = 4.48$ and $C_{vortex(r.m.s.)} = 2.29$ considerably higher than $C_V = 1.40$ and $C_{vortex(r.m.s.)} = 0.37$ in the free vibration. However, the total and vortex phases of the tracking case are more complicated. Figure 4.15 (d) and (f) show that the total phase is fluctuating slightly around $\phi_{total} = 233^\circ$ and the vortex phase is fairly stable at $\phi_{vortex} \approx 207^\circ$. More different tracking vibration tests (each over 100 oscillation cycles), as shown in Figure 4.17, reveal that they undergo complicated switching phenomena, suggesting that the wake mode undergoes switching between three different modes: $2S$ mode where both ϕ_{total} and ϕ_{vortex} are around 0° , $2P_o$ mode where ϕ_{total} is around 0° and ϕ_{vortex} is around or above 180° , and $2P$ mode where both ϕ_{total} and ϕ_{vortex} are around or above 180° . The switching process between the phase modes is completed quickly within approximately two oscillation cycles. Further, the wake modes identified by the total and vortex phases are confirmed by the vorticity field measurements. Figure 4.18 shows that the resultant $2S$ mode in (a) and $2P_o$ mode in (b). More phase-averaged $2P$ results are shown in Figure 4.19 (b1) and (b2), and the results of $2P_o$ mode are shown in (b3) and (b4) compared to the $2P_o$ of the free vibration case in (a). Although the ϕ_{total} and ϕ_{vortex} in the tracking vibration can switch simultaneously to around 0° , careful comparison still shows the instantaneous C_y and C_{vortex} do not match those of the free vibration case during in the zero-phase ranges, which indicates significant differences in the vortex strength between the two vibration cases.

Sinusoidal forced vibration under the same flow conditions was also investigated. The oscillation amplitude was set to $A_o^* = 0.823$ equal to the A_{10}^* value of the free vibration, and the oscillation frequency was set to the same of the free vibration, $f_e = f = 0.804$ Hz yielding $f^* = f/f_{nw} = 1.09$ and $f/f_{St} = 0.886$. Time traces of the response are shown in Figure 4.20. The total and vortex forces are fairly periodic. Compared to the free and tracking vibrations, the total lift measured over 200 oscillation cycles has a similar magnitude of $C_Y = 2.72$, but a much higher root-mean-square value of $C_{y(r.m.s.)} = 1.69$ showing that the fluid force is more periodic than the other two cases. The vortex force, on the other hand, also has a similar magnitude of $C_V = 4.1$, but has a higher root-mean-square value of $C_{vortex(r.m.s.)} = 2.67$. Both the total and vortex phases are constantly at $\phi_{total} \approx 236^\circ$ and $\phi_{vortex} \approx 211^\circ$, respectively, which agree well with the results of Morse & Williamson (2009a) shown in Figure 2.20. Even though the cylinder is forced to oscillate sinusoidally at the dominant frequency and the A_{10}^* amplitude (approximately 6% less than $A_{max}^* = 0.877$) of the free vibration

4.3. Comparison of a free cylinder and a tracking cylinder

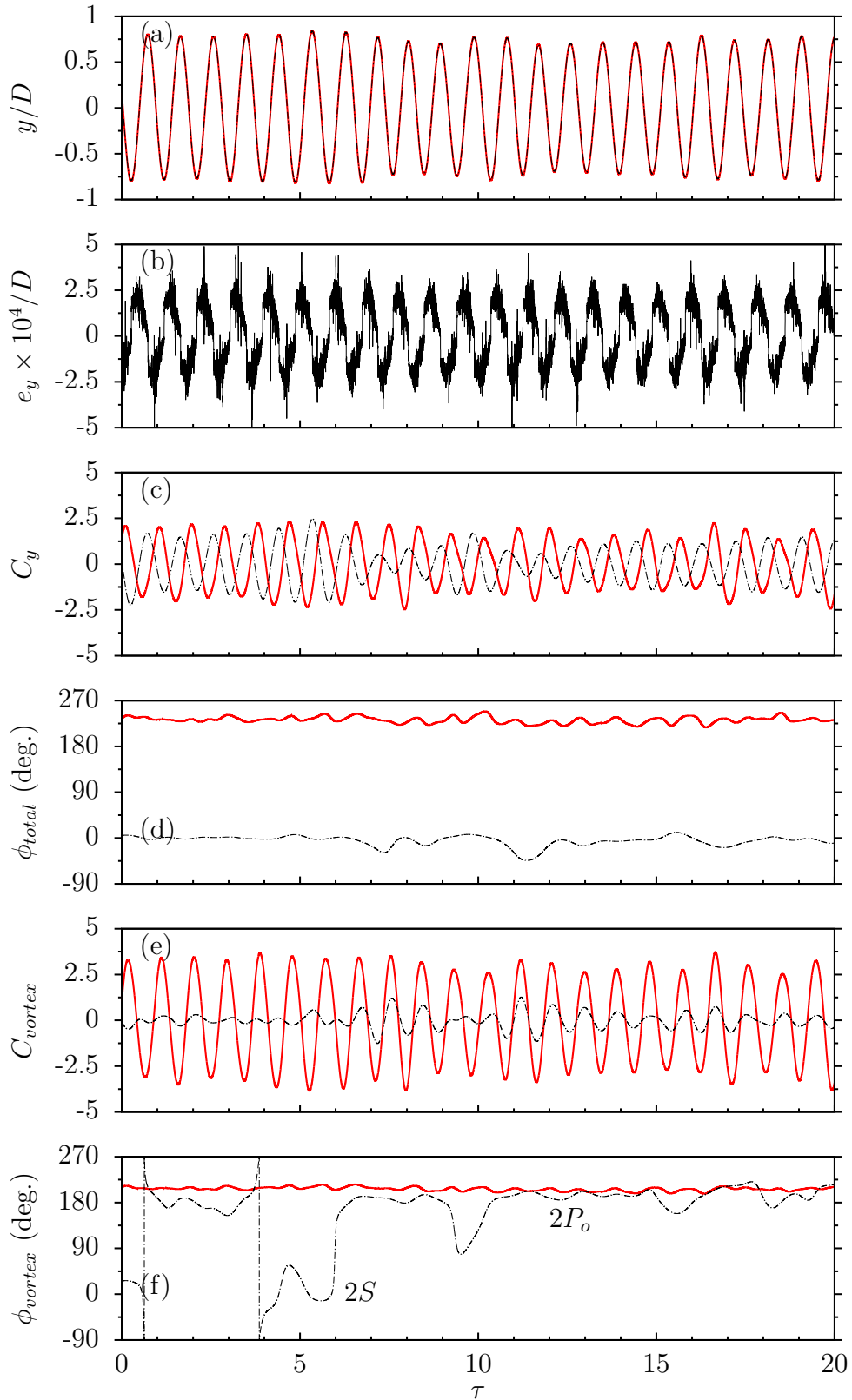


FIGURE 4.15: Time traces of the fluid forces and phases of free and tracking vibrations of a cylinder at $U^* = 5.91$ and $Re = 2860$: (a) the body motion, (b) the position tracking errors, e_y , (c) the transverse lift coefficient, (d) the total phase, (e) the vortex force coefficient, and (f) the vortex phase. The black dot-dashed lines represent the response of freely-vibrating cylinder and the solid red lines represent the response of the tracking cylinder.

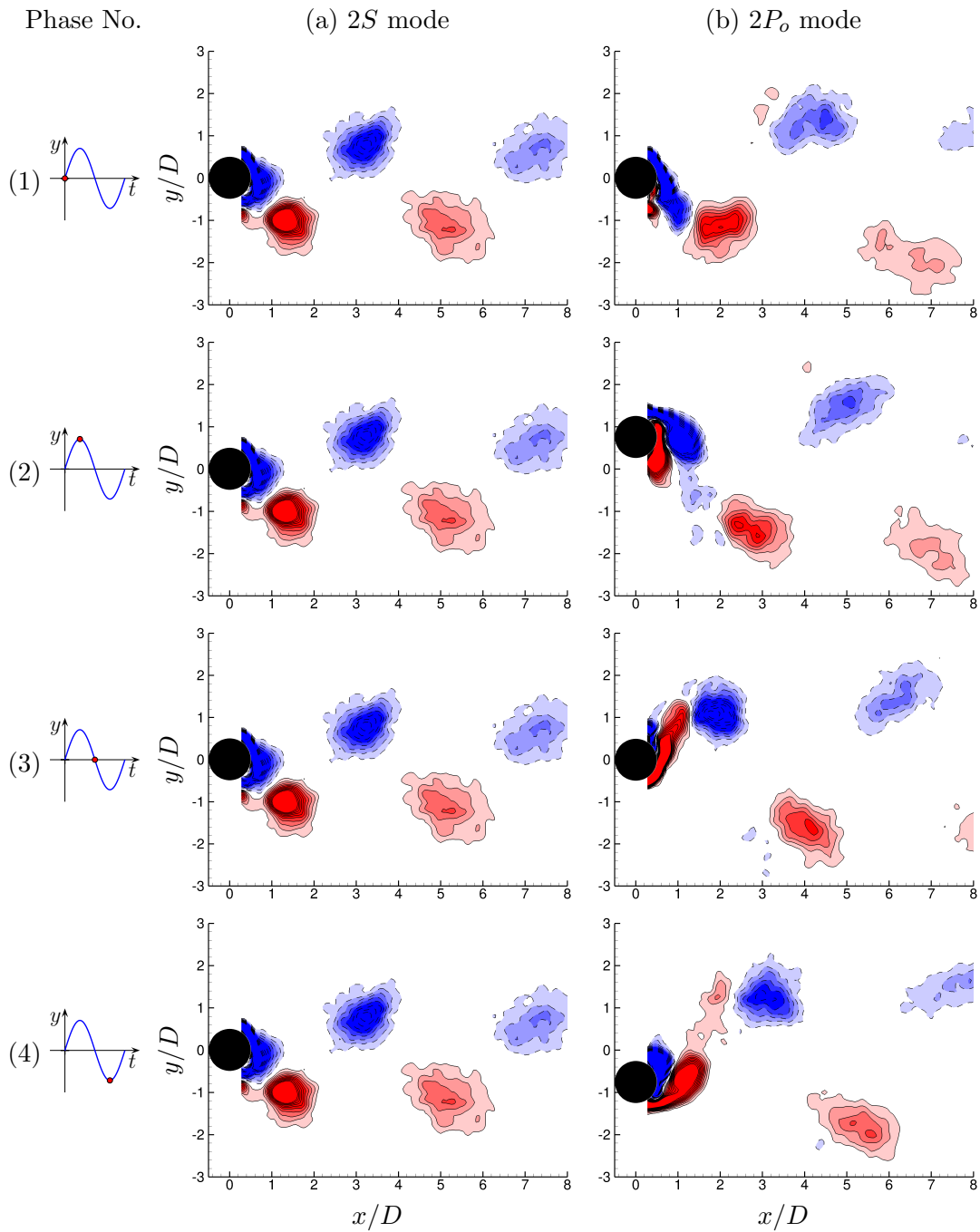


FIGURE 4.16: Phase-averaged PIV results showing both $2S$ and $2P_o$ wake modes co-exist at $U^* = 5.91$ in the middle of the upper branch of free vibration. The Reynolds number is $Re = 2860$. Four phases are shown over one oscillation cycle. The dashed iso-lines (filled blue) represent clockwise (negative) vorticity, and the solid iso-lines (filled red) represent counter-clockwise (positive) vorticity.

4.3. Comparison of a free cylinder and a tracking cylinder

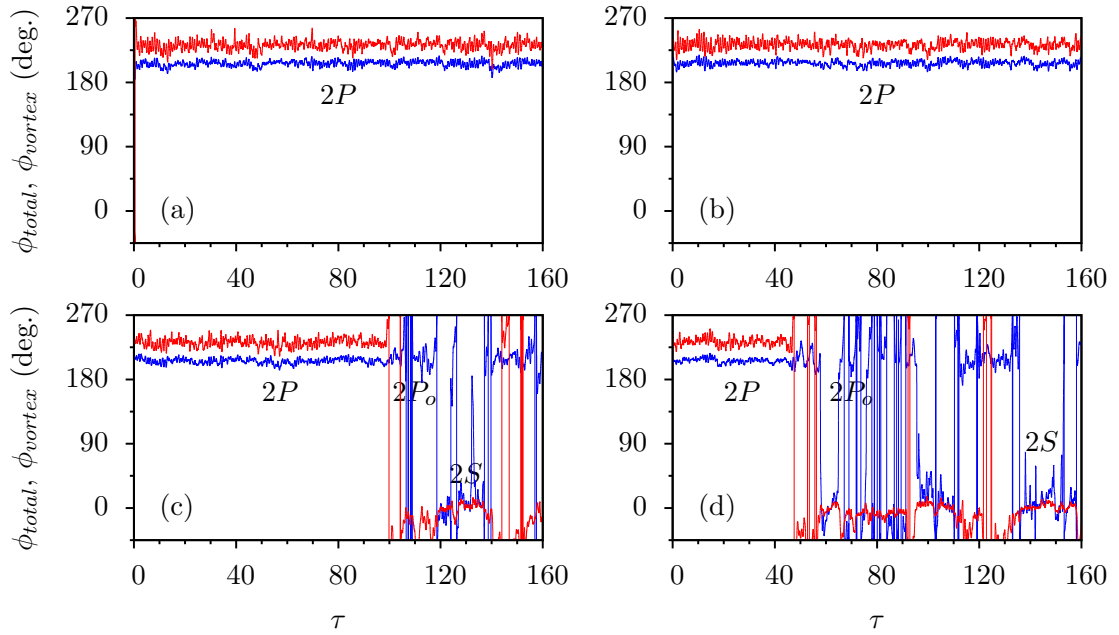


FIGURE 4.17: Time traces of the total phase and vortex phase of tracking vibration of a cylinder at $\lambda^* = 5.45$ in four different experimental tests. The total phase, ϕ_{total} , is represented by the red lines, while the vortex phase, ϕ_{vortex} , is represented by the blue lines. The $\phi_{total} \approx 233^\circ$ and $\phi_{vortex} \approx 207^\circ$ are clearly above 180° in the test (a) and (b), suggesting only $2P$ wake mode is present; while both the ϕ_{total} and ϕ_{vortex} experience complicated switching phenomena in (c) and (d), suggesting the presence of three wake modes, $2S$, $2P_o$, and $2P$ modes.

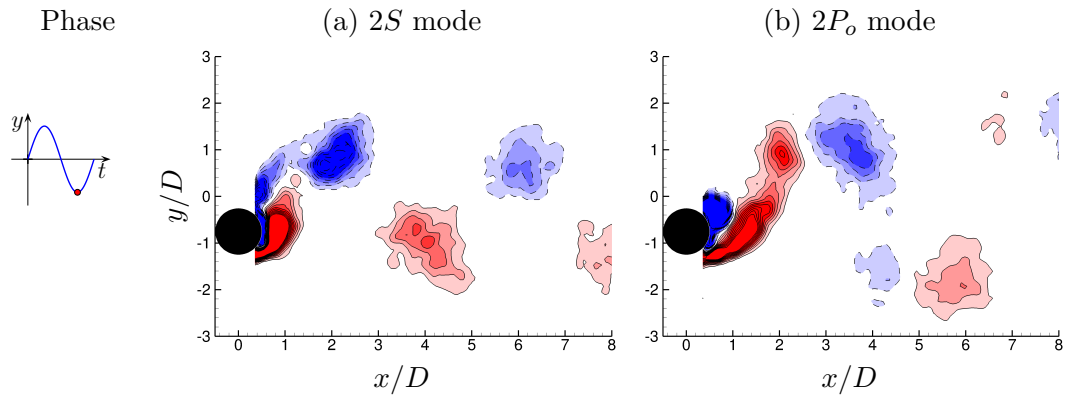


FIGURE 4.18: Phase-averaged PIV results showing that both $2S$ and $2P$ wake modes co-exist in tracking forced vibration of a cylinder at $\lambda^* = 5.45$. The Reynolds number is $Re = 2860$. The dashed iso-lines (filled blue) represent clockwise (negative) vorticity, and the solid iso-lines (filled red) represent counter-clockwise (positive) vorticity.

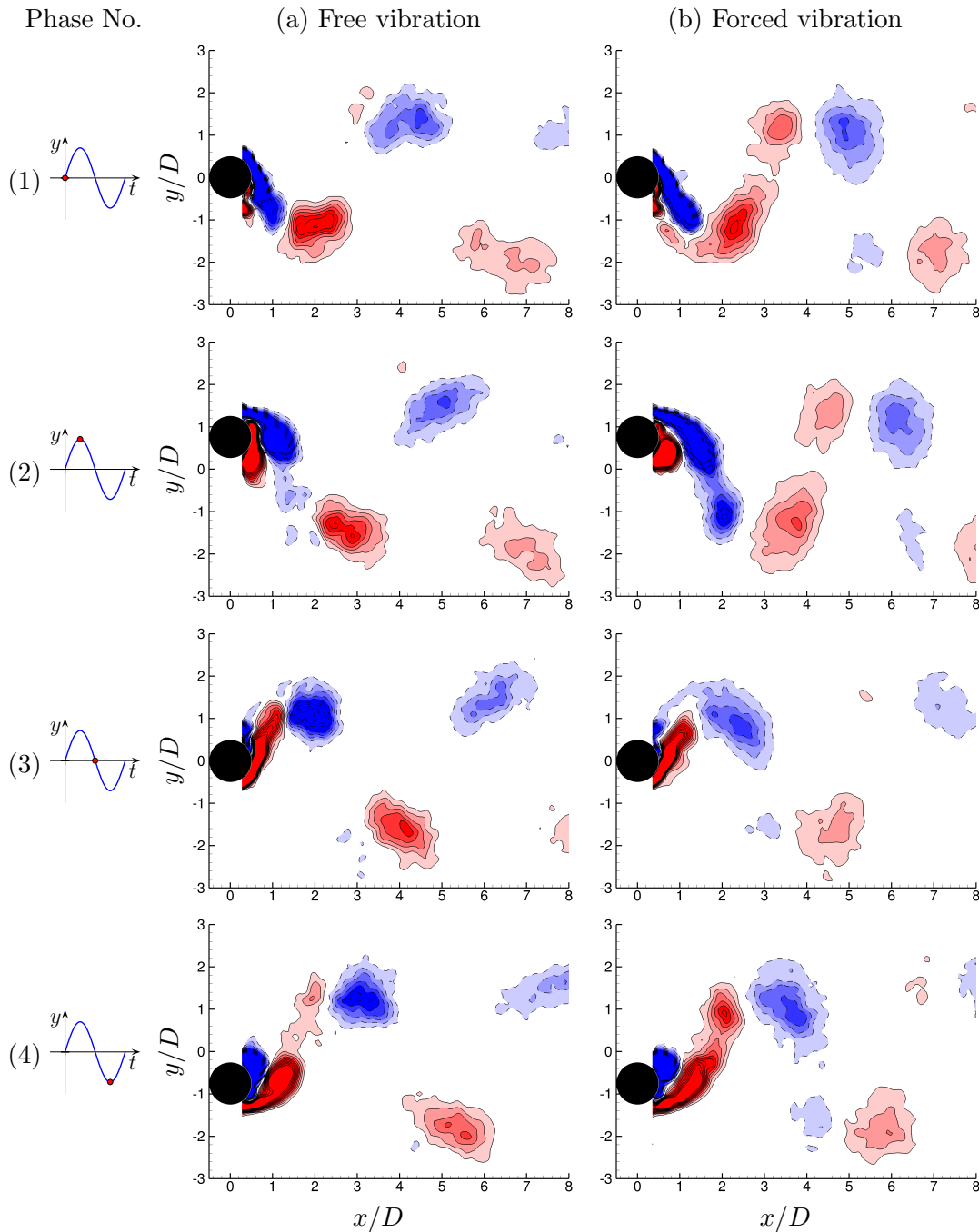


FIGURE 4.19: Phase-averaged vorticity fields of a freely vibrating cylinder with $m^* = 2.66$ at $U^* = 5.91$, and a tracking cylinders at $\lambda^* = 5.45$. The Reynolds number of both cases is $Re = 2860$. The wake mode for the cylinder in free vibration is $2P_o$ mode, while the cylinder in tracking vibration experiences the wake mode switching among $2S$ mode (not shown in this figure), $2P_o$ mode in (b3) and (b4), and $twop$ mode in (b1) and (b2). The dashed iso-lines (filled blue) represent clockwise (negative) vorticity, and the solid iso-lines (filled red) represent counter-clockwise (positive) vorticity.

case, the resultant phases are clearly above 180° , indicating that the energy transfer is negative from the structure to the fluid. The vorticity fields in Figure 4.21 show that the wake mode is $2P$ in sinusoidal forced vibration, with the secondary vortex in each pair much stronger than that of the $2P_o$ in free vibration.

The fourth comparison location was conducted at $\lambda = 6.31$, corresponding to $U^* = 8.05$ and $f^* = 1.276$ in the lower branch of free vibration. Figure 4.22 shows time traces of the dynamic responses of both the free and tracking vibrations. As expected, the vibration of the free body is highly periodic with very stable amplitudes of $A_{\max}^* \approx 0.61$ and a well-defined frequency of $f^* = 1.276$. Again, both the total and vortex forces of the vibration cases are also highly periodic and match each other remarkably well. The magnitude and root-mean-square values of C_y measured in the free vibration are $C_Y = 0.67$ and $C_{y(r.m.s.)} = 0.42$, closely matching $C_Y = 0.64$ and $C_{y(r.m.s.)} = 0.41$ measured in the tracking vibration. However, the total and vortex phases are both constantly at 180° with respect to the cylinder displacement. The vorticity fields in Figure 4.23 show that the wake mode of both two cases appear to be $2P$ mode. Since the previous comparison at $\lambda^* = 4.33$ shows the wake patterns of eight phases in the tracking vibration case are highly similar to the free vibration case, PIV measurements were conducted at only one phase for this flow velocity. Despite slight differences at the downstream location of $x/D \approx 6$, the vortex structures are highly similar in the very near wake of the body.

The dynamic response of the sinusoidal forced vibration is shown in Figure 4.24. The oscillation amplitude is $A_o^* = A_{10}^* = 0.584$ and the oscillation frequency is $f_e = 0.944$ Hz resulting in $f_e/f_{nw} = 1.276$ and $f_e/f_{St} = 0.766$. As expected, the forces are highly periodic. The magnitude and root-mean-square values of the total lift are $C_Y = 0.66$ and $C_{y(r.m.s.)} = 0.45$, respectively, which are consistent with the results of the free and tracking vibrations. On the other hand, the magnitude and root-mean-square values of the vortex force are $C_V = 1.68$ and $C_{vortex(r.m.s.)} = 1.17$, respectively, which are slight higher than the results of both the free and tracking vibrations. Additionally, the total and vortex phases are constantly at 180° throughout the tests. Correspondingly, the vorticity field measurements in Figure 4.25 show that the wake mode appears to be $2P$ in (b), with the vortex structures significantly similar to results of the free vibration case. The present results are consistent with the literature that the dynamic response in the lower branch of free vibration is represented well by sinusoidal functions (see Leontini 2007).

4.4 Summary of the chapter

This chapter has presented results of cross-flow VIV of circular cylinders with low mass and damping ratio. The experimental rigs and methodologies used have been validated by comparing with the literature. As part of the thesis, the dynamic responses of a cylinder undergoing free vibration have been compared to the cases of the cylinder undergoing precise tracking and sinusoidal vibrations under the same flow conditions.

The results of VIV of freely-vibrating cylinders are consistent with the previous studies. Three distinct amplitude response branches are observed, depending on the reduced velocity: the initial, the upper and lower branches. The body oscillations in the initial branch are characterised by quasi-periodic motion influenced primarily by the vortex shedding frequency and the natural frequency of the system. The amplitude response undergoes a jump to the upper branch at $U^* \approx 1/St$, as the oscillation frequency passes through the natural frequency of the system in water, indicating the

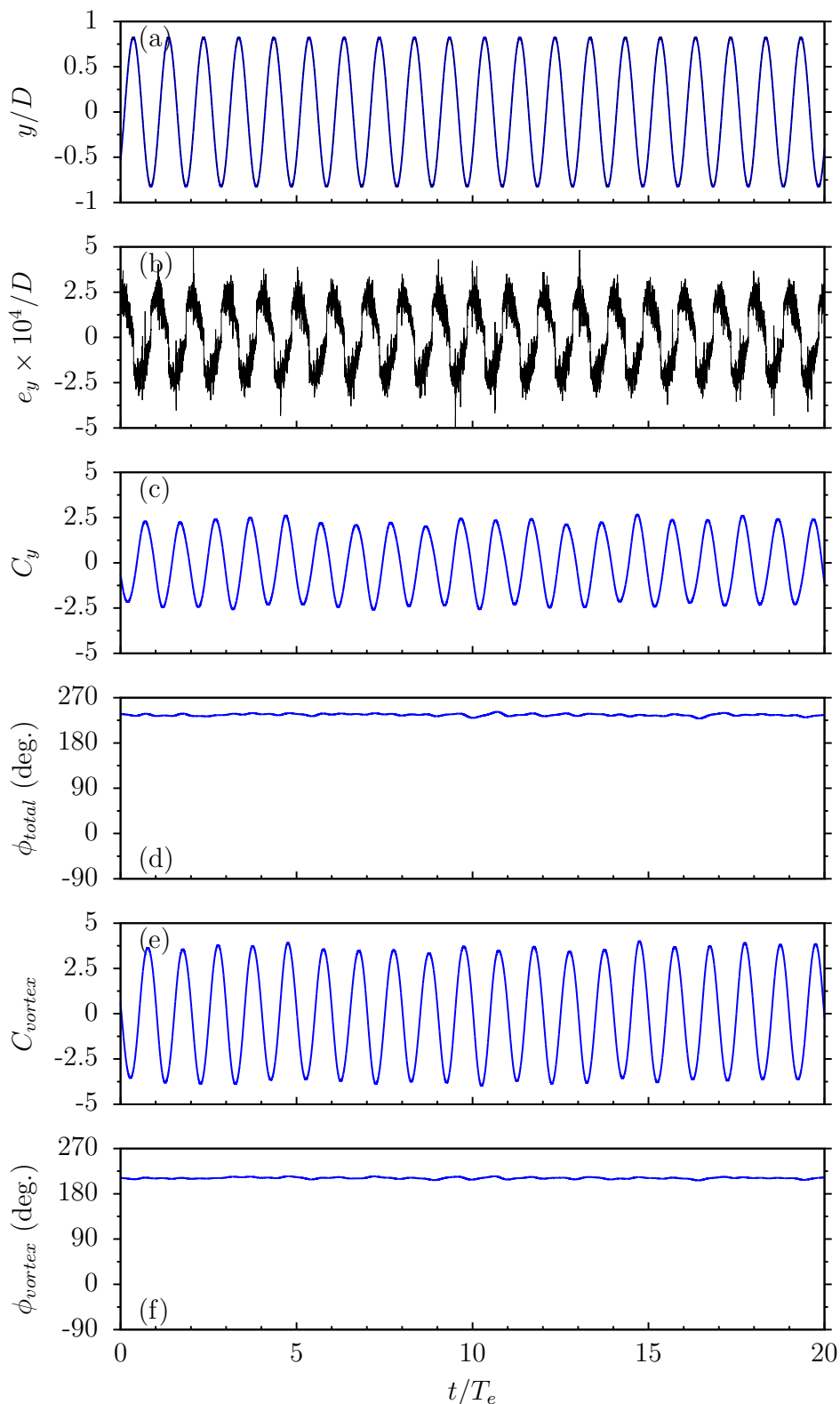


FIGURE 4.20: Time traces of the fluid forces and phases of a cylinder undergoing sinusoidal forced oscillations with $A^* = 0.823$, $f/f_{nw} = 1.09$ and $f_e/f_{St} = 0.886$ at $\lambda^* = U_\infty/(f_e D) = 5.45$ and $Re = 2860$: (a) the body motion, (b) the position tracking errors, e_y , (c) the transverse lift coefficient, (d) the total phase, (e) the vortex force coefficient, and (f) the vortex phase. The black dot-dashed lines represent the position reference and the solid blue lines represent the response of the tracking cylinder. Note that $T_e = 1/f_e$ is the cylinder oscillation period.

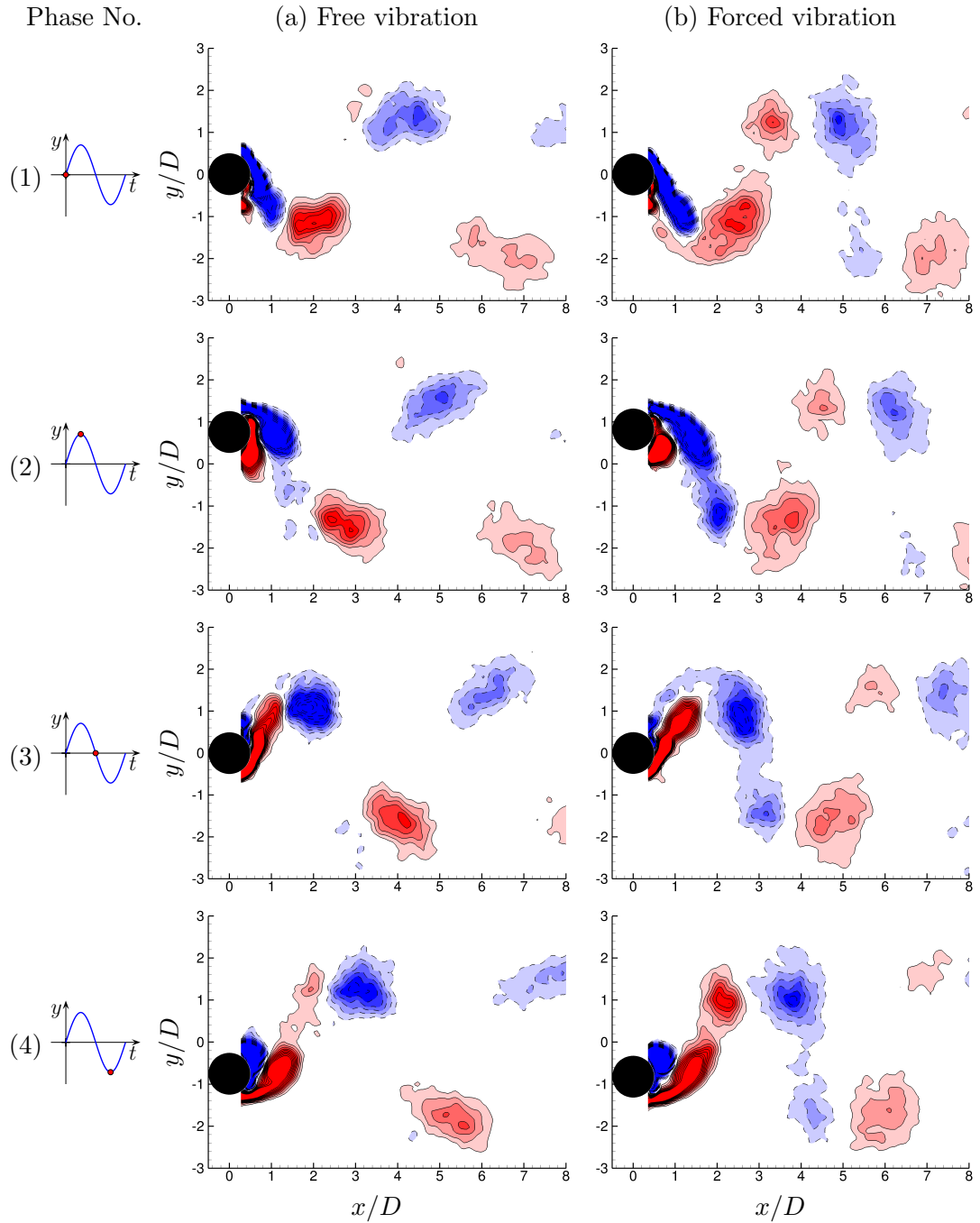


FIGURE 4.21: Phase-averaged PIV results showing the presence of *twopo* mode in free vibration of a cylinder with $m^* = 2.66$ at $U^* = 5.91$, and *twop* mode in sinusoidal forced vibration at $\lambda^* = 5.45$. The Reynolds number of both cases is $Re = 2860$. Four phases are shown over one oscillation cycle. The dashed iso-lines (filled blue) represent clockwise (negative) vorticity, and the solid iso-lines (filled red) represent counter-clockwise (positive) vorticity.

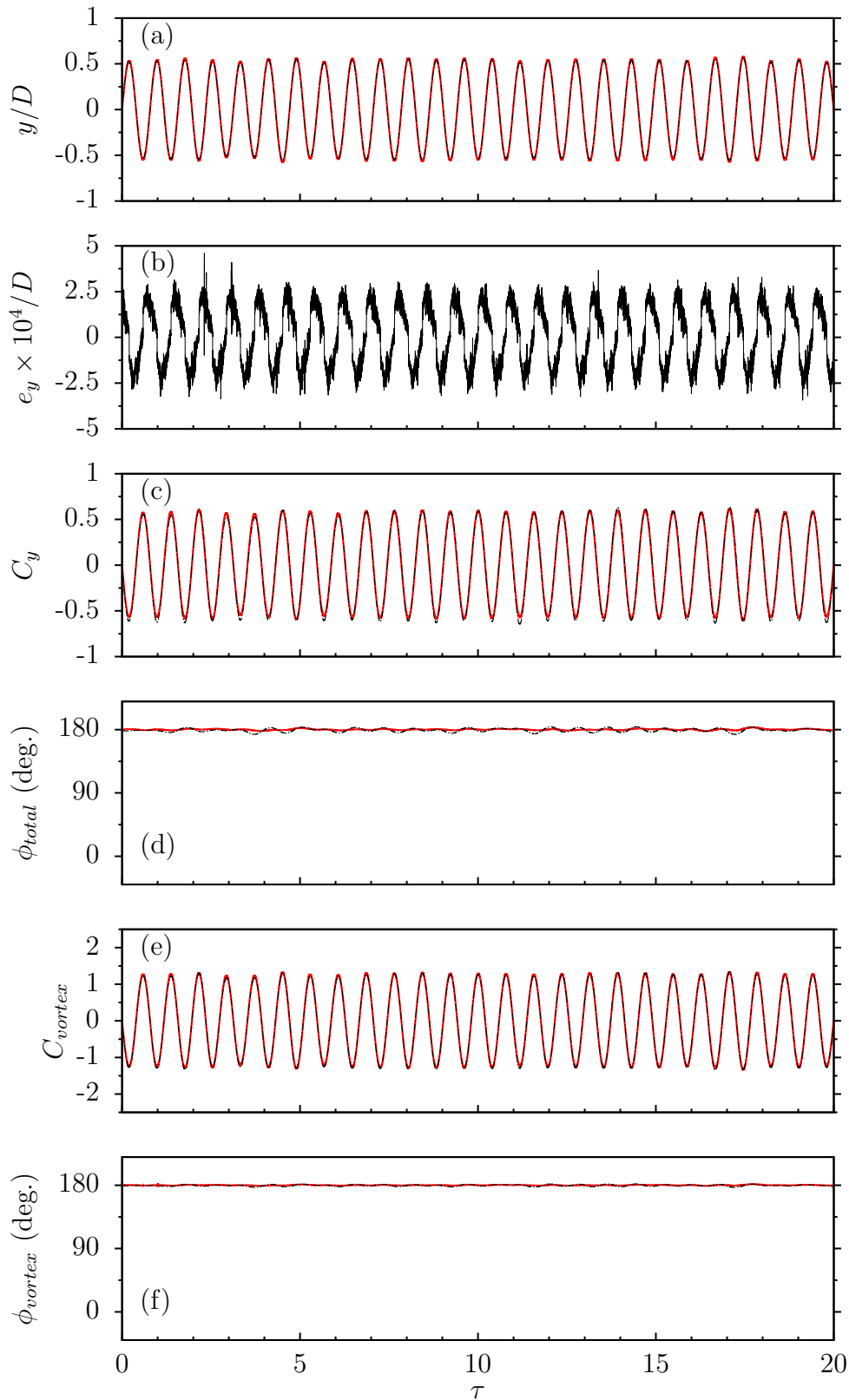


FIGURE 4.22: Time traces of the fluid forces and phases of free and tracking vibrations of a cylinder at $U^* = 8.05$ and $Re = 3900$: (a) the body motion, (b) the position tracking errors, e_y , (c) the transverse lift coefficient, (d) the total phase, (e) the vortex force coefficient, and (f) the vortex phase. The black dot-dashed lines represent the response of freely-vibrating cylinder and the solid red lines represent the response of the tracking cylinder.

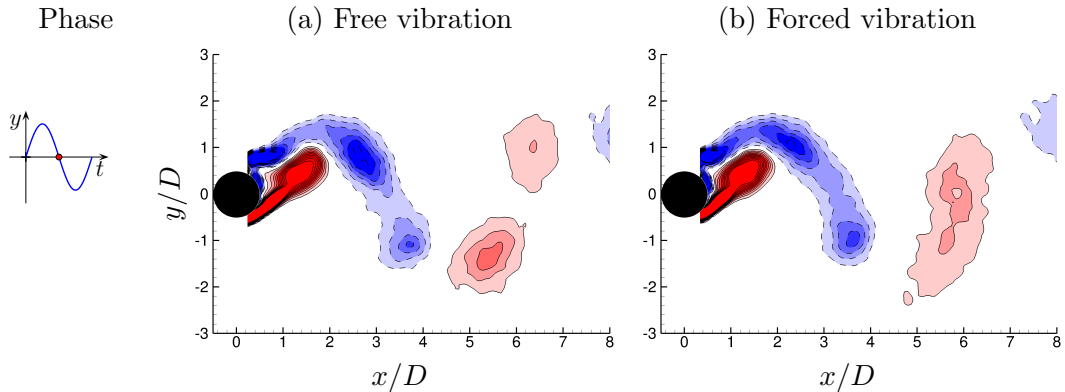


FIGURE 4.23: Phase-averaged PIV results showing that presence of the $2P$ mode in both free and tracking vibrations of a cylinder at $\lambda^* = 6.31$. The Reynolds number is $Re = 3900$. The dashed iso-lines (filled blue) represent clockwise (negative) vorticity, and the solid iso-lines (filled red) represent counter-clockwise (positive) vorticity.

onset of the lock-in region. At this point, Govardhan & Williamson (2000) demonstrated that a cylinder with $m^* = 8.63$ underwent a wake mode transition of $2S \leftrightarrow 2P$ modes, corresponding to a sharp jump in the vortex phase, $\phi_{vortex} = 0^\circ \leftrightarrow 180^\circ$. However, the present results of a cylinder with $m^* = 2.66$ show that $2S$ mode is observed at the beginning of the upper branch where the body oscillation frequency is equal to the natural frequency of the system, $f^* = 1$, and the vortex phase is constantly at $\phi_{vortex} \approx 0^\circ$. Adding to the previous studies, the measurements of the forces and vorticity fields confirm that the $2S$ mode co-exists with a $2P_o$ mode in the middle of upper branch at $U^* = 5.91$, where the body experiences largest-scale vibration. The amplitude response undergoes an intermittent-switching transition of between the upper and lower branches at higher reduced velocities. This response branch transition is associated with a sharp jump in the total phase between 0° and 180° , and a $2P_o \leftrightarrow 2P$ wake mode transition. In the lower branch, the fluid force and the cylinder motion are highly periodic.

Following this, the dynamic response of forced vibrations is directly compared with that of free vibration at four locations in the three typical amplitude response branches. The results of a cylinder forced to precisely follow the trajectories of its free vibration show that the dynamic response of free vibration can be replicated at three locations in the amplitude-wavelength plane, where the total and vortex phases are constantly at either around 0° or 180° . In the middle of the upper branch, comparison has shown significant differences in the dynamic response between free and forced tracking vibrations. Although similar values of the magnitude of the total lift are measured in both vibration cases, significant differences arise from the total phase, the decomposed vortex force and phase, and the wake modes. The total and vortex phases of the tracking vibration undergo more complicated switching behaviours. Additionally, the force and vorticity field measurements have illustrated three wake modes ($2S$, $2P_o$ and $2P$ modes) co-exist at this location in the forced tracking vibration, while only two wake modes ($2S$ and $2P_o$) are observed in the free vibration. The fluid-structure system seems to be very sensitive to any slight perturbations in the middle of the upper branch. However, the causes for the differences between the two vibration cases remain unclear.

Furthermore, the results of sinusoidal forced vibrations agree well with the recent study of Morse & Williamson (2009a). Compared closely with the free vibration, the

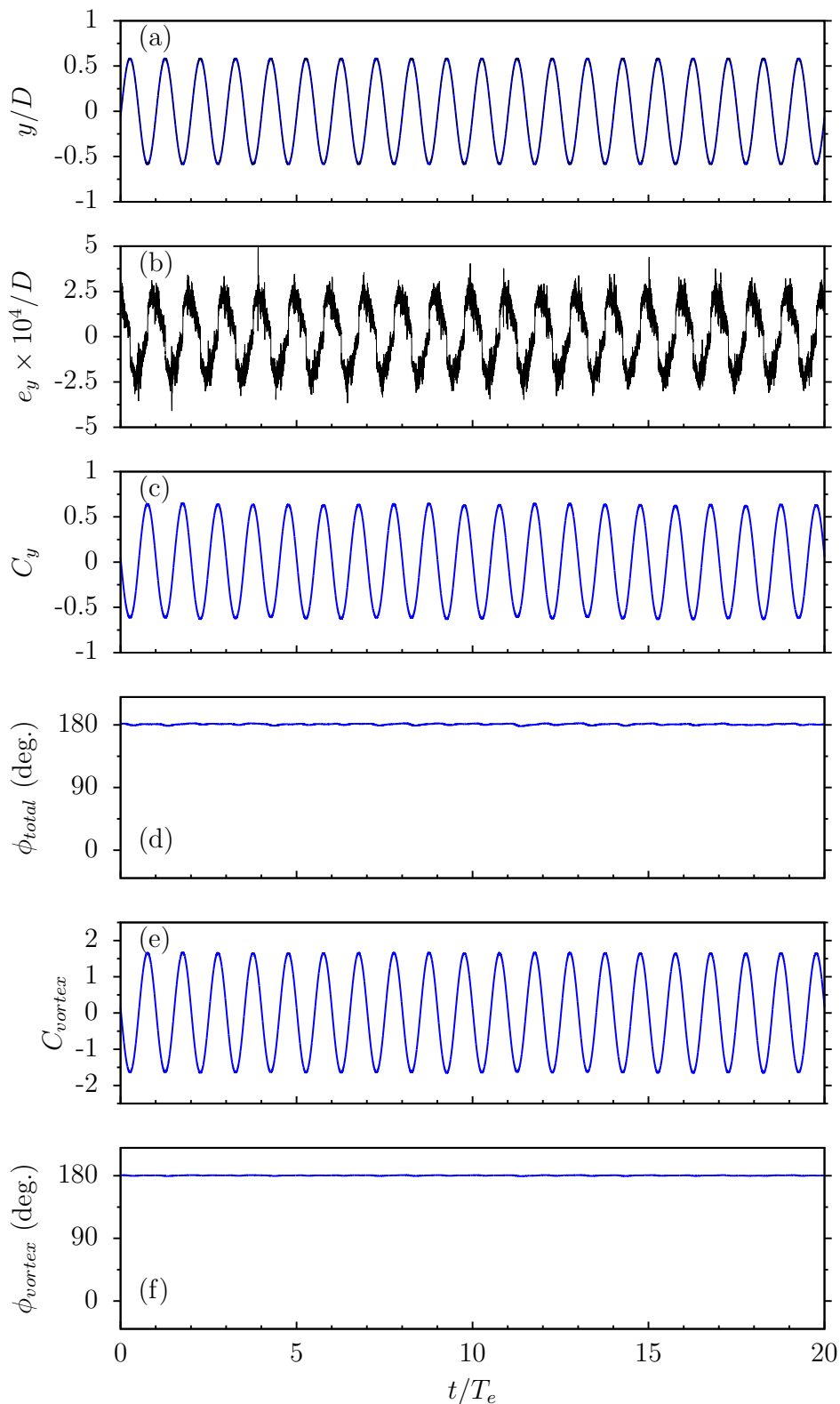


FIGURE 4.24: Time traces of the fluid forces and phases of a cylinder undergoing sinusoidal forced oscillations with $A^* = 0.584$ and $f_e/f_{St} = 0.766$ at $\lambda^* = 6.31$ and $Re = 3900$: (a) the body motion, (b) the position tracking errors, e_y , (c) the transverse lift coefficient, (d) the total phase, (e) the vortex force coefficient, and (f) the vortex phase. The black dot-dashed lines represent the position reference and the solid blue lines represent the response of the tracking cylinder. Note that $T_e = 1/f_e$ is the cylinder oscillation period.

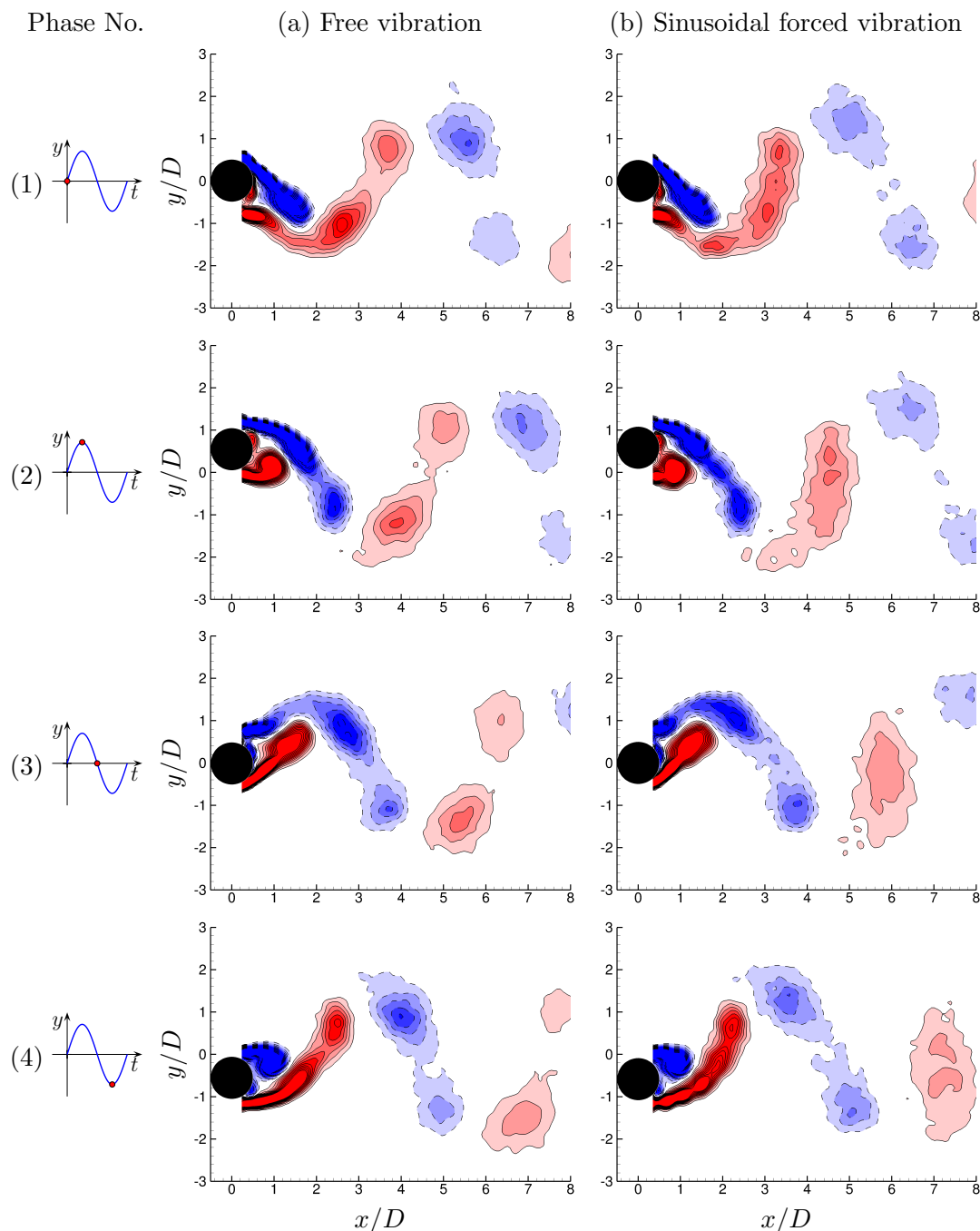


FIGURE 4.25: Phase-averaged PIV results showing the presence of $2P$ wake mode for both a freely vibrating cylinder at $U^* = 8.05$, and a sinusoidally-driven cylinder with $A^* = 0.584$ and $f_e/f_{St} = 0.766$ at $\lambda^* = 6.31$. The Reynolds number of both cases is $Re = 3900$. Four phases are shown over one oscillation cycle. The dashed iso-lines (filled blue) represent clockwise (negative) vorticity, and the solid iso-lines (filled red) represent counter-clockwise (positive) vorticity.

results have confirmed that sinusoidal forced vibration is an adequate model for free vibration in the lower branch. At the locations corresponding to the upper branch of free vibration, even though the cylinder is forced to oscillate at the A_{10}^* amplitude response value of the free vibration, the total and vortex phases are found to be significantly above 180° , indicating the energy transfer is negative, from the oscillating structure to the fluid. This implies sinusoidal forced vibration may not be an adequate model for VIV in the upper branch.

Chapter 5

Flow-Induced Vibrations of A Square Cylinder

5.1 Introduction

It has been well documented in the literature that a square cylinder experiences galloping when the reduced velocity is higher than a critical value. Parkinson & Brooks (1961) and Parkinson & Smith (1964) developed the foundations for the current state of the art with a model that predicts the galloping response of a square cylinder at zero angle of attack, using a quasi-steady theory based on the lift forces on the stationary body at different angles of attack. The quasi-steady theory can successfully predict the amplitude response of a square cylinder, including the critical reduced velocity required for the onset of galloping and a velocity dependent hysteresis phenomenon in the amplitude response. Irrespective of their orientation, square cross-sectional cylinders have fixed flow separation points and an “afterbody”, meaning that they are susceptible to both galloping and VIV. Parkinson & Wawzonek (1981) showed that the onset of galloping of rectangular cross-sections can lie in the range of velocities at which a body can also experience VIV, with the possibility that a combination of galloping and VIV could occur simultaneously. Bokaian & Geoola (1984) observed experimentally a combination of galloping and VIV leading to a modified quasi-steady theory to account for the combined effects. Further experiments by Bearman *et al.* (1987) on the mixed modes of galloping and VIV of square cross-section revealed surface pressure frequencies at both the vortex shedding frequency of the stationary body and the oscillation frequency of the body, with the oscillation dominating near the VIV resonant region. Corless & Parkinson (1988, 1993) applied the Hartlin-Currie VIV wake-oscillator model and the quasi-steady theory to model the combined effects with multiple time scales, and the results agreed reasonably well with the experiments of Bearman *et al.* (1987).

In contrast to VIV of a circular cylinder and galloping of a square cylinder at zero angle of attack, however, much less research has been undertaken to investigate FIV of a square cylinder with varying physical angle of attack. Naudascher & Wang (1993) have reviewed the effect of angle of incidence on flow over prismatic structures but this was not extended to the study of the transition between galloping and VIV or their combined effect. A square cylinder with a physical angle of attack of 45° with respect to the free stream, would be expected to experience a VIV response, as the locations of its symmetric fixed flow separation points would be similar to those of a circular cylinder case. Therefore, of primary interest in this thesis is the influence of the angle of attack on the dynamic response of a freely vibrating square cylinder with low mass-damping

ratio.

The experimental results of FIV of a square cylinder with varying angle of attack are presented in §5.2. Initially, two limiting angles of attack, $\alpha = 45^\circ$ and $\alpha = 0^\circ$, are discussed in §5.2.2 and §5.2.3, respectively. §5.2.4 presents the dynamic response of a square cylinder over a parameter map of the reduced velocity and angle of attack. Further experimental results of VIV of a diamond cylinder at different mass ratios are presented in §5.3. Lastly, a brief summary of this chapter is given in §5.4.

5.2 FIV of a square cylinder with angle of attack variation

5.2.1 Experimental details

Two bluff body models, a square cross-sectional cylinder and a circular cylinder, were used for the experiments discussed in this section. The square cylinder model used was the cylinder Body V in Table 3.3 in §3.5. The side width of the cylinder was $W = 25$ mm, and the immersed length of the body was $L = 778$ mm, giving a displaced water mass of $m_d = \rho W^2 L = 483$ g. The total mass of the oscillating system was $m = 1065$ g, resulting in a mass ratio of $m^* = 2.2$. The natural frequencies in air and water were $f_{na} = 0.769$ Hz and $f_{nw} = 0.635$ Hz, respectively. The structural damping ratio was $\zeta = 2.95 \times 10^{-3}$. The free end of the cylinder was located with a small gap of 2 mm to the water channel floor. On the other hand, the circular cylinder had an outside diameter of $D = 25$ mm, a mass ratio $m^* = 2.2$ (the same as the square cylinder), and also a 2 mm-gap free end condition.

The angle of attack of the square cylinder, as schematically shown in Figure 3.15 in § 3.5, was varied from $\alpha = 0^\circ$ to $\alpha = 45^\circ$ with the increments of $\Delta\alpha = 2.5^\circ$. The reduced velocities investigated ranged from $U^* = 2.2$ to $U^* = 18$, corresponding to a Reynolds number range of $2500 \leq Re_H \leq 12500$. Experimental results were recorded over a 20 min period for each parameter combination of velocity and angle of attack. This recording length provided accurate representation of the FIV phenomena for a minimum of 800 oscillation cycles, and was found to be sufficient to successfully capture the intermittent behaviour in the transitional regions.

5.2.2 VIV response at $\alpha = 45^\circ$

The flow-induced vibrations of the square cylinder are first investigated for the limiting case of $\alpha = 45^\circ$ (also referred to the diamond cylinder in this study). The vibrational response and wake modes are compared against the well-known VIV response of a circular cylinder. The diamond orientation enforces symmetric flow separation points at the side corners of the body, leaving half the body immersed in the separated wake, *i.e.* the so-called afterbody. These features are comparable to those of a circular cylinder, producing a wake morphology similar to the one generated by a circular cylinder.

5.2.2.1 Amplitude, frequency and phase responses

Figure 5.1 shows the amplitude, frequency and phase responses of the diamond cylinder compared along with the results of a circular cylinder at the same mass ratio. As shown in Figure 5.1 (a), the A_{\max}^* and A_{10}^* results of the diamond cylinder exhibit an amplitude response fashion that is comparable to the circular cylinder case. The oscillations of the diamond cylinder starts with very low amplitudes ($A_{10}^* \approx 0.1$) at low reduced velocities ($U^* < 3$), and then the oscillation amplitudes suddenly increase to $A_{10}^* \approx 0.31$ at

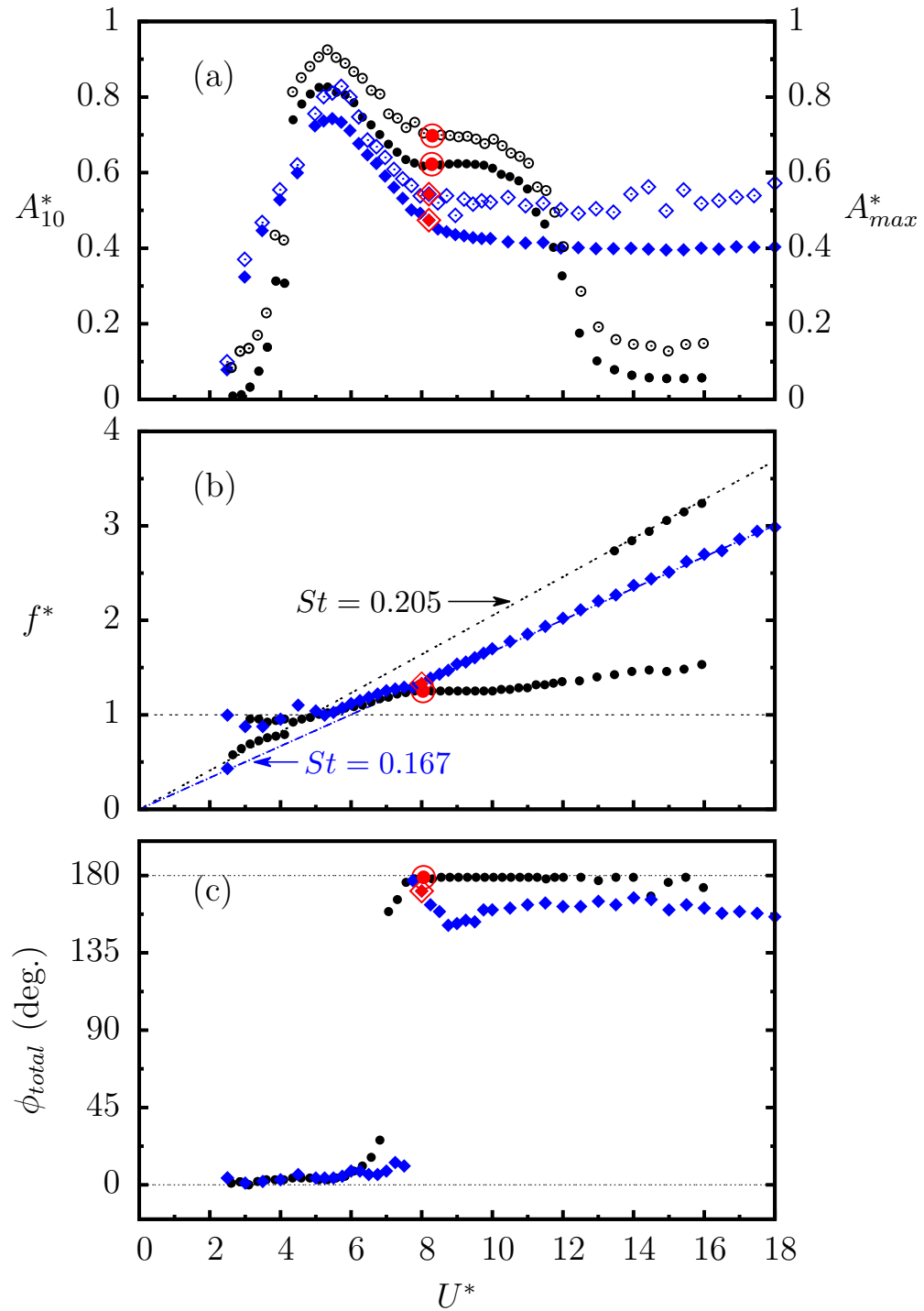


FIGURE 5.1: Comparison of the normalised amplitude and frequency responses, and the total phase of a circular cylinder and a diamond cylinder. In (a), the black solid and open circles represent the A_{10}^* and A_{max}^* , respectively, of the circular cylinder ($m^* = 2.2$ and $\zeta = 2.95 \times 10^{-3}$); the blue solid and open diamonds represent the A_{10}^* and A_{max}^* , respectively, of the diamond cylinder ($m^* = 2.2$ and $\zeta = 2.95 \times 10^{-3}$). In (b) and (c), the black solid circles resp-resent the results of the circular cylinder, and the blue solid diamonds resp-resent the results of the diamond cylinder. The black dashed line represents the normalised vortex shedding frequency, $St = 0.205$, of the stationary circular cylinder, while the blue dashed line represents $St = 0.167$ of the stationary diamond cylinder. The symbols highlighted in red brackets represent locations where the wake vorticity field is measured.

$U^* = 3.5$. As U^* is further increased, the A_{10}^* response follows a linear growth trend to a resonant upper branch without a clear “initial – upper” branch jump such as is observed in the circular cylinder case. For both geometries, the upper branch begins at $U^* = 1/St$ when the oscillation frequency passes through the natural frequency in water, namely $f^* = f/f_{nw} = 1$. The peak value of A_{10}^* of the diamond cylinder is $A_{10}^* = 0.75$ (correspondingly $A_{\max}^* = 0.85$) at $U^* = 6.0$, which is 10% lower than that ($A_{10}^* = 0.84$) of the circular cylinder. However, it should be noted that the amplitudes are normalised by the characteristic length, H , complicating direct comparisons between the amplitude response of the two geometries. Both bodies follow the same gradual decrease from the upper branch with no intermittent behaviour, due to the influence of the end conditions [see Morse *et al.* (2008)]. At the reduced velocities of $8 < U^*$, the maximum amplitude remains in a range of $0.5 < A_{\max}^* < 0.6$, diverging from the circular cylinder case where there is a drop in amplitude to small oscillations when the body’s vibrations and the vortex shedding desynchronise. However, the A_{10}^* maintains a constant value of $A_{10}^* = 0.4$ over this reduced velocity range. Figure 5.2 illustrates that the diamond cylinder’s motion gradually loses its periodicity as the reduced velocity is increased from the resonance region to higher values.

The amplitude response of the diamond cylinder clearly exhibits a VIV response. The current results also suggest that, compared to the typical three-branch response of the circular cylinder, the diamond’s oscillation amplitude increases to the upper branch more gradually with no independent initial branch for the same mass ratio.

Figure 5.1 (b) shows the frequency response of the two bodies. The results of the circular cylinder exhibit a classic VIV frequency response fashion for low mass-damping ratio. At low reduced velocities in the initial branch, the circular cylinder’s oscillation frequency response exhibits two main components, with one component following the Strouhal number functional trend of the stationary body ($St = 0.205$) and the other component remaining close to the natural frequency of the system in water ($f^* = 1$). As the amplitude response jumps up to the upper branch, the body’s oscillations are highly periodic with a well-defined dominant normalised frequency close to unity. The f^* departs away from the Strouhal number function trend and increases monotonically as the reduced velocity is increased up to $U^* \approx 7.5$. As U^* is further increased, the amplitude response jumps down to the lower branch, and the normalised frequency remains to a constant value of $f^* = 1.3$ throughout the lower branch. At higher reduced velocities of $13.5 < U^*$, the cylinder’s oscillations lose periodicity with the amplitudes gradually dropping down to $A_{10}^* \approx 0.12$ (correspondingly $A_{\max}^* \approx 0.2$), whereas the frequency response exhibits two main components with one component close to $f^* = 1.5$, and a secondary component following the Strouhal number function trend again. These results agree well with those of a circular cylinder with low mass-damping ratio reported in the literature and other experiments from the present study.

The frequency response of the diamond cylinder behaves differently. At the lowest velocity investigated, $U^* = 2.5$, the body oscillation frequency has two main components: one at the natural frequency of the system in water and the other matching the vortex shedding frequency of the body at rest, $f^*/U^* = St = 0.167$. For all the other velocities, the oscillations are dominated by a single frequency. For $2.5 < U^* < 5$, the response is clearly influenced by the natural frequency of the system, with values fluctuating in a range of $0.8 < f^* < 1.2$ and coinciding with the transition to the upper branch on the amplitude plot. In the reduced velocity range of $5 \leq U^* \leq 8$, the frequency response f^* increases monotonically with U^* , which is comparable to the circular cylinder case. In this region, the diamond cylinder, similar to the circular cylinder

5.2. FIV of a square cylinder with angle of attack variation

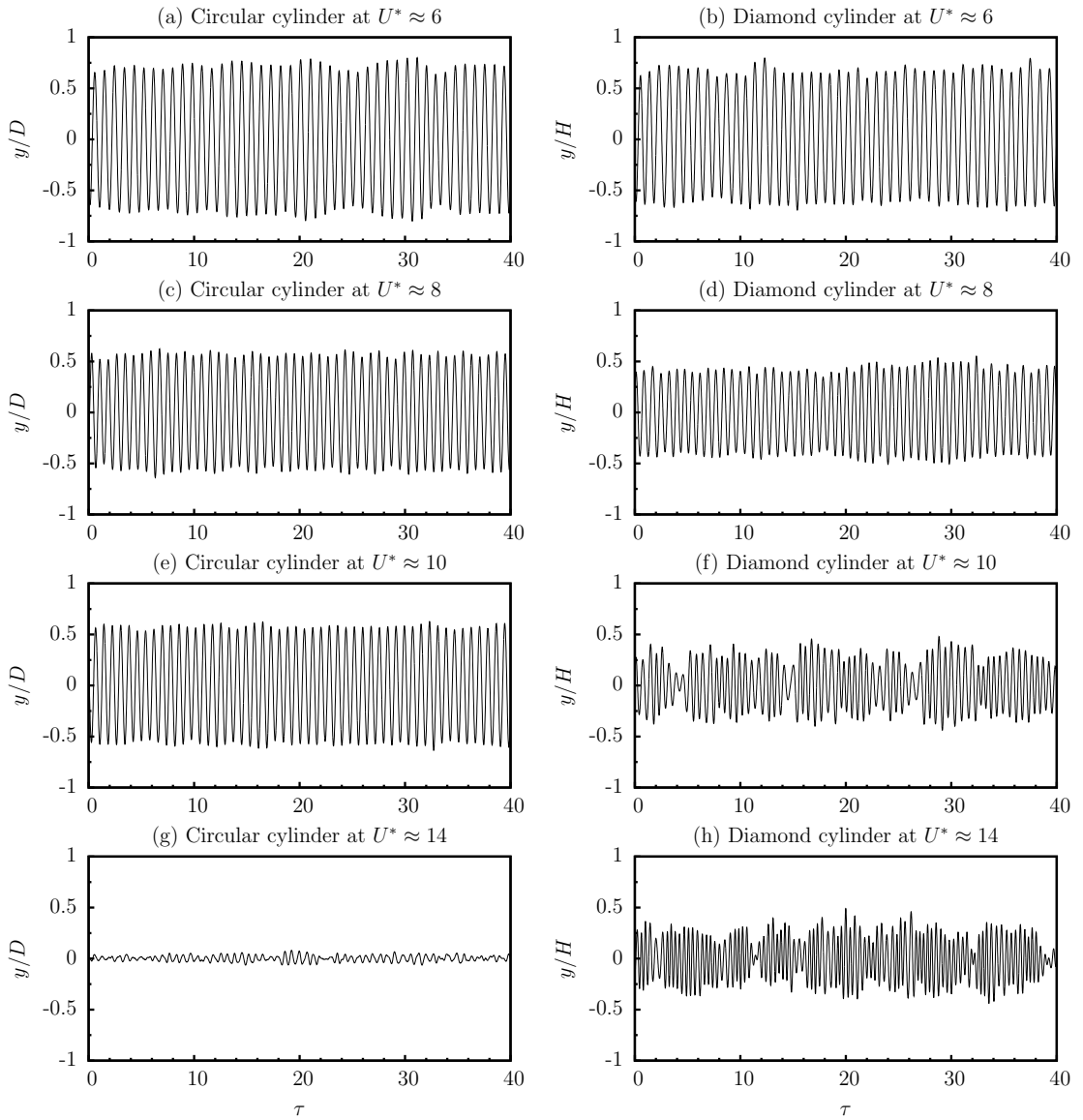


FIGURE 5.2: Displacement time histories of the circular cylinder (in the left column) and diamond cylinder (in the right column) illustrating the loss periodicity in the oscillations with increasing reduced velocity. The circular cylinder's oscillations are periodic in the upper and lower branches as shown in (a), (c) and (e), and then lose their periodicity in the desynchronisation region as shown in (g). The diamond cylinder's oscillations, on the other hand, are periodic in the resonant region as shown in (b) and (d), and then lose their periodicity at higher reduced velocities of $U^* > 8$.

case, experiences resonance with the largest-amplitude oscillations. For $U^* > 8$, the diamond cylinder's oscillations are dominated by the vortex shedding frequency, with f^* following the Strouhal number function trend of $St = 0.167$. However, the body's oscillations lose their periodicity as evidenced by the time-histories in Figure 5.2 (g).

Figure 5.1 (c) shows the corresponding total phase difference, ϕ_{total} , between the transverse lift force and the body's displacement. The transverse lift force and the displacement of the circular cylinder remains in-phase, just above $\phi_{total} = 0^\circ$ throughout the initial and upper branches before jumping sharply out of phase to around $\phi_{total} = 180^\circ$ at $U^* \approx 7.8$. This jump has been well discussed previously in § 4 where it is associated with the upper – lower branch transition and that it occurs when the body oscillation frequency passes through the natural frequency of the system in air (Govardhan & Williamson 2000). The phase relationship for the diamond cylinder shows a similar phase jump from $\phi_{total} = 0^\circ$ to $\phi_{total} = 180^\circ$ at $U^* = 7.5$ as the circular cylinder. However, the ϕ_{total} of the diamond cylinder gradually dips to $\phi_{total} = 150^\circ$ at $U^* = 7.75$ before fluctuating around $\phi_{total} = 170^\circ$ with the dominant oscillation frequency following the Strouhal number function trend for higher reduced velocities. The frequency and phase responses of the diamond cylinder clearly behave in a VIV fashion. Compared to the circular cylinder, the geometry of the diamond weakens the coupling of the body's oscillation to the natural frequency of the system – the oscillations remain fixed to the timing of the vortex shedding for $U^* > 8$.

5.2.2.2 Wake modes

Recent investigations into oscillating circular cylinder have studied the vortex structures in the maps and classifications of vortex modes for a freely vibrating (Govardhan & Williamson 2000) body and a sinusoidally-driven oscillating body (Leontini *et al.* 2006a; Carberry *et al.* 2004b; Morse & Williamson 2009a). Govardhan & Williamson (2000) showed that a circular cylinder with low mass-damping ratio undergoes a transition of wake mode from $2S$ to $2P$ when the amplitude response jumps from the initial branch to the upper branch.

Vorticity contours of the wake mode of the diamond cylinder are shown alongside those of the circular cylinder in Figure 5.3 for a reduced velocity of $U^* = 8$. The sequence of phase averaged plots of the vorticity contours recovers the known $2P$ -vortex shedding mode for the circular cylinder, as captured originally by Govardhan & Williamson (2000), for the lower branch. The figure shows the vortex shedding in 8 phases of one oscillation cycle, with dashed iso-lines representing negative, clockwise (CW) vorticity, and solid iso-lines representing positive, counter-clockwise (CCW) vorticity. At the beginning of the oscillation cycle, phase No.1 in Figure 5.3 (a), the circular cylinder is moving upwards and crosses the centerline in the positive direction, shedding a CCW vortex from the bottom shear layer. CW vorticity attached to the top shear layer is being drawn across the center-line of the wake. As the body reaches the top of the oscillation cycle in phase No.3, the top shear layer sheds a weak vortex that is advected downstream in the wake and pairs with the stronger vortex of opposite sign (shed in phase No.1) forming a counter-rotating vortex pair. The process is mirrored about the centerline in phases No.5-8, as the negative sign shear layer moves back across the centerline and sheds a strong CW vortex in phase No.5, separating as the positive vorticity moves upwards into the shear layer. This is paired by a weaker CCW vortex (in phase No.8) as the body completes one oscillation cycle. This final pair is observable in the far wake of the first phase of the next cycle (as shown in phase No.1). The secondary weak vortex in these pairs is shed due to the stretching of the shear

5.2. FIV of a square cylinder with angle of attack variation

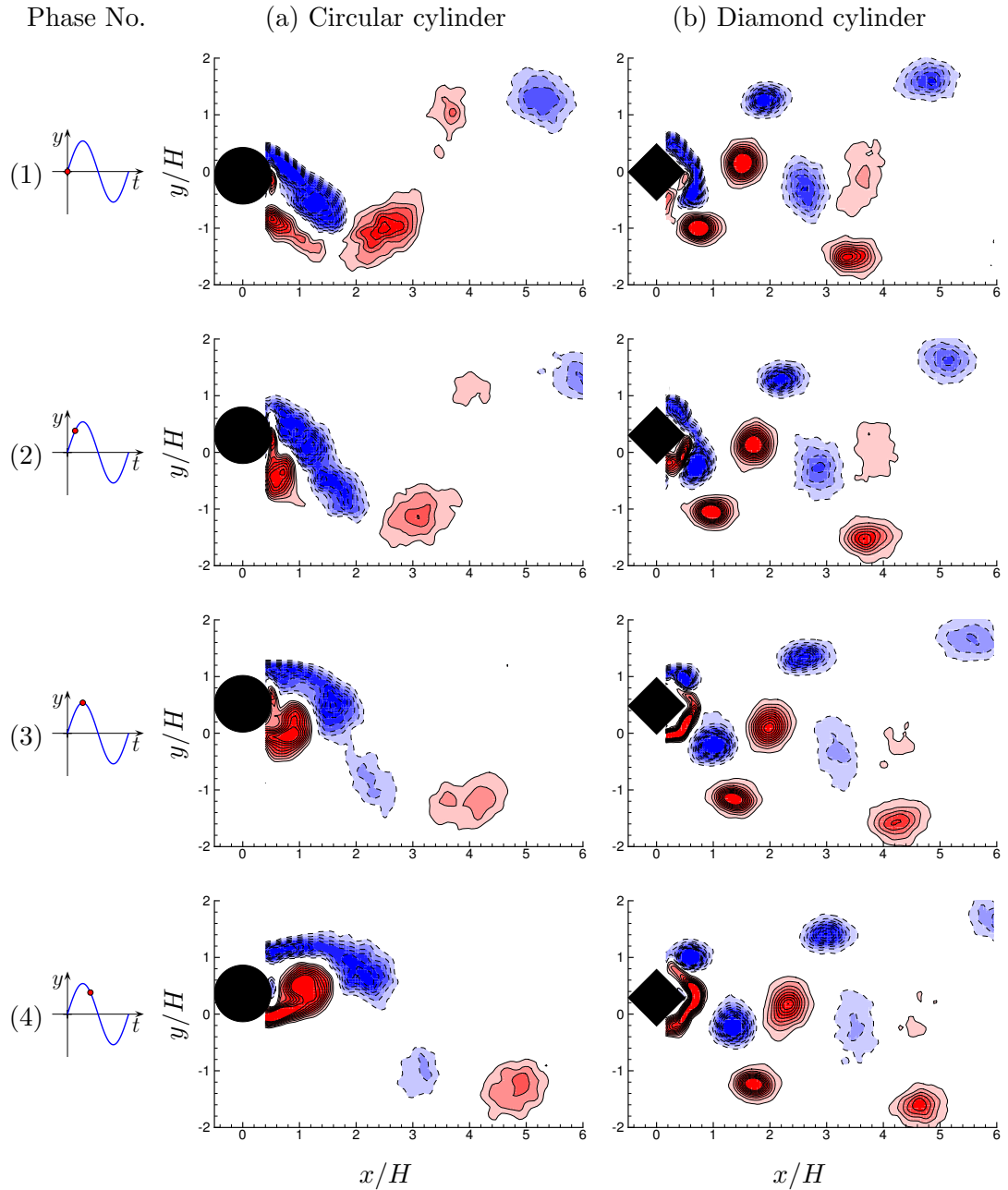


FIGURE 5.3: Phase-averaged PIV results showing the lower branch $2P$ shedding modes of a circular cylinder and a diamond cylinder at $U^* = 8$. Eight phases are shown over one oscillation cycle. The dashed iso-lines (filled blue) represent clockwise (negative) vorticity, and the solid iso-lines (filled red) represent counter-clockwise (positive) vorticity.

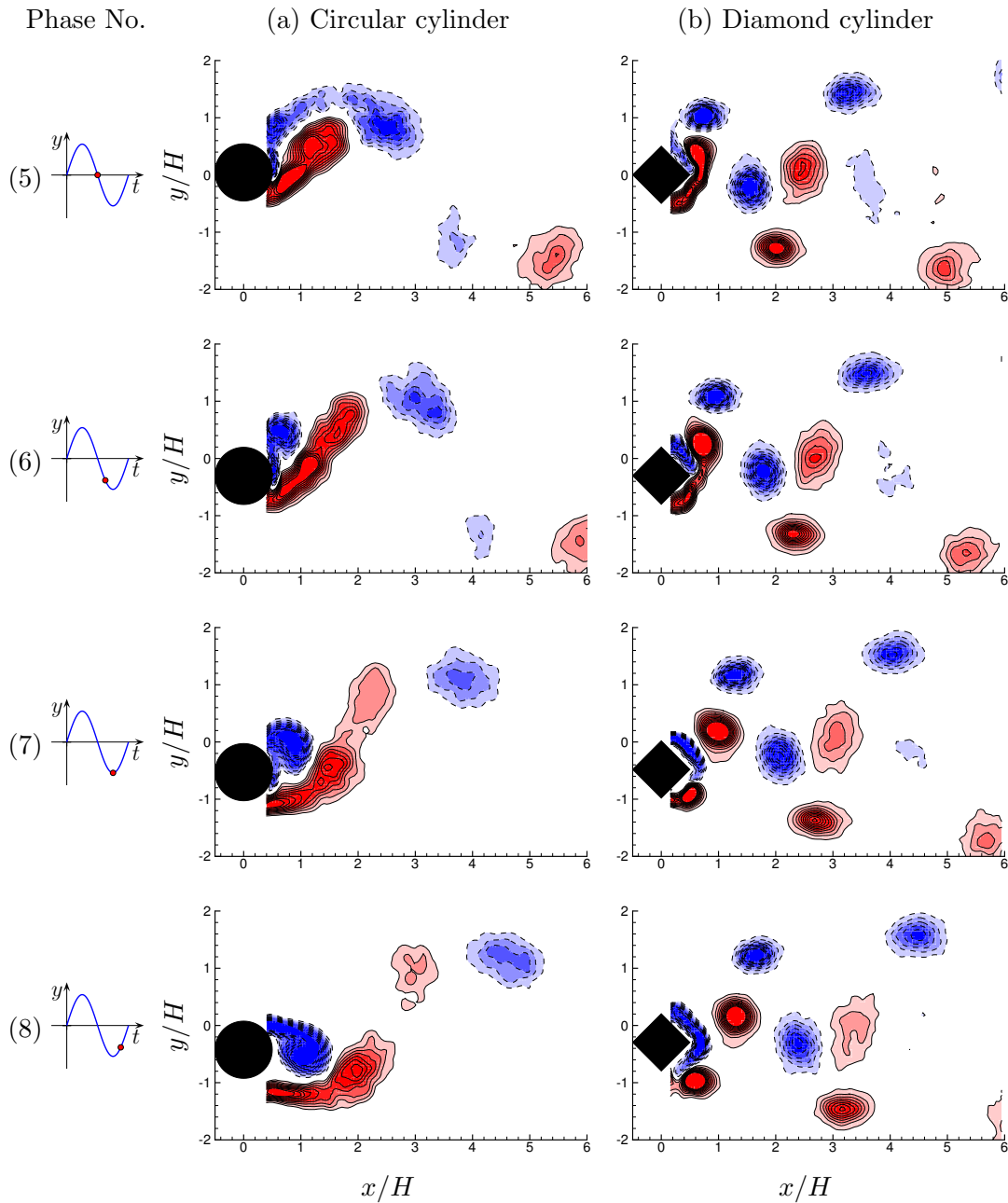


FIGURE 5.3: Phase-averaged PIV results showing the lower branch $2P$ shedding modes of a circular cylinder and a diamond cylinder at $U^* = 8$. Eight phases are shown over one oscillation cycle. The dashed iso-lines (filled blue) represent clockwise (negative) vorticity, and the solid iso-lines (filled red) represent counter-clockwise (positive) vorticity. (*Continued*).

5.2. FIV of a square cylinder with angle of attack variation

layer across the centre line as the body changes direction. The stronger vortices are separated from the shear layer in the high strain field where large vorticity of opposite signs interact behind the body.

On the other hand, as shown in Figure 5.3 (b), the diamond cylinder also reveals the same $2P$ shedding mode as the circular cylinder, albeit with different features. The corners of the diamond fix the location of the shear layer separation and so determine where the vortex roll-up begins, while the sharp after-body creates a high strain field behind the trailing edge. This results in more concentrated vortex cores that separate from the shear layer closer to the body than for the circular cylinder. This earlier spatial evolution of the vortex splitting also leads to a different organisation of vortices in the far wake. The same vortex shedding phases are presented as discussed above with respect to the circular cylinder. In the phase No.1, the negative vorticity around the body crosses the centerline and splits in the high strain field at the trailing edge. It then advects downstream (in the phases No.2-4) near the center-line with only a streamwise component of motion. The CCW vortex closest to the body is advected with the wake. As for the circular cylinder, this is mirrored along the center-line (in the phases No.5-8) with vortices of the opposite sign. The first vortex shed from the shear layers in each phase is weaker than the second one. However, in the diamond cylinder's wake they do not pair with vortices of the opposite sign, forming instead a four row vortex arrangement over the first $5H$ of the wake length. In this region the wake is characterised by strong vortices that expand out into the wake and have vorticity of the same sign as the shear layer on that side of the wake. Weaker vortices advect downstream in a path that remains close to the center-line, in a line of alternating sign.

The phase averaged plots show that the vortices from the diamond cylinder are more compact than those seen in the wake of a circular cylinder. This, at least in part, can be attributed to two factors: the vortices have smaller cores because of how they are generated, and because there is less variation in the position of the vortices across the individual PIV snapshots. Both of these factors arise from the body's geometry and its fixed separation points. The difference in vortex spacing between the two bodies can also be attributed to differences in the characteristic length, H , which appears in both the length scale and the reduced velocity, U^* . Additional wake visualisations (not shown) revealed that the wake transition from a $2S$ mode to a $2P$ occurred over the reduced velocity range of $3.75 \leq U^* \leq 4.25$ for both body geometries.

5.2.3 Galloping response at $\alpha = 0^\circ$

The flow-induced vibrations discussed above are for one limiting case, the diamond orientation, and revealed a VIV response that compared well with the VIV of a circular cylinder. The second limiting case for the square cross-section is at $\alpha = 0^\circ$, the square orientation. This configuration shares the same symmetries as the diamond case, but has been shown to be susceptible to galloping at a similar reduced velocity range for low mass-damping ratios (Bearman *et al.* 1987). Galloping of square cylinders is briefly reviewed here based on results taken with this experimental facility, primarily to validate and to contrast it with the VIV seen in the diamond case.

5.2.3.1 Amplitude and frequency responses

The amplitude and frequency responses of the present square orientation undergoing galloping are shown in Figure 5.4 (a) and (b), respectively. Figure 5.4 (c) shows a comparison of the amplitude response of the present study and other experiments in

the literature. To account for varying mass ratios the amplitude is re-normalised as $A' = A^*/2m^*$, and the reduced velocity is re-normalised as $U' = U^*/2m^*$ – similar to the method used by Parkinson (1989). The present results of the amplitude response agree well with the prior work, which covers a wider mass ratio range of $5 \leq m^* \leq 15$. The variation of amplitudes across the studies is attributable to different experimental conditions (Parkinson 1989) and turbulence intensities of the experiments. A noticeable deviation from the trend occurs around $U' = 0.55$, where the amplitude deviates from the linear growth – this will be addressed later in this section.

As shown in Figure 5.4 (a), the amplitude response of the square cylinder is characterised by a monotonic increase with velocity and, unlike VIV, it is not self-limited. Hence, for the reduced velocities above $U^* = 9$, the A_{10}^* amplitudes of galloping are much larger than those achieved in the VIV upper branch. The maximum A_{10}^* observed is $A_{10}^* = 1.5D$ at the maximum investigated reduced velocity of $U^* = 18$. Around $U^* = 14$, the body experiences a slight deviation from the linear amplitude growth trend. This “kink” in behaviour has also been observed by Bearman *et al.* (1987) in their wind-tunnel experiments with low damping ratio, it was not, however, predicted by the quasi-steady theory. Bearman *et al.* (1987) correlated it with a transverse force component occurring at three times the body oscillation frequency, a result also found in the present force measurements. They also attributed the “kink” behaviour to complex vortex formation caused by the high strain imposed by the sharp afterbody corners on the shear layers.

The frequency response shows that the initial vibrations of the square orientation occurs with the dominant frequencies above the natural frequency of the system, $f^* > 1$. The body starts to oscillate at very low reduced velocities ($U^* < 4$), due to the imposed lift force exerted by the vortex shedding. At $U^* = 4$ the oscillation frequency drops down to $f^* \approx 0.4$, which is lower than the vortex shedding frequency and indicates that the body experiences galloping. For $4 \leq U^* \leq 8$, the body oscillation frequency increases gradually until it reaches a value of $f^* = 0.6$ at $U^* = 8$. After that it remains constant over $9 \leq U^* \leq 11$, and then increases again to reach a peak value $f^* = 0.8$ at $U^* = 15$. The f^* values drop down to $f^* \approx 0.6$ for higher U^* . This change occurs just after the “kink” in the amplitude response.

5.2.3.2 Wake modes

Figure 5.5 shows a comparison of the wake mode of the square cylinder and the circular cylinder at the same reduced velocity, $U^* = 8$. The wake structures of a body undergoing galloping is a combination of vortices shed at the body’s shedding frequency, and that of the body’s vibration frequency, with two vortex system coexisting. Flow separation from the square cylinder occurs at the leading corners, with a shear layer visibly extending to the rear of the body. The square body can be seen to shed large vortices of similar initial size to the circular cylinder, which remain attached to the shear layer up to $1.5D$ downstream of the afterbody. These vortices, however, diffuse rapidly further downstream.

The nature of the wake modes of a bluff body undergoing galloping has received little interest in the literature, unsurprising given that it is not the driving cause of the vibrations. It would have been interesting, however, to obtain better insight into the vortex formation in the region of the amplitude “kink” where the lift force shows a third frequency component. However, the current visualisation of position-based phase averaged vorticity could not capture the cause of the third harmonic in the lift force shedding.

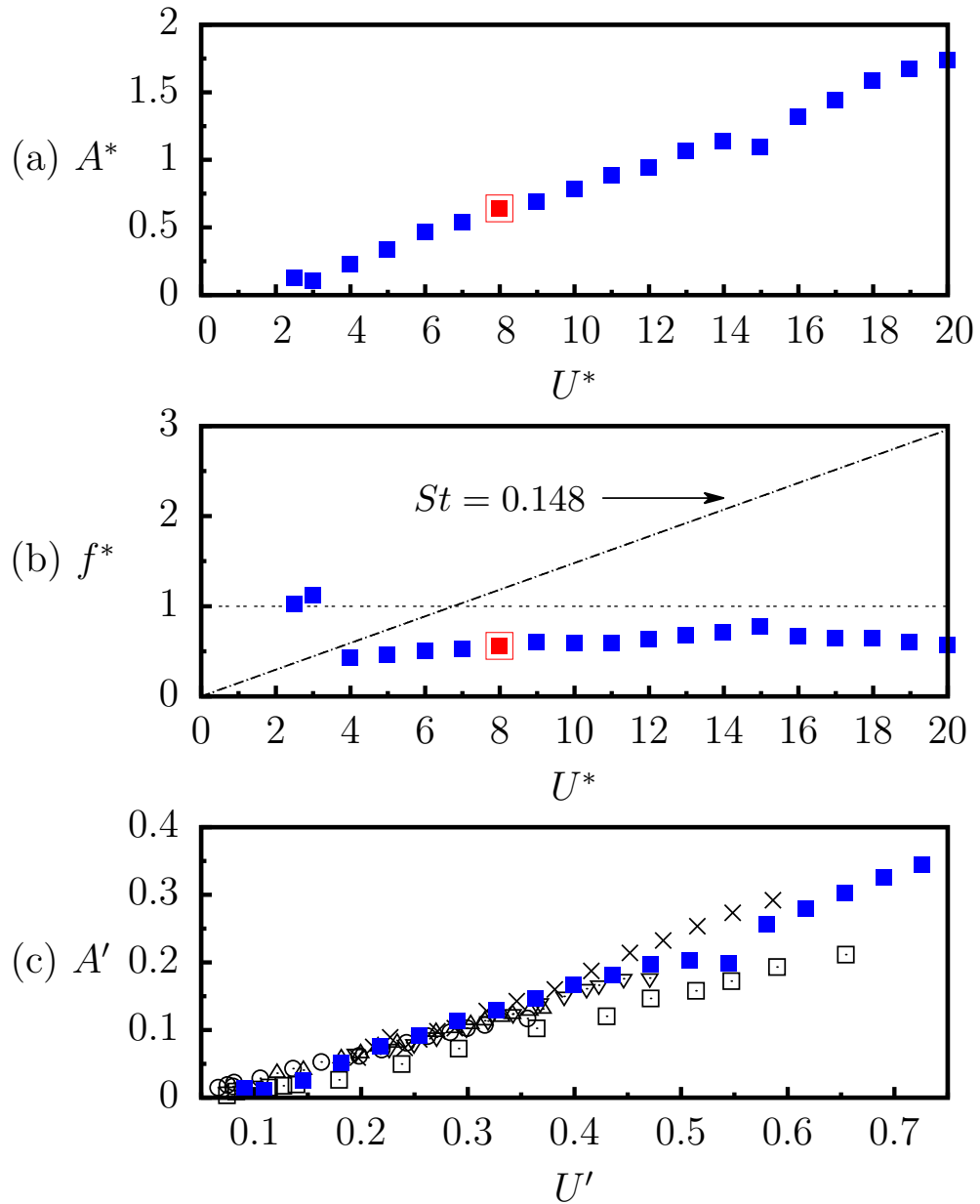


FIGURE 5.4: Galloping response of a square cylinder at $\alpha = 0^\circ$ over a range of reduced velocities investigated: (a) amplitude response and (b) frequency response. The red bordered symbols are locations where the PIV measurements were taken for wake structures. (c) Validation of the current response (filled squares) re-normalised and compared to galloping data from Parkinson (1989). Circles represent at $m^* = 15.1$; triangles represent $m^* = 9.6$; inverted triangles represent $m^* = 5.3$ by Bouclin (1977); crosses represent $m^* = 5.1$ by Santosham (unpublished work used in Parkinson 1989); open squares represent $m^* = 8.2$ by Bokaian & Geoola (1983). The symbols highlighted in red brackets represent locations where the wake vorticity field is measured.

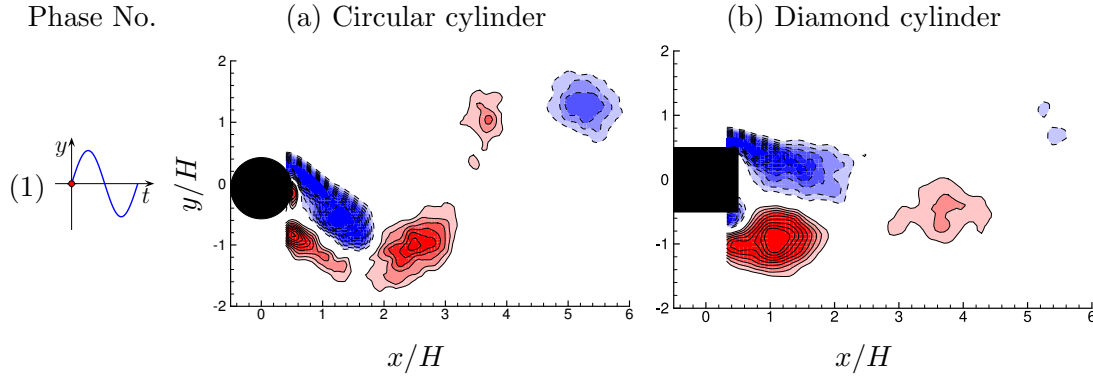


FIGURE 5.5: Vorticity plots of shedding modes of (a) the circular cylinder in the lower branch 2P shedding modes and (b) the square cylinder with 2S mode at the same reduced velocity $U^* = 8$.

5.2.4 Dynamic response with varying angle of attack

The previous results have shown that square cross-sectional cylinders are susceptible to galloping at $\alpha = 0^\circ$ and VIV at $\alpha = 45^\circ$. This section will present how the angle of attack affects the response of the freely vibrating cylinder, with a particular focus on the transition from VIV to galloping.

5.2.4.1 Amplitude response

Figure 5.6 shows the A_{10}^* amplitude response to reduced velocity with varying angle of attack. Figure 5.6 (a) reveals the three distinct responses of the square section: (i) from $\alpha = 45^\circ$ down to $\alpha = 25^\circ$ the amplitude response follows the VIV fashion of the diamond orientation, with both upper and lower branches present. The peak A_{10}^* ridge of the VIV upper branch is shown in Figure 5.6; (ii) for the angle range of $0^\circ \leq \alpha \leq 7.5^\circ$, the body's oscillations follow a trend of increasing amplitude with velocity, as seen in galloping of the square section. This response has a distinct boundary at $\alpha = 7.5^\circ$; (iii) a third region lies between the VIV and galloping dominated regimes. It has a high amplitude resonant branch not seen in galloping, and separate to the upper branch seen in VIV amplitude branches. This higher branch (HB) reaches a maximum amplitude close to $\alpha = 20^\circ$ at $U^* = 8$. The peak ridge of this branch is highlighted with a blue line in Figure 5.6 (a).

The amplitude response is VIV dominated for angles of attack of $25^\circ \leq \alpha \leq 45^\circ$ and resembles that of the diamond orientation. The peak value of the resonant upper branch decreases from $A_{10}^* = 0.76$ to 0.56 as the angle of attack moves away from the diamond configuration. The change in angle also reduces the geometry's shedding frequency that drives the resonant oscillations, and therefore shifts the peak of the resonant upper branch from $U^* = 1/St = 5.5$ at $\alpha = 45^\circ$ to $1/St = 6.5$ at $\alpha = 25^\circ$. A consequence of this is the onset of the upper branch occurring at increasingly higher velocities, thereby revealing an initial branch in the amplitude response. This branch is similar to that seen in circular cylinder results. The upper to lower branch transition approaches a linear gradient until there is no clear distinction between the two amplitude branches.

A new amplitude branch is observed in Figure 5.6 over the angle of attack range of $10^\circ \leq \alpha \leq 22.5^\circ$. Its amplitude is considerably higher than that seen in the upper branch associated with VIV. The peak amplitude of $A_{10}^* = 0.9$ is at $U^* = 8$ and at an

5.2. FIV of a square cylinder with angle of attack variation

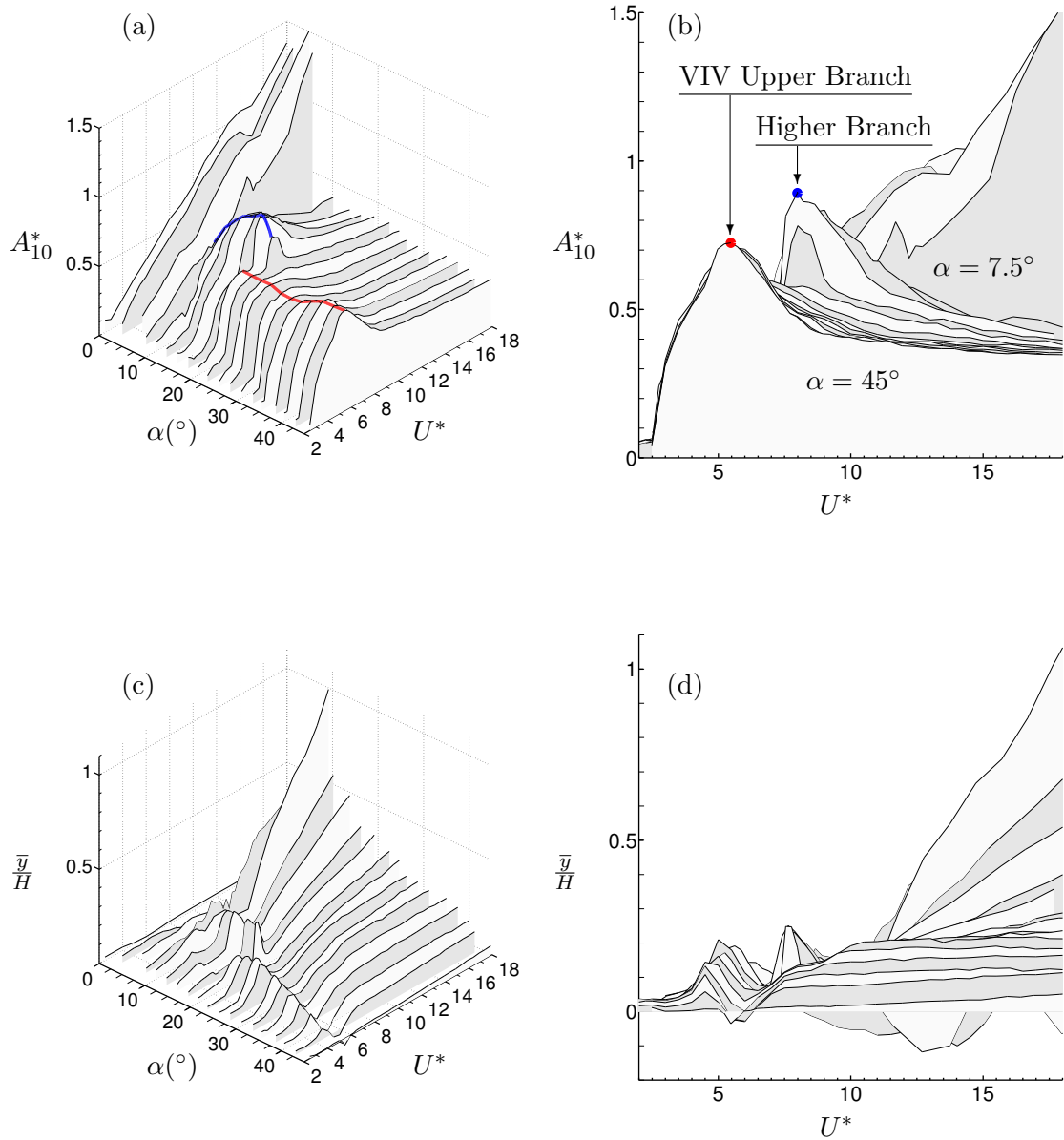


FIGURE 5.6: (a) A 3D plot showing the amplitude response, A_{10}^* , of the dominant oscillation frequency against the reduced velocity, U^* , and angle of attack, α . (b) A 2D plot showing the same amplitude response as a function of the reduced velocity, with all angles superimposed, with the diamond, $\alpha = 45^\circ$, at front. The response curves are in decreasing increments of 2.5° . The sharp transition from a galloping to a combined response is seen in the plots between 7.5° to 10° . The peak of the VIV upper branch (VIV UB) occurs at $\alpha = 45^\circ$, $U^* = 5.75$, and the new amplitude branch (HB) peak occurs at $\alpha = 20^\circ$, $U^* = 8$. (c) A 3D plot showing the mean amplitude response, \bar{y}/H , for the same angle and reduced velocity regimes. (d) A 2D plot for the same mean amplitude response. Angles of attack of 2.5° and 5° show a *negative* mean amplitude response centred around $U^* \approx 13$, while the maximum deviation of the mean from the zero position is seen at $\alpha = 10^\circ$. The influence of the upper and higher branch on the mean amplitude is visible in the positive peaks centred around $U^* = 5$ and $U^* = 8$.

angle of $\alpha = 20^\circ$ and, unlike the upper branch of VIV, the extent of the velocity range of the HB is strongly dependent on the angle of attack. The two resonant branches (VIV upper branch and the higher branch) are seen to co-exist in the range of $20^\circ \leq \alpha \leq 22.5^\circ$, with the HB amplitude jumping sharply over a narrow velocity range, suggesting a rapid switch in the dominant oscillation mode. This is confirmed in the frequency analysis using the wavelet method. For velocities above those where the HB and VIV UB occur, the A_{10}^* oscillation amplitudes decrease with velocity and are consistent in magnitude for the two branches.

When the angle of attack is reduced below $\alpha = 10^\circ$ the oscillation amplitude response dramatically changes as the square orientation is approached and the galloping mode dominates the response. At $\alpha = 7.5^\circ$ the oscillations no longer follow the lower branch trend of VIV but increase in amplitude with increased velocity — neither the VIV upper branch nor the HB resonant characteristics are present in the amplitude response. As the angle of attack approaches the symmetric square orientation, the amplitude response smooths out to the response seen in classical galloping response.

The distinct boundary seen in the A_{10}^* response separating galloping and the new higher branch regimes only reveals part of the transition. The change in oscillation amplitudes occurs simultaneously with the body's average position moving away from the mean position at rest due to the net mean lift acting on the body (shown in Figure 5.6 (c) and (d)). The largest offset in the mean occurs at $\alpha = 10^\circ$, corresponding to the oscillations switching from large amplitude and low frequency galloping oscillations to higher frequency oscillations with smaller amplitudes.

An observation of the mean body position in Figure 5.6 (c) and (d) highlights two important features of the mean amplitude behaviour. Firstly, the mean position deviates from the zero position at parameter values matching the VIV upper branch and the higher branch resonant peaks. In these resonant regions the oscillations are dominated by a single frequency with varying amplitude, as seen in the upper branch of low mass-damping circular cylinders. Secondly, outside of the peak resonant regions, the deviation of the mean from the zero position increases as the angle of attack moves away from the diamond case, due to the square's pressure distribution generating an increasing net lift. The growth is gradual in the VIV dominated region of $22.5^\circ \leq \alpha \leq 45^\circ$, and then becomes rapid in the HB region reaching the largest deviation at $\alpha = 10^\circ$. At angles of attack below this the zero mean position is recovered as the body approaches the symmetric square cylinder orientation. Unexpected results observed in Figure 5.6 (d) are the negative values in the mean position of the body at low angles of attack ($\alpha < 10^\circ$), with a deviation from the zero position of up to $\bar{y}/H = -0.1$ for selected reduced velocities in the range of $8 < U^* < 15$.

The amplitude response with varying angle of attack clearly reveals the various flow-induced vibration modes of the square. The oscillation amplitude and mean position show a clear transition in the behaviour from $\alpha = 7.5^\circ$ to 10° , due in part to the location of the separation points imposed by the corners of the square. As the body is rotated clockwise in Figure 3.15, the separation point attached to the top leading corner of the square moves with the geometry's corner towards the centre line. As the angle of attack α increases, the flow reattaches to the bottom surface of the square and the bottom separation point shifts from the leading bottom corner to the trailing corner, which in turn approaches the centre line as the body rotates further. The jump in location of the bottom separation point is the probable cause of the transition between the galloping and higher branch behaviour.

5.2.4.2 Frequency response

The frequency responses at different angles of attack are shown in Figure 5.7. The symbols on the plots represent frequency power spectrum peaks and the contours represent the relative normalised energy of the frequency spectra. Symbols are associated with the different frequency response regimes classified as follows: Filled circles represent frequencies associated with VIV behaviour, including the body’s shedding frequency and those close to the body’s natural frequency. The open circles represent frequencies in the higher amplitude branch. The open squares are for lower frequencies associated with galloping oscillations. Symbol size indicates the relative energy contained by the dominant frequency of oscillation at each reduced velocity, a useful visualisation aid when there are multiple frequencies present in the signal, as it can show the rate of transfer of spectral energy between dominant frequencies as a function of reduced velocity. The normalised frequency contours superimposed on the plots also reveal energy transfer as well as indicating the periodicity of the signal. In the case of $\alpha = 45^\circ$ in Figure 5.7, the contours expand over an increasingly larger frequency range as U^* increases, simultaneously the filled circles shrink in size. This can be interpreted as the energy in the system remaining centred around the dominant frequency (the shedding frequency here), but distributed over an increasingly wider band of frequencies. The wider band signals a loss in the periodicity of the oscillations as the reduced velocity is increased. Such insight into the frequency response of the diamond is not apparent when inspecting solely the peak frequency values as shown in Figure 5.1. Two guide lines are also shown in the figures, one at $St = 0.167$, the shedding frequency of the diamond cylinder, and the other at its first sub-harmonic.

Inspecting the frequency response in the VIV dominated regime over the domain $\alpha = 25\text{--}45^\circ$ shows that the body follows the same trend as the diamond cylinder. At each angle of attack within this region, increased velocity causes the frequency response to follow a line of constant gradient outside of the resonant region of the upper branch. This gradient, $f^*/U^* = St$, is equal to the frequency of the static body’s vortex shedding at the specified angle of attack. The change in the gradient within the VIV response region shows the decrease in shedding frequency as the angle of attack is decreased. At high reduced velocities the contours reveal low broadband oscillation frequencies, as the VIV lower branch loses periodicity. This low frequency component is a result of mixed mode behaviour caused by the body’s susceptibility to galloping.

At an angle of attack of $\alpha = 22.5^\circ$ the cylinder’s motion maintains the shedding frequency except in the region of $7.75 \leq U^* \leq 9$, where it is dominated by a lower frequency. This, unsurprisingly, coincides with the higher branch amplitude response and is the associated characteristic frequency trend observed over the angle range of $5^\circ \leq \alpha \leq 22.5^\circ$. It is represented by open circles in Figure 5.7. The oscillation has a frequency below that of the VIV response, and locks to a constant Strouhal value.

At lower angle of attack values of ($10^\circ < \alpha < 15^\circ$) the response contains multiple low frequency bands, indicative of complicated fluid-structure interactions. A mixed mode of vibration that is a non-linear combination of galloping and VIV is however probable.

For values below $\alpha = 10^\circ$ the response contains only the low frequency oscillations observed in galloping. The kink seen in the galloping amplitude response in Figure 5.6 (also observed by Bearman *et al.* (1987)) for the angles of $\alpha = 0\text{--}10^\circ$ occurs along with a change in oscillation frequency response. For the square symmetric orientation and the small angle of $\alpha = 2.5^\circ$, there are two low frequency branches: the first is seen up to a $U^* = 15$ for the square and up to $U^* = 14$ for $\alpha = 2.5^\circ$, characterised

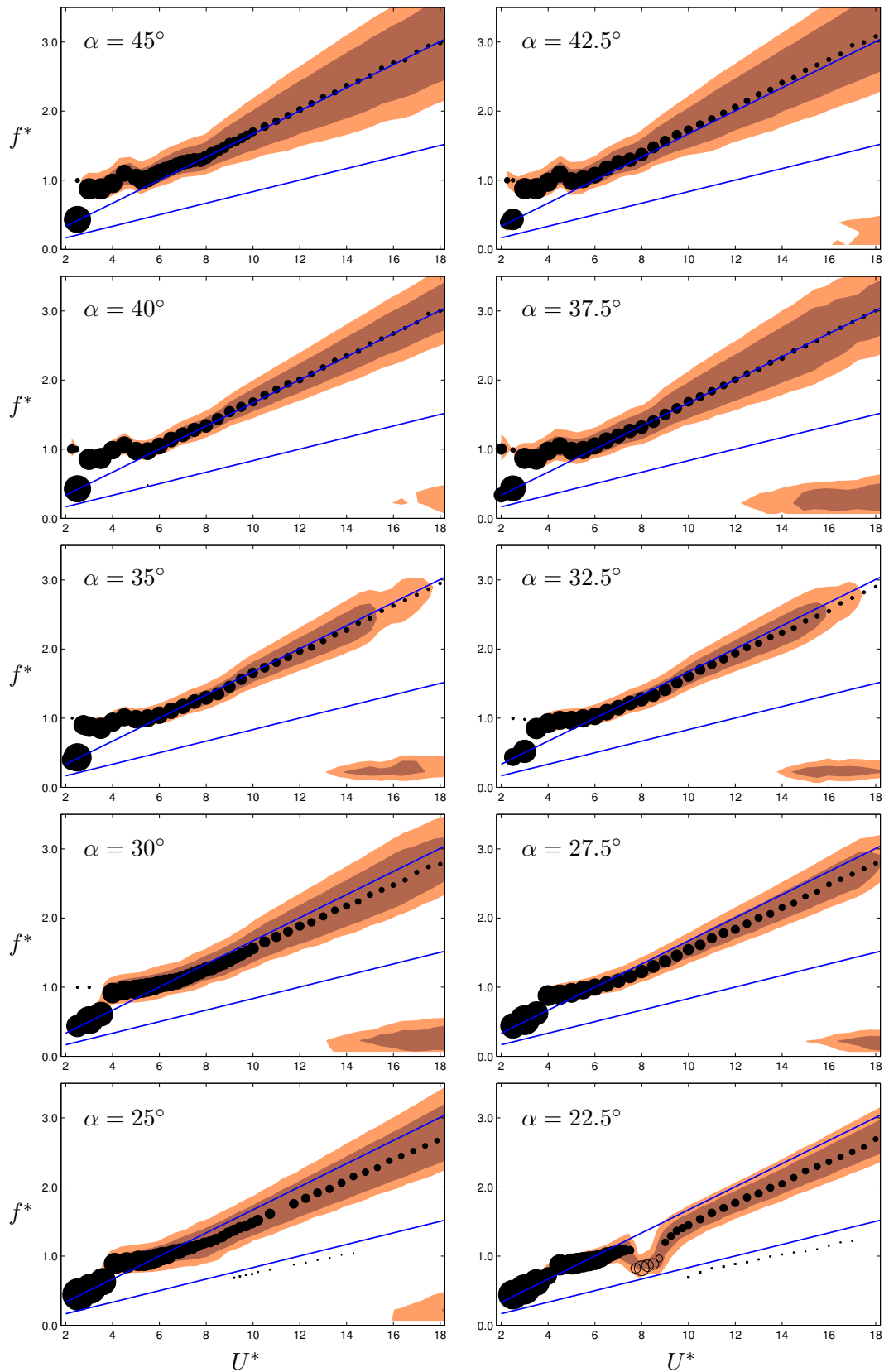


FIGURE 5.7: Square cylinder oscillation frequency response f^* to increasing reduced velocity U^* , at various angle of attack α . Shaded regions are contours of relative normalised intensity in wavelet energy. Filled circles represent shedding frequencies; Open circles represent frequencies associated with higher branch. (*To be continued*).

5.2. FIV of a square cylinder with angle of attack variation

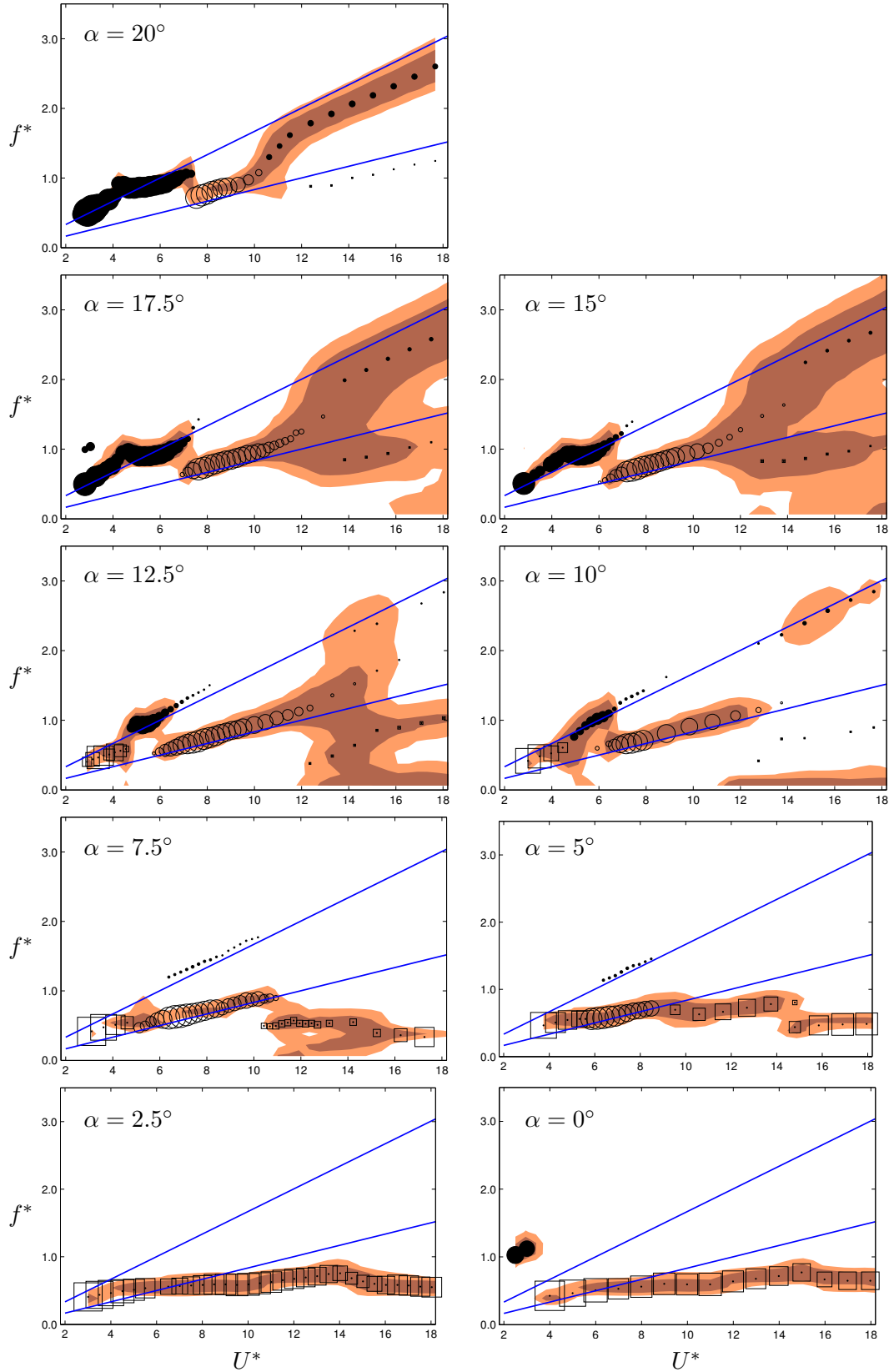


FIGURE 5.7: Open squares represent lower frequencies including those associated with galloping. The size of the symbols relate the power magnitude of the peaks. The dashed lines represent the Strouhal frequency $St = 0.167$ of the diamond cylinder and its first subharmonic. (*Continued*).

by a gradual increase in f^* with U^* ; the second behaviour is a decrease in frequency approaching $f^* = 0.5$. These two branches form a continuous trend at $\alpha = 0-2.5^\circ$, but become discontinuous at $\alpha = 5^\circ$ (located at $U^* = 15$), leading to a sudden jump in the frequency of oscillations.

5.2.4.3 Wake modes

Figure 5.8 shows four phases of the shedding modes for (a) the VIV upper branch and (b) the combined FIV higher branch at $\alpha = 20^\circ$ over one oscillation period. Of immediate interest from the perspective of circular cylinder studies is the vortex formation for the VIV upper branch. At $U^* = 5$, the square cylinder is in the centre of the resonant region in the upper branch of VIV, which we have shown in § 5.2.2.2 produces a 2P mode for in the diamond orientation.

At the beginning of the oscillation period [(1) in Figure 5.8 (a)], the square cylinder is moving upwards across the centreline of the oscillation cycle, and a clockwise (CW) vortex forms on the topside of the cylinder, with a counter clockwise (CCW) vortex, already shed, behind the cylinder. At the second phase (2), near the top of the body motion, CCW vorticity from the bottom wraps around the trailing edge of the body, and the top vorticity sheet splits in the strain region where the vortices meet near the top-right corner of the cylinder, causing the shedding of a CW vortex. The positive vorticity around the body increases (3) as the body moves back down through the centreline, forcing the top shear layer to shift further from the body. At the bottom of the motion (4), the top vortex sheet sheds another CW vortex, and vorticity of the same sign develops on the rear of the body, leading to the CCW vortex that is shed in the first phase of the cycle from bottom corner of the cylinder. Thus a P+S shedding mode is observed with two vortices shed from the top side of the cylinder in each cycle. The first vortex shed from the top side in this phase description of the body motion is significantly weaker than the other two and diffuses rapidly in the downstream wake. In the third phase (3), the counter clockwise vorticity on the topside of the square can be assumed to be separated near the corner of the square and is then cross-annihilated by its interaction with the top shear layer by the fourth phase.

These $P + S$ near-wake vortex interactions are not revealed in the VIV lift and oscillation frequency response. This is not unusual, as any energy contributed to the body from the vortex splitting of the pair would be minimal. The angle variation is responsible for the location of the square's corners and therefore a determining parameter influencing whether the shear layers encounter the high strain region located near the corners of the square. The PIV phase images indicate that the genesis of the vortex splitting is within these high strain regions, supporting the observation that the angle of attack defines the wake modes observed. As the square is rotated counter-clockwise from $\alpha = 45^\circ$ (decreasing angle of attack), the rear corner and its associated high strain region moves upwards, and less of the bottom shear layer wraps around the body. Eventually, as the body approaches the square orientation each shear layer interacts with a symmetry resulting in the 2S mode observed in Figure 5.5.

The higher branch vortex mode, shown in Figure 5.8(b) at $U^* = 8^\circ$ and $\alpha = 20^\circ$ displays a 2P wake. Comparing the two resonant regions wake states highlights the difference in timing of the vortex shedding with respect to the body's oscillation. For the higher branch the bottom shear layer in the first phase [Figure 5.8(b) (1)] extends further into the wake than at the lower velocity where VIV occurs, and results in a splitting that leads to the 2P wake structure. The first vortices shed from each side are close to the centre line and weaker than the second vortices, as seen for the diamond

5.2. FIV of a square cylinder with angle of attack variation

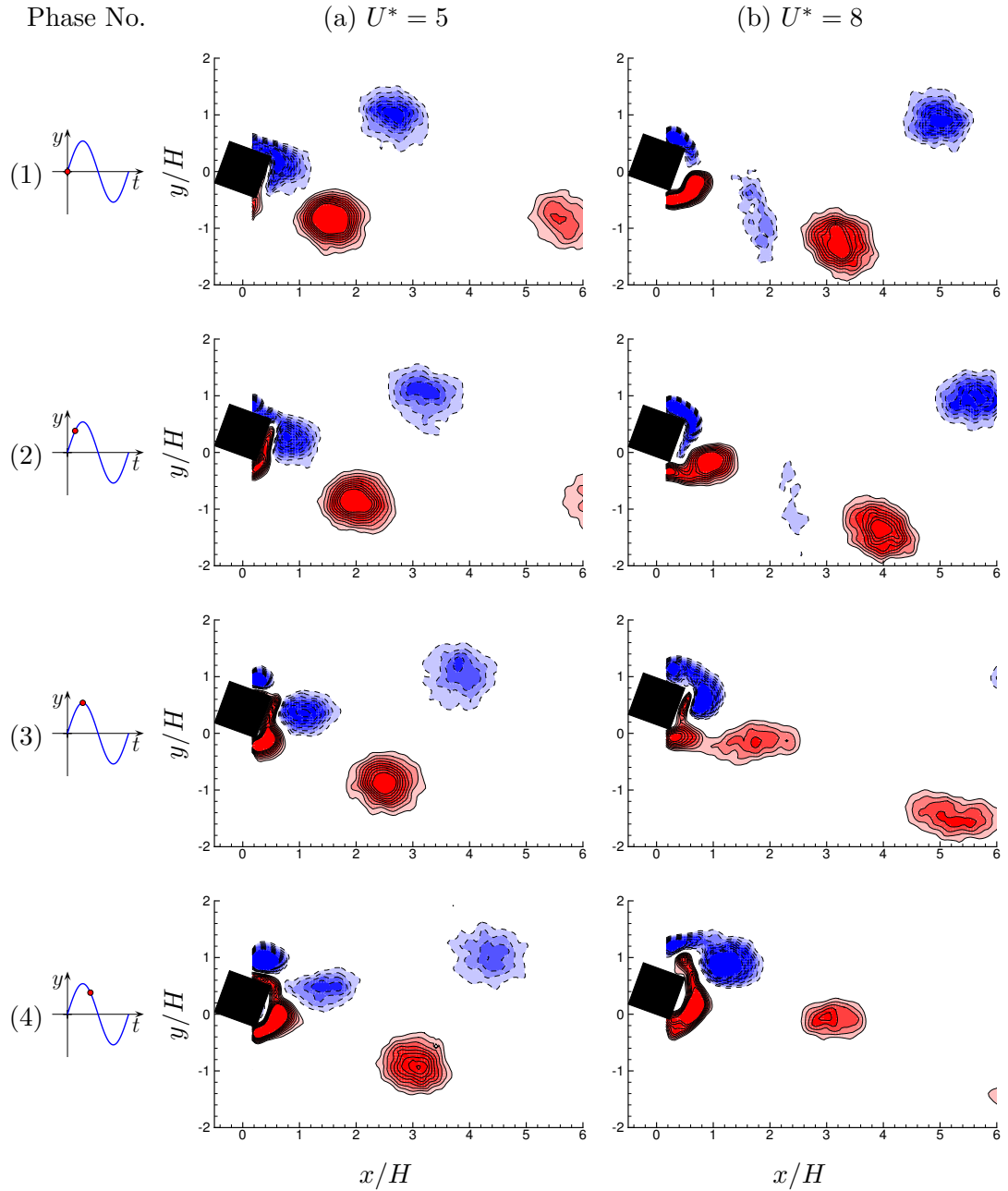


FIGURE 5.8: Phase-averaged PIV results showing the square cylinder oriented at $\alpha = 20^\circ$ with a $P+S$ shedding mode at $U^* = 5$ in (a), and a $2P$ mode at $U^* = 8$ in (b). Eight phases are shown over one oscillation cycle. The dashed iso-lines (filled blue) represent clockwise (negative) vorticity, and the solid iso-lines (filled red) represent counter-clockwise (positive) vorticity. (*To be continued*).

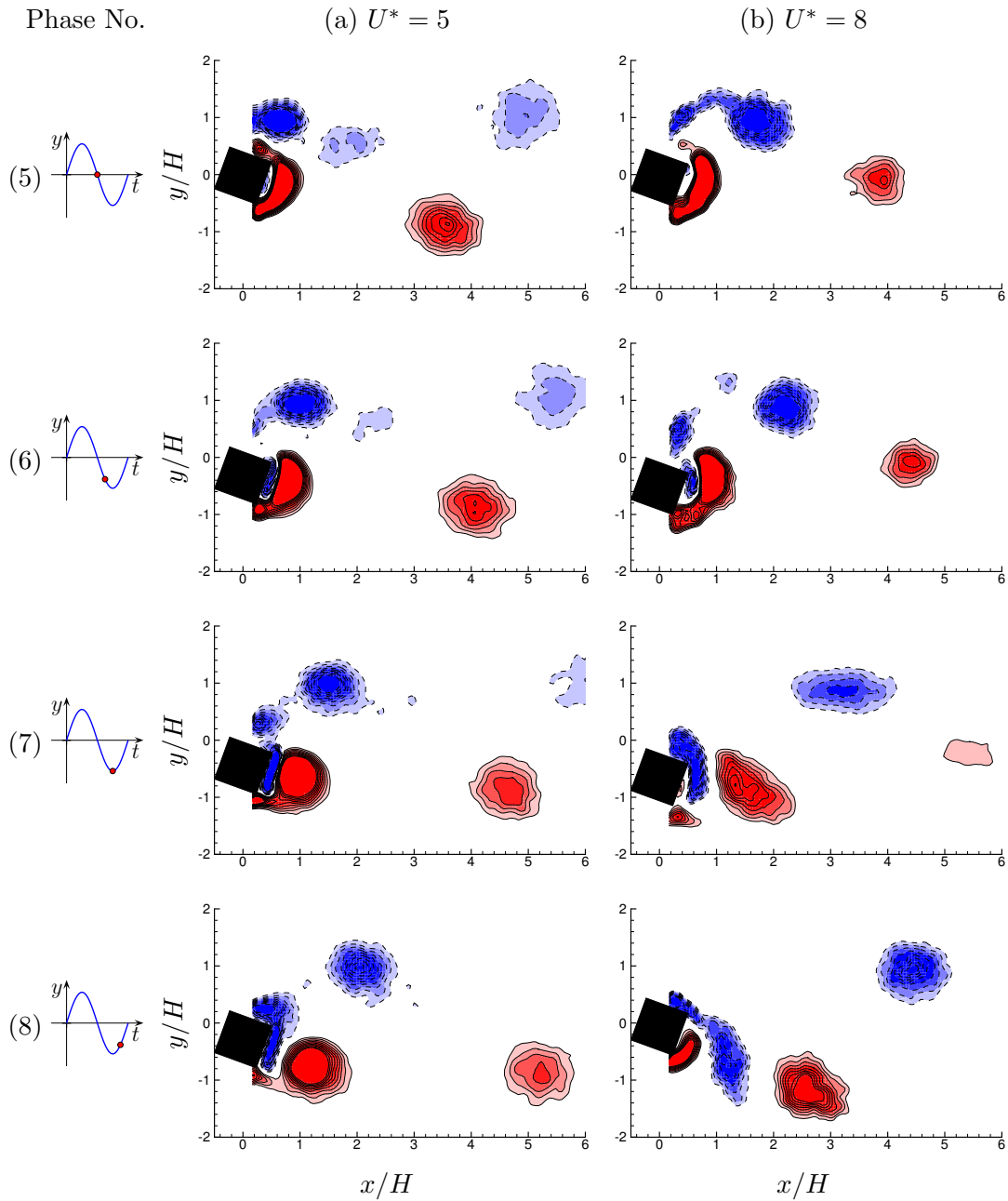


FIGURE 5.8: Phase-averaged PIV results showing the square cylinder oriented at $\alpha = 20^\circ$ with a $P+S$ shedding mode at $U^* = 5$ in (a), and a $2P$ mode at $U^* = 8$ in (b). Eight phases are shown over one oscillation cycle. The dashed iso-lines (filled blue) represent clockwise (negative) vorticity, and the solid iso-lines (filled red) represent counter-clockwise (positive) vorticity. (*Continued*).

5.3. VIV of a diamond cylinder with different mass ratios

VIV in Figure 5.3. The first vortex shed from the top of the cylinder is considerably weaker, diffusing rapidly in the near wake.

5.2.5 Intermittency

It is informative to discuss the intermittent behaviour observed in the oscillation response time series. In the higher branch the square cylinder oscillations undergo an intermittent phenomena that is not seen in either the VIV or galloping dominated regimes. This intermittency is isolated to the fringes of the higher branch regime, at $\alpha = 22.5^\circ$ and at $\alpha = 7.5^\circ$ (these are highlighted in darker shades on the map in Figure 5.9). Figure 5.10 shows the CWT of the oscillation measurements for increasing velocities at $\alpha = 7.5^\circ$. As the velocity is increased the oscillations experience a distinct and ultimately total loss of periodicity. Analysis of the frequencies was extended to cover a broader range than is shown here but no significant spectral energy contribution was found. The contours at $U^* = 7.9$ show a highly periodic signal with two distinct frequency bands, with peaks at $f = 0.458$ and its harmonic $f = 0.916$, and occasional loss of periodicity. As the velocity is increased, the loss of periodicity is more prominent, with no discernible frequency and, in fact, the cylinder barely oscillates. The duration and timing of the periodic loss appears chaotic, characteristic of intermittency.

5.3 VIV of a diamond cylinder with different mass ratios

The previous investigations in §5.2.2 have shown that a freely-vibrating diamond cylinder with low mass and damping ratios behaves in a VIV response fashion. One of the interesting findings is that the amplitude response A_{10}^* remains constantly at $A_{10}^* = 0.4$ in the desynchronisation region, which is much higher than that of a circular cylinder. This motivates further experiments to investigate the dynamic behaviours of a freely-vibrating diamond cylinder with different mass ratios.

5.3.1 Experimental details

The square cylinder model used in this section was the Body VI described in Table 3.3. This cylinder had an outside width of $W = 25$ mm and an immersed length of $L = 620$ mm, giving an aspect ratio of $AR = L/W = 24.8$ and a displaced water mass of $m_d = \rho W^2 L / 4 = 373.2$ g. Other system parameter values, such as the total mass of the system, the natural frequency in air and water, and the structural damping ratio, are given in Table 5.1. The total mass of the oscillating system was varied in a range of $985.4 \text{ g} \leq m \leq 5598 \text{ g}$, by adding extra weights on top of the air bearing system's carriage, which resulted in a mass ratio range of $2.64 \leq m^* \leq 15$ for the investigation. Correspondingly in the cases ($7.5 \leq m^*$) with excessive weights, the stiffness of the system was adjusted by adding extension spring pairs to ensure the reduced velocity range ($2 < U^* < 18$) of interest remained within the capacity of the water channel facility. The corresponding Reynolds number range was $1800 < Re < 16\,000$. The structural damping ratio measured was in a relatively low range of $1.31 \times 10^{-3} \leq \zeta \leq 2.58 \times 10^{-3}$. Additionally, the end condition was controlled using a platform with a gap of approximately 1 mm between the cylinder's free end.

To investigate the $2S \rightarrow 2P$ wake mode transition, PIV measurements were conducted at two reduced velocities. The PIV images were sampled using the phase-locked

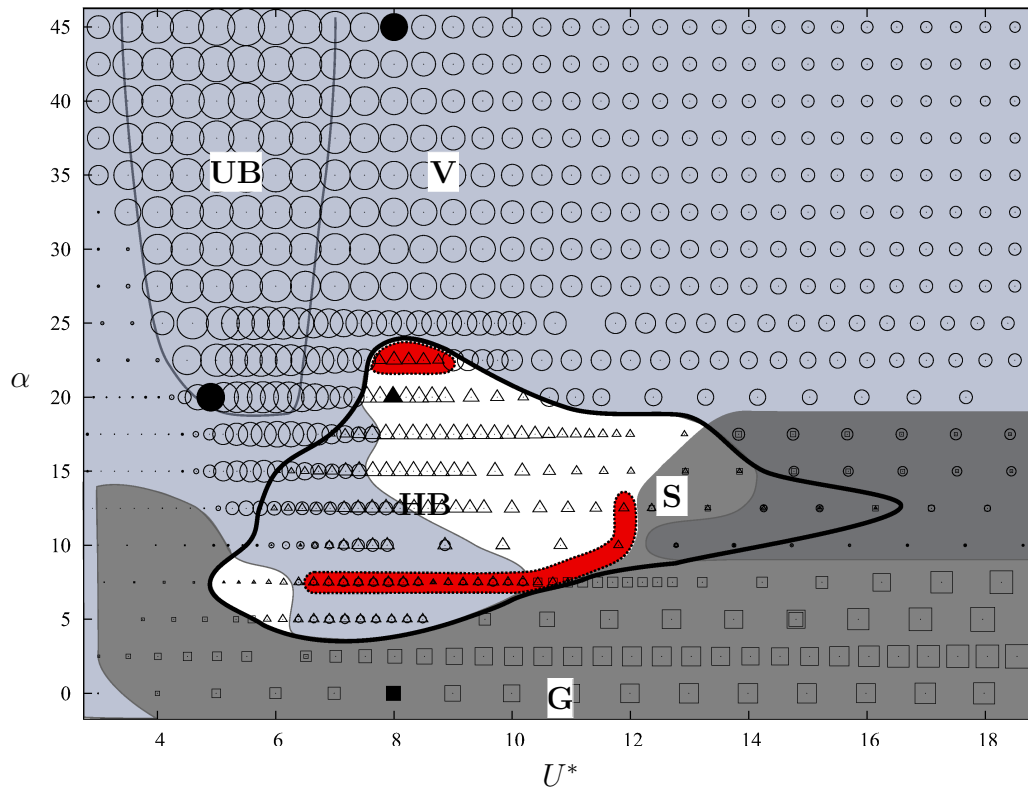


FIGURE 5.9: (Colour online) Map of flow-induced vibration response of a square cylinder with variation in the angle of attack, α , and reduced velocity, U^* . Regions are labelled according to response type. Shaded light blue region contains (UB) upper amplitude branch of VIV bounded by solid line, and (V) VIV dominated frequency response; region bound by thick solid line: Higher branch (HB) frequency response with black line bounding the high amplitude response region; dark shaded region: Galloping response (G) with low frequency galloping and low frequency dominated response with other frequency contributions. The region (S) represents a region where the HB frequency splits into diverging frequencies. Red regions bounded by dashed borders contain intermittency in the responses. Force and position measurement locations are shown by symbols representing the dominant frequency selection of the cylinder motion: Shedding frequency (circles); higher branch frequency (triangles); and lower frequencies (squares). The relative size of the symbols denote the relative energy of the dominant frequencies in the system. Filled symbols mark points where PIV measurements of the near wake were taken.

5.3. VIV of a diamond cylinder with different mass ratios

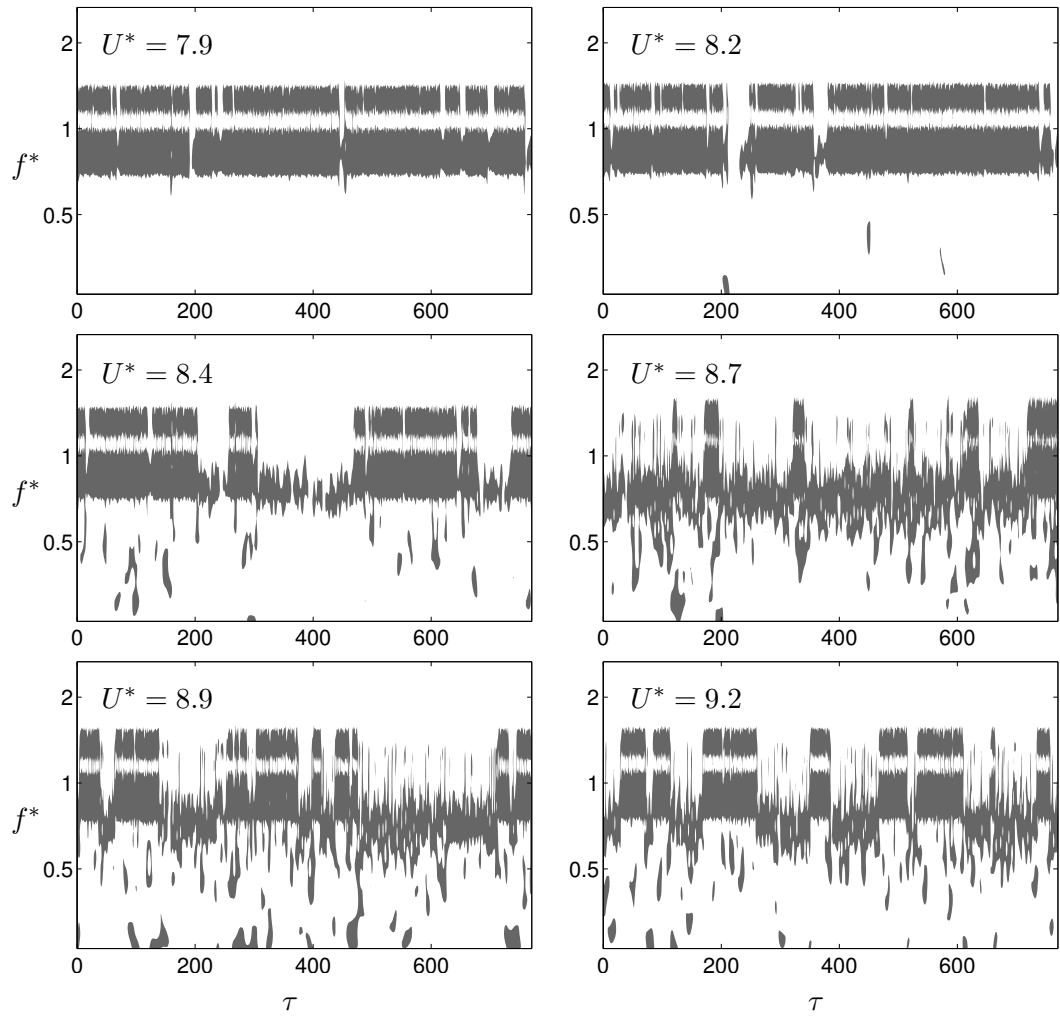


FIGURE 5.10: Time history of energy contour plots of frequency at $\alpha = 7.5$. The gaps in the contours highlight regions where the cylinder's periodic oscillation is disrupted.

m^*	m	m_d	f_{na}	f_{nw}	ζ	Spring Pairs
2.64	985.4 g	373.2 g	0.803 Hz	0.648 Hz	2.58×10^{-3}	1
3.0	1119.6 g	373.2 g	0.753 Hz	0.618 Hz	2.51×10^{-3}	1
3.5	1306.2 g	373.2 g	0.700 Hz	0.587 Hz	2.46×10^{-3}	1
4.0	1492.8 g	373.2 g	0.654 Hz	0.557 Hz	2.54×10^{-3}	1
5.0	1866 g	373.2 g	0.586 Hz	0.515 Hz	2.46×10^{-3}	1
7.5	2799 g	373.2 g	0.656 Hz	0.603 Hz	1.70×10^{-3}	2
10.0	3732 g	373.2 g	0.570 Hz	0.530 Hz	1.57×10^{-3}	2
15.0	5598 g	373.2 g	0.565 Hz	0.544 Hz	1.31×10^{-3}	3

TABLE 5.1: A table showing the experimental parameters of the total mass, the natural frequency in air and water, the structural damping ratio of a diamond cylinder system at different mass ratios

sampling technique (described in § 3.6.4) at eight different phases of the cylinder oscillation cycles, each phase containing 256 image pairs for vorticity field calculations. Along with the PIV measurements, the body displacement and fluid force were also measured simultaneously for more than 2000 oscillation cycles (> 1 hour).

5.3.2 Amplitude and frequency responses

Figure 5.11 shows the amplitude and frequency responses of the diamond cylinder with different mass ratios. Unsurprisingly, the amplitude and frequency responses of all mass ratio cases display a VIV response in general. The oscillations of all cases begin with very low amplitudes ($A_{10}^* < 0.06$) at low reduced velocities, while the oscillation frequencies follow the Strouhal number function trend, $St = 0.176$, of the stationary body. This Strouhal number measured with a platform end control is 5% higher than that of $St = 0.167$ measured with the body's free end given a small gap (2 mm) to the channel floor, suggesting the Strouhal number of a stationary diamond cylinder is more sensitive than a circular cylinder (within 1% in difference based on the previously presented results) to the effect of boundary layer associated with the channel floor. As the reduced velocity is increased, the oscillation frequencies are dominated by the natural frequency of the system, and the amplitudes jumps sharply to the initial branch with $A_{10}^* > 0.25$. The onset of U^* required for this initial amplitude jump depends slightly on the mass ratio. In the initial branch, the body's oscillations are highly periodic, with the oscillation frequency approaching to the natural frequency of the system. The amplitude response grows up to the upper branch when the oscillation frequency passes through the natural frequency of the system, namely $f^* = 1$. For the low mass ratio cases ($m^* \leq 5$), the A_{10}^* response grows gradually without sharp discontinuity from the initial to upper branch, while an obvious jump in the A_{10}^* are observed in the cases of $m^* > 5$. The maximum amplitude occurs in the reduced range of $5 < U^* < 6$ when the f^* response dips to a minimum value in that U^* range. The maximum A_{10}^* response of the case $m^* = 2.64$ observed is $A_{10}^* = 0.76$ at $U^* = 5.4$, while the case of $m^* = 15$ reaches its maximum A_{10}^* value of $A_{10}^* = 0.7$ at $U^* = 5.2$. After the maximum amplitude, the amplitudes of case $m^* = 2.64$ drops gradually to lower amplitudes of $A_{10}^* = 0.43$ at $U^* = 8$, and the oscillation frequencies follow the Strouhal number function trend again at higher reduced velocities, indicating the end of the synchronisation region. As the mass ratio is increased, the amplitude trends in the desynchronisation region are significantly suppressed from $A_{10}^* \approx 0.4$ for $m^* = 2.6$ to $A_{10}^* \approx 0.07$ for $m^* = 15$. Additionally, the upper limit the synchronisation region is reduced from $U^* = 8$ for $m^* = 2.64$ to $U^* = 7$ for $m^* = 15$.

In contrast to what is seen in the classic circular cylinder geometry, these results the amplitude response in the desynchronisation region can be suppressed significantly by the effect of mass ratio.

5.3.3 Wake mode transition

The previous results have shown that a $2P$ wake mode is observed in the case with $m^* = 2.2$ at $U^* = 8.0$ in §5.2.2.2, while other PIV measurements (not presented in this thesis) also revealed a wake mode transition from a $2S$ mode at $U^* = 3.25$ to a $2P$ mode at $U^* = 4.25$. Thus, it is of interest to understand the relationship between wake mode transition and the vortex phase of a freely-vibrating diamond cylinder. On the basis of previous studies of VIV of circular cylinders, a sharp jump in the vortex phase from 0° to 180° is expected to be associated with the wake mode transition from $2S$ to

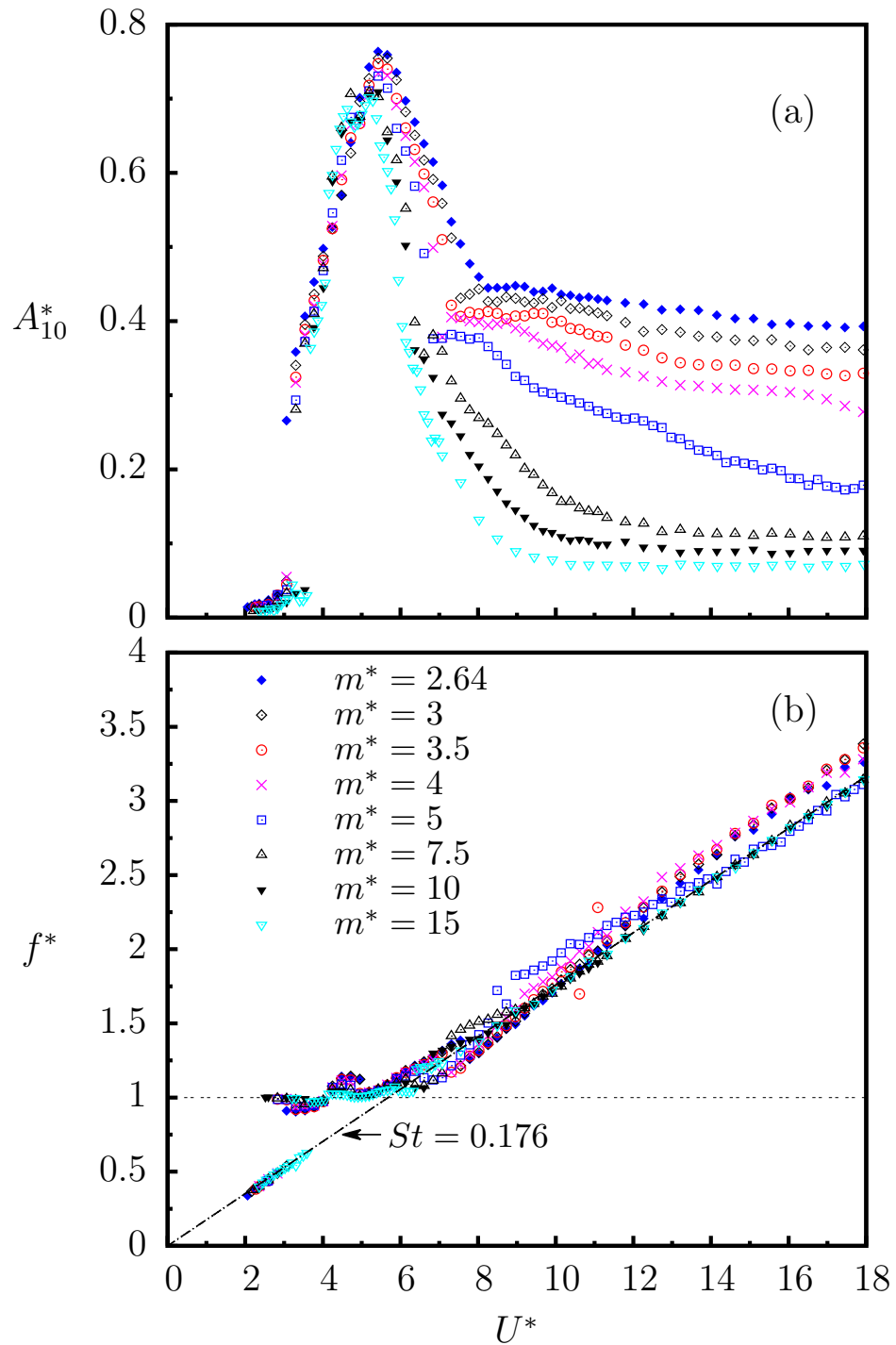


FIGURE 5.11: The amplitude and frequency responses of a diamond cylinder with different mass ratios.

$2P$ in the diamond cylinder case. To reveal this relationship, PIV measurements were conducted on a diamond cylinder with a relatively high mass ratio of $m^* = 15$.

Figure 5.12 shows the diamond cylinder's vortex phase response in (c), along with the amplitude and frequency responses that have been presented previously in Figure 5.11. The locations of the PIV measurements at $U^* = 3.75$ and $U^* = 4.2$ are highlighted in red brackets. Like other cases of different mass ratios, the diamond cylinder's oscillations begin with very low amplitudes ($A_{10}^* < 0.06$) and the reduced frequency f^* following the Strouhal number function trend of the fixed body, and then the oscillation amplitudes jump with $A_{10}^* \approx 0.4$ when the dominant oscillation frequency is well defined with a single peak value and jumps up close to the natural frequency of the system in water. Unlike the cases with lower mass ratios (i.e. $m^* \leq 5$) having a gradual amplitude growth without discontinuity from the initial branch to the upper branch, the present amplitude response experiences an obvious jump from the initial branch to the upper branch, with $A_{10}^* = 0.46$ jumping to $A_{10}^* = 0.58$ at $U^* \approx 4.1$. Corresponding to this jump, the vortex phase also undergoes a jump from $\phi_{vortex} = 0^\circ$ to $\phi_{vortex} = 180^\circ$ when the oscillation frequency passes through the natural frequency of the system in water. The ϕ_{vortex} remains constantly around 180° over a reduced velocity range of $4.1 < U^* < 6.4$, before it jumps gradually down to $\phi_{vortex} \approx 155^\circ$ as the oscillation frequency moves back to follow the Strouhal number function trend for higher reduced velocities. It should be noted that the vortex phase calculations are conducted only when the oscillations are highly periodic, due to the assumption that the oscillations can be approximated to a sinusoidal function (Govardhan & Williamson 2000).

Figure 5.14 shows PIV measurement results of the diamond cylinder undergoing a wake mode transition from a $2S$ mode at $U^* = 3.75$ to a $2P$ mode at $U^* = 4.20$. In Figure 5.14 (a), as the body moves upwards from the centre position in (1) to the top position ($y \approx 0.4H$) in (3), the negative vorticity of the shear layer forming from the upper side corner of the body gradually becomes stronger causing a positive CCW vortex (red) formed on the lower side to shed in (3). After the first single vortex has been shed, the body is beginning to move back to the centre position, and the positive vorticity of the shear layer forming from the bottom side corner gradually becomes stronger and rolls up to initiate the shedding of a negative CW vortex when the body reaches the bottom position ($y \approx -0.4H$) in (7). This vortex shedding procedure repeats itself to shed off two single vortices per oscillation cycle. Due to the fixed flow separation points and high strain caused by the sharp trailing edge, the vortices are shed off alternately in the very near wake and are organised in a stable double-row configuration with a parallel wake width of $2H$, while a single-row $2S$ mode is widely reported to exist in the initial branch of the circular cylinder cases.

Figure 5.14 (b) shows the $2P$ mode, which is similar to that of the case with $m^* = 2.2$ at $U^* = 8.0$ shown in Figure 5.3 (b). At the beginning in (1), the body moves upwards from the centre position, and a CCW vortex is being shed from the bottom shear layer. As the body continues moving towards to the top position of the oscillation cycle in (2) – (3), a negative CW vortex is shed off from the body's trailing edge to form the a first vortex pair with the previously shed CCW vortex. This procedure is mirrored as the body is moving downwards from the top to the bottom position of the oscillation cycle, as shown in (4) – (7), causing a second vortex pair to shed. As in the case shown in Figure 5.3 (b), the vortices travelling close to the centre line are relatively weaker, and they dissipate at $x \approx 4H$ in the downstream. The CCW and CW vortices shed from the body side corners, on the other hand, are spread much wider than those in the $2S$

5.3. VIV of a diamond cylinder with different mass ratios

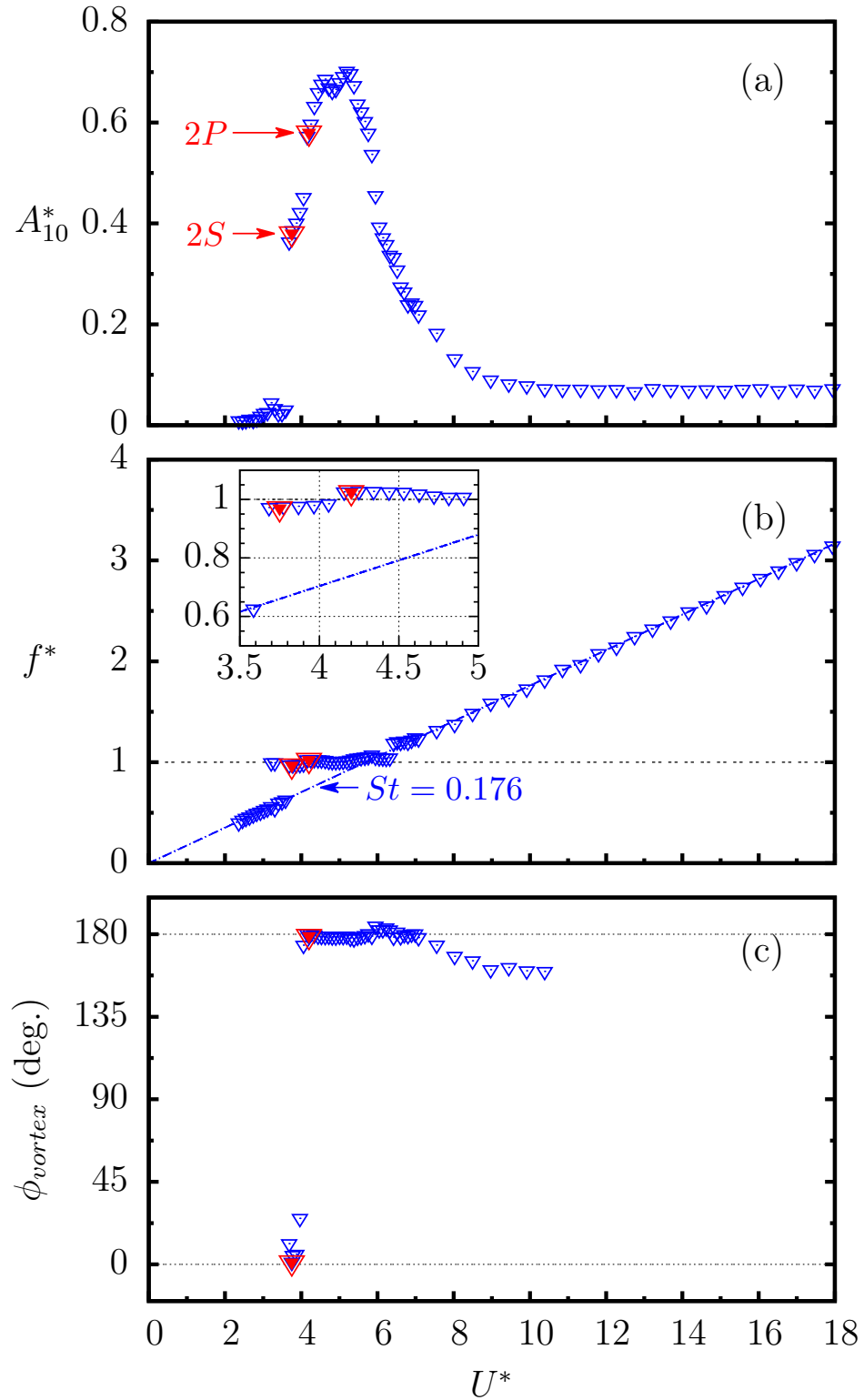


FIGURE 5.12: Plots of the amplitude, frequency and vortex phases responses of a diamond cylinder with $m^* = 15.0$. The symbols highlighted in red brackets represent locations where the wake vorticity field is measured using PIV technique. The diamond cylinder undergoes a wake mode transition of from a $2S$ to a $2P$ mode associated with a vortex phase jump from 0° to 180° in (c), as the amplitude response jumps from the initial branch to the upper branch in (a) and the oscillation frequency passes through the natural frequency of the system in water at $U^* \approx 4.1$ in (b).

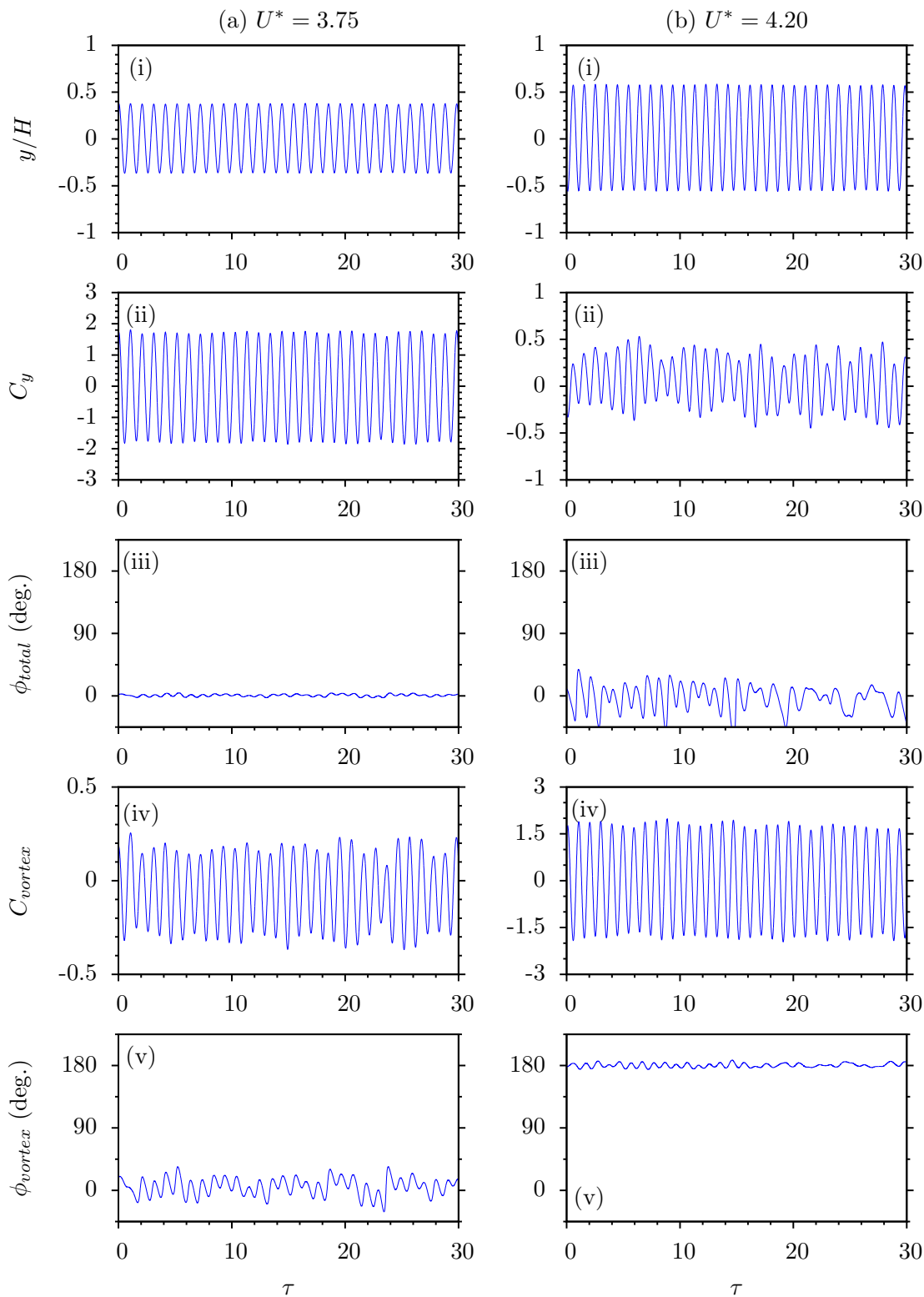


FIGURE 5.13: Time traces of the displacement, total transverse lift, total phase, vortex force and vortex phase of a diamond cylinder with $m^* = 15.0$ and $\zeta = 1.31 \times 10^{-3}$ at $U^* = 3.73$, corresponding to $Re = 2755$, in (a) and $U^* = 4.20$, corresponding to $Re = 3085$, in (b). As the oscillation frequency passes through the natural frequency of the system, the vortex phase, ϕ_{vortex} , experiences a sharp jump from around 0° to 180° , which is associated with a wake mode transition from $2S$ to $2P$ mode. This wake mode transition causes a change in the timing of vortex shedding, and then results in significant increase of the magnitude of the vortex force.

mode due to larger oscillation amplitudes, and they travel with an oblique angle with respect to the centre line. Compared to the $2P_o$ mode behind an oscillating circular cylinder when $\phi_{total} \approx 0^\circ$ and $\phi_{vortex} \approx 180^\circ$, the present vorticity fields of the diamond show that the second vortex in each vortex pair is much stronger than that of the $2P_o$ mode of circular cylinders.

In conclusion, the results have shown that a freely vibrating diamond cylinder undergoes a wake mode transition from a $2S$ to a $2P$ mode, which is associated with a jump in the vortex phase and a jump in the amplitude response from the initial to the upper branch, as the oscillation frequency passes through the natural frequency of the system in water. This wake mode transition is similar to the case of a circular cylinder with $m^* = 8.63$ studied by Govardhan & Williamson (2000). However, both the force and vorticity measurements of the diamond cylinder cases ($m^* = 2.2$ and 15) do not observe the coexistence of $2S$ and $2P$ (or $2P_o$) modes that have been found in VIV of a circular cylinder with $m^* = 2.66$ presented previously in § 4.3.3, which may suggest the coexistence of $2S$ and $2P$ (or $2P_o$) modes are present only in the circular cylinder cases with very low mass and damping ratio.

5.4 Summary of the chapter

This chapter has shown cross-flow FIV response of a freely vibrating square cylinder with low mass-damping ratio. Investigations are firstly undertaken on two symmetric orientations: the diamond orientation ($\alpha = 45^\circ$) and the square orientation ($\alpha = 0^\circ$). Similar to the circular cylinder case, the diamond orientation behaves in a VIV response fashion over an investigated reduced velocity range of $2 < U^* < 18$. The results show that the diamond cylinders experience a narrower resonant region comparable to that of the circular cylinder cases with similar mass and damping ratio. The results also reveal the influence of the shear layer separation on the fluid forces experienced by the body, indicated by the oscillation frequency of the body following the Strouhal shedding frequency of the stationary. Furthermore, the lift force decomposition of the diamond cylinder shows two similar jumps in the total lift force phase and the vortex phase that have been seen in the previous circular cylinder cases. The PIV measurements for the wake modes also clearly reveal that a wake mode transition from $2S$ to $2P$ is associated with a jump in the vortex phase from 0° to 180° . As expected, the square orientation, on the other hand, experiences galloping phenomenon with the oscillation amplitude growth in good agreement with the literature.

As the angle of attack is varied from $\alpha = 45^\circ$ to $\alpha = 0^\circ$, the square cylinder experiences transitions of body-oscillator phenomena from VIV to a complex non-linear combination mode of VIV and galloping, and then to galloping. A new higher branch (HB) having an oscillation envelop in excess of amplitudes produced by either VIV and galloping is uncovered in the combined mode region. This new branch is also characterised by multiple-frequency oscillations with a frequency component close to the sub-harmonic of the vortex shedding frequency of the stationary body. However, the current body oscillator models do not account for this new branch, nor does the quasi-steady theory. Galloping response of a square cylinder with low mass-damping ratio is limited to the angle of attack of $\alpha < 10^\circ$.

The current work has shown body geometry is an important control parameter in the formation and shedding of vortices from a square cross-sectional cylinder. As a result of body geometry, the dynamic FIV response of the body is significantly influenced.

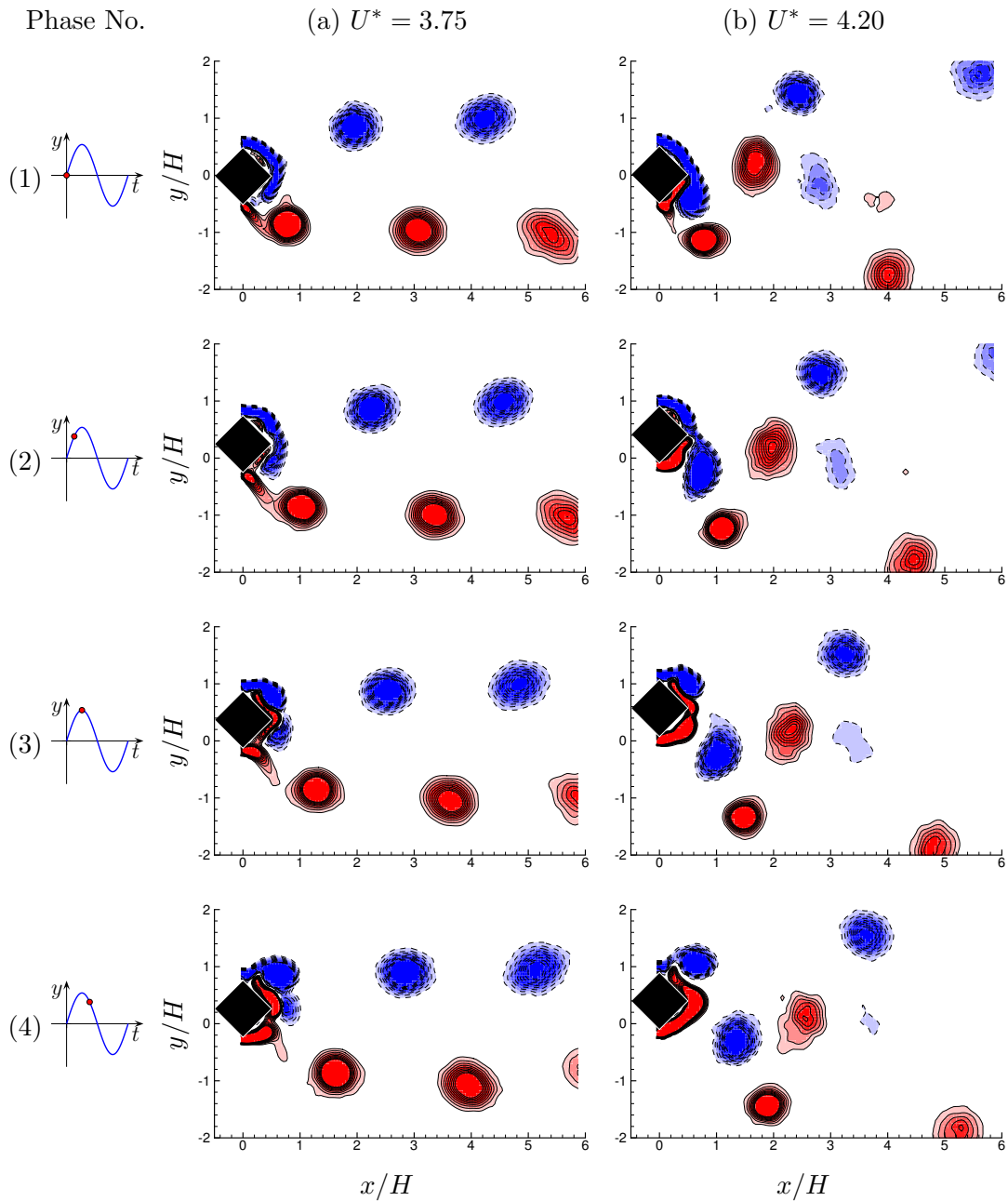


FIGURE 5.14: Phase-averaged PIV results showing a double-row $2S$ shedding mode of a diamond cylinder with $m^* = 15$ at $U^* = 3.75$, and a $2P$ mode at $U^* = 4.20$. Eight phases are shown over one oscillation cycle. The dashed iso-lines (filled blue) represent clockwise (negative) vorticity, and the solid iso-lines (filled red) represent counter-clockwise (positive) vorticity.

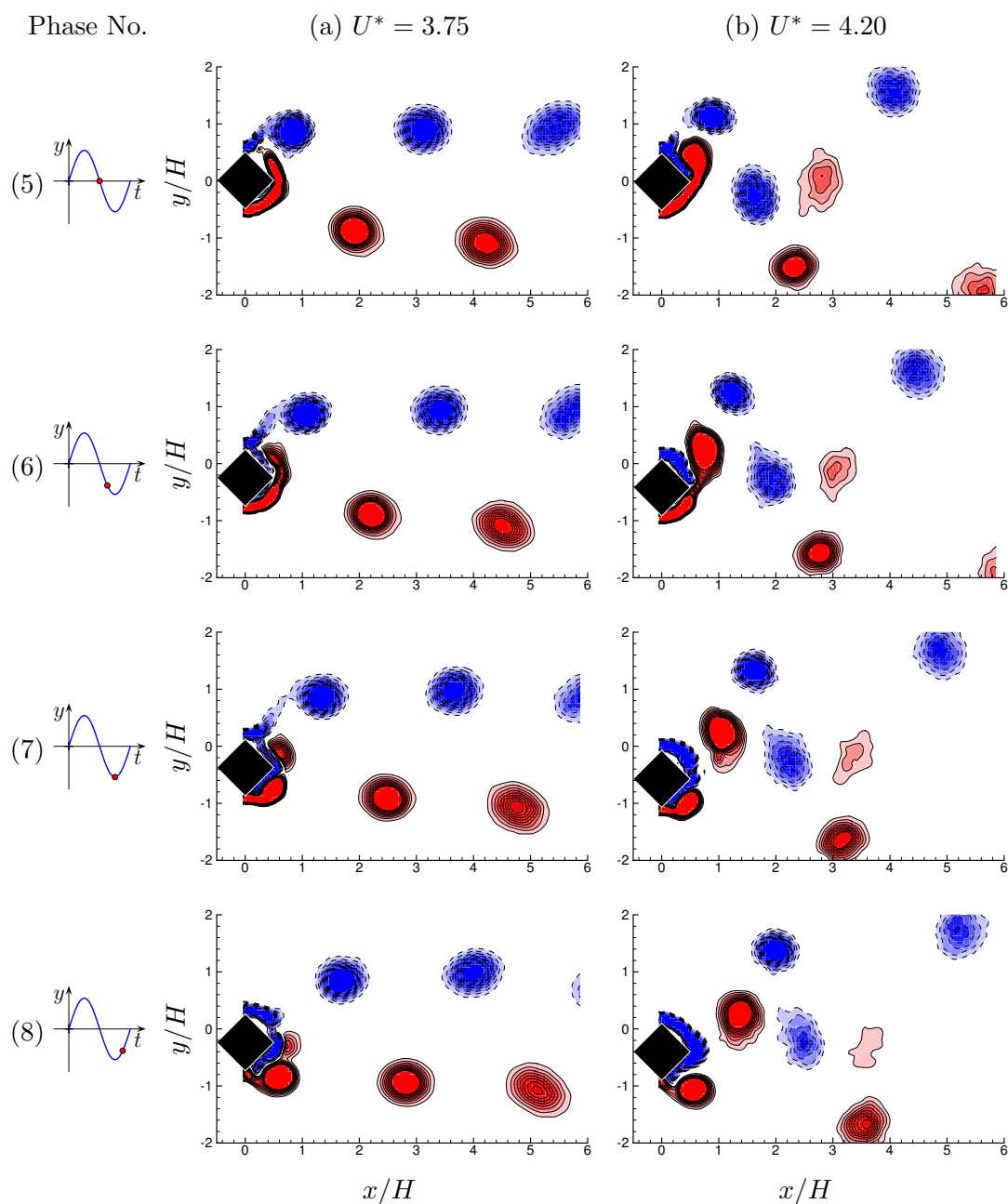


FIGURE 5.14: Phase-averaged PIV results showing a double-row $2S$ shedding mode of a diamond cylinder with $m^* = 15$ at $U^* = 3.75$, and a $2P$ mode at $U^* = 4.20$. Eight phases are shown over one oscillation cycle. The dashed iso-lines (filled blue) represent clockwise (negative) vorticity, and the solid iso-lines (filled red) represent counter-clockwise (positive) vorticity. (*Continued*).

Chapter 6

Conclusions and Recommendations for Future Work

6.1 Conclusions

In this thesis, transverse flow-induced vibrations of circular and square cylinders with low mass and damping have been investigated experimentally over a range of parameter space, such as the reduced velocity, mass ratio, and angle of attack in the square cylinder cases. In particular, the dynamic response of two typical body-oscillator phenomena of FIV, vortex-induced vibration and galloping, were fundamentally studied using simultaneous measurements of the body displacement, the fluid forces on the body and the vortex structures in the near wake. A summary of the main findings from this study are outlined in the following sections.

6.1.1 Vortex-induced vibration of a circular cylinder

The results of VIV of circular cylinders with low mass and damping, which agree well with the prior studies in the literature, have shown there are three amplitude response branches, depending on the reduced velocity: the initial, the upper and the lower branches. The body oscillations in the initial branch are characterised by quasi-periodic motion influenced primarily by the vortex shedding frequency and the natural frequency of the system. The amplitude response undergoes a jump to the upper branch at $U^* \approx 1/St$, as the oscillation frequency passes through the natural frequency of the system in water, indicating the onset of the lock-in region. Across this amplitude jump, Govardhan & Williamson (2000) proposed that a cylinder underwent a wake mode transition of $2S \leftrightarrow 2P$ modes corresponding to a sharp jump in the vortex phase, $\phi_{vortex} = 0^\circ \leftrightarrow 180^\circ$. However, the present results of a cylinder with $m^* = 2.66$ have shown that a $2S$ mode is observed at the beginning of the upper branch where the body oscillation frequency is equal to the natural frequency of the system, $f^* = 1$, and the vortex phase is constantly at $\phi_{vortex} \approx 0^\circ$. Further, the measurements of the forces and vorticity fields have confirmed the coexistence of the $2S$ and the $2P_o$ modes in the middle of upper branch at $U^* = 5.91$, where the body experiences the largest amplitude vibration. These observations have not previously reported in the previous studies of free vibration of circular cylinders. As the reduced velocity is further increased, the amplitude response undergoes an intermittent-switching transition of between the upper

and lower branches at higher reduced velocities. This response branch transition is associated with sharp changes in the total phase between 0° and 180° , and a $2P_o \leftrightarrow 2P$ wake mode transition. It is widely accepted that the fluid force and the cylinder motion are highly periodic in the lower branch.

The dynamic response of a freely-vibrating cylinder has been compared with that of the forced vibrations of the cylinder following the free-vibration and sinusoidal trajectories. The comparison results have shown that the transverse lift and vortex forces, total and vortex phases, and the wake mode patterns of free vibration can be replicated by the forced vibration precisely following the free-vibration trajectory when the total and vortex phases are constant over time in the initial branch, the beginning of the upper branch and the lower branch. While in the middle of the upper branch of free vibration where the body experiences largest-scale oscillations and complicated sharp changes in the total and vortex phases, comparison results have shown significant differences between the free and the trajectory-following vibrations arise primarily from the total phase, the decomposed vortex force and phase, and the wake modes. In particular, the tracking vibration presents coexistence of three wake modes, the $2S$, the $2P_o$ and the $2P$ modes, compared to only two modes, $2S$ and $2P_o$ modes, coexisting in the free vibration case. However, the causes for the differences between the two vibration cases have still not been fully explained.

On the other hand, the results from a cylinder forced to oscillate sinusoidally agree well with the literature. It has been shown that sinusoidal forced vibration is an adequate model for free vibration in the lower branch, where the total and vortex forces are well represented by sinusoidal functions and the phases are constantly around 180° . Compared directly with free vibrations in the upper branch, sinusoidal forced vibrations with the A_{10}^* amplitude were found to have both the total and vortex phases above 180° indicating the energy transfer was from the structure to the fluid.

6.1.2 Flow-induced vibration of a square cylinder

FIV of a square cylinder was initially examined at $m^* = 2.2$ on two symmetric orientations: the diamond ($\alpha = 45^\circ$) orientation and the square ($\alpha = 45^\circ$) orientation. The results showed that the response of a diamond cylinder behaves in a VIV fashion over an investigated reduced velocity range of $2 < U^* < 18$. Compared with the case of a circular cylinder, VIV of a diamond cylinder was found to have a narrower resonant region with the maximum oscillation amplitudes approximately 15% less than the circular cylinder case with similar mass and damping ratio. Interestingly, the A_{10}^* amplitude response throughout the desynchronisation region was constantly around $A_{10}^* = 0.4$, much larger than that of the circular cylinder case, $A_{10}^* \approx 0.1$. Like the circular cylinder cases, force decomposition also revealed that VIV of a diamond cylinder also experiences two sharp jumps in the total phase and the vortex phase. A sharp jump in the vortex phase from around 0° to 180° was found to be associated with a jump in the amplitude response from the initial branch to the upper branch, as the body oscillation frequency passes through the natural system in water. Corresponding to this jump, vorticity measurements also demonstrated that the wake mode undergoes a transition from the $2S$ to the $2P$ mode, rather than from the $2S$ to the $2P_o$ mode (the weak $2P$ mode) that has been seen in the circular cylinder case. There is also a sharp jump in the total phase around 0° to 180° at the end of resonant region indicated by the oscillation frequency following the Strouhal frequency for the stationary body. However, the wake mode still remains as the same $2P$ mode. Later, subsequent experiments have investigated the effect of mass ratio on the amplitude response of

the desynchronisation region, showing that the A_{10}^* response was considerably reduced from around 0.4 to 0.1 as the m^* was increased from 2.2 to 15. As expected, the results of the square orientation, on the other hand, have shown that the cylinder experiences galloping phenomenon with the oscillation amplitude growth in good agreement with the literature.

Further, the results of the square cylinder with angle of attack variation have shown that the vibration response of the body can be influenced significantly by the physical angle of attack with respect to the free-stream flow. The body experiences transitions of body-oscillator phenomenon from VIV to a complex non-linear combination mode of VIV and galloping, and then to galloping, as the angle of attack is varied from $\alpha = 45^\circ$ to 0° . A new higher branch (HB) having an oscillation envelop in excess of amplitudes produced by either VIV or galloping is observed in the combined mode region over $10^\circ \leq \alpha \leq 22.5^\circ$. This new branch is also characterised by multiple-frequency oscillations with a frequency component close to the subharmonic of the vortex shedding frequency of the stationary body. However, the current body oscillator models do not account for this new branch, nor does the quasi-steady theory. Galloping response of a square cylinder with low mass-damping ratio is limited to the angle of attack of $\alpha < 10^\circ$.

6.2 Recommendations for future work

It is hoped that the present study has provided some additional understanding of the dynamic response of FIV of circular and square cylinders. However, it has inevitably raised a number of fundamental issues that could be investigated. In this final section, some of these issues are listed below under separate headings for vortex-induced vibration of a circular cylinder, and flow-induced vibration of a square cylinder.

6.2.1 Vortex induced vibration of a circular cylinder

- Further investigation of the wake mode overlapping region in the upper branch. If the causes responsible for the switching phenomena of the total and vortex phases could be addressed, it would be helpful to develop a more accurate model for the VIV response in the upper branch. This may involve modulating the amplitude and the frequency of forced motion to characterize the forces on the body, the corresponding phases, and the wake modes in the near wake.
- Active control of VIV. As the results have shown that slight modulation in the forced motion can result in significant differences in the forces, the phases and the wake modes, active control of VIV, by introducing perturbations either into the oscillating structure or the flow, could be explored on the basis of the air-bearing rig and the real-time feedback control system.

6.2.2 Flow-induced vibration of a square cylinder

- Investigation of FIV a diamond cylinder with angle of attack variation at low Reynolds number (*i.e.* $Re < 1000$). This could be done using numerical simulations. As it is extremely difficult to experimentally investigate the shear layer structures around an square cylinder undergoing combined galloping and VIV, a numerical study would also help to explain the influence of flow separation on the

Chapter 6. Conclusions and Recommendations for Future Work

dynamic responses of the oscillating body, which is believed to have significant impact on the body-oscillator phenomena.

- Prediction of VIV of a diamond cylinder with low mass and damping ratio. This could be done, using the air-bearing rig and the motion control system developed, by comparing the free vibration and forced vibration. Within this framework, contributions would be made for contours of the fluid forces, the phases, and the wake mode regimes, providing better understanding of the flow past an oscillating bluff body.
- Further investigation of the effect of mass ratio on the amplitude and frequency responses of FIV a square cylinder with angle of attack variation, especially the responses of the higher branch in the combined mode region of VIV and galloping.

Appendix A

Wheatstone Bridge

A Wheatstone bridge circuit (as shown in Figure A.1) is most frequently used for strain measurements. It is noted that a full Wheatstone bridge circuit configured with four active gauges has an important effect to achieve temperature compensation.

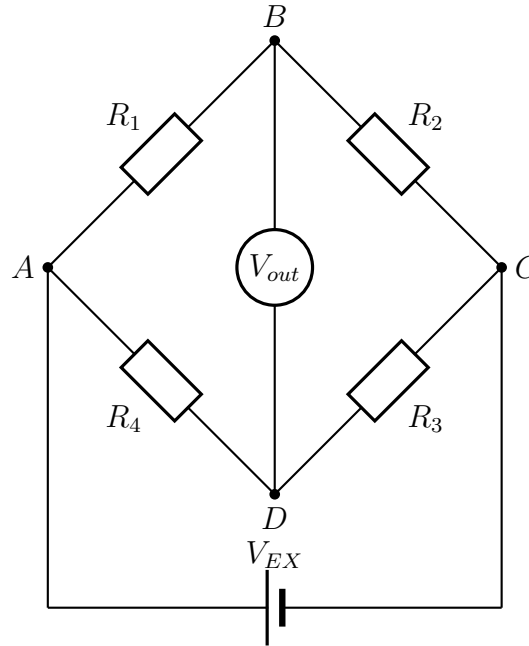


FIGURE A.1: A diagram of full Wheatstone bridge circuit.

According to Kirchhoff's first rule, the currents in junctions B and D can be found by the following equations:

$$I_1 - I_2 + I_G = 0 \quad (\text{A.1})$$

$$I_4 - I_3 - I_G = 0, \quad (\text{A.2})$$

where I_G is the current flowing through the galvanometer between the points B and D . Thus, the voltage in the loops of ABD and BCD can be found using Kirchhoff's second rule by the following equations:

$$I_1 \cdot R_1 - I_4 \cdot R_4 - I_G \cdot R_G = 0 \quad (\text{A.3})$$

$$I_2 \cdot R_2 - I_3 \cdot R_3 + I_G \cdot R_G = 0. \quad (\text{A.4})$$

Appendix A. Wheatstone Bridge

If the bridge is balanced and $I_G = 0$, the above set of equations can be rewritten as follows:

$$I_1 \cdot R_1 = I_4 \cdot R_4 \quad (\text{A.5})$$

$$I_2 \cdot R_2 = I_3 \cdot R_3. \quad (\text{A.6})$$

Thus, the output voltage V_{out} is determined by the following equation:

$$V_{out} = \left(\frac{R_2}{R_1 + R_2} - \frac{R_3}{R_3 + R_4} \right) V_{EX}. \quad (\text{A.7})$$

Differentiating Eq. A.7 yields:

$$\frac{dV_{out}}{V_{EX}} = \frac{R_1 R_2}{(R_1 + R_2)^2} \left(\frac{dR_2}{R_2} - \frac{dR_1}{R_1} \right) - \frac{R_3 R_4}{(R_3 + R_4)^2} \left(\frac{dR_3}{R_3} - \frac{dR_4}{R_4} \right). \quad (\text{A.8})$$

If $R_1 = R_2 = R_3 = R_4$, the above Equation A.8 can be rewritten as follows:

$$\frac{dV_{out}}{V_{EX}} = \frac{1}{4} \left[\left(\frac{dR_2}{R_2} - \frac{dR_1}{R_1} \right) - \left(\frac{dR_3}{R_3} - \frac{dR_4}{R_4} \right) \right] \quad \text{for subtracting circuit,} \quad (\text{A.9})$$

or

$$\frac{dV_{out}}{V_{EX}} = \frac{1}{4} \left[\left(\frac{dR_2}{R_2} - \frac{dR_1}{R_1} \right) + \left(\frac{dR_4}{R_4} - \frac{dR_3}{R_3} \right) \right] \quad \text{for adding circuit.} \quad (\text{A.10})$$

References

- ADRIAN, R. 1991 Particle-imaging techniques for experimental fluid mechanics. *Annual Review of Fluid Mechanics* **23** (1), 261–304.
- ANG, K., CHONG, G. & LI, Y. 2005 PID control system analysis, design, and technology. *Control Systems Technology, IEEE Transactions on Control Systems Technology* **13** (4), 559–576.
- ÅSTRÖM, K. & HÄGGLUND, T. 2006 *Advanced PID Control*. ISA.
- BARKLEY, D., TUCKERMAN, L. & GOLUBITSKY, M. 2000 Bifurcation theory for three-dimensional flow in the wake of a circular cylinder. *Physical Review E* **61** (5), 5247–5252.
- BEARMAN, P. W. 1984 Vortex Shedding from Oscillating Bluff Bodies. *Annual Review of Fluid Mechanics* **16** (1), 195–222.
- BEARMAN, P. W., GARTSHORE, I., MAULL, D. & PARKINSON, G. V. 1987 Experiments on flow-induced vibration of a square-section cylinder. *Journal of Fluids and Structures* **1** (1), 19–34.
- BÉNARD, H. 1908 Formation de centres de giration a l’arriere d’un obstacle en mouvement. *C.R. Acad. Sci. Paris* **147**, 839.
- BISHOP, R. & DORF, R. 2011 *Modern Control Systems*, 12th edn. Prentice Hall College Division.
- BISHOP, R. E. D. & HASSAN, A. Y. 1964 The lift and drag forces on a circular cylinder oscillating in a flowing fluid. *Proceedings of the Royal Society of London, series A* **277** (1368), 51–75.
- BLACKBURN, H. M. & KARNIADAKIS, G. E. 1993 Two- and three-dimensional simulations of vortex-induced vibration of a circular cylinder. In *Proceedings of the Third International Offshore and Polar Engineering Conference, Singapore*.
- BLEVINS, R. 1977 *Flow-Induced Vibration*. Van Nostrand Reinhold Co.
- BLEVINS, R. 1990 *Flow-Induced Vibration*, 2nd edn. Malabar: Krieger Publishing Company.
- BOKAIAN, A. R. & GEOOLA, F. 1983 On the cross flow response of cylindrical structures. *Proc. Inst. Cir. Eng* **75**, 397–418.
- BOKAIAN, A. R. & GEOOLA, F. 1984 Hydroelastic instabilities of square cylinders. *Journal of Sound and Vibration* **92**, 117–141.

References

- BOUCLIN, D. N. 1977 Hydroelastic oscillations of square cylinders. Master's thesis, University of British Columbia, Vancouver, BC, Canada.
- BRANKOVIĆ, M. 2004 Vortex-induced vibration attenuation of circular cylinders with low mass and damping. PhD thesis, Imperial College London.
- BRIKA, D. & LANEVILLE, A. 1993 Vortex-induced vibrations of a long flexible circular cylinder. *Journal of Fluid Mechanics* **250**, 481–481.
- BUDYNAS, R. & NISBETT, J. 2008 *Shigley's Mechanical Engineering Design*, , vol. 10. McGraw-Hill.
- CALLENDER, A., HARTREE, D. & PORTER, A. 1936 Time-lag in a control system. *Philosophical Transactions of the Royal Society of London. Series A, Mathematical and Physical Sciences* **235** (756), 415.
- CARBERRY, J. 2002 Wake states of a submerged oscillating cylinder and of a cylinder beneath a free-surface. PhD thesis, Monash University.
- CARBERRY, J., GOVARDHAN, R., SHERIDAN, J., ROCKWELL, D. & WILLIAMSON, C. H. K. 2004a Wake states and response branches of forced and freely oscillating cylinders. *European Journal of Mechanics - B/Fluids* **23** (1), 89–97.
- CARBERRY, J., SHERIDAN, J. & ROCKWELL, D. 2001 Force and wake modes of an oscillating cylinder. *Journal of Fluids and Structures* **15**, 523–532.
- CARBERRY, J., SHERIDAN, J. & ROCKWELL, D. 2004b Cylinder oscillations beneath a free-surface. *European Journal of Mechanics - B/Fluids* **23** (1), 81–88.
- CARBERRY, J., SHERIDAN, J. & ROCKWELL, D. 2005 Controlled oscillations of a cylinder: forces and wake modes. *Journal of Fluid Mechanics* **538**, 31–69.
- CORLESS, R. & PARKINSON, G. V. 1988 A model of the combined effects of vortex-induced oscillation and galloping. *Journal of Fluids and Structures* **2** (3), 203–220.
- CORLESS, R. M. & PARKINSON, G. V. 1993 Mathematical modelling of the combined effects of vortex-induced vibration and galloping. Part II. *Journal of Fluids and Structures* **7**, 825–848.
- DEN HARTOG, J. 1932 Transmission Line Vibration Due to Sleet. *Transactions of the American Institute of Electrical Engineers* **51** (4), 1074–1076.
- DEN HARTOG, J. 1956 *Mechanical Vibrations*. McGraw-Hill Book Company.
- DUSTING, J. C. 2006 An analysis of flows within cell culture bioreactors with vortex breakdown. PhD thesis, Monash University.
- FENG, C. 1968 The measurement of vortex-induced effects in flow past stationary and oscillating circular and D-section cylinders. Master's thesis, University of British Columbia.
- FEY, U., KÖNIG, W. & ECKELMANN, H. 1998 A new Strouhal–Reynolds-number relationship for the circular cylinder in the range $47 < Re < 2 \times 10^5$. *Physics of Fluids* **10** (7), 1547–1549.

- FOURAS, A., LO JACONO, D. & HOURIGAN, K. 2008 Target-free stereo PIV: A novel technique with inherent error estimation and improved accuracy. *Experiments in Fluids* **44** (2), 317–329.
- FOURAS, A. & SORIA, J. 1998 Accuracy of out-of-plane vorticity measurements derived from in-plane velocity field data. *Experiments in Fluids* **25** (5–6), 409–430.
- GABBAI, R. & BENAROYA, H. 2005 An overview of modeling and experiments of vortex-induced vibration of circular cylinders. *Journal of Sound and Vibration* **282** (3–5), 575–616.
- GASTER, M. 1969 Vortex shedding from slender cones at low Reynolds numbers. *Journal of Fluid Mechanics* **38** (Part 3), 565–576.
- GASTER, M. 1971 Vortex shedding from circular cylinders at low Reynolds numbers. *Journal of Fluid Mechanics* **46**, 749–756.
- GERRARD, J. 1966 The mechanics of the formation region of vortices behind bluff bodies. *Journal of Fluid Mechanics* **25** (2), 401–413.
- GOPALKRISHNAN, R. 1993 Vortex-induced forces on oscillating bluff cylinders. PhD thesis, Massachusetts Institute of Technology.
- GOVARDHAN, R. & WILLIAMSON, C. H. K. 2000 Modes of vortex formation and frequency response of a freely vibrating cylinder. *Journal of Fluid Mechanics* **420**, 85–130.
- GOVARDHAN, R. & WILLIAMSON, C. H. K. 2002 Resonance forever: existence of a critical mass and an infinite regime of resonance in vortex-induced vibration. *Journal of Fluid Mechanics* **473**, 147–166.
- GOVARDHAN, R. & WILLIAMSON, C. H. K. 2006 Defining the modified Griffin plot in vortex-induced vibration: revealing the effect of Reynolds number using controlled damping. *Journal of Fluid Mechanics* **561**, 147.
- GRIFFIN, O. & KOOPMANN, G. 1977 The vortex-excited lift and reaction forces on resonantly vibrating cylinders. *Journal of Sound and Vibration* **54** (3), 435–448.
- GRIFFIN, O. M. & HALL, M. S. 1991 Review of vortex shedding lock-on and flow control in bluff body wakes. *Journal of Fluids Engineering-Transactions of the ASME* **113**, 526–537.
- GRINSTED, A., MOORE, J. C. & JEVREJEVA, S. 2004 Nonlinear processes in geophysics application of the cross wavelet transform and wavelet coherence to geophysical time series. *Nonl. Procs. Geophysics* **11**, 561–566.
- GU, W., CHYU, C. & ROCKWELL, D. 1994 Timing of vortex formation from an oscillating cylinder. *Physics of Fluids* **6** (11), 3677–3682.
- HAMMACHE, M. & GHARIB, M. 1991 An experimental study of the parallel and oblique vortex shedding from circular cylinders. *Journal of Fluid Mechanics* **232**, 567–590.
- HART, D. 2000 PIV error correction. *Experiments in Fluids* **29** (1), 13–22.
- HENDERSON, R. 1997 Nonlinear dynamics and pattern formation in turbulent wake transition. *Journal of Fluid Mechanics* **352** (1), 65–112.

References

- HENDERSON, R. D. & BARKLEY, D. 1996 Secondary instability in the wake of a circular cylinder. *Physics of Fluids* **8**, 1683–1685.
- HIBBELER, R. C. 2008 *Mechanics of Materials*, 7th edn. Prentice Hall.
- HOVER, F. S. 1997 Vortex-induced vibration of marine cables: Experiments using force feedback. *Journal of Fluids and Structures* **11** (3), 307–326.
- HOVER, F. S., TECHET, A. H. & TRIANTAFYLLOU, M. S. 1998 Forces on oscillating uniform and tapered cylinders in crossflow. *Journal of Fluid Mechanics* **363**, 97–114.
- HUERRE, P. & MONKEWITZ, P. 1990 Local and global instabilities in spatially developing flows. *Annual Review of Fluid Mechanics* **22** (1), 473–537.
- INMAN, D. 2008 *Engineering Vibrations*. Pearson Prentice Hall.
- VON KÁRMÁN, T. 1911 Über den mechanismus des widerstands, den ein bewegter bewegter körper in einer flüssigkeit erfährt. *Göttingen Nach. Math. Phys. Kl.* pp. 509–519.
- KARNIADAKIS, G. E. & TRIANTAFYLLOU, G. S. 1989 Frequency selection and asymptotic states in laminar wakes. *Journal of Fluid Mechanics* **199**, 441–469.
- KHALAK, A. & WILLIAMSON, C. H. K. 1996 Dynamics of a Hydroelastic Cylinder With Very Low Mass and Damping. *Journal of Fluids and Structures* **10** (5), 455–472.
- KHALAK, A. & WILLIAMSON, C. H. K. 1997a Fluid forces and dynamics of a hydroelastic structure with very low mass and damping. *Journal of Fluids and Structures* **11** (8), 973–982.
- KHALAK, A. & WILLIAMSON, C. H. K. 1997b Investigation of relative effects of mass and damping in vortex-induced vibration of a circular cylinder. *Journal of Wind Engineering & Industrial Aerodynamics* **69**, 341–350.
- KHALAK, A. & WILLIAMSON, C. H. K. 1999 Motions, forces and mode transitions in vortex-induced vibrations at low mass-damping. *Journal of Fluids and Structures* **13** (7-8), 813–851.
- KLAMO, J., LEONARD, A. & ROSHKO, A. 2006 The effects of damping on the amplitude and frequency response of a freely vibrating cylinder in cross-flow. *Journal of Fluids and Structures* **22** (6-7), 845–856.
- KLAMO, J. T. 2007 Effects of Damping and Reynolds Number on Vortex-Induced Vibrations. PhD thesis, California Institute of Technology.
- KOOPMANN, G. 1967 The vortex wakes of vibrating cylinders at low Reynolds numbers. *Journal of Fluid Mechanics* **28**, 501—512.
- LEONTINI, J. S. 2007 A numerical investigation of transversely-oscillating cylinders in two-dimensional flow. PhD thesis, Monash University.
- LEONTINI, J. S., STEWART, B. E., THOMPSON, M. C. & HOURIGAN, K. 2006a Predicting vortex-induced vibration from driven oscillation results. *Applied Mathematical Modelling* **30**, 1096–1102.

- LEONTINI, J. S., STEWART, B. E., THOMPSON, M. C. & HOURIGAN, K. 2006b Wake state and energy transitions of an oscillating cylinder at low Reynolds number. *Physics of Fluids* **18** (3), 067101.
- LEONTINI, J. S., THOMPSON, M. C. & HOURIGAN, K. 2006c The beginning of branching behaviour of vortex-induced vibration during two-dimensional flow. *Journal of Fluids and Structures* **22** (6), 857–864.
- LEONTINI, J. S., THOMPSON, M. C. & HOURIGAN, K. 2007 Three-dimensional transition in the wake of a transversely oscillating cylinder. *Journal of Fluid Mechanics* **577**, 79–104.
- LEWEKE, T. 2002 FLAIR Water Channel - Characterisation of Flow Quality. *Tech. Rep.*. Monash University, Melbourne, Australia.
- LIENHARD, J. 1966 *Synopsis of Lift, Drag, and Vortex Frequency Data for Rigid Circular Cylinders*. Technical Extension Service, Washington State University.
- LIGHTHILL, J. 1986 Fundamentals concerning wave loading on offshore structures. *Journal of Fluid Mechanics* **173**, 667–681.
- LIM, F. & HOWELLS, H. 2000 Deepwater riser VIV, fatigue and monitoring. In *Deep-water Pipeline and Riser Technology Conference, Houston*, pp. 6–9.
- LUO, S. & BEARMAN, P. W. 1990 Predictions of fluctuating lift on a transversely oscillating square-section cylinder. *Journal of Fluids and Structures* **4** (2), 219–228.
- LUO, S., CHEW, Y. & NG, Y. 2003 Hysteresis phenomenon in the galloping oscillation of a square cylinder. *Journal of Fluids and Structures* **18** (1), 103–118.
- MENEGHINI, J. R. & BEARMAN, P. W. 1995 Numerical simulation of high amplitude oscillatory flow about a circular cylinder. *Journal of Fluids and Structures* **9**, 435–455.
- MINORSKY, N. 1962 *Nonlinear Oscillations*. Princeton: D. Van Nostrand.
- MORSE, T. L., GOVARDHAN, R. & WILLIAMSON, C. H. K. 2008 The effect of end conditions on the vortex-induced vibration of cylinders. *Journal of Fluids and Structures* **24** (8), 1227–1239.
- MORSE, T. L. & WILLIAMSON, C. H. K. 2006 Employing controlled vibrations to predict fluid forces on a cylinder undergoing vortex-induced vibration. *Journal of Fluids and Structures* **22** (6-7), 877–884.
- MORSE, T. L. & WILLIAMSON, C. H. K. 2009a Fluid forcing, wake modes, and transitions for a cylinder undergoing controlled oscillations. *Journal of Fluids and Structures* **25** (4), 697–712.
- MORSE, T. L. & WILLIAMSON, C. H. K. 2009b Prediction of vortex-induced vibration response by employing controlled motion. *Journal of Fluid Mechanics* **634**, 5.
- NAUDASCHER, E. & ROCKWELL, D. 2005 *Flow-Induced Vibrations: An Engineering Guide*. Dover Publications.
- NAUDASCHER, E. & WANG, Y. 1993 Flow-induced vibrations of prismatic bodies and grids of prisms. *Journal of Fluids and Structures* **7**, 341–373.

References

- NAZARINIA, M. 2010 Flow around oscillating circular cylinders. PhD thesis, Monash University.
- NAZARINIA, M., LO JACONO, D., THOMPSON, M. C. & SHERIDAN, J. 2009 Flow behind a cylinder forced by a combination of oscillatory translational and rotational motions. *Physics of Fluids* **21** (5), 051701.
- NILSSON, J.W. AND RIEDEL, S. 1996 *Electric Circuits*, 5th edn. Addison-Wesley, Reading, Massachusetts.
- NISHIOKA, M. & SATO, H. 1978 Mechanism of determination of the shedding frequency of vortices behind a cylinder at low reynolds numbers. *Journal of Fluid Mechanics* **89** (Part 1), 49–60.
- NORBERG, C. 1993 Flow around rectangular cylinders: pressure forces and wake frequencies. *Journal of Wind Engineering and Industrial Aerodynamics* **49** (1-3), 187–196.
- NORBERG, C. 1994 An experimental investigation of the flow around a circular cylinder: influence of aspect ratio. *Journal of Fluid Mechanics* **258**, 287 – 316.
- NORBERG, C. 2001 Flow around a circular cylinder: aspects of fluctuating lift. *Journal of Fluids and Structures* **15**, 459–469.
- NOVAK, M. 1969 Aeroelastic galloping of prismatic bodies. *American Society of Civil Engineers, Journal of the Engineering Mechanics Division* **95**, 115–142.
- NOVAK, M. 1972 Galloping oscillations of prismatic structures. *Journal of the Engineering Mechanics Division* **98** (1), 27–46.
- NOVAK, M. & TANAKA, H. 1974 Effect of turbulence on galloping instability. *Journal of the Engineering Mechanics Division* **100** (1), 27–47.
- PAÏDOUSSIS, M., PRICE, S. & DE LANGRE, E. 2010 *Fluid-Structure Interactions: Cross-Flow-Induced Instabilities*. Cambridge University Press.
- PARKINSON, G. V. 1989 Phenomena and modelling of flow-induced vibrations on bluff bodies. *Progress in Aerospace Sciences* **26**, 169–224.
- PARKINSON, G. V. & BROOKS, N. P. H. 1961 On the aeroelastic instability of bluff cylinders. *Journal of Applied Mechanics* **28**, 252.
- PARKINSON, G. V. & SMITH, J. D. 1964 The square prism as an aeroelastic non-linear oscillator. *The Quarterly Journal of Mechanics and Applied Mathematics* **17** (2), 225.
- PARKINSON, G. V. & WAWZONEK, M. A. 1981 Some considerations of combined effects of galloping and vortex resonance. *Journal of Wind Engineering and Industrial Aerodynamics* **8** (1-2), 135–143.
- RAFFEL, M., WILLERT, C., WERELEY, S. & KOMPENHANS, J. 2007 *Particle Image Velocimetry: A Practical Guide*, 2nd edn. Springer.
- ROBINSON, A. & SAFFMAN, P. 1982 Three-dimensional stability of vortex arrays. *Journal of Fluid Mechanics* **125**, 411–427.

-
- ROSHKO, A. 1993 Perspectives on bluff body aerodynamics. *Journal of Wind Engineering and Industrial Aerodynamics* **49** (1-3), 79–100.
- RYAN, K., THOMPSON, M. & HOURIGAN, K. 2005 Variation in the critical mass ratio of a freely oscillating cylinder as a function of Reynolds number. *Physics of Fluids* **17**, 038106.
- SARPKAYA, T. 1977 Transverse oscillations of a circular cylinder in uniform flow, part 1. revised. *Tech. Rep.*. DTIC Document.
- SARPKAYA, T. 1978 Fluid forces on oscillating cylinders. *NASA STI/Recon Technical Report A* **78**, 46523.
- SARPKAYA, T. 1995 Hydrodynamic damping, flow-induced oscillations, and biharmonic response. *Journal of Offshore Mechanics and Arctic Engineering* **117**, 232.
- SARPKAYA, T. 2004 A critical review of the intrinsic nature of vortex-induced vibrations. *Journal of Fluids and Structures* **19** (4), 389–447.
- STANSBY, P. K. 1976 The locking-on of vortex shedding due to the cross-stream vibration of circular cylinders in uniform and shear flows. *Journal of Fluid Mechanics* **74**, 641–665.
- STAUBLI, T. 1983 Calculation of the vibration of an elastically mounted cylinder using experimental data from forced oscillation. *Journal of Fluids Engineering* **105**, 225.
- STROUHAL, V. 1878 Uber eine besondere Art der Tonerregung. *Ann. Physik. Chem.* **5** (10), 216–251.
- SULLIVAN, P. 1977 Aeroelastic galloping of tall structures in simulated winds. PhD thesis, University of British Columbia.
- SUMER, B. & FREDSSØE, J. 1997 *Hydrodynamics Around Cylindrical Structures*, 1st edn., *Advanced Series on Ocean Engineering*, vol. 12. World Scientific.
- SZEPESSY, S. & BEARMAN, P. W. 1992 Aspect ratio and end plate effects on vortex shedding from a circular cylinder. *Journal of Fluid Mechanics* **234**, 191–217.
- TANEDA, S. 1956 Experimental investigation of the wakes behind cylinders and plates at low Reynolds numbers. *Journal of the Physical Society of Japan* **11** (3), 302–307.
- THOMPSON, M., HOURIGAN, K. & SHERIDAN, J. 1996 Three-dimensional instabilities in the wake of a circular cylinder. *Experimental Thermal and Fluid Science* **12** (2), 190–196.
- THOMPSON, M. & LE GAL, P. 2004 The Stuart-Landau model applied to wake transition revisited. *European Journal of Mechanics-B/Fluids* **23** (1), 219–228.
- TRITTON, D. J. 1959 Experiments on the flow past a circular cylinder at low Reynolds numbers. *Journal of Fluid Mechanics* **6**, 547–567.
- VAN DYKE, M. 1982 *An Album of Fluid Motion*. Stanford, CA: Parabolic Press.
- WAWZONEK, M. A. 1979 Aeroelastic Behavior of Square Section Prisms in Uniform Flow. PhD thesis, University of British Columbia.

References

- WHITE, F. M. 2003 *Fluid Mechanics*, 5th edn. The McGraw-Hill Companies, Inc.
- WILLIAMSON, C. H. K. 1988 The existence of two stages in the transition to three-dimensionality of a cylinder wake. *Physics of Fluids* **31**, 3165.
- WILLIAMSON, C. H. K. 1989 Oblique and parallel mode of vortex shedding in the wake of a circular cylinder at low Reynolds numbers. *Journal of Fluid Mechanics* **206**, 579–627.
- WILLIAMSON, C. H. K. 1996 Vortex Dynamics in the Cylinder Wake. *Annual Review of Fluid Mechanics* **28**, 477–539.
- WILLIAMSON, C. H. K. & BROWN, G. 1998 A Series in $1/\sqrt{Re}$ Represent the Strouhal-Reynolds Number Relationship of the Cylinder Wake. *Journal of Fluids and Structures* **12**, 1073–1085.
- WILLIAMSON, C. H. K. & GOVARDHAN, R. 2004 Vortex-induced vibration. *Annual Review of Fluid Mechanics* **36**, 413–455.
- WILLIAMSON, C. H. K. & ROSHKO, A. 1988 Vortex formation in the wake of an oscillating cylinder. *Journal of Fluids and Structures* **2** (4), 355–381.
- ZDRAVKOVICH, M. M. 1997 *Flow Around Circular Cylinders, Vol 1: Fundamentals*. Oxford University Press, Oxford.
- ZIEGLER, J. G. & NICHOLS, N. B. 1942 Optimum settings for automatic controllers. *Transactions, ASME* **64** (8), 759–768.